The Effect of Pressure Oscillations on Respiratory Performance

Prasika Inderjeeth Reddy

A thesis submitted to Auckland University of Technology
in fulfilment of the degree of
Doctor of Philosophy

Auckland, New Zealand

DECLARATIONS

I hereby declare that I am the sole author of this thesis.

I authorize the Auckland University of Technology to lend this thesis to other institutions or individuals for the sole purpose of scholarly research

_____

Prasika I. Reddy

I further authorize the Auckland University of Technology to reproduce this thesis by photocopying or by other means, in total or in part, at the request of other institutions or individuals for the sole purpose of scholarly research.

_____

Prasika I. Reddy

BORROWERS PAGE

The Auckland University of Technology requires the signatures of all people using or photocopying this thesis. Accordingly, all borrowers are required to fill out this page.

Date	Name	Address	Signature

To my parents,

Inder and Prema Manilal

ACKNOWLEDGEMENTS

There are many people I would like to formally thank for their contribution to this thesis. The first and most significant being my academic supervisor, Professor Ahmed Al-Jumaily, for his dedication, knowledge and attentive supervision at every stage of this research and for the most incredible support and encouragement he has given not just to me but to all his students. I also owe a great deal to my industrial supervisor, Dr. Geoff Bold who made sure that I had the best available resources, training and specialized support through him and other colleagues in the field. Your analytical approach and humility towards research, and the world in general, will stay with me always.

I like to acknowledge the Tertiary Education Commission and Fisher & Paykel Healthcare Ltd. for generously funding this research.

My thanks to Associate Prof. Jane Pillow for providing the in-vivo data that served as the validation for this work and to her, Prof. Alan Jobe and their team in Perth for sharing their clinical knowledge, guidance and resources during the animal trials. Also, I thank Chris Butcher and Christian Saville for their assistance during this time. I'm grateful to David White, Phil Lacey, Dr. Max Ramos, Ross Reichardt, Bradley Scott, Chris Whyburd and Yan Wang from the School of Engineering for the technical expertise and priority that you attached to the project despite your busy schedules. Thank you to my fellow students, Drs. Alex Du and Robert Paxton, Gijs Ijpma, Joe El-Aklouk, Hai Lan and Ashis Mookerji for your academic, technical and brotherly help throughout the years and making IBTEC an all round great place to be.

On a personal note, Thank you to my relatives and friends for always supporting and encouraging me to do my best. Thank you Arnz, for being an "excellent" proof reader. To my husband and inspiration, Murali, who has had to share my burdens and has been constantly at my side, a simple "Thank you" will not suffice. It is with you that I share this work. To Mum and Dad, I hope that this in some small way makes up for the all the sacrifices you've had to make for my education and happiness. Finally, a quiet thank you to God, for all the grace and strength you have given me. I offer this work to you.

ABSTRACT

This thesis is aimed at understanding the effective operation of the Bubble CPAP System when treating neonates with respiratory distress syndrome (RDS). It is also aimed at determining the effect that pressure oscillations have on respiratory performance in terms of the work of breath (WOB) and surfactant dynamics. The principle objectives were to:

- Create an original multi-compartmental model of the neonatal lung that includes compartment-specific inertance and viscoelasticity for 128 day (premature) and 142 day (near-term) gestation lambs.
- Validate the model with experimental data obtained from clinical trials.
- Use the model to determine the effect of pressure oscillations as produced by the Bubble CPAP System on respiratory performance.
- Determine the frequencies of oscillation that provide the optimal respiratory support.
- Build a surface tension model that simulates surface tension dynamics in an alveolus exposed to pressure oscillation frequencies in the range typically produced by the Bubble CPAP System.
- Validate the surface tension model with experiments conducted on a custom-built pulsating bubble surfactometer (PBS).

To fulfill the first four objectives, a mathematical model of the neonatal ovine lung was developed in Simulink within the Matlab environment. Mechanical and physical parameters that were required for the model were either empirically determined from measurements on preterm lamb lungs or derived from the literature. Simulations were then performed to determine the effectiveness of Bubble CPAP and the use of 'optimal frequencies' in neonatal respiration.

To study the surface tension dynamics, a PBS was constructed to study the effect of frequencies on a surfactant bubble which simulated an alveolus. Modulated frequencies (10-70 Hz) were superimposed on the breath cycle at 3 different amplitudes expressed as a percentage of the tidal volume (TV) excursion (15%TV, 22.5%TV and 30%TV). A numerical model was also built in Matlab to characterize the surfactant behaviour and help determine the mechanisms responsible for any observed changes in surface tension.

The experimental results and computer simulations resulted in the following conclusions:

- The model is able to accurately predict the respiratory parameters at the airway opening during CPAP and Bubble CPAP operation.
- The model shows the ability to predict the uneven ventilation profiles in the neonatal lung.
- Both model predictions and experimental measurements show the trend that the mechanical WOB is greater (improved) during ventilation under Bubble CPAP when compared to CPAP.
- Pressure oscillation frequencies which show improved WOB measures in the 128 day gestation lamb lung were identified as 19, 23, 28, 33, 44, 49, 54, 81, 88, 99, 111 and 113 Hz.
- Model predictions showed that the improvement in WOB (due to mechanical effects) relative to CPAP-only treatment was 1-2% when introducing single frequencies at the generator, but increased to 4-6% when introducing 'mixed frequencies' at the generator and 4-10% when introducing 'mixed frequencies' at the patient interface.
- It was shown that the Bubble CPAP System delivers frequencies similar to the identified optimal frequencies of the 128 day gestation lung (17 and 23 Hz) which contribute to the noticed improvement in WOB.
- The average trends of all the experiments on a PBS and results from the numerical model revealed that the minimum and maximum surface tension in an alveolus decreases with increasing frequency and increasing amplitude.
- The mechanism of improvement of surface tension in the alveolus with frequency and amplitude is due to the increased diffusion and adsorption of surfactant molecules to the air-liquid interface, increasing the interfacial surface concentration and decreasing the surface tension.

TABLE OF CONTENTS

LIST OF FIGURES

LIST OF TABLES

LIST OF NOTATIONS

α	Dimensionless diffusion coefficient
a	Scaling coefficient
A	Time varying area of a bubble
A^*	Interfacial area corresponding to equilibrium surface tension
$A_{\gamma_{min}}$	Interfacial area corresponding to minimum surface tension
A_{lobe}	Alveolar surface area of a lobe
$A_{\text{L card}}$	Alveolar surface area of left cardiac lobe
$A_{\text{L diaph}}$	Alveolar surface area of left diaphragmatic lobe
A_{pleural}	Surface area of pleural surface
$A_{\text{R api}}$	Alveolar surface area of right apical lobe
$A_{\text{R card}}$	Alveolar surface area of right cardiac lobe
$A_{\text{R diaph}}$	Alveolar surface area of right diaphragmatic lobe
b	Scaling coefficient
B_{pleural}	Effective bulk modulus of pleural fluid
c	Scaling coefficient
c_{damp}	Damping coefficient
C	Concentration
C_{bot}	Concentration at the midpoint of the upwind node
C_{bulk}	Bulk liquid concentration
C_{CW}	Chest wall compliance
C_L	Lung compliance
$C_{\text{L card lobe}}$	Conductance in the left cardiac lobe
$C_{\text{L diaph lobe}}$	Conductance in the left diaphragmatic lobe
C_{lobe}	Conductance in a lobe
$C_{\text{R api lobe}}$	Conductance in the right apical lobe
$C_{\text{R card lobe}}$	Conductance in the right cardiac lobe
$C_{\text{R diaph lobe}}$	Conductance in the right diaphragmatic lobe

C_T	Total respiratory system compliance
C_{top}	Concentration at the midpoint of the downwind lobe
ΔP_{airway}	Pressure difference across an airway
ΔP_{total}	Total static pressure loss in an airway segment
$\Delta P_{poiseuille}$	Poiseuille pressure loss in an airway segment
d	Scaling coefficient
D	Diffusion coefficient
$D_{\text{L card}}$	Diameter of left cardiac bronchus
$D_{\text{L main}}$	Diameter of left main bronchus
$D_{\text{L maj diaph}}$	Diameter of left major diaphragmatic bronchus
$D_{\text{low trachea}}$	Diameter of lower trachea
$D_{\text{L post diaph}}$	Diameter of left posterior diaphragmatic bronchus
$D_{\text{R ant diaph}}$	Diameter of right anterior diaphragmatic bronchus
$D_{\text{R api}}$	Diameter of right apical bronchus
$D_{\text{R card}}$	Diameter of right cardiac bronchus
$D_{\text{R main}}$	Diameter of right main bronchus
$D_{\text{R maj diaph}}$	Diameter of right major diaphragmatic bronchus
$D_{\text{R post diaph}}$	Diameter of right posterior diaphragmatic bronchus
$D_{section}$	Diameter of an airway section
$D_{\text{up trachea}}$	Diameter of upper trachea
E_L	Lung elastance
$f_{\text{L card}}$	Constant viscous resistance in left cardiac lobe
$f_{\text{L diaph}}$	Constant viscous resistance in left diaphragmatic lobe
f_{lobe}	Constant viscous resistance in a lobe
$f_{\text{R api}}$	Constant viscous resistance in right apical lobe
$f_{\text{R card}}$	Constant viscous resistance in right cardiac lobe
$f_{\text{R diaph}}$	Constant viscous resistance in right diaphragmatic lobe

f_{pleural}	Viscous resistance of pleural compartment and chest wall
F_{th}	Thoracic Force
Γ	Interfacial concentration
Γ^*	Equilibrium interfacial concentration
Γ_{max}	Maximum interfacial concentration
γ	Surface Tension
γ^*	Equilibrium surface tension
γ_{min}	Minimum surface tension
γ_0	Surface tension of water
J	Diffusive flux
κ	Surface dilational viscosity
k_1	Adsorption coefficient
k_2	Desorption coefficient
$k_{\text{L card}}$	Variable spring stiffness of left cardiac lobe
$k_{\text{L diaph}}$	Variable spring stiffness of left diaphragmatic lobe
k_{lobe}	Variable spring stiffness in a lobe
$k_{\text{R api}}$	Variable spring stiffness of right apical lobe
$k_{\text{R card}}$	Variable spring stiffness of right cardiac lobe
$k_{\text{R diaph}}$	Variable spring stiffness of right diaphragmatic lobe
k_{pleural}	Variable spring stiffness of pleural compartment and chest wall
l_D	Diffusive length
l_A	Adsorptive length
L_∞	Depth of bulk liquid
$L_{\text{L card}}$	Length of left cardiac bronchus
$L_{\text{L main}}$	Length of left main bronchus
$L_{\text{L maj diaph}}$	Length of left major diaphragmatic bronchus
$L_{\text{low trachea}}$	Length of lower trachea
$L_{\text{L post diaph}}$	Length of left posterior diaphragmatic bronchus

$L_{\text{R ant diaph}}$	Length of right anterior diaphragmatic bronchus
$L_{\text{R api}}$	Length of right apical bronchus
$L_{\text{R card}}$	Length of right cardiac bronchus
$L_{\text{R main}}$	Length of right main bronchus
$L_{\text{R maj diaph}}$	Length of right major diaphragmatic bronchus
$L_{\text{R post diaph}}$	Length of right posterior diaphragmatic bronchus
L_{section}	Length of an airway section
$L_{\text{up trachea}}$	Length of upper trachea
μ	dynamic viscosity
m_1	Slope of isotherm in regime 1
m_2	Slope of isotherm in regime 2
m_{in}	Mass that enters a section/lobe
m_{lobe}	Mass of air in a lobe
m_{out}	Mass that leaves a section/lobe
$m_{\text{sec}tion}$	Mass of air in a section
M	Mass of surfactant at the interface
$M_{\text{L card}}$	Mass of left cardiac lobe
$M_{\text{L diaph}}$	Mass of left diaphragmatic lobe
M_{lobe}	Mass of a lobe
M_{pleural}	Mass of pleural compartment and chest wall
$M_{\text{R api}}$	Mass of right apical lobe
$M_{\text{R card}}$	Mass of right cardiac lobe
$M_{\text{R diaph}}$	Mass of right diaphragmatic lobe
$\dot{m}_{\text{L bronchi}}$	The sum of $\dot{m}_{\text{L post diaph}}$, $\dot{m}_{\text{L maj diaph}}$ and $\dot{m}_{\text{L card}}$
$\dot{m}_{\text{L card}}$	Mass flow rate into the left cardiac bronchus
$\dot{m}_{\text{L card lobe}}$	Mass flow rate into left cardiac lobe
$\dot{m}_{\text{L card wall}}$	Mass flow rate due to left cardiac lobe wall movement
$\dot{m}_{\text{L diaph lobe}}$	Mass flow rate into left diaphragmatic lobe

$\dot{m}_{\text{L diaph wall}}$	Mass flow rate due to left diaphragmatic lobe wall movement
$\dot{m}_{\text{L main}}$	Mass flow rate into the left main bronchus
$\dot{m}_{\text{L maj diaph}}$	Mass flow rate into the left major diaphragmatic bronchus
$\dot{m}_{\text{L maj diaph lobe}}$	Mass flow rate leaving left major diaphragmatic bronchus
$\dot{m}_{\text{mid trachea}}$	Mass flow rate into the mid trachea
$\dot{m}_{\text{lobe wall}}$	Mass flow rate due to lobe wall movement
$\dot{m}_{\text{low trachea}}$	Mass flow rate into the lower trachea
$\dot{m}_{\text{L post diaph}}$	Mass flow rate into the right posterior diaphragmatic bronchus
$\dot{m}_{\text{L post diaph lobe}}$	Mass flow rate leaving left posterior diaphragmatic bronchus
$\dot{m}_{\text{R ant diaph}}$	Mass flow rate into the right anterior diaphragmatic bronchus
$\dot{m}_{\text{R ant diaph lobe}}$	Mass flow rate leaving right anterior diaphragmatic bronchus
$\dot{m}_{\text{R api}}$	Mass flow rate into the right apical bronchus
$\dot{m}_{\text{R api lobe}}$	Mass flow rate leaving right apical bronchus
$\dot{m}_{\text{R api wall}}$	Mass flow rate due to right apical lobe wall movement
$\dot{m}_{\text{main}}$	Mass flow rate into the main bronchi
$\dot{m}_{\text{R bronchi}}$	The sum of $\dot{m}_{\text{R post diaph}}$, $\dot{m}_{\text{R ant diaph}}$, $\dot{m}_{\text{R maj diaph}}$ and $\dot{m}_{\text{R card}}$
$\dot{m}_{\text{R card}}$	Mass flow rate into the right cardiac bronchus
$\dot{m}_{\text{R card lobe}}$	Mass flow rate leaving right cardiac bronchus
$\dot{m}_{\text{R card wall}}$	Mass flow rate due to right cardiac lobe wall movement
$\dot{m}_{\text{R diaph lobe}}$	Mass flow rate into right diaphragmatic lobe
$\dot{m}_{\text{R maj diaph lobe}}$	Mass flow rate leaving right major diaphragmatic bronchus
$\dot{m}_{\text{R diaph wall}}$	Mass flow rate due to right diaphragmatic lobe wall movement
$\dot{m}_{\text{R main}}$	Mass flow rate into the right main bronchus
$\dot{m}_{\text{R maj diaph}}$	Mass flow rate into the right major diaphragmatic bronchus
$\dot{m}_{\text{R post diaph}}$	Mass flow rate into the right posterior diaphragmatic bronchus
$\dot{m}_{\text{R post diaph lobe}}$	Mass flow rate leaving right posterior diaphragmatic bronchus
$\dot{m}_{\text{sec}tion}$	Mass flow rate in a section

$\dot{m}_{\text{up trachea}}$	Mass flow rate into the upper trachea
N_C	Number of cycles
N_{SC}	Number of time steps per cycle
N_{SN}	Number if special nodes
ω	Cycling frequency
P	Pressure
P_{atm}	Atmospheric Pressure
$P_{\text{interface}}$	Pressure in patient interface
$P_{\text{L card}}$	Pressure in left cardiac bronchus
$P_{\text{L card lobe}}$	Pressure in the left cardiac lobe
$P_{\text{L diaph lobe}}$	Pressure in the left diaphragmatic lobe
P_{lobe}	Absolute pressure within a section
$P_{\text{low trachea}}$	Pressure in lower trachea
$P_{\text{L main}}$	Pressure in left main bronchus
$P_{\text{L maj diaph}}$	Pressure in left major diaphragmatic bronchus
$P_{\text{L post diaph}}$	Pressure in left posterior diaphragmatic bronchus
P_{pleural}	Pleural Pressure
$P_{\text{R ant diaph}}$	Pressure in right anterior diaphragmatic bronchus
$P_{\text{R api}}$	Pressure in right apical bronchus
$P_{\text{R api lobe}}$	Pressure in the right apical lobe
$P_{\text{R card}}$	Pressure in right cardiac bronchus
$P_{\text{R card lobe}}$	Pressure in the right cardiac lobe
$P_{\text{R diaph lobe}}$	Pressure in the right diaphragmatic lobe
$P_{\text{R main}}$	Pressure in right main bronchus
$P_{\text{R maj diaph}}$	Pressure in right major diaphragmatic bronchus
$P_{\text{R post diaph}}$	Pressure in right posterior diaphragmatic bronchus
$P_{\text{up trachea}}$	Pressure in upper trachea

P_{upwind}	Pressure on the upwind boundary of a lumped segment
$P_{section}$	Absolute pressure within a section
Q	Volume flow rate
ρ	Density
r	Radius of a bubble
R	Specific gas constant of air
$R(t)$	Time varying radius of a bubble
R^2	Best-fit coefficient
Re	Reynolds number
R_{lobe}	Airway Resistance in a lobe
$R_{\text{lobes total}}$	Total airway resistance of all lobes
t	Time
T	Temperature in Kelvin
T_{cycle}	Cycle time
v	Velocity of the bulk fluid
V	Volume
V_{cycle}	Cyclic volume of bubble
$V_{\text{L card}}$	Volume of left cardiac bronchus
$V_{\text{L card lobe}}$	Volume of the left cardiac lobe
$V_{\text{L diaph lobe}}$	Volume of the left diaphragmatic lobe
$V_{\text{L main}}$	Volume of left main bronchus
$V_{\text{L maj diaph}}$	Volume of left major diaphragmatic bronchus
V_{lobe}	Volume of a lobe
$V_{\text{low trachea}}$	Volume of lower trachea
$V_{\text{L post diaph}}$	Volume of left posterior diaphragmatic bronchus
V_{max}	Maximum bubble volume
V_{mean}	Mean bubble volume
V_{min}	Minimum bubble volume
V_{pleural}	Volume of pleural fluid

$V_{\text{R api}}$	Volume of right apical bronchus
$V_{\text{R api lobe}}$	Volume of the right apical lobe
$V_{\text{R ant diaph}}$	Volume of right anterior diaphragmatic bronchus
$V_{\text{R card}}$	Volume of right cardiac bronchus
$V_{\text{R card lobe}}$	Volume of the right cardiac lobe
$V_{\text{R diaph lobe}}$	Volume of the right diaphragmatic lobe
v_{rel}	Relative velocity of the bubble interface
v_{relbot}	Velocity at the midpoint of the upwind node
v_{reltop}	Velocity at the midpoint of the downwind node
$V_{\text{R main}}$	Volume of right main bronchus
$V_{\text{R maj diaph}}$	Volume of right major diaphragmatic bronchus
$V_{\text{R post diaph}}$	Volume of right posterior diaphragmatic bronchus
$V_{\text{sec}tion}$	Volume of a section
$V_{\text{up trachea}}$	Volume of upper trachea
$\overline{WOB}$	Mean work of breath
$\overline{WOB}_{\text{exp}}$	Mean work of breath during expiration
$\overline{WOB}_{insp}$	Mean work of breath during inspiration
$\overline{WOB}_{total}$	Mean work of breath in one breath cycle
ξ	Damping factor
x	Distance
$x_{\text{L card wall}}$	Displacement of left cardiac wall
$x_{\text{L diaph wall}}$	Displacement of diaphragmatic wall
$x_{\text{lobe wall}}$	Displacement of a lobe wall
x_{pleural}	Displacement of pleural compartment
$x_{\text{R api wall}}$	Displacement of right apical wall
$x_{\text{R card wall}}$	Displacement of right cardiac wall
$x_{\text{R diaph wall}}$	Displacement of right diaphragmatic wall
Z_L	Respiratory system impedance

ABBREVIATIONS

BPD	Bronchopulmonary dysplasia
BVV	Biologically variable ventilation
CBS	Captive bubble surfactometers
CFD	Computational fluid dynamics
CPAP	Continuous positive airway pressure
CT	Computer tomography
ERV	Expiratory reserve volume
fps	Frames per second
FiO_2	Fraction of inspired oxygen
FRC	Functional residual capacity
HFFI	High-frequency flow interruption
HFJV	High-frequency jet ventilation
HFO	High-frequency oscillation
HFPPV	High-frequency positive pressure ventilation
HFPV	High-frequency percussive ventilation
HFV	High-frequency ventilation
IC	Inspiratory capacity
IMV	Intermittent mandatory ventilation
IRV	Inspiratory reserve volume
KOH	Potassium Hydroxide
MV	Mechanical Ventilation
nCPAP	Nasal continuous positive airway pressure
NaCl	Sodium chloride
NICUs	Neonatal intensive care units
$PaCO_2$	Partial pressure of arterial carbon dioxide
PaO_2	Partial pressure of arterial oxygen
PBS	Pulsating bubble surfactometers
PCV	Pressure-controlled ventilation
PFV	Photron Fastcam Viewer
PIP	Peak inspiratory pressure
PSD	Power spectral density
P-V	Pressure-Volume

RDS	Respiratory distress syndrome
RV	Residual volume
SIMV	synchronized intermittent mandatory ventilation
TLC	Total lung capacity
TV	Tidal volume
VC	Vital capacity
VCV	Volume-controlled ventilation
WOB	Work of breathing
WTP	Work-time product

CHAPTER 1

Introduction

1.1. Background

The most common reason to initiate ventilation of a neonate (newborn infant) is respiratory failure. This can be caused by conditions that arise either from a failure of the central nervous system or where there is a ventilation-perfusion mismatch caused by physiological disruptions. Conditions arising from the first type are apnoea due to prematurity, intracranial haemorrhage, birth asphyxia and drug overdose. In these cases, the neonate does not breathe because the respiratory drive is suppressed and hence mechanical ventilation (MV) is absolutely necessary. In the second type, pulmonary gas exchange is inadequate to sustain required partial pressures of arterial carbon dioxide ($PaCO_2$) and oxygen (PaO_2). The inadequacy in gas exchange is caused by diseases stemming from physiological changes, inflammation and infection of membranes in the respiratory system, such as respiratory distress syndrome (RDS), pneumonia, pneumothorax, diaphragmatic hernia and tumours [1]. Of specific interest for this research is RDS (previously called hyaline membrane disease).

Respiratory distress syndrome is the most common respiratory illness to affect neonates. It remains the leading cause of infant mortality and morbidity. With the progress in technology, there are increasing options for providing quality respiratory ventilation for neonates. Irrespective of the type of respiratory ventilation, the goals of ventilation remain the same, namely to maintain adequate gas exchange in the lungs and reduce the work of breath (WOB) of the patient while minimizing injury to the lungs and maintaining the highest level of patient comfort. The traditional method of respiratory ventilation has been mechanical ventilators. However, the use of such ventilators on

delicate premature lungs causes many of the survivors of RDS to develop bronchopulmonary dysplasia (BPD) resulting from barotrauma [2-4]. Ventilation at low lung volumes also worsen lung injury due to the repetitive opening and closing of collapsed regions (atelectrauma) [5, 6].A variety of other respiratory support techniques have been administered since in an effort to reduce the possibility of over-distension of the airways and shear stresses on the epithelial walls, as is common in mechanical ventilation.

The Bubble Continuous Positive Airway Pressure (CPAP) System developed by Fisher & Paykel Healthcare is one such respiratory support device which combines the effects of traditional CPAP and pressure oscillations. It has clinically reported benefits over mechanical ventilation [7-14]; however, the mechanisms of lung recruitment and the role that the pressure oscillations may play in optimising the operation of the system require more and is thus the subject of investigation in this thesis.

1.2. Respiratory Distress Syndrome

Respiratory distress syndrome is caused by insufficient surfactant production in the alveoli (air sacs) and underdeveloped lung structure [1, 15-17]. Surfactant and lung structure development can be explained in the context of gestational age with the aid of Figure 1.1 [1, 15]. Lung development is partitioned into five phases: (1) Embryonic phase (3-6 weeks), (2) Pseudoglandular phase (6-16 weeks), (3) Canalicular phase (16-26 weeks), (4) Saccular phase (26-36 weeks), (5) Alveolar phase (36 weeks – 3 years). The expected date of delivery is calculated at 40 weeks of pregnancy. Normal pregnancy is considered to occur between 37 to 42 weeks. Infants born before 37 weeks of age are considered to be preterm and infants are termed as neonates up to 28 days after birth.

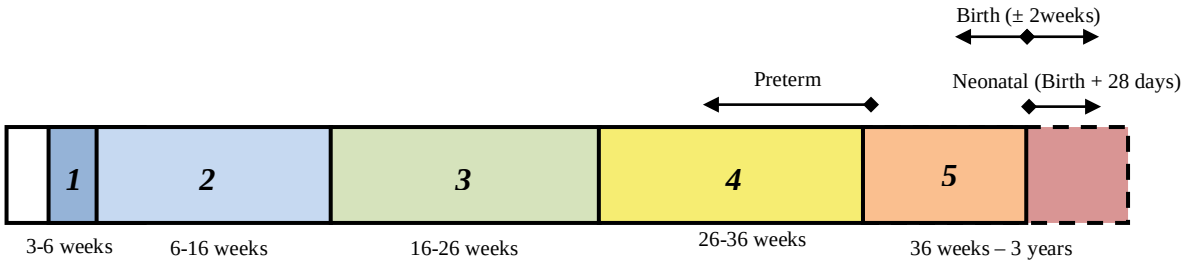

Figure 1.1 Human lung development with gestation.

Surfactant is produced by the alveolar type II cells in lamellar bodies. It performs the function of decreasing the surface tension forces at the air-liquid interface in the alveoli and is therefore a prerequisite to breathing. Once secreted by the lamellar bodies, the surfactant is transported to the air-liquid interface where it spreads as a monolayer and acts to reduce the surface tension. This process starts around week 26 post conception and is not yet fully completed in the saccular phase (26-36 weeks). Infants born in this period have lungs with insufficient surfactant and alveoli to facilitate adequate ventilation. A lack of surfactant in preterm infants means that the surface tension forces in their alveoli are much higher and act to decrease the surface area of the alveoli to such an extent that they collapse, marking the onset of RDS.

Traditional surfactant therapies and ventilation techniques have been used in neonatal intensive care units (NICUs) to treat RDS. These are discussed in Sections 1.2.1 and 1.2.2 respectively.

1.2.1. Surfactant Therapy

Natural surfactants that are currently used in the treatment of RDS are lipid extracts of bovine lung mince (Surfactant TA and Survanta), extracts of bovine lung washes (Infasurf, Alveofact and BLES) and extracts of porcine lung mince (Curosurf).

Examples of synthetic surfactants are Exosurf and Pumactant. The main incentive towards their development is the high price of natural surfactant. They are usually highly simplified mixtures of phospholipids and do not contain the surfactant proteins that natural surfactants contain which usually enhance the surface tension lowering ability of the surfactant. Surfaxin and Venticute contain additives that have surfactant protein-like properties. However, to date there is no clinical evidence to suggest which natural surfactant is superior and whether synthetic surfactants are superior to natural preparations [18, 19].

Surfactant treatments have shown to improve oxygenation and lung mechanics as well as lower the mean airway pressures and the percentage concentration of oxygen in the gas (fraction of inspired oxygen - FiO_2) delivered by ventilators to premature infants with RDS. Surfactant can be administered either prophylactically (within ten minutes of

birth), as an early treatment (within 2 hours of birth) or as a rescue treatment (when RDS has been established). Although there are no trials comparing prophylactic treatment with early treatment, clinical trials have been done to show that early treatment is definitely more effective than delaying treatment until RDS has been established [1, 18, 19].

1.2.2. Traditional Ventilation Treatments

It was not until the 1970s that the practice of neonatal mechanical ventilation advanced and dramatically improved the treatment of neonates with RDS. Traditional modes of mechanical ventilation include intermittent mandatory ventilation (IMV) and synchronized intermittent mandatory ventilation (SIMV) with pressure and volume control modes. Early techniques of IMV functioned by taking over the role of the respiratory muscles by facilitating gas exchange. The ventilator could be pre-set to deliver "mechanical breaths" at regular breath cycles. The disadvantage was that infants often breathed asynchronously with the mechanical breaths, which lead to inefficient gas exchange, gas trapping and air leaks [20-22].

This non-synchronization between the infant and the ventilator led to the development of an improved type of ventilator called synchronized intermittent mandatory ventilation (SIMV). This type of ventilator synchronized the mechanical breaths with the infant's spontaneous breath. In simpler terms, the ventilator looked for a spontaneous breath from the patient within a timing window each time it was supposed to cycle and would either start or delay the mechanical breaths if a spontaneous breath was detected [20, 21]. Although this synchronized the inspiratory process, the expiratory process was still subject to asynchrony.

Clinicians have the option within a ventilatory mode to choose between pressure-controlled ventilation (PCV) or volume-controlled ventilation (VCV). Controlling the applied pressure works such that if a consistent peak inspiratory pressure (PIP) were set, the volume of air delivered to the patient would be dependent on the compliance of the lung. This meant that if the compliance was poor, the infant would receive a lower volume than required and if the compliance improved, the infant would receive a higher volume. Controlling the tidal volume however, does not present much improvement of

the undesirable possibility of generating high pressures in the lung. A reduced compliance, increased resistance or active exhalation increases the risk of ventilator-induced lung injury such as BPD [20-22].

Bronchopulmonary dysplasia is a type of lung injury in preterm infants brought on by too much oxygen and mechanical ventilation [2, 20, 23-25]. Mechanical ventilation not only causes damage and inflammation in the delicate premature lungs but also impairs the lungs' ability to repair itself and develop further. Clinical investigations using mechanical ventilation performed on a number of species showed that lungs that were exposed to high levels of oxygen in an attempt to achieve higher levels of oxygen saturation in the blood, developed significant persistent lung disease [25]. Studies on preterm animals also showed that mechanical ventilation damaged lungs by causing an inflammatory response [24, 26, 27].

Due to the high risks involved with mechanical ventilation, other ‘gentler’ techniques have been developed such as high-frequency ventilation (HFV), biologically variable ventilation (BVV) and CPAP to avoid neonates from progressing to respiratory failure. HFV is characterized by high frequency rates up to 15 Hz at volumes less than the dead space of the lung while BVV uses a computer controller to deliver typical physiological variations in tidal volume and breath rate. These methods along with the traditional method of CPAP are discussed in detail in Section 2.2. The Bubble CPAP System is a modified form of traditional CPAP and is discussed in further detail here in Section 1.3 since it is the focus of this research.

1.3. The Bubble CPAP System

The Bubble CPAP System by Fisher & Paykel Healthcare was released in the year 2000 with Hudson prongs. The system was designed to offer respiratory support to spontaneously breathing neonates suffering from RDS. It applies a mean CPAP accompanied by pressure oscillations to the airways and alveoli throughout the respiratory cycle. This maintains a degree of lung inflation during expiration, thus preventing lung collapse and making it easier for the neonate to breathe since a partially inflated alveolus is easier to expand than a fully collapsed one.

Pioneering work underpinning the Bubble CPAP System was performed at Columbia Presbyterian Medical Centre by Dr. Jen-Tien Wung and colleagues in 1974 [3]. The studies focused on trying to provide respiratory support to neonates with RDS to prevent them from progressing to respiratory failure. The early system (Figure 1.2) consisted of a humidifier, a circuit for gas flow, a nasal prong to connect the circuit to the infant's airway and a bottle containing water into which the distal end of the expiratory tubing is immersed to create a positive pressure in the circuit.

The Bubble CPAP System operates under the same principles but has been improved with additional features that offer more accuracy in maintaining required mean pressures and flows and further features that consider patient comfort. The system (Figure 1.3) includes a delivery system and a patient interface. The delivery system consists of the MR290 humidification chamber, a single-heated breathing circuit, CPAP generator, and pressure manifold. The patient interface consists of the nasal tubing, nasal prongs and infant bonnet. Head gear may be used in place of the bonnet and chin straps (not shown) may also be added to the patient interface to optimise the effect of Bubble CPAP. The individual components (shown as they would appear in operation in Figure 1.3) are briefly described as follows.

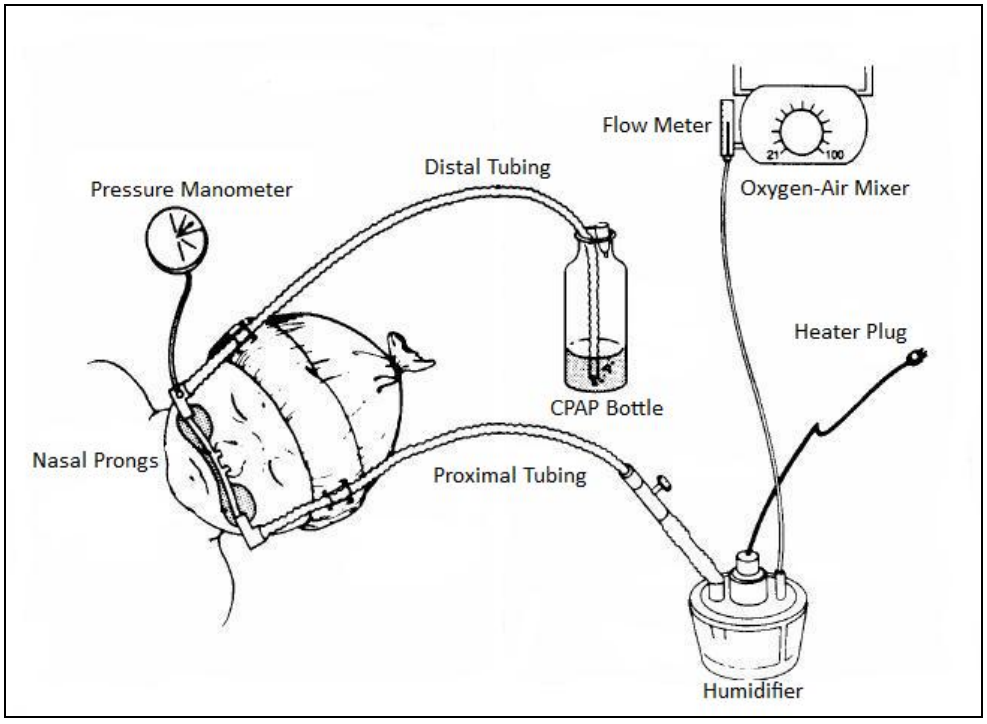

Figure 1.2 Initial Bubble CPAP as used by Columbia Presbyterian Medical Centre [28].

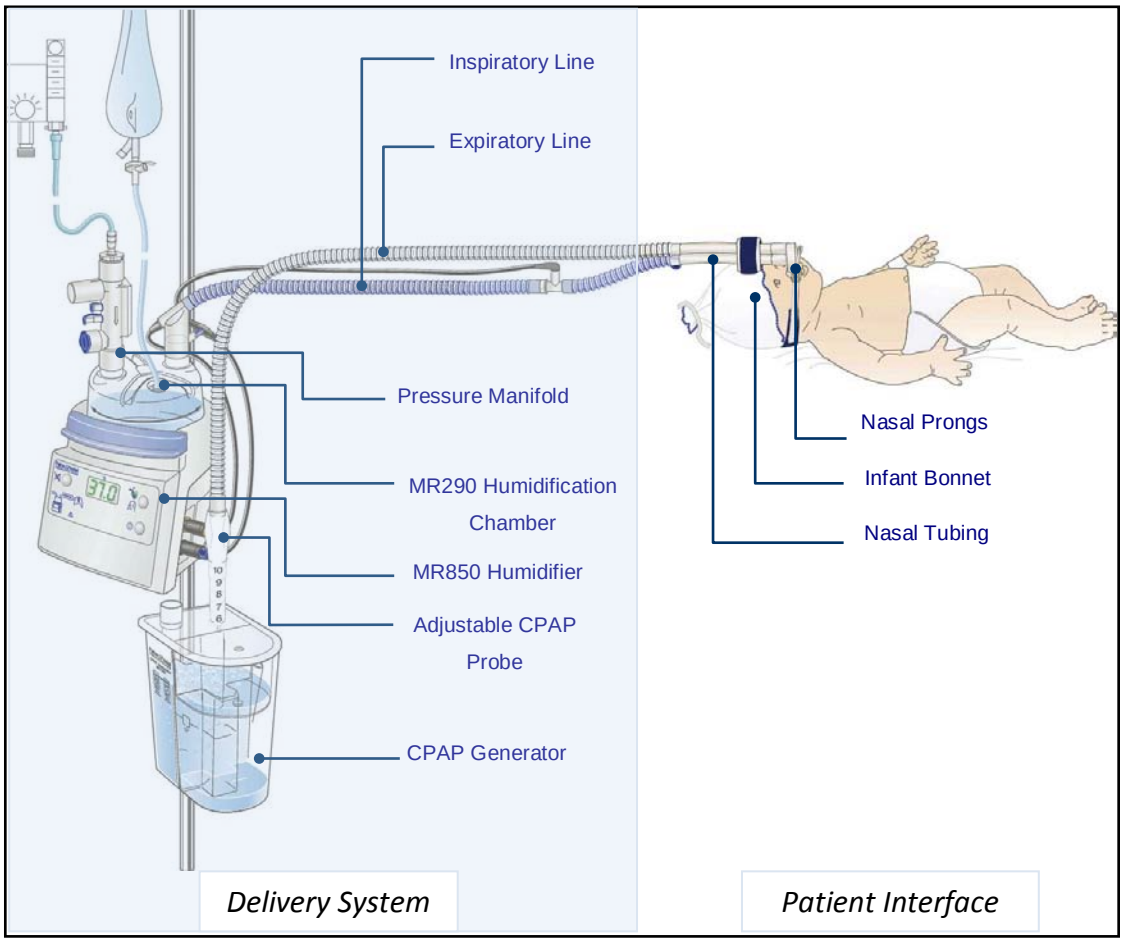

Figure 1.3 Bubble CPAP System Components.

1.3.1. MR290 Humidification Chamber

The chamber is the source of the humidity required by the neonate. Sterile water is fed into the chamber from a flexible bag. The water level is controlled by a dual float mechanism. The float prevents the chamber from flooding and provides a closed system and a constant mean CPAP pressure.

1.3.2. Single-Heated Breathing Circuit

The breathing circuit (consisting of the inspiratory and expiratory lines) links the flow source, humidification chamber, patient interface and CPAP generator. The inspiratory line connects the humidifier to the patient interface and the transparent expiratory line connects the patient interface to the CPAP generator.

1.3.3. Pressure Manifold

The pressure manifold is a pressure relief mechanism situated upstream of the neonate that limits the maximum pressure in the system to 17 cm H_2O at a flow rate of 8 L/min in the event of an occlusion in the delivery system. It also has measurement ports for pressure and air/oxygen analysis.

1.3.4. CPAP Generator

The CPAP generator is the innovative version of the early system of Bubble CPAP used at the Columbia Presbyterian Medical Centre since 1974. Either lowering or raising the adjustable probe in the water container creates the required level of positive pressure in the circuit. Achievable mean pressures range from 3 to 10 cm H_2O. Excess water spills out into an overflow container ensuring that the mean CPAP pressure is constant. As air enters the water through the CPAP probe, it creates bubbles, which in turn create pressure oscillations about a mean CPAP level.

1.3.5. Nasal Tubing, Nasal Prongs and Infant Bonnet

The nasal tubing directs the air into the neonate and allows a balanced flow into the nares. Nasal prongs of different sizes, to address the variety of nare diameters and septum gaps, can be attached onto the end of the nasal tubing. The specially designed infant bonnet allows for the nasal tubing to be fixed in position and allows repositioning of the nasal prongs with the infant's movements. Head gear as an alternative to the infant bonnet is also available. Chin straps are also available to prevent excessive leaks from the mouth thereby preventing significant pressure loss.

Clinical studies on Bubble CPAP have shown that its use decreases minute ventilation, respiratory rate [12], the need for ventilation [8] and the number of days on respiratory support [9]. It has also been speculated that the vibrations produced by the pressure oscillations enhance gas exchange and respiratory mechanics [13]. However, these findings in relation to the current research will be further discussed in Chapter 2.

1.4. Respiratory System Structure and Function

The primary function of the respiratory system is to supply the blood with oxygen and to enable carbon dioxide to move out. It is made up of a gas exchange organ (the lungs)

and a respiratory pump (the chest wall and respiratory muscles). The organs and process of respiration are explained in this section [15, 29-31].

1.4.1. Anatomy

The respiratory system consists of several organs that include the nasal cavity, throat (pharynx), voice box (larynx), wind pipe (trachea), bronchi, lungs and respiratory muscles. This is illustrated in Figure 1.4. The nostrils and proceeding nasal cavity herald the beginning of the human respiratory tract. Their primary functions are to filter out mechanical aerial contaminants and to warm and humidify the inhaled air. The intervening pharynx acts primarily as a conduit between the aforementioned passages and the trachea. The trachea itself is a musculo-cartilaginous tube, which further moistens the inflowing air and additionally filters smaller diameter particles.

The trachea in turn branches at the carina (Figure 1.4) into the primary conducting airways supplying each lung, i.e. the right and left primary bronchi. Hereafter, each bronchus divides again, forming secondary, tertiary and smaller bronchi (Figure 1.5)

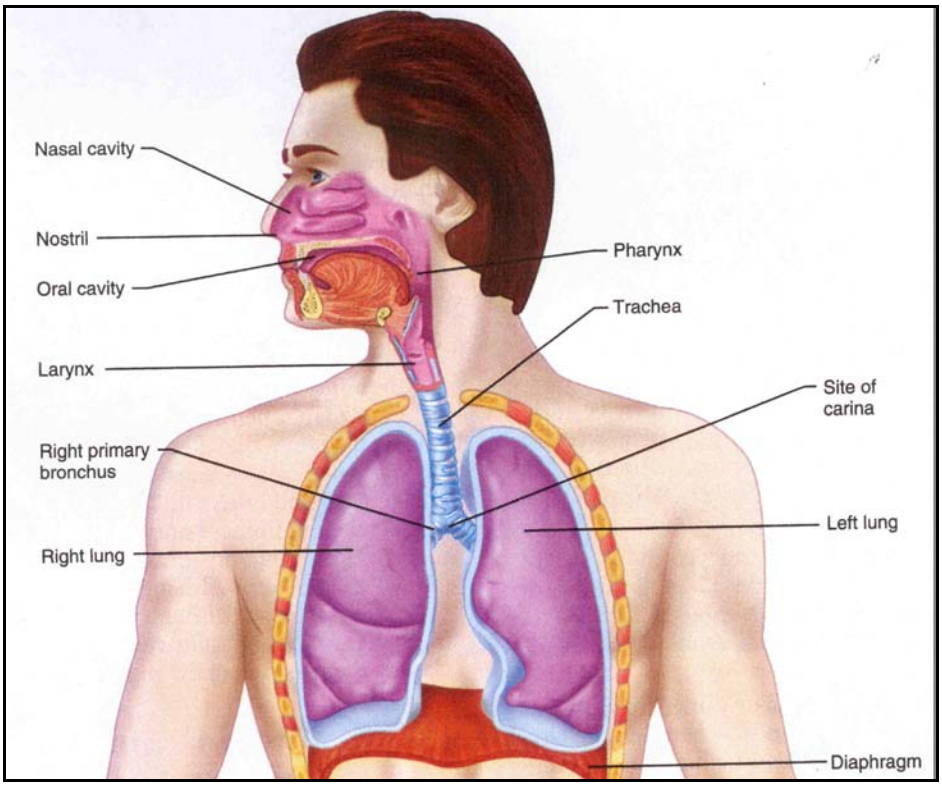

Figure 1.4 Respiratory System Organs [30] .

such that they become smaller and more numerous as they penetrate deeper into the lungs, forming lobar, then segmental bronchi. Figure 1.5 also shows the 5 lobes of the lungs (3 in the right lung and 2 in the left lung).

The division of the bronchi continues down to the terminal bronchioles (the smallest airways without alveoli). The airways from the trachea to the terminal bronchioles are called the conducting airways. Their function is to lead the inspired air from the exterior to the gas exchange region or respiratory zone of the lung (shown in Figure 1.6). The respiratory zone is made up of respiratory bronchioles (which have occasional alveoli budding from their walls), alveolar ducts and alveoli. There are about 300 million alveoli in the human lung, each about 1/3 mm diameter.

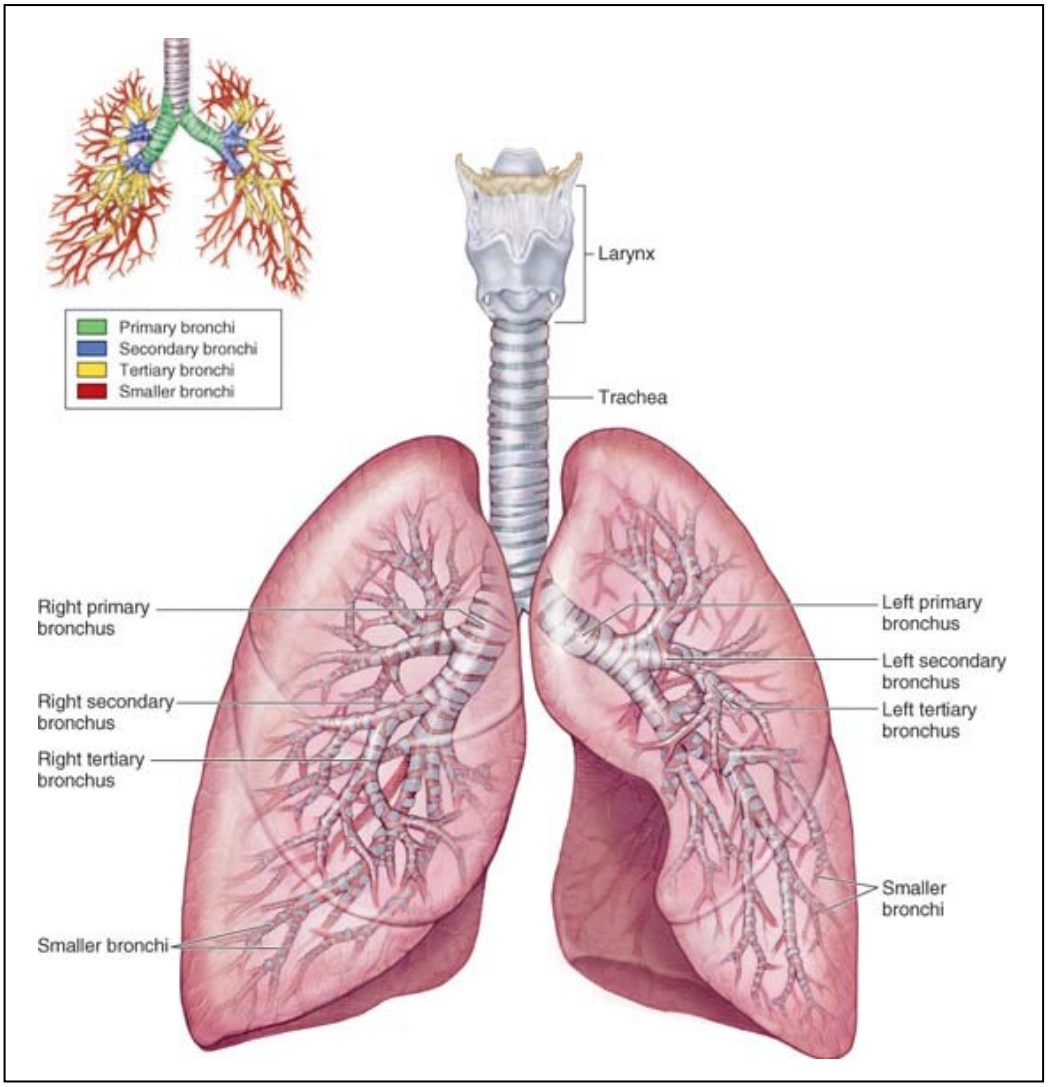

Figure 1.5 Branching of conducting airways in the lung [31].

The distance from the terminal bronchiole to the most distal alveolus is only a few millimetres but the respiratory zone constitutes most of the lung. The alveoli are surrounded by pulmonary capillaries which form a dense network in the walls of the alveoli (Figure 1.6) such that it forms an almost continuous sheet of blood on the alveolar wall surface (which is about 70-85 m^2 in adult humans). The barrier between the air and the blood is only about 0.5 µm apart such that oxygen and carbon dioxide can diffuse through the barrier with ease.

Four generations of respiratory bronchioles develop before birth and several million alveoli form in the last few weeks of birth, underscoring the importance of the last few weeks of gestation [16].

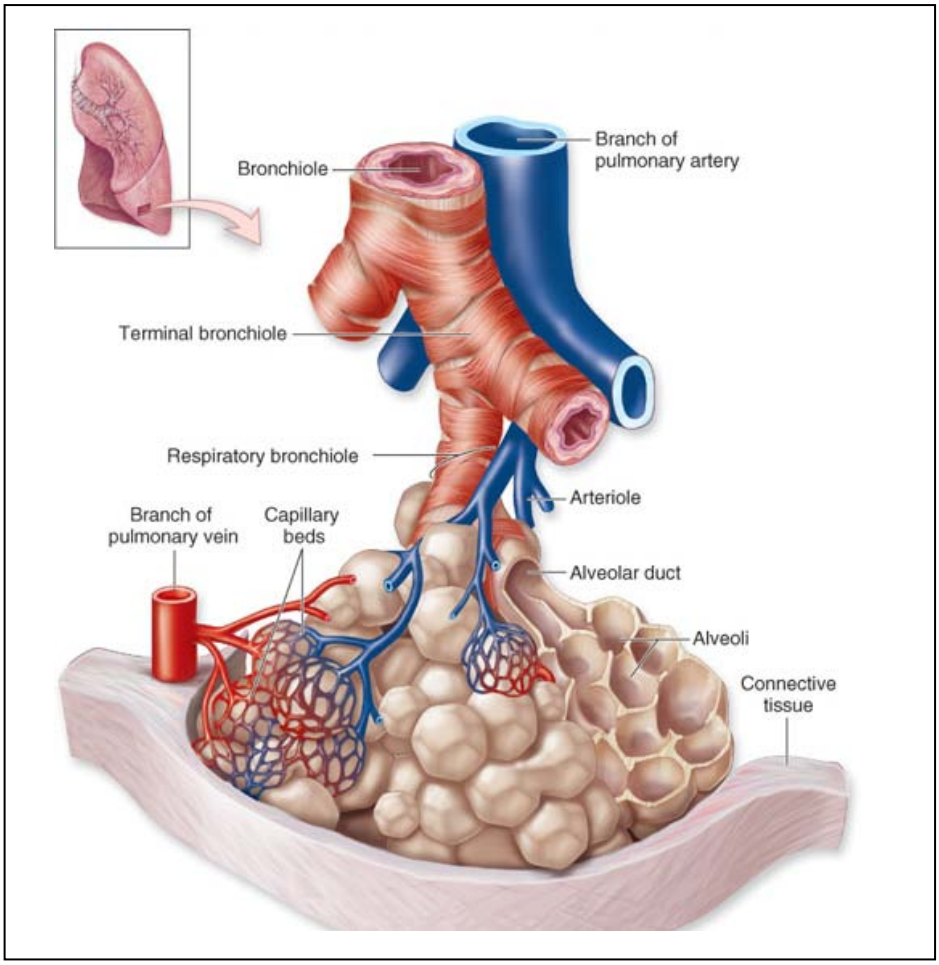

Figure 1.6 Respiratory zone of the lung [31].

Premature infants born before or during this important stage of alveolarization are subjected to mechanical ventilation before the development of alveoli. This could disrupt the normal process of lung development and lead to BPD [16, 29, 30, 32].

The alveoli are lined by two types of epithelial cells (as seen in Figure 1.7). Type I cells are the primary lining cells. Type II cells are thicker and secrete surfactant. The alveoli also contain macrophages which clean off inhaled dust particles and microorganisms. Figure 1.7 also shows the pulmonary capillaries and red blood cells (erythrocytes).

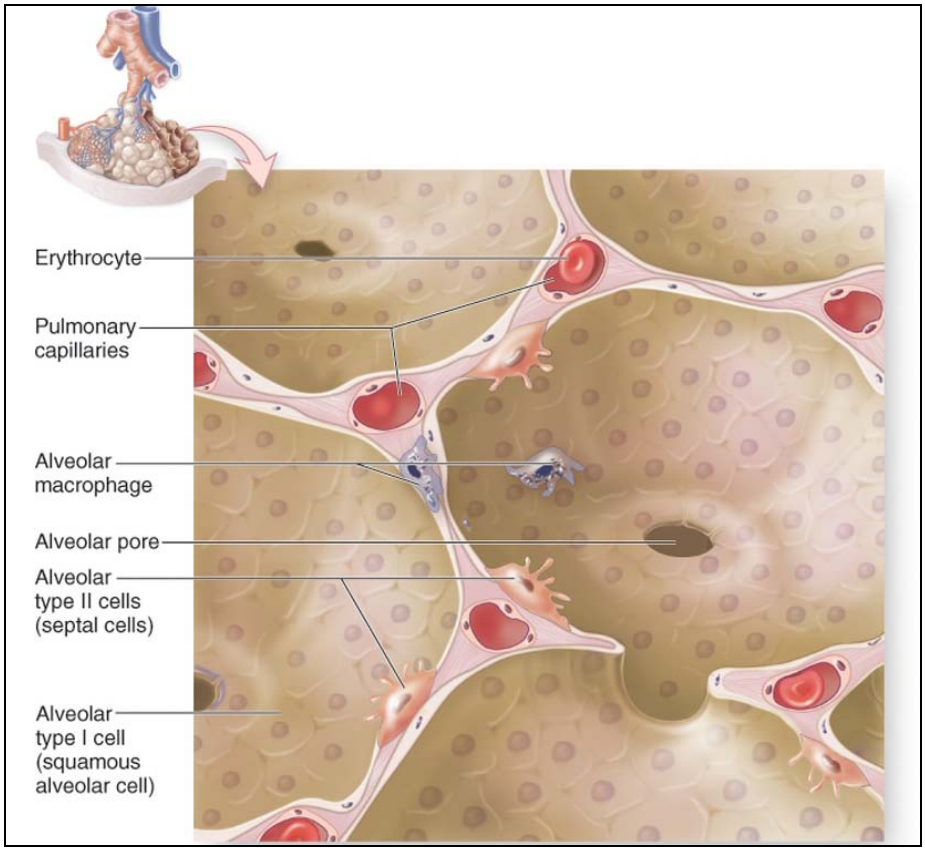

Figure 1.7 Cells in the alveoli [31].

1.4.2. Inspiration, Expiration and the Respiratory Muscles

The inspiration and expiration processes during quiet breathing are illustrated in Figure 1.8 and Figure 1.9 respectively and explained as follows [29-32]. Inspiration is an active process. The most important muscle of inspiration is the diaphragm which accounts for 75% of the change in intrathoracic volume. It is a thin dome-shaped sheet of muscle that is attached at the bottom of the thoracic cage.

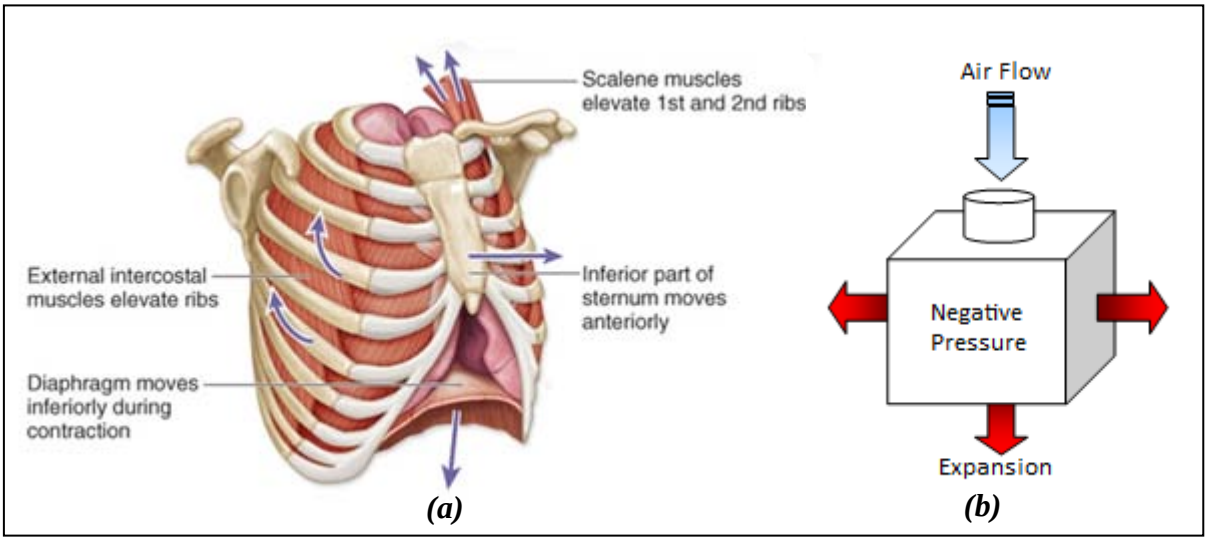

Figure 1.8 Inspiration process during quiet breathing [31].

It moves downward like a piston when it contracts and the vertical dimension of the chest cavity is increased (Figure 1.8a). The external intercostals muscles run obliquely forward and downward, connecting the ribs. When they contract, they pull the ribs upward and forward (in a “bucket-handle” motion) such that the sternum is also pushed outward. The scalene muscles also elevate the first two ribs. There is little activity by the scalene muscles during quite breathing but they may contract vigorously during exercise.

The increase in intrathoracic volume by the contraction of all the respiratory muscles causes a decrease in pressure in the lung according to the ideal gas law since the volume increases due to temperature changes are small (Figure 1.8b). This causes air to rush into the lung from the atmosphere since fluid flows down along a pressure gradient. As a result, the pressure within the lung (intrapulmonary pressure) decreases to negative values during inspiration. The inspiration process ends when the intrapulmonary pressure and the atmospheric pressure become equal.

Expiration is a passive process in that it depends on the elasticity of the lungs and the chest wall. As the diaphragm and other inspiratory muscles relax, the lungs and chest wall recoil to their resting position (Figure 1.9a). Thus the lung volume is decreased and the intrapulmonary pressure increases to positive values during expiration. The pressure

gradient now forces air out of the lungs (Figure 1.9b). During exercise, however, expiration becomes active.

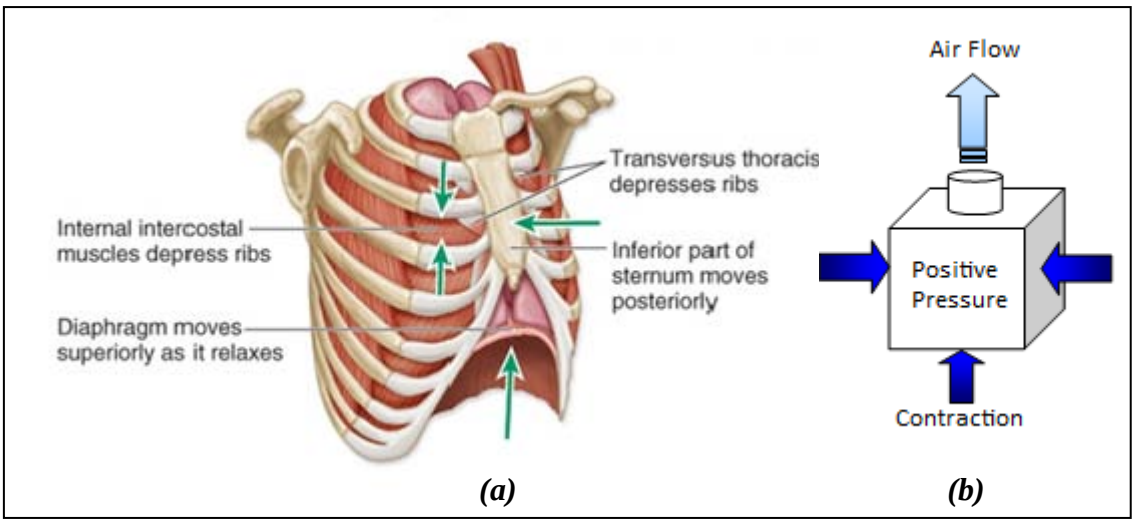

Figure 1.9 Expiration Process during quiet breathing [31].

The internal intercostals muscles contract, pulling the rib cage downward and thereby decreasing the thoracic volume. Muscles in the abdomen also contract, raising the intra-abdominal pressure, thus pushing the diaphragm upward.

The lungs and the chest wall are elastic structures that are connected by a common pleural cavity and pleurae as seen in Figure 1.10. The pleura is a membrane that folds back on itself to create a double-layered membrane. The parietal pleura (outer pleura) is attached to the chest wall and the visceral pleura (inner pleura) is attached to the lung surface. The thin space between the pleura (the pleural cavity), is filled with a lubricating fluid called the pleural fluid. The pleural fluid allows the lung to slide easily on the chest wall and prevent pleural separation due to the surface tension of the pleural fluid. This is akin to two moist pieces of glass that can slide on each other but resist being separated. Thus, the pressure in the pleural cavity (the intrapleural pressure) is subatmospheric. The tendency for the chest wall to recoil at the end of quiet expiration is balanced by the tendency for the lung to recoil away from the chest wall. If the chest wall is opened, the lungs collapse and if the lungs lose their elastic recoil, the chest expands and becomes barrel shaped.

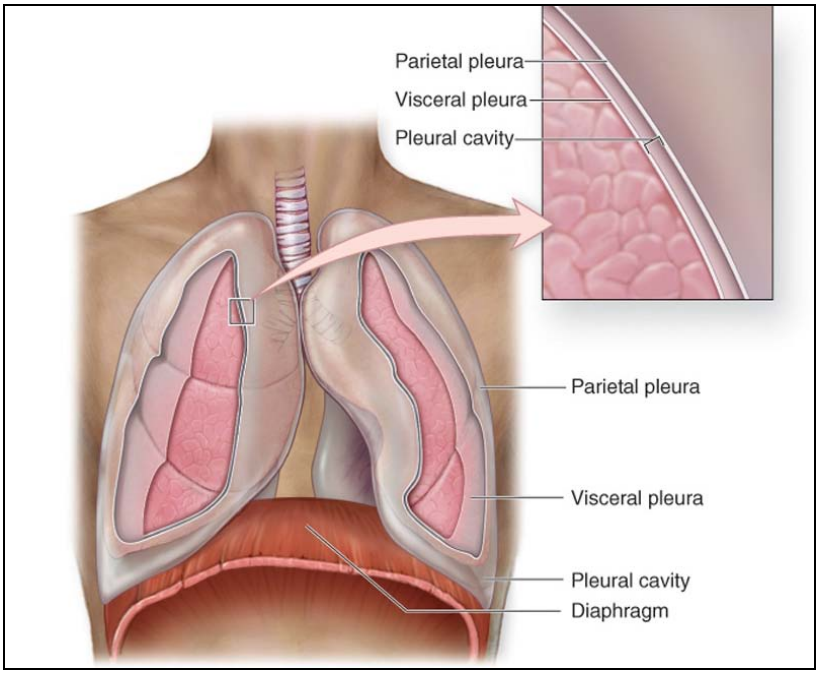

Figure 1.10 The pleural cavity [31].

1.4.3. Respiratory Volumes and Capacities

The respiratory or lung volumes and the names applied to combinations of them (the respiratory capacities) are shown in Figure 1.11 [16, 32]. During quiet breathing, the amount of air that moves into the lungs with normal inspiration (or the amount that moves out during expiration) is called the tidal volume (TV). The amount of air that can be forcibly inspired beyond the tidal volume is the inspiratory reserve volume (IRV). The volume of air that can be forcibly exhaled after quiet expiration is the expiratory reserve volume (ERV). The air left in the lungs after a forced expiration is the residual volume (RV), which helps to keep the airways open and hence prevent lung collapse. The volume of the conducting zone of the lungs is called the respiratory dead space since there is no diffusion of respiratory gases into and out of the blood in this section of the lung. Respiratory capacities always incorporate two or more lung volumes.

The inspiratory capacity (IC) is the sum of the TV and the IRV and is the amount of air that can be inspired after a quiet expiration. The amount of air that remains in the lungs after a quiet expiration is the functional residual capacity (FRC). This combines the RV and the ERV. The vital capacity (VC) is the sum of the TV, ERV and IRV, which is

effectively the total amount of exchangeable air. The sum of all the lung volumes is known as the total lung capacity (TLC).

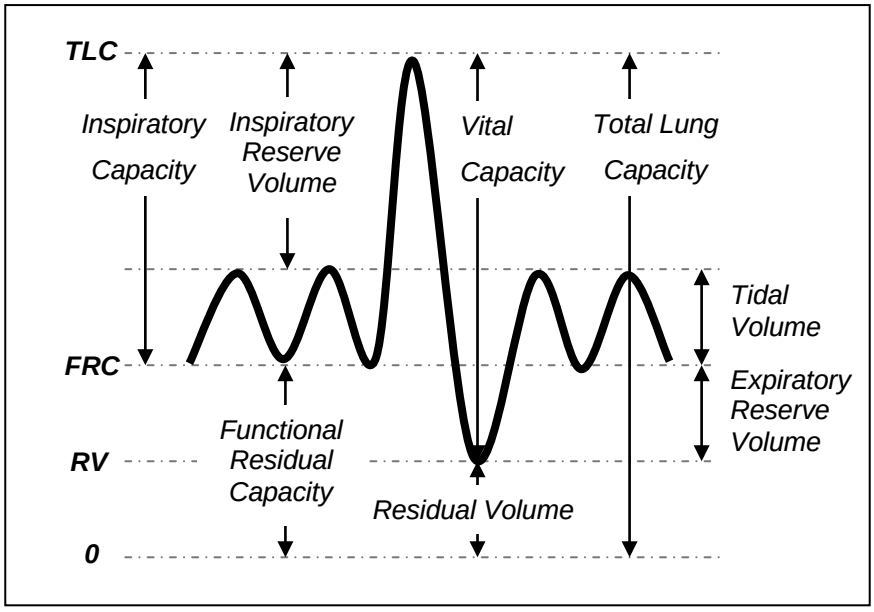

Figure 1.11 Respiratory Volumes and Capacities.

1.5. Mechanics of Respiration

This section introduces the mechanical aspects of air flow in the respiratory system. The parameters introduced are commonly used parameters in clinical practice and experimentation to assess respiratory mechanics and performance. They deal with the forces that move the lung and chest wall and the resisting forces that they have to overcome.

1.5.1. Airway Resistance

Airway resistance is the major source of non-elastic impediment encountered in the lung. It can be measured at the airway opening as the total resistance encountered in all the airway branches combined. In the lung, a pressure difference exists between the atmosphere and the alveoli where the airways are a series of branching tubes in-between. Each airway can be considered as a tube where a pressure difference (ΔP_{airway}) exists between the ends which is a function of the rate and the pattern of flow (Q). In laminar flow, ΔP_{airway} is proportional to Q and a constant K. such that:

$$\Delta P_{airway} = KQ \quad \textbf{(1.1)}$$

However, in turbulent flow, ΔP_{airway} is not proportional to Q, but to its square. In a complex system of branching tubes such as the bronchial tree, with its various bifurcation angles, surface roughnesses and diameters, the application of a simple expression for ΔP_{airway} is difficult. Laminar flow is most likely to occur in the terminal bronchioles and fully developed turbulent flow is most likely to occur in the trachea. However, for most of the bronchial tree, the flow is most likely to be transitional.

1.5.2. Compliance

The compliance is the ratio of the change in pressure (ΔP) and the change in volume (ΔV) and reflects the elastic properties of the respiratory system. The lung compliance (C_L) is expressed as

$$C_L = \frac{\Delta V}{\Delta P} = \frac{1}{E_L} \quad \textbf{(1.2)}$$

where the elastance of the lung (E_L) is the reciprocal of the lung compliance (C_L). Static lung compliance measurements can be made by measuring the transpulmonary pressure (which is the pressure difference between the alveolar and pleural pressure) before and after inflation with a known volume. This is measured at the mouth and oesophagus. The chest wall compliance (C_{CW}) can be measured in a similar manner by recording the difference between pleural and atmospheric pressures. A pressure-volume curve can be made by recording the pressures at several different volumes. Figure 1.12 shows typical lung and chest wall expansion curves for a neonatal lung [32]. The sum of the two is the total compliance (C_T). It is apparent that the compliance is not linear across the entire range of expansion, with the compliance getting smaller at higher expanding pressures, as seen by the flatter slope of the curves at higher pressures. Compliance is a useful measure of diseased states. It is reduced in conditions of pulmonary fibrosis, alveolar edema and atelectasis which prevent the inflation of the

lung. Compliance increases in pulmonary emphysema and in the aging lung where the elastic properties of the tissue alter.

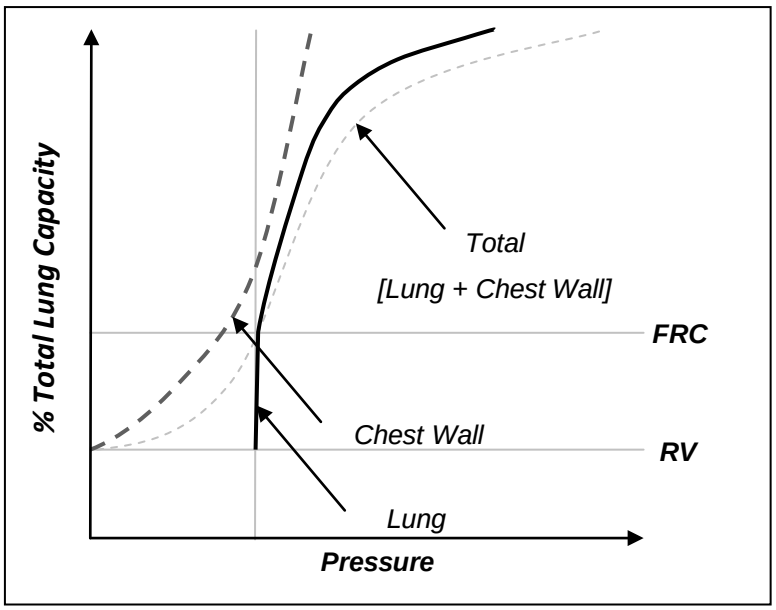

Figure 1.12 Neonatal lung and chest wall compliance.

1.5.3. Impedance

The impedance of the respiratory system (Z_L) is an expression of the overall impediment to flow in the respiratory system [33]. It is the result of a combination of the resistive, elastic and inertive elements and is given by

$$Z_L = \left|\frac{P}{Q}\right| \tag{1.3}$$

where P is the instantaneous pressure at the airway opening.

1.5.4. Alveolar Surface Tension

Alveolar surface tension is the force acting across an imaginary line (1 cm in length) on the liquid lining of surfactant and hence has the SI units of N/m but is commonly expressed in the literature as “dynes/cm”. It is an important factor that affects the pressure-volume relationship of the lung. This can be measured by inflating excised

lungs with saline at various volumes, to abolish the air-liquid interface in the alveoli, thereby reducing the surface tension to almost zero. A typical resulting pressure-volume curve such as that seen in Figure 1.13 [29, 32] is one that measures only the tissue elasticity, whereas similar measurements done with air measure the effects of both tissue elasticity and surface tension. Figure 1.13 shows that the saline filled lungs have a higher compliance and less hysteresis than air-filled lungs, indicating that surface tension contributes to a large part of the static recoil force of the lung.

The surface tension-reducing mechanism of surfactant can be better understood by looking at the intermolecular forces between the surfactant molecules. Pulmonary surfactant is made up of 90% phospholipids and 10% proteins. Phospholipid is the primary surface-tension lowering component of pulmonary surfactant and makes up most of its mass. The proteins enhance the surface tension lowering ability of the surfactant. The surfactant associated proteins are SP-A, SP-B, SP-C and SP-D. Figure 1.14 shows the composition of mammalian surfactant. Although there is some variation in surfactant across species, the compositions given are representative since composition in mammals in general is considered to be similar.

Phospholipid content can be divided in 25-30% dipalmitoylphospatidylcholine (DPPC), 25-30% unsaturated phospatidylcholine (PC), 10-15% phosphatidylglycerol (PG) plus phosphatidylinositol (PI), 5-10% neutral lipids, 5-10% proteins and about 2% each of sphingomyelin (SM) and lyso-bis-phosphatic acid (LYSO).

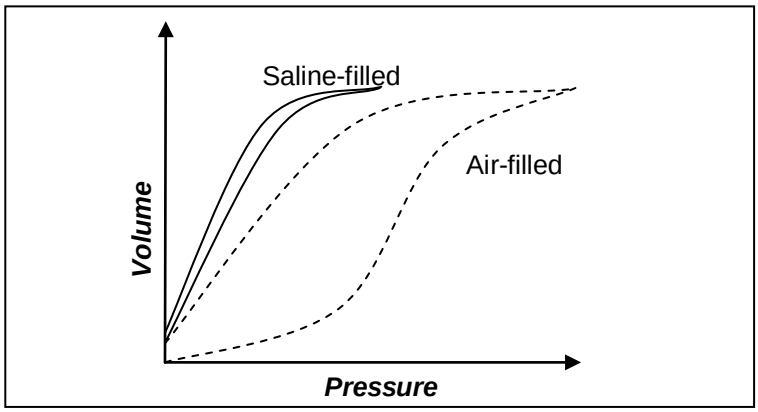

Figure 1.13 Pressure-volume curves of air-filled and saline-filled lungs.

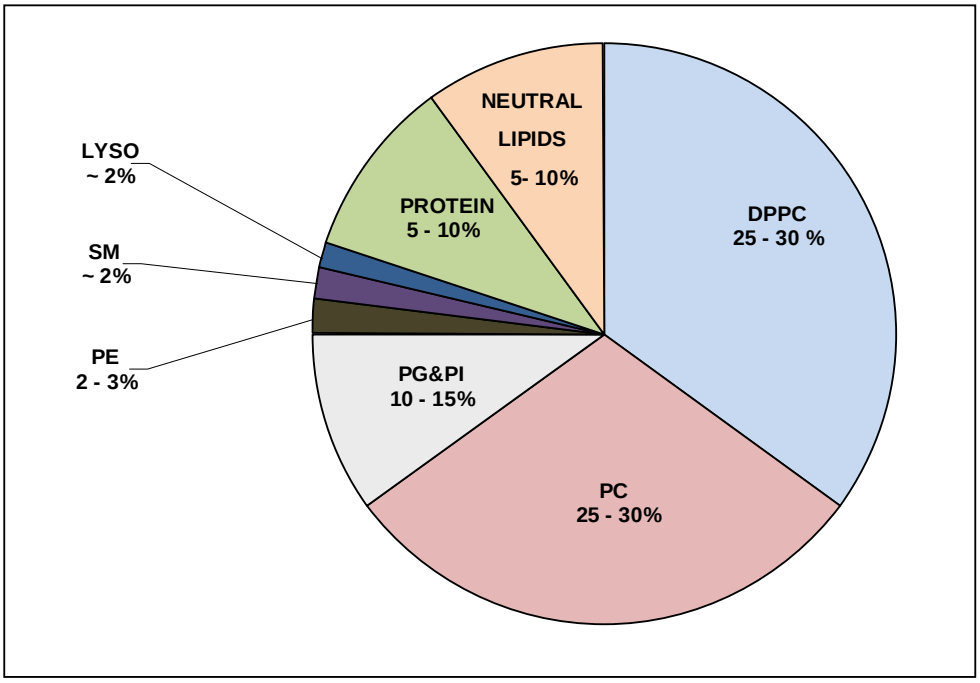

Figure 1.14 Mammalian surfactant composition.

Phospholipids are mainly responsible for giving the surfactant its surface tension-reducing capacity and this is discussed in greater detail as follows. Phospholipid molecules contain a hydrophobic tail and a hydrophilic head (Figure 1.15) and exist as aggregates because they are insoluble in the aqueous mixture that lines the alveoli.

At the air-liquid interface of the alveoli, water molecules are attracted to each other and to molecules in the bulk liquid, thereby creating a contractive force known as surface tension. The surface tension acts to reduce the surface area of the air-liquid interface to create a stable position at minimal surface area. Surface tension has a value of 0.7 mN/cm for water at 37^{o}C (more commonly expressed as 70 dynes/cm). This resists expansion of the alveoli in the lung in diseased states where there is no surfactant.

To increase the surface area sufficiently for adequate ventilation requires large amounts of distending pressure to be generated and hence, more work. This explains why a premature infant, who is unable to produce pulmonary surfactant, is faced with the further difficulty of having to perform more muscle work to counter the tendency of the alveoli to collapse.

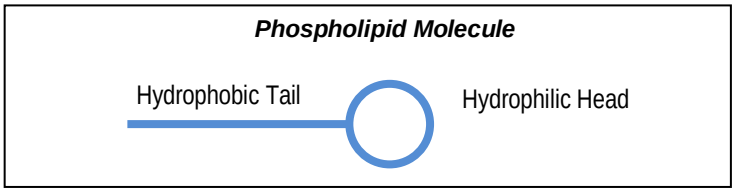

Figure 1.15 Phospholipid Molecule.

In the presence of surfactant in a healthy lung, the hydrophilic heads of the phospholipids interact with the water molecules and the hydrophobic tails extend towards the air (as seen in Figure 1.16). This displaces the water molecules at the air-liquid interface (which are attracted to each other by electrostatic forces known as Van de Waals forces), thus reducing the surface tension to equilibrium values of approximately 25 dynes/cm [16, 34].

Surface tension forces in the alveoli can be described by the static Young-Laplace equation [1, 32, 34] most commonly applied to a small spherical air bubble in a surfactant suspension which is pulsated at regular frequencies between a fixed minimum and maximum radius (Equation (1.4)).

$$\Delta P = \frac{2\gamma}{r} \qquad \textbf{(1.4)}$$

Here ΔP is the pressure drop across the air-liquid interface that is needed to stabilize the system, r is the radius of the bubble and γ is the surface tension.

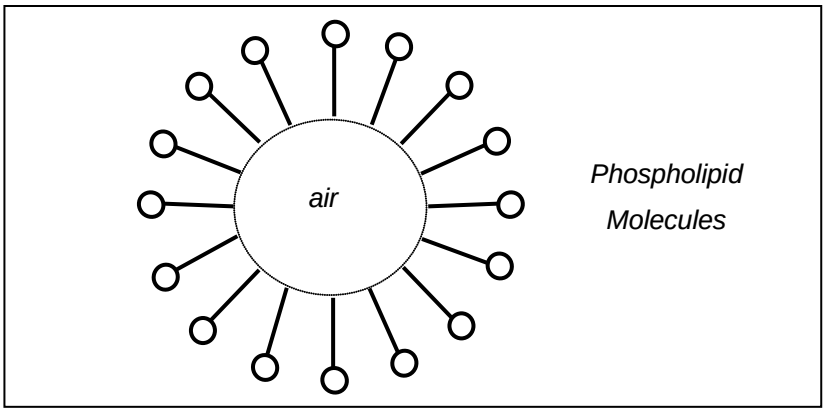

Figure 1.16 Phospholipid molecules at the air-liquid interface.

In the absence of surfactant, the surface tension increases and Equation (1.4) illustrates that more distending pressure is required to stop the alveoli from collapsing. If the radius of the alveolus is small, this too necessitates a larger distending pressure to keep it open. In a premature infant whose alveoli are deficient in surfactant and naturally smaller in radius than normal infants, surfactant therapies and ventilation are thus required to expand the alveoli to prevent collapse at the end of expiration. Equation (1.4) ignores the dynamic effects of surface dilational viscosity κ which affects the interfacial pressure drop when the bubble changes dynamically. A complete description of the interfacial behaviour is given by Equation (1.5) which is a function of radius r, surface tension γ and surface dilational viscosity κ [35]:

$$\Delta P = \frac{2\gamma}{r} + \frac{4\kappa\dot{r}}{r^2} \qquad \textbf{(1.5)}$$

These effects, if ignored during experiments, can result in significant errors, however for the purposes of a basic explanation, the Young-Laplace equation suffices.

1.5.5. Work of Breath

Generally, the work of breath (WOB) refers to the mechanical work performed by the respiratory muscles against the lung and chest wall during respiration [29, 32]. It is most convenient to measure work as the product of pressure and volume change which has the same units as work (Nm). The work of breath can be calculated from a relaxation pressure curve such as previously shown in Figure 1.12. The work of breath is complex and difficult to measure without sophisticated analysis to quantify the movement and distortion of the chest wall [32, 36].

However, in many cases, measuring the work performed against an external load may provide sufficient information for the purposes of respiratory performance [36]. The work measured at the mouth or airway opening estimates the work performed by all the respiratory muscles. Alternatively, it can be measured using the transpulmonary pressure for measurement of the chest wall and its muscles against the lung and airways.

The work of breath can be expressed as the work done per breath, work per minute or work per litre [37].

1.6. Closure

This chapter has introduced the background of RDS and the role of ventilation and surfactant therapy in its treatment. The Bubble CPAP System has been introduced with further details on clinical trials to be discussed in the following chapter. The anatomy and physiology of the respiratory system relevant to this research have been highlighted and the mechanics of respiration and the function of surfactant have also been explained.

CHAPTER 2

Literature Review

2.1. Introduction

This chapter presents a review of the relevant research performed on oscillatory ventilation techniques to treat RDS. HFV and BVV are discussed with their proposed mechanisms of improvement. The clinical research performed on the use of the Bubble CPAP System is also presented to highlight the potential benefits it offers with the introduction of pressure oscillations superimposed on the mean CPAP pressure. The research to date on the modeling of respiratory system mechanics and surfactant dynamics in the alveoli are also discussed. The objectives of the research are then presented in the hopes of extending the use of neonatal mechanical and 'surface tension' models to study the effect of pressure oscillations on neonatal respiratory performance.

2.2. Ventilation Techniques using Pressure Oscillations

The use of pressure oscillations in ventilation before the introduction of Bubble CPAP was not entirely unknown. This section presents a review of the literature focusing on the description of the ventilation techniques that use pressure oscillations, their clinical benefits and proposed mechanisms of improvement.

2.2.1. High Frequency Ventilation

High frequency ventilation was a radical departure from mechanical ventilation in that it delivered gas at small tidal volumes (less than the dead space of the lung) at frequencies up to 15 Hz. The pulses of small gas volumes at rapid rates created lower pressures in the alveoli, decreasing the incidence of lung tissue injury [38-41]. It has been suggested

that the vibratory or pulsing nature of the airflow causes a "sloshing motion" of air in the lungs, known as pendelluft and that this feature of HFV may offer better gas transport to the respiratory zone of the lung [42, 43]. Clinical results [44, 45] have shown that early, exclusive use of HFV decreases the incidence of BPD in premature infants with RDS when compared to mechanical ventilation. Infants also required a much shorter period on ventilator support.

A number of mechanisms of gas transport during HFV have been suggested. During normal breathing frequencies, bulk convection and molecular diffusion take place. These mechanisms also occur during HFV but other mechanisms have also being suggested. Chang [42] proposed that the following modes of gas transport are collectively responsible during HFV:

Direct alveolar ventilation - Alveoli that lie proximal to the trachea still receive direct ventilation. Even though the tidal volumes are small, as long as they are above a certain limit, some alveoli will receive fresh gas with every inspiration.

Pendelluft - When neighbouring regions in the lung are different in compliance, resistance and time constants of inflation and deflation, this leads to “fast” units which fill faster and more easily (Figure 2.1a) and “slow” units which may still be in the process of inhalation when the fast units are exhaling (Figure 2.1b). During high velocity flow this phenomenon is magnified and the neighbouring units mutually exchange gas in an effect known as pendelluft. As a result, there is a more homogeneous mixing of gas, allowing the use of smaller volumes of gas to reach more alveoli and as a result decrease the required tidal volume required for respiration.

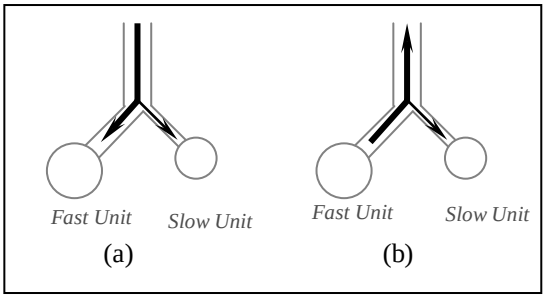

Figure 2.1 Pendelluft phenomenon showing filling and emptying of units.

Convective Gas Transport - During inspiration the velocity profile of the gas is parabolic (Figure 2.2b) but during expiration the velocity profile is flatter (Figure 2.2c). The resulting displacement of a particle of gas that was situated in the centre of the airway at the start of inspiration (Figure 2.2a) is now situated to the right (Figure 2.2d) (i.e. working its way down the tracheo-bronchial tree to the alveoli) and the gas particles near the walls are situated to the left of their original position.

Facilitated diffusion - The fast pulses of low volumes in HFV move down the airways with larger axial spikes (Figure 2.3b) than slower pulses (Figure 2.3a) which create a larger boundary for lateral diffusion of oxygen and carbon dioxide in laminar flow.

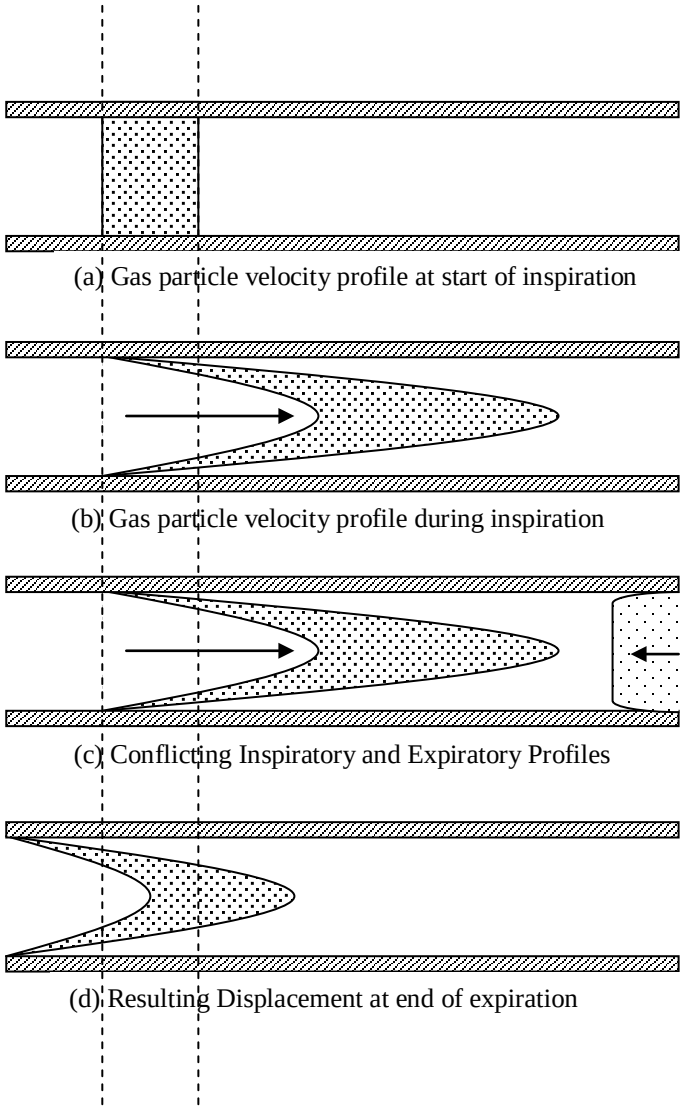

Figure 2.2 Velocity profiles during convective gas transport.

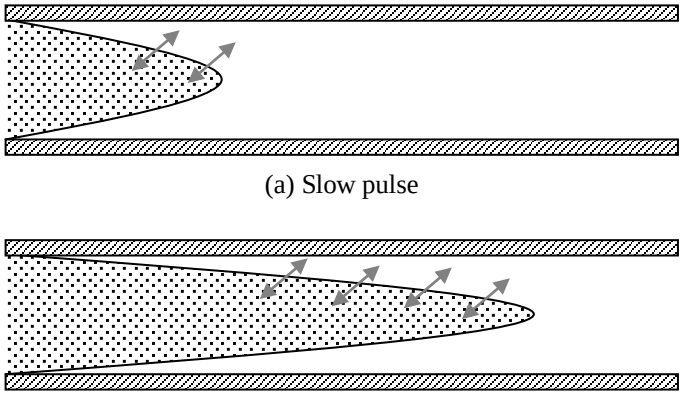

(a) Slow pulse

(b) Fast pulse

Figure 2.3 Facilitated Diffusion during HFV.

Lateral diffusion can also occur in turbulent flow and at bifurcations due to eddies. Thus, it said that diffusion is facilitated in these cases.

Molecular Diffusion - This refers to the molecular diffusion of respiratory gases at the alveolar-capillary membrane. This mechanism always exists as along as gas exists there at a temperature above absolute zero and hence is not an HFV-specific mechanism. Molecular diffusion of oxygen and carbon dioxide will occur across the alveolar-capillary membrane to maintain an equilibrium between partial pressures of these gases. De Jong [34] also suggested that another factor of importance for HFV is surfactant efficiency. The fact that HFV has lower pressures may mean that they do not "disturb" the critical alveoli (which have a relatively low surfactant concentration) and so they will not collapse.

Although all six modes of gas transport discussed may exist during HFV, it is possible that certain modes are more dominant in certain regions of the respiratory system. It has been suggested that direct ventilation and facilitated diffusion dominate ventilation in the trachea, while pendelluft or convective gas transport dominate in the medium-sized airways. Smaller airways are ventilated by pendelluft and alveoli by molecular diffusion. There are many variants of the HFV technique, but they all contain three basic elements, a high pressure flow generator, a valve for flow interruption and a breathing circuit to be connected to the patient. Variants include high-frequency jet ventilation (HFJV), high-frequency flow interruption (HFFI), high-frequency (push-

pull) oscillation (HFO), high-frequency positive pressure ventilation (HFPPV) and high-frequency percussive ventilation (HFPV).

2.2.2. Continuous Positive Airway Pressure (CPAP) with Pressure Oscillations

Nasal Continuous Positive Airway Pressure (nCPAP) is a non-invasive type of respiratory support in comparison to endotracheal ventilation. It applies a continuous positive pressure to the alveoli (through nasal prongs or tubes) throughout the respiratory cycle and has been increasingly used in hospitals to treat neonates with RDS [10, 46]. The positive pressure applied to the lung is created by a variable resistance at exhalation. It produces a more regular breathing pattern when compared to mechanical ventilation since it allows the infant to breathe spontaneously. The continuous distending pressure provided by nCPAP increases lung volume and promotes better gas exchange in the alveoli by keeping them open [16, 20]. Studies have shown that nCPAP reduced the need for mechanical ventilation in neonates with moderate RDS and proved to be an adequate form of ventilation by improving oxygenation without posing any addition harmful side effects [10, 47-50].

The Bubble CPAP System as discussed in Chapter 1 uses a water column rather than a variable resistor to produce the required CPAP to the alveoli. The bubbles produced in the CPAP bottle as the air leaves the system produce pressure oscillations (reported to be between 15-30 Hz [12]) in addition to the mean pressure. There has been some evidence based on studies on infants between 750 and 2500g birthweight that using Bubble CPAP decreases the respiratory rate and minute ventilation in neonates with RDS without decreasing alveolar ventilation [12], meaning that the infant has to perform less muscle work to achieve adequate respiration. It was proposed that Bubble CPAP may facilitate better gas exchange in the lung which may be caused by mechanisms seen in HFV.

Hospital and clinical studies have identified several benefits of Bubble CPAP that make it a feasible device for managing RDS in neonates. Hospital studies on preterm and extremely low birthweight infants concluded that the use of Bubble CPAP reduces the possibility of lung injury by reducing the need and number of days required for mechanical ventilation [10, 51, 52]. Studies also showed that hospitals that used Bubble

CPAP to a greater extent on preterm infants with RDS reported a significantly lower rate of BPD than hospitals that did not [14, 48, 53].

A notable study by Pillow et al. [13] on preterm lambs showed that (in comparison to constant pressure CPAP) Bubble CPAP improved arterial oxygen levels (due to the improved gas exchange offered by the pressure oscillations), stabilised lung volumes at low pressure and enhanced lung mechanics (by increasing compliance and FRC and decreasing airway resistance).

Also, studies on preterm lambs have shown that Bubble CPAP improves the compliance of the lung by preventing repetitive inflammatory stresses on the preterm lung and preserving surfactant function better than mechanical ventilation [11]. It has also been speculated that the noisy pressure signal may also promote surfactant secretion in the lung [7].

The improvements noted in ventilatory parameters during Bubble CPAP could be due to a number of physiological, chemical and mechanical mechanisms. These include the avoidance of aggressive initiation of ventilation with high tidal volumes and inadvertent hyperventilation of the lung [11, 52], those similar to those seen in HFV [12] and that of stochastic resonance resulting from the superimposed noisy pressure signal from the bubbling action [13]. However, the relative contributions of the different proposed mechanisms are yet to be established.

The essence of stochastic resonance in relation to the Bubble CPAP System can be explained as follows. When ‘noise’ is added to the input into a non-linear system (like the lung), the response is first improved. However it is possible that if the timing or the pressure amplitude of the noise is increased further it can produce a detrimental effect. This suggests that noise can be tuned in such a way to provide optimal ventilation [54, 55]. This improvement has been illustrated in terms of the net volume recruited due to the non-linearity of the pressure-volume curves of the lung. However, the stochastic resonance effect due to the overall mechanical response of the respiratory system is yet to be determined and is of interest to this research.

To date no clinical studies have ventured so far as to determine the optimum amplitude and frequencies of pressure oscillations in the treatment of RDS. Some analytical studies [56, 57] have been done that demonstrate the ability of using the Bubble CPAP System to optimise the amplitudes and frequencies of pressure oscillations produced by the system but these remain to be validated by clinical studies.

2.2.3. Biologically Variable Ventilation

Biologically variable ventilation or "noisy ventilation" has been clinically shown to have benefits as well. BVV uses a computer controller to mimic the normal variability in a spontaneously breathing lung by producing random variations in tidal volume and breath rate. Studies on porcine [58, 59] and rodent [54] models showed that such techniques improve the oxygenation of arterial blood and have enhanced the performance of mechanical ventilators. Mathematical models [55] that were developed also suggest that mechanical ventilation accompanied by randomly varying breath patterns improved alveolar recruitment by opening collapsed alveoli and increasing the net lung volume without causing increases in mean airway pressures.

The mechanisms of alveolar recruitment for this technique are also not fully understood, although theories do exist on the mechanisms of gas transport. These are mostly associated with the benefits due to the better mixing of gases in noisy ventilation [42, 43, 60].

Various authors suggest that noisy ventilation (like BVV and Bubble CPAP) is an example of stochastic resonance [54, 55, 58, 59]. Studies on small animals [54, 59] have shown that respiratory support systems can optimize lung recruitment by tuning parameters such as the timing and amplitude of the pressure fluctuations. Whether this is applicable to larger animals and humans remains to be proven.

2.2.4. The Role of Vibration

The pressure oscillations produced in Bubble CPAP not only facilitate gas transport but also vibrate the lung and chest wall. These can be felt if one's hand is placed on the infant's chest. Investigations on the mechanical response of the lung walls to high

frequencies are a recent field of study and the relationship is not fully developed. Simulations of normal adult lungs [61] and experiments on canine lungs [62] show that the geometry and mechanical properties of the lung are important factors in the mechanical response of the lung. Furthermore, it is suggested that vibrations caused by pressure oscillations improve the elastic condition of the lung walls [61, 62] and that the behaviour of the lung is susceptible to the frequency of those pressure oscillations [56, 57, 63]. However, any effect that pressure oscillations have on respiratory parameters due to the mechanical properties and dynamics of the respiratory system is unknown.

Longitudinal vibrations (up to 37 Hz) to canine trachea smooth muscles [64] showed a decrease in muscle stiffness with an increase in vibration frequency. A three-fold reduction in stiffness was recorded for frequencies around 35 Hz. It was postulated that mechanically inducing vibrations to lung tissue disrupted the cohesive mechanical interactions between protein filaments (cross bridges) during contraction, resulting in a lengthening or relaxation of the tissue. However, studies by other authors propose a different mechanism [65-67] related to lung relaxation saying that it is conceivable that ventilators such as BVV, oscillatory CPAP and HFV which induce lung vibration at frequencies of 8-28 Hz, positively affect breathing by stimulating pulmonary receptors which send information to the brain.

2.2.5. Overview

There have been a variety of respiratory ventilators developed to combat the negative effects of mechanical ventilation. Clinical and analytical studies have shown that there are physiological benefits to adding pressure oscillations to respiratory treatment. However, the mechanisms for gas transport and the effect of the mechanical and surfactant properties on the dynamic response of the lungs still require further study. The concept of stochastic resonance or tuning the amplitude and frequency of pressure oscillations in ventilation has been proposed and studies on smaller animals support such theories. Whether the same applies to human neonatal lungs is still to be determined, in addition to the optimal frequencies required for any particular lung.

To summarise, it is apparent that vibrations or pressure oscillations affect different elements of the respiratory system in different ways as seen in Figure 2.4. In the context

of neonatal respiratory mechanics, lung maturity and surfactant function are the major contributors to lung disease and so the current thesis focuses on the effect that pressure oscillations have on respiratory performance due to mechanical and surface tension effects of the lung.

Quantitative clinical and analytical studies on the optimal frequency and amplitude generation capable by the Bubble CPAP System are still in their infancy and depend on accurate mathematical models of the neonatal lung. Sections 2.3 and 2.4 discuss the respiratory models found in the literature and their usefulness in predicting the response of neonatal lungs to respiratory support techniques.

Section 2.3 details the morphometric and mechanical models which can be built on to assess the mechanical effect of pressure oscillations on respiratory performance in lobes and at the airway opening. Section 2.4 details the models to date on surfactant dynamics which can be used to assess the effect that oscillations have on surfactant function in the alveoli.

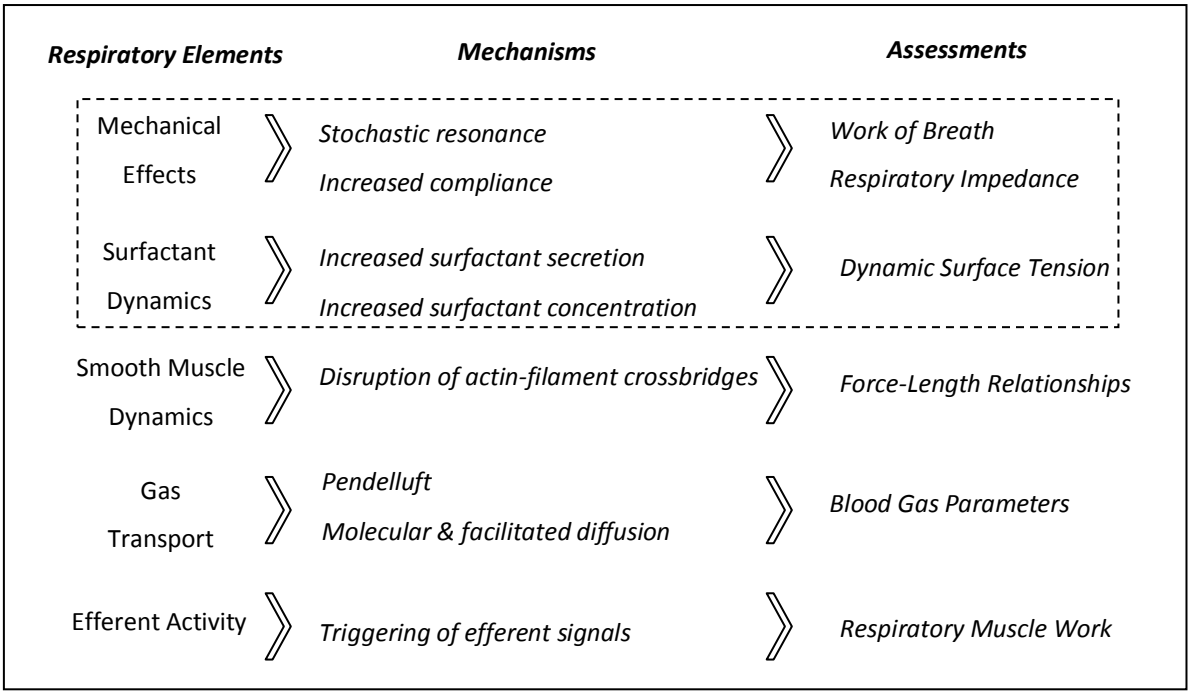

Figure 2.4 The effect of pressure oscillations of different elements of respiration.

2.3. Modelling Respiratory System Dynamics

A variety of models are available in the literature which include poroelastic, computational fluid dynamics (CFD), morphometric and mechanical models. A search of the literature reveals that the approach and complexity of modelling the respiratory system depends on the research question. The effects of gas mixing, efferent activity and ventilation-perfusion effects are not studied in this work. Models that incorporate geometric, physical, mechanical and flow characteristics are considered, so a review on the morphometric and mechanical models found in the literature is discussed in this section.

2.3.1. Morphometrics Models

Morphometric models represent the branching structure of the airways along with other data such as the dimensions, branching angles as well as cross sectional areas and volumes of alveoli. Weibel [68] developed a symmetric model of the human adult lung lung which incorporated 23 generations of symmetrically dividing tubes and 300 million alveoli. The Weibel model is widely used in analytical and numerical prediction because of the convenient symmetric structure [34]. However, the airway branching in the real lung does not end abruptly at generation 23, so Hansen and Ampaya [69] refined the Weibel model by performing detailed analyses of the alveolar regions, concluding that the lung has 27 generations of airways. Also, the system developed by Weibel with the doubling of the airways at each generation was replaced by a system where the number of airways was increased at each generation up to generation 24, then decreased until generation 27. Hansen and Ampaya distinguished 6 different types of alveoli and concluded that there were in fact 450 million alveoli in the lung.

Horsfield [70] developed a more realistic model where the branching structure of the airways is asymmetric but this pattern of asymmetry is constant. In reality, the terminal bronchioles require a different pattern of asymmetry, so for more sophisticated computational analyses, computer models developed from computer tomography (CT) scans show more promise [71]. For the current research, however, the interest in airway branching structure is focused on the first few generations and so the Weibel and Horsfield models are adequate.

2.3.2. Mechanical Models

Computer models that use lumped parameters to describe lung mechanics are often used to investigate the effects of lung development and diseases on respiratory measurements. Such models can also be used to determine the interaction of the respiratory system with respiratory support equipment and ventilation techniques.

The simplest model to describe lung mechanics is a single compartment model (Figure 2.5a) consisting of a single compliance *C* and a single resistance *R* (the RC model) [72]. This model is suitable for simple tidal breathing predictions but is inadequate for higher frequency analysis due to the lack of inertance *I*. Adding inertance to the model (the RIC model in Figure 2.5b) means that it is useful in the study of simple maturation studies due to the small number of required model parameters [73].

Mead [74] suggested a model with seven parameters (Figure 2.5d); inertance *I*, central and peripheral resistances (R_c and R_p) and lung, chest wall, bronchial and extrathoracic compliances (C_l, C_w, C_b and C_e). Although it considers these further properties and is able to simulate the influences of mask leaks and compliance on the respiratory system as well as the effects of bronchiole obstruction, it still remains an extended version of a single compartment model and cannot simulate uneven ventilation.

Viscoelastic models that separate airway and tissue properties into separate regions are also available in the literature. Athanasiades et al. [75] used a viscoelastic model (shown in Figure 2.6) to calculate the work of breath in normal adults.

R_u, R_c, R_s and R_{ve} are the upper airways, collapsible airways, small airways and viscoelastic element resistances. C_c, C_l, C_{ve} and C_{cw} are the collapsible airways, lung tissue, viscoelastic element and chest wall compliances. P_{mus} and P_{atm} are the pressure due to muscle activity and the atmosphere. Liu et al. [76] used the same type of model but added a pulmonary circulation model (to describe gas exchange at the alveolar-capillary membrane) which could accurately predict the expired gas concentrations. These models however, do not include the inertance which make it inadequate for simulations that involve frequencies much higher than breathing frequencies and also

like the Mead model [74] are single compartment models as well which limit their use in ventilation distribution studies.

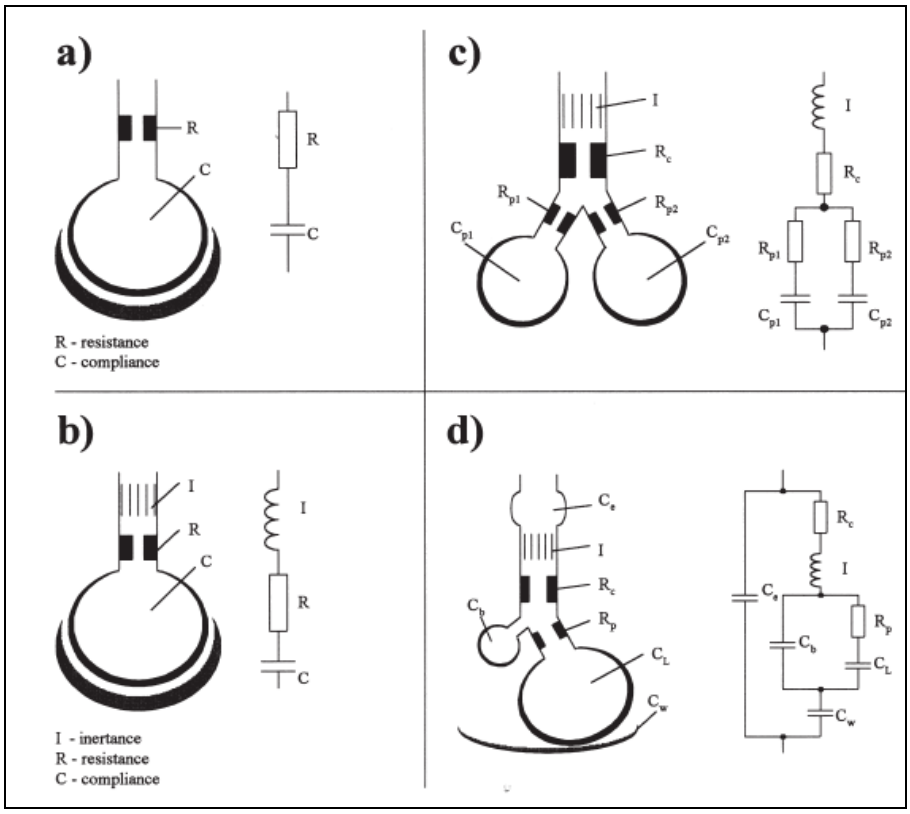

Figure 2.5 Lung models to model respiratory system mechanics [73].

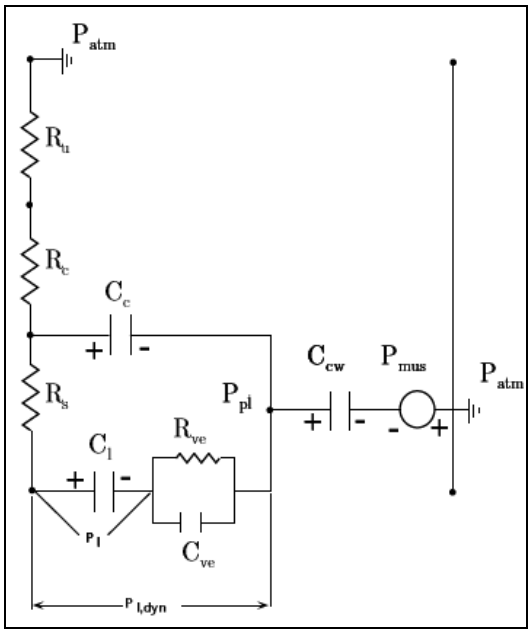

Figure 2.6 Viscoelastic model as used by Athanasiades et al. [75].

Tomlinson et al. [77, 78] also uses a single compartment model of an adult lung to simulate pressure, flow and volume. However, unlike Mead [74] and Athanasiades [75], the Tomlinson model includes flow-dependant resistance in the upper airways as well as lung and chest wall viscoelasticity and inertance. More experimental data is still required to correlate with the model, however, it does show promise in being used in dynamic studies.

A two-compartment model (Figure 2.5c) as proposed by Schmidt [73] and Crooke and Head [79] is well suited to investigations of uneven ventilation. The values of *C*, *I* and *R* can be adjusted to reflect different pathologies. These models can predict tidal volumes, flows and pressures in each compartment that could be of interest to clinicians. The models however do not include airway and chest wall compliance. These types of models, although an improvement from the single compartment model, do not consider flow dependant resistance which is important in describing the upper airways [80].

A model by Polak and Lutchen [81] uses an asymmetric Horsfield bronchial tree that leads to several independent alveolar compartments. Viscoelastic properties of the lobes and the inertia of airway walls are neglected. Also, the mechanical properties are assumed not to vary between compartments such that the only source of compartmental flow heterogeneity is the asymmetry of the bronchial tree. The model predicts expiratory flow and pressure but predictions are not dynamic or validated.

2.3.3. Overview

A review of the morphometric and mechanical models available in the literature have been presented. Single compartment models, regardless of the various regional resistances and compliances that may be incorporated are still not able to model the effects of uneven ventilation. Multi-compartmental models in the literature neglect inertance, chest wall mechanics or a variation in mechanical properties between compartments. Thus, there exists a need for models that incorporate inertance to enable analysis at frequencies higher than typical breathing frequencies and multiple compartments that have individual mechanical and physical properties to better model the uneven distribution of ventilation in diseased lungs. Also, model predictions in the literature mostly represent adult values with only a few infant models predicting overall

respiratory variables. The lack of neonatal lung parameters makes it difficult to accurately quantify predictions for neonates.

2.4. Modelling Surfactant Dynamics

Surfactant dysfunction plays a major role in RDS. Understanding the mechanisms of surfactant transport during oscillatory treatments such as Bubble CPAP will help understand the possible benefits of using surfactant therapy in conjunction with Bubble CPAP. Measurements on dynamic surfactant function (as occurs in the alveoli) have been performed using surface tension measuring devices such as pulsating bubble surfactometers (PBS) and captive bubble surfactometers (CBS). Mathematical models have also been developed that help to understand the mechanisms of surfactant transport under different ventilation types and surfactant therapies. They are frequently approximated as a single spherical alveolus surrounded by fluid. A review of the mathematical models developed to date are presented in this section due to their promise in being used in the present research to identify the possible surface tension benefits of introducing pressure oscillations at the level of the alveoli.

Horn and Davis [82] were the first to introduce a comprehensive model that described surface tension in surfactant that underwent dynamic area changes. The alveolus was approximated as a spherical elastic membrane that contained a shell of incompressible liquid surrounding a gas. The gas-liquid interface (as with subsequent models) is the site of surfactant activity. The model considered diffusion and adsorption of surfactant molecules and viscoelastic behavior of the bulk and interface. They concluded that although bulk viscosity did not contribute to lung hysteresis (since the alveolar lining is too thin), surface viscosity had significant effects. The use of the Horn and Davis model is restricted to near equilibrium behaviour however, since it made no provision for over-compression or “squeeze-out” of surfactant from the surfactant layer at the gas-liquid interface.

Otis et al. [83] modelled surfactant behaviour of Surfactant TA as observed in a PBS. The problem was simplified by assuming that the spherical bubble of air was surrounded in an infinite solution of surfactant. The adsorption and desorption of surfactant to and from the gas-liquid interface was characterized by Langmuir kinetics

and three interfacial surfactant concentration regimes. Diffusion was neglected but in reality a diffusional boundary layer will develop around the gas-liquid interface making the transport through this boundary layer more complex. However, the model did have success in describing the steady-state oscillatory dynamics in that it provided good agreement with experimental values at steady state for a variety of cycling frequencies (1-100 cycles/min) and bulk concentrations.

Morris et al. [84, 85] incorporated the effects of diffusion into the Otis model. By using the methods of Chang and Franses [86], they incorporated the convection-diffusion equation into the model such that the bulk concentration becomes time and space dependant. The Morris model was able to simulate transient effects and surfactant concentrations just below the gas-liquid interface. It also showed an increased agreement with experimental results on Curosurf (a commercial surfactant) performed by Schurch et al. [87].

To date, the models discussed have been used to investigate surface tension behaviour under typical breathing frequencies and amplitudes. Its ability to be used to investigate the effect of adding pressure oscillations superimposed on the breath signal have not yet been performed. Also, no such experiments on surface tension measuring devices have been performed to date with which to validate such predictions.

2.5. Research Plan and Objectives

A review of the literature reveals that although there are a variety of respiratory system models in the literature, predictions on neonatal respiratory parameters still remains largely undefined mostly due to the lack of input parameters. Models that include viscoelastic and inertive properties often are single-compartment models and multi-compartment models either ignore inertance or have uniform mechanical properties across compartments. Previous models have managed to simulate respiratory behaviour during normal and forced breathing movements and during ventilation. The response of the respiratory system to oscillatory techniques such as the Bubble CPAP System is still to be accurately modelled.

Thus, there is a need for more descriptive multi-compartmental models that seek to model the effect of pressure oscillations on neonatal respiratory performance. Also, surfactant behavior has been modelled in the literature for normal breathing frequencies and volume excursions. The behavior of surface tension in the alveoli under the influence of added pressure oscillations has not been modelled or experimentally determined.

Therefore, the objectives of the current research are to:

- Create an original multi-compartmental model of the neonatal lung that includes compartment-specific inertance and viscoelasticity as well as better defined mechanical and physical parameters determined from measurements on actual neonatal lungs.

- Validate the model with experimental data obtained from clinical trials.

- Use the model to determine the mechanical effect of pressure oscillations as produced by the Bubble CPAP System on respiratory performance.

- Determine the role that frequencies of oscillation play in providing the optimal respiratory support.

- Build a surface tension model that simulates surface tension dynamics in an alveolus exposed to pressure oscillation frequencies in the range typically produced by the Bubble CPAP System.

- Validate the surface tension model with experiments conducted on a custom-built PBS.

2.6. Closure

This chapter presented the knowledge to date on the known effects and mechanisms of improvement of ventilatory treatments that use pressure oscillations. HFV, BVV and the

Bubble CPAP System were highlighted as the major examples. Clinical studies proposing the benefits of using Bubble CPAP have been discussed. The relevant models that have been developed to date on respiratory mechanics and surfactant dynamics were mentioned and the value of those models to the current research field was noted. As a result, the objectives of the research were developed to further experimentally and theoretically investigate the mechanical effect of pressure oscillations on neonatal respiratory performance.

CHAPTER 3

Respiratory System Model

3.1. Introduction

This chapter contains the complete derivation of the ovine respiratory system model used to predict the work of breath (WOB) at predefined locations within the respiratory system. Also, the parameters used in the model are fully defined for both 128 day (preterm) and 142 day (near-term) gestation lambs in this chapter. Section 3.2 discusses the philosophy of the model formulation and describes the lumped parameter model used in this research. Expressions for the pressures in each identified section of the lumped model are derived. Section 3.3 describes the expressions of the mass flow rates in each section, derived from the non-dimensional, empirical Reynolds-Lee relationships for the airways and from simple resistance relationships for the lobes. Section 3.4 contains the derivations that describe the wall motion in each lobe and the pleural compartment. The methods and results for the empirically measured parameters (lung/lobe masses, pressure-volume curves and airway dimensions) that were needed for the model are presented in Section 3.5. Parameters that were obtained from the existing literature for the model are summarised in Section 3.6. The Simulink model and its use within the Matlab environment is described in Section 3.7.

3.2. Model Formulation

The bronchial tree is a complex bifurcating network of airways which according to the Weibel model [68] divides 23 times before forming millions of alveolar sacs in humans. However, when defining the different elements of the respiratory system using lumped parameter modelling, the complexity of the mathematical model can be reduced so that pressures, flows and volumes are assumed to be uniform within well defined control

volumes. The lung can then be described as a system of branched airways, consisting of the trachea (windpipe) and bronchi (subsequent airways), leading to 5 chambers that represent the 5 separate lobes present in the actual lung. Each lobe has its own set of mechanical properties that are described in terms of elasticity, inertia and damping elements. As a result, the model developed in this chapter is able to account for the behaviour of a 5-compartment lung with differing mechanical properties and lung capacities, as well as disparities between inspiratory and expiratory airway resistances. It was not physically possible to accurately obtain empirical measurements such as pressure-volume, mass and dimension measurements for sub-lobar segments to determine regional mechanical and physical properties within each lobe, thus restricting the current model to a maximum of 5 compartments. The output of the model includes airway pressures, flow rates and volumes at the airway opening and at the individual lobes. These are used to calculate the WOB at each location as a measure of respiratory performance under different ventilation strategies.

The ovine respiratory system is modelled in this chapter. Preterm and near-term respiratory outputs can be modelled by changing the parameters to suit. Ovine lungs are used frequently in clinical trials on neonatal respiratory mechanics due to the similarity in size, physiological parameters and established relationships between ovine and human gestations. Moreover, limitations on human experimentation make the ovine model an attractive alternative to investigate respiratory parameters.

The 12 airways and 5 lobar regions represented in the ovine respiratory system model are shown in Figure 3.1 (not to scale) and named in Table 3.1 in such a way as to reflect anatomical location.

The dynamics of the model are formulated by assuming that a uniform (but time varying) pressure exists in each section and that the rate of change of that pressure is dependent on the flow into and out of the section as well as any elastic, resistive or inertive forces present. A schematic diagram of the lumped sections of the lung is shown in Figure 3.2. The tracheo-bronchial tree, starting from the trachea, divides successively into the various secondary bronchi that lead to their respective lobes. The

respective pressures and mass flow rates present in each section are shown in the figure and defined in more detail thereafter. The numbers correspond to those in Table 3.1.

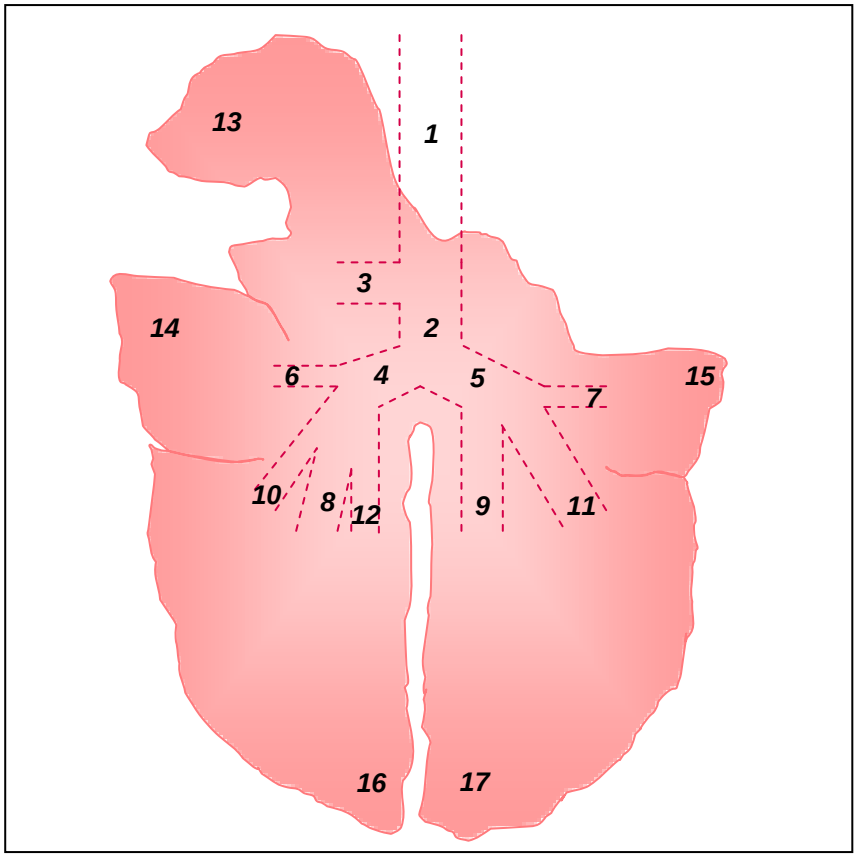

Figure 3.1 The elements of the ovine respiratory system model.

Table 3.1 The 17 elements of the ovine respiratory system model.

1 - Upper trachea	10 - Right posterior diaphragmatic bronchus
2 - Lower trachea	11 - Left posterior diaphragmatic bronchus
3 - Right apical bronchus	12 - Right anterior diaphragmatic bronchus
4 - Right main bronchus	13 - Right apical lobe
5 - Left main bronchus	14 - Right cardiac lobe
6 - Right cardiac bronchus	15 - Left cardiac lobe
7 - Left cardiac bronchus	16 - Right diaphragmatic lobe
8 - Right major diaphragmatic bronchus	17 - Left diaphragmatic lobe
9 - Left major diaphragmatic bronchus	

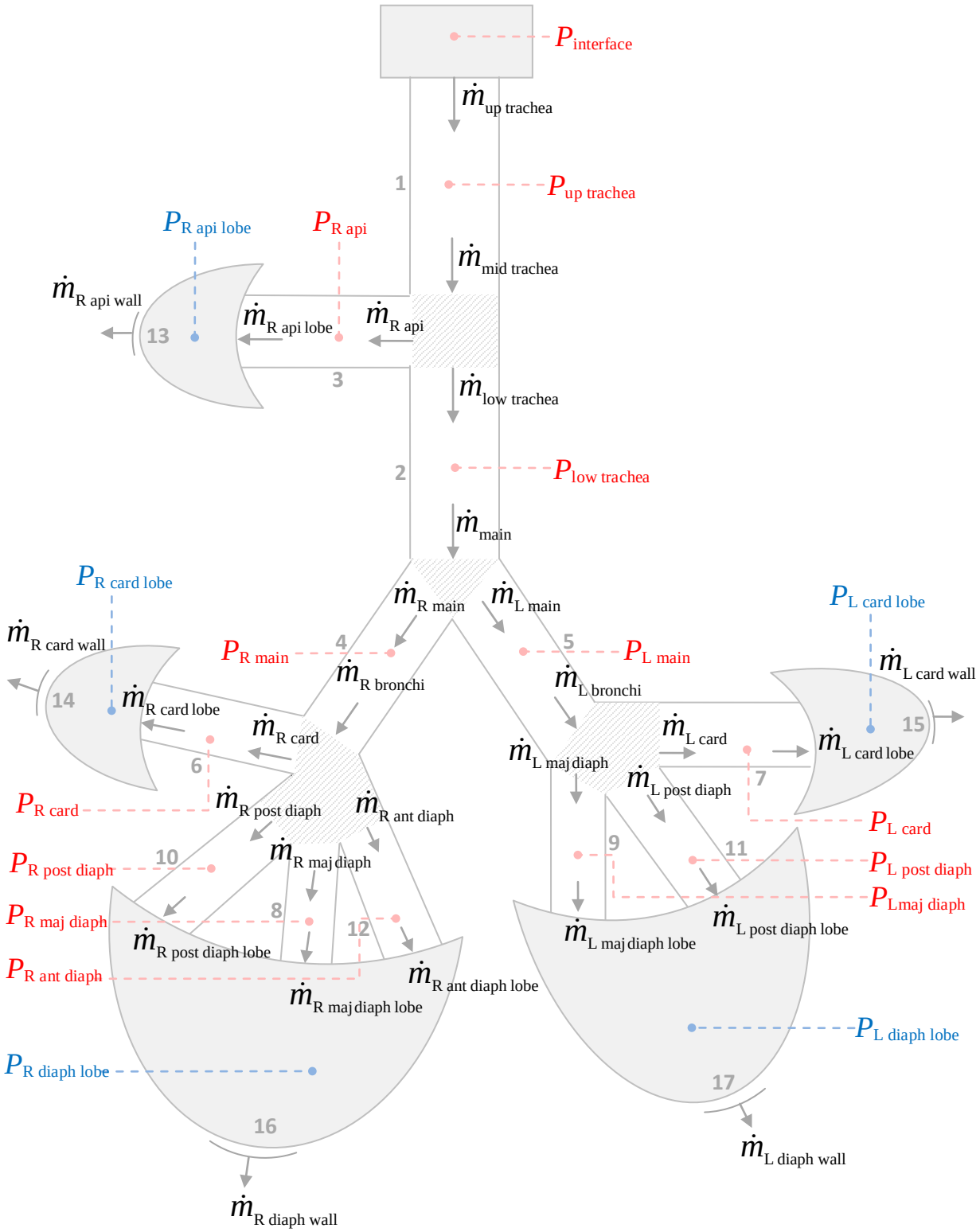

Figure 3.2 Schematic diagram of the lumped respiratory system (showing section numbering)

3.2.1. Model Assumptions

- Humidity effects are neglected and all physical properties and constants are evaluated at a constant temperature of 39 ^{o}C (312 K) i.e. lamb rectal temperature.
- Resistances of the airways in the lobe and the collective resistance of the lobes are assumed to be constant and the only interaction between lobes is assumed to occur at the branch points of the bronchi leading to the lobes.
- Ideal gas is assumed and gas compressibility is neglected since the Mach numbers have been calculated to be <0.2 for typical flows in all airways.
- Lobe surface area is assumed to remain constant unlike reality where the area changes with lung volume. Since this relationship is uncharacterised for premature lambs, a constant surface area is assumed.
- Lobe and airway pressures are assumed to be uniform. Although in reality there are variations in pressure within the lobe, this assumption is adequate for the present level of investigation where the trends in overall differences in respiratory parameters across lobes are of consideration. Such effects can be added to the model in the future by adding more compartments to the individual lobes to account for regional pressure variations.
- The airways are assumed to be straight with constant circular cross-section. Airways can also be modelled as collapsible tubes if desired, based on the cross-sectional area-transmural pressure relationship. This relationship is undefined in the literature for premature neonatal lambs. The trachea and primary bronchi contain cartilage and some remnants of cartilage which are still present at the level of the secondary bronchi. This makes these airways more rigid than the rest of the conducting airways. Therefore, to reduce the complexity of the model and increase solver efficiency, elementary dissipative pressure losses in a bifurcating airway system is modelled as the primary pressure-loss phenomenon. However, the model retains fundamental features of airway branching, mechanical and physical properties. It is also constructed so as to facilitate the addition of bronchial wall complaince in future studies that may be conducted in this area.

3.2.2. Model Development

The rate of change of pressure in sections 1-12 can be derived from the ideal gas equation of state.

$$P_{section}V_{section} = m_{section}RT \quad \textbf{(3.1)}$$

where

$P_{section}$ is the absolute pressure within the section (Pa)

$V_{section}$ is the volume of the section (m^3)

$m_{section}$ is the mass of air in the section (kg)

R is the specific gas constant of air at 312 K ($Pa.m^3/(kg.K)$)

T is the temperature in Kelvin (K)

If we consider a time varying pressure in any particular section, equation (3.1) becomes

$$\frac{d(P_{section}V_{section})}{dt} = \frac{d(m_{section}RT)}{dt} \quad \textbf{(3.2)}$$

Assuming $V_{section}$, R and T constant, equation (3.2) becomes

$$\frac{dP_{section}}{dt} = \frac{RT}{V_{section}}\frac{dm_{section}}{dt} \quad \textbf{(3.3)}$$

Applying the conservation of mass to a section gives the change in the mass of air in that section, $\Delta m_{section}$. This can be written as

$$\Delta m_{section} = m_{in} - m_{out} \quad \textbf{(3.4)}$$

where m_{in} is the mass that enters the section and m_{out} is the mass that leaves the section. For a time varying system,

$$\frac{dm_{section}}{dt} = \frac{d(m_{in} - m_{out})}{dt} \quad \textbf{(3.5)}$$

and thus

$$\frac{dm_{section}}{dt} = \frac{d}{dt}\left(m_{in} - m_{out}\right) = \dot{m}_{in} - \dot{m}_{out} \qquad \textbf{(3.6)}$$

Equation (3.3) can now be written as

$$\frac{dP_{section}}{dt} = \frac{RT}{V_{section}}\left(\dot{m}_{in} - \dot{m}_{out}\right) \qquad \textbf{(3.7)}$$

For regions 13 to 17 (the lobes), where the volume of the region varies with time, equation (3.3) changes to

$$\frac{d(P_{lobe}V_{lobe})}{dt} = \frac{dm_{lobe}}{dt}RT \qquad \textbf{(3.8)}$$

which can be expanded to the following form.

$$\frac{dP_{lobe}}{dt}V_{lobe} + \frac{dV_{lobe}}{dt}P_{lobe} = \left(\dot{m}_{in} - \dot{m}_{out}\right)RT \qquad \textbf{(3.9)}$$

Equations (3.7) and (3.9) can be used to obtain expressions of the pressure in the individual airway segments and lobes respectively. The mass flow rates and pressures involved are those presented in Figure 3.2. Applying equation (3.7) to sections 1-12 leads to:

$$\frac{dP_{\text{up trachea}}}{dt} = \frac{RT}{V_{\text{up trachea}}}\left(\dot{m}_{\text{up trachea}} - \dot{m}_{\text{mid trachea}}\right) \qquad \textbf{(3.10)}$$

for the upper trachea, where

$$\dot{m}_{\text{mid trachea}} = \dot{m}_{\text{low trachea}} + \dot{m}_{\text{R api}} \qquad \textbf{(3.11)}$$

For the lower trachea

$$\frac{dP_{\text{low trachea}}}{dt} = \frac{RT}{V_{\text{low trachea}}}\left(\dot{m}_{\text{low trachea}} - \dot{m}_{\text{main}}\right) \quad \textbf{(3.12)}$$

where

$$\dot{m}_{\text{main}} = \dot{m}_{\text{L main}} + \dot{m}_{\text{R main}} \quad \textbf{(3.13)}$$

For the right apical bronchus

$$\frac{dP_{\text{R api}}}{dt} = \frac{RT}{V_{\text{R api}}}\left(\dot{m}_{\text{R api}} - \dot{m}_{\text{R api lobe}}\right) \quad \textbf{(3.14)}$$

For the right main bronchus

$$\frac{dP_{\text{R main}}}{dt} = \frac{RT}{V_{\text{R main}}}\left(\dot{m}_{\text{R main}} - \dot{m}_{\text{R bronchi}}\right) \quad \textbf{(3.15)}$$

where

$$\dot{m}_{\text{R bronchi}} = \dot{m}_{\text{R card}} + \dot{m}_{\text{R maj diaph}} + \dot{m}_{\text{R post diaph}} + \dot{m}_{\text{R ant diaph}} \quad \textbf{(3.16)}$$

For the left main bronchus

$$\frac{dP_{\text{L main}}}{dt} = \frac{RT}{V_{\text{L main}}}\left(\dot{m}_{\text{L main}} - \dot{m}_{\text{L bronchi}}\right) \quad \textbf{(3.17)}$$

where

$$\dot{m}_{\text{L bronchi}} = \dot{m}_{\text{L card}} + \dot{m}_{\text{L maj diaph}} + \dot{m}_{\text{L post diaph}} \quad \textbf{(3.18)}$$

For the right cardiac bronchus

$$\frac{dP_{\text{R card}}}{dt} = \frac{RT}{V_{\text{R card}}}\left(\dot{m}_{\text{R card}} - \dot{m}_{\text{R card lobe}}\right) \quad \textbf{(3.19)}$$

For the left cardiac bronchus

$$\frac{dP_{\text{L card}}}{dt} = \frac{RT}{V_{\text{L card}}}\left(\dot{m}_{\text{L card}} - \dot{m}_{\text{L card lobe}}\right) \quad \textbf{(3.20)}$$

For the right major diaphragmatic bronchus

$$\frac{dP_{\text{R maj diaph}}}{dt} = \frac{RT}{V_{\text{R maj diaph}}}\left(\dot{m}_{\text{R maj diaph}} - \dot{m}_{\text{R maj diaph lobe}}\right) \quad \textbf{(3.21)}$$

For the left major diaphragmatic bronchus

$$\frac{dP_{\text{L maj diaph}}}{dt} = \frac{RT}{V_{\text{L maj diaph}}}\left(\dot{m}_{\text{L maj diaph}} - \dot{m}_{\text{L maj diaph lobe}}\right) \quad \textbf{(3.22)}$$

For the right posterior diaphragmatic bronchus

$$\frac{dP_{\text{R post diaph}}}{dt} = \frac{RT}{V_{\text{R post diaph}}}\left(\dot{m}_{\text{R post diaph}} - \dot{m}_{\text{R post diaph lobe}}\right) \quad \textbf{(3.23)}$$

For the left posterior diaphragmatic bronchus

$$\frac{dP_{\text{L post diaph}}}{dt} = \frac{RT}{V_{\text{L post diaph}}}\left(\dot{m}_{\text{L post diaph}} - \dot{m}_{\text{L post diaph lobe}}\right) \quad \textbf{(3.24)}$$

For the right anterior diaphragmatic bronchus

$$\frac{dP_{\text{R ant diaph}}}{dt} = \frac{RT}{V_{\text{R ant diaph}}}\left(\dot{m}_{\text{R ant diaph}} - \dot{m}_{\text{R ant diaph lobe}}\right) \quad \textbf{(3.25)}$$

Using equation (3.9), the pressure in each lobe (regions 13-17) can be written as follows.

For the right apical lobe

$$\frac{dP_{\text{R api lobe}}}{dt} V_{\text{R api lobe}} + \frac{dV_{\text{R api lobe}}}{dt} P_{\text{R api lobe}} = \left(\dot{m}_{\text{R api lobe}} - \dot{m}_{\text{R api wall}}\right)RT \quad \textbf{(3.26)}$$

For the right cardiac lobe

$$\frac{dP_{\text{R card lobe}}}{dt}V_{\text{R card lobe}} + \frac{dV_{\text{R card lobe}}}{dt}P_{\text{R card lobe}} = \left(\dot{m}_{\text{R card lobe}} - \dot{m}_{\text{R card wall}}\right)RT \qquad \textbf{(3.27)}$$

For the left cardiac lobe

$$\frac{dP_{\text{L card lobe}}}{dt}V_{\text{L card lobe}} + \frac{dV_{\text{L card lobe}}}{dt}P_{\text{L card lobe}} = \left(\dot{m}_{\text{L card lobe}} - \dot{m}_{\text{L card wall}}\right)RT \qquad \textbf{(3.28)}$$

For the right diaphragmatic lobe

$$\frac{dP_{\text{R diaph lobe}}}{dt}V_{\text{R diaph lobe}} + \frac{dV_{\text{R diaph lobe}}}{dt}P_{\text{R diaph lobe}} = \left(\dot{m}_{\text{R diaph lobe}} - \dot{m}_{\text{R diaph wall}}\right)RT \qquad \textbf{(3.29)}$$

where

$$\dot{m}_{\text{R diaph lobe}} = \dot{m}_{\text{R maj diaph lobe}} + \dot{m}_{\text{R post diaph lobe}} + \dot{m}_{\text{R ant diaph lobe}} \qquad \textbf{(3.30)}$$

For the left diaphragmatic lobe

$$\frac{dP_{\text{L diaph lobe}}}{dt}V_{\text{L diaph lobe}} + \frac{dV_{\text{L diaph lobe}}}{dt}P_{\text{L diaph lobe}} = \left(\dot{m}_{\text{L diaph lobe}} - \dot{m}_{\text{L diaph wall}}\right)RT \qquad \textbf{(3.31)}$$

where

$$\dot{m}_{\text{L diaph lobe}} = \dot{m}_{\text{L maj diaph lobe}} + \dot{m}_{\text{L post diaph lobe}} \qquad \textbf{(3.32)}$$

In this section, expressions have been derived to describe the change in pressure in each section due to the flow rates and physical properties of each section. The mass flow rates in equations (3.10) to (3.32) still need to be determined by separate relationships to resolve the model. These are derived in the following section.

3.3. Mass Flow Rate Expressions

Thus far, the mass flow rates in the derivation represent the mass flow at specific points i.e. at the boundaries of each section. The walls in sections 1-12 contain varying amounts of cartilage and so may be considered to be vastly more rigid than subsequent airways. In order to simplify the model for the purposes of this study, sections 1-12 are assumed to be rigid.

This implies that there is no variation in mass in sections 1-12. The sections are also very short (in the order of a few centimetres) such that any pressure variations within the section are very small and can be ignored. It can thus be assumed that the pressure at each boundary is equal to the pressure in the section that is situated upwind from that boundary.

In the simplest case, mass flow rate can be determined by the pressure-flow characteristics as described by Poiseuille's equation for laminar flow in straight, circular tubes. However, the mass flow rate in a monopodial branching network can be more accurately determined by empirical relations developed by Reynolds and Lee [88] where the total pressure loss in a canine airway segment ΔP_{total} was found to be related to the flow rate and its square for Reynolds numbers tested up to 10,000. The following calculations show how the Reynolds-Lee equations [88] can be used to describe the inspiratory and expiratory mass flows in the tracheal and bronchial segments as a function of Poiseuille pressure drop across that segment ($\Delta P_{poiseuille}$) and the Reynolds Number (Re).

Reynolds and Lee describe their data using a dimensionless Rohrer equation:

$$\Delta P_{total} = (a + b\,\mathrm{Re})\Delta P_{poiseuille} \qquad \textbf{(3.33)}$$

where *a* and *b* are scaling coefficients as defined by Reynolds and Lee and are listed in Table 3.2 for the trachea and subsequent airways. The values of *a* are much larger for expiration than for inspiration for a given airway, meaning that static pressure drop is much larger for expiration than inspiration. The values for *b* remain similar for both

inspiration and expiration in a particular airway. Reynolds and Lee attribute the increased loss in pressure during expiration to the effects of the bifurcations preceding tracheal flow as air travels up from the smaller airways, out to the airway opening.

Table 3.2 Scaling factors in Reynolds-Lee equation [88].

	Inspiration		Expiration	
	a	*b*	*a*	*b*
Tracheal Segments	24	0.0162	50	0.0162
All Airways Below Trachea	15	0.0146	40	0.0116

The static pressure drop across the section $\Delta P_{section}$ can be expressed as:

$$\Delta P_{section} = P_{upwind} - P_{section} = (a + b\,\mathrm{Re})\Delta P_{poiseuille} \qquad \textbf{(3.34)}$$

where P_{upwind} is the pressure on the upwind boundary and

$$\Delta P_{poiseuille} = \frac{128\mu L_{section}}{\pi D_{section}{}^{4}\rho}\dot{m}_{section} \qquad \textbf{(3.35)}$$

In equation (3.35) $L_{section}$ and $D_{section}$ are the length and diameter of the section respectively. $\dot{m}_{section}$ is the mass flow through the section and μ and ρ are the dynamic viscosity and density of the air at 312.5K.

Combining equations (3.34) and (3.35) and solving for the mass flow rate gives

$$\dot{m}_{\mathrm{in}} = \frac{\Delta P_{section}}{(a + b\,\mathrm{Re})}\frac{\pi D_{\mathrm{section}}{}^{4}\rho}{128\mu L_{\mathrm{section}}} \qquad \textbf{(3.36)}$$

Substituting values for *a* and *b* for each respective airway, we arrive at the following expressions for the individual airway segments (sections 1 to 12).

For inspiration:

The mass flow rate in the upper trachea is

$$\dot{m}_{\text{up trachea}} = \frac{P_{\text{interface}} - P_{\text{up trachea}}}{(24 + 0.0162\,\text{Re})} \frac{\pi D_{\text{up trachea}}{}^4 \rho}{128 \mu L_{\text{up trachea}}} \quad \textbf{(3.37)}$$

The mass flow rate in the lower trachea is

$$\dot{m}_{\text{low trachea}} = \frac{P_{\text{up trachea}} - P_{\text{low trachea}}}{(24 + 0.0162\,\text{Re})} \frac{\pi D_{\text{low trachea}}{}^4 \rho}{128 \mu L_{\text{low trachea}}} \quad \textbf{(3.38)}$$

The mass flow rate in the right apical bronchus is

$$\dot{m}_{\text{R api}} = \frac{P_{\text{up trachea}} - P_{\text{R api}}}{(15 + 0.0146\,\text{Re})} \frac{\pi D_{\text{R api}}{}^4 \rho}{128 \mu L_{\text{R api}}} \quad \textbf{(3.39)}$$

The mass flow rate in the left main bronchus is

$$\dot{m}_{\text{L main}} = \frac{P_{\text{low trachea}} - P_{\text{L main}}}{(15 + 0.0146\,\text{Re})} \frac{\pi D_{\text{L main}}{}^4 \rho}{128 \mu L_{\text{L main}}} \quad \textbf{(3.40)}$$

The mass flow rate in the right main bronchus is

$$\dot{m}_{\text{R main}} = \frac{P_{\text{low trachea}} - P_{\text{R main}}}{(15 + 0.0146\,\text{Re})} \frac{\pi D_{\text{R main}}{}^4 \rho}{128 \mu L_{\text{R main}}} \quad \textbf{(3.41)}$$

The mass flow rate in the left cardiac bronchus is

$$\dot{m}_{\text{L card}} = \frac{P_{\text{L main}} - P_{\text{L card}}}{(15 + 0.0146\,\text{Re})} \frac{\pi D_{\text{L card}}{}^4 \rho}{128 \mu L_{\text{L card}}} \quad \textbf{(3.42)}$$

The mass flow rate in the left major diaphragmatic bronchus is

$$\dot{m}_{\text{L maj diaph}} = \frac{P_{\text{L main}} - P_{\text{L maj diaph}}}{(15 + 0.0146\,\text{Re})} \frac{\pi D_{\text{L maj diaph}}{}^4 \rho}{128 \mu L_{\text{L maj diaph}}} \quad \textbf{(3.43)}$$

The mass flow rate in the left posterior diaphragmatic bronchus is

$$\dot{m}_{\text{L post diaph}} = \frac{P_{\text{L main}} - P_{\text{L post diaph}}}{\left(15 + 0.0146\,\text{Re}\right)} \frac{\pi D_{\text{L post diaph}}{}^{4} \rho}{128 \mu L_{\text{L post diaph}}} \tag{3.44}$$

The mass flow rate in the right cardiac bronchus is

$$\dot{m}_{\text{R card}} = \frac{P_{\text{R main}} - P_{\text{R card}}}{\left(15 + 0.0146\,\text{Re}\right)} \frac{\pi D_{\text{R card}}{}^{4} \rho}{128 \mu L_{\text{R card}}} \tag{3.45}$$

The mass flow rate in the right major diaphragmatic bronchus is

$$\dot{m}_{\text{R maj diaph}} = \frac{P_{\text{R main}} - P_{\text{R maj diaph}}}{\left(15 + 0.0146\,\text{Re}\right)} \frac{\pi D_{\text{R maj diaph}}{}^{4} \rho}{128 \mu L_{\text{R maj diaph}}} \tag{3.46}$$

The mass flow rate in the right posterior diaphragmatic bronchus is

$$\dot{m}_{\text{R post diaph}} = \frac{P_{\text{R main}} - P_{\text{R post diaph}}}{\left(15 + 0.0146\,\text{Re}\right)} \frac{\pi D_{\text{R post diaph}}{}^{4} \rho}{128 \mu L_{\text{R post diaph}}} \tag{3.47}$$

The mass flow rate in the right anterior diaphragmatic bronchus is

$$\dot{m}_{\text{R ant diaph}} = \frac{P_{\text{R main}} - P_{\text{R ant diaph}}}{\left(15 + 0.0146\,\text{Re}\right)} \frac{\pi D_{\text{R ant diaph}}{}^{4} \rho}{128 \mu L_{\text{R ant diaph}}} \tag{3.48}$$

For expiration:

The mass flow rate in the upper trachea is

$$\dot{m}_{\text{up trachea}} = \frac{P_{\text{int}} - P_{\text{up trachea}}}{\left(50 + 0.0162\,\text{Re}\right)} \frac{\pi D_{\text{up trachea}}{}^{4} \rho}{128 \mu L_{\text{up trachea}}} \tag{3.49}$$

The mass flow rate in the lower trachea is

$$\dot{m}_{\text{low trachea}} = \frac{P_{\text{up trachea}} - P_{\text{low trachea}}}{\left(50 + 0.0162\,\text{Re}\right)} \frac{\pi D_{\text{low trachea}}{}^{4} \rho}{128 \mu L_{\text{low trachea}}} \tag{3.50}$$

The mass flow rate in the right apical bronchus is

$$\dot{m}_{\text{R api}} = \frac{P_{\text{up trachea}} - P_{\text{R api}}}{\left(40 + 0.0146\,\text{Re}\right)} \frac{\pi D_{\text{R api}}{}^{4} \rho}{128 \mu L_{\text{R api}}} \tag{3.51}$$

The mass flow rate in the left main bronchus is

$$\dot{m}_{\text{L main}} = \frac{P_{\text{low trachea}} - P_{\text{L main}}}{\left(40 + 0.0146\,\text{Re}\right)} \frac{\pi D_{\text{L main}}{}^{4} \rho}{128 \mu L_{\text{L main}}} \tag{3.52}$$

The mass flow rate in the right main bronchus is

$$\dot{m}_{\text{R main}} = \frac{P_{\text{low trachea}} - P_{\text{R main}}}{\left(40 + 0.0146\,\text{Re}\right)} \frac{\pi D_{\text{R main}}{}^{4} \rho}{128 \mu L_{\text{R main}}} \tag{3.53}$$

The mass flow rate in the left cardiac bronchus is

$$\dot{m}_{\text{L card}} = \frac{P_{\text{L main}} - P_{\text{L card}}}{\left(40 + 0.0146\,\text{Re}\right)} \frac{\pi D_{\text{L card}}{}^{4} \rho}{128 \mu L_{\text{L card}}} \tag{3.54}$$

The mass flow rate in the left major diaphragmatic bronchus is

$$\dot{m}_{\text{L maj diaph}} = \frac{P_{\text{L main}} - P_{\text{L maj diaph}}}{\left(40 + 0.0146\,\text{Re}\right)} \frac{\pi D_{\text{L maj diaph}}{}^{4} \rho}{128 \mu L_{\text{L maj diaph}}} \tag{3.55}$$

The mass flow rate in the left posterior diaphragmatic bronchus is

$$\dot{m}_{\text{L post diaph}} = \frac{P_{\text{L main}} - P_{\text{L post diaph}}}{\left(40 + 0.0146\,\text{Re}\right)} \frac{\pi D_{\text{L post diaph}}{}^{4} \rho}{128 \mu L_{\text{L post diaph}}} \tag{3.56}$$

The mass flow rate in the right cardiac bronchus is

$$\dot{m}_{\text{R card}} = \frac{P_{\text{R main}} - P_{\text{R card}}}{(40 + 0.0146\,\text{Re})} \frac{\pi D_{\text{R card}}{}^4 \rho}{128 \mu L_{\text{R card}}} \qquad \textbf{(3.57)}$$

The mass flow rate in the right major diaphragmatic bronchus is

$$\dot{m}_{\text{R maj diaph}} = \frac{P_{\text{R main}} - P_{\text{R maj diaph}}}{(40 + 0.0146\,\text{Re})} \frac{\pi D_{\text{R maj diaph}}{}^4 \rho}{128 \mu L_{\text{R maj diaph}}} \qquad \textbf{(3.58)}$$

The mass flow rate in the right posterior diaphragmatic bronchus is

$$\dot{m}_{\text{R post diaph}} = \frac{P_{\text{R main}} - P_{\text{R post diaph}}}{(40 + 0.0146\,\text{Re})} \frac{\pi D_{\text{R post diaph}}{}^4 \rho}{128 \mu L_{\text{R post diaph}}} \qquad \textbf{(3.59)}$$

The mass flow rate in the right anterior diaphragmatic bronchus is

$$\dot{m}_{\text{R ant diaph}} = \frac{P_{\text{R main}} - P_{\text{R ant diaph}}}{(40 + 0.0146\,\text{Re})} \frac{\pi D_{\text{R ant diaph}}{}^4 \rho}{128 \mu L_{\text{R ant diaph}}} \qquad \textbf{(3.60)}$$

The mass flow rates that enter the lobes are dependent on the conductance of the individual lobes and the difference in pressure between the lobe and the section preceding it. Values for the total conductance of the airways that make up the individual lobes are assumed to be constants. The mass flow rate into a particular lobe may be expressed as

$$\dot{m}_{\text{in}} = (P_{\text{section}} - P_{\text{lobe}}) \times C_{\text{lobe}} \qquad \textbf{(3.61)}$$

Applying this to each lobe gives the following mass flow rates:

The mass flow rate into right apical lobe

$$\dot{m}_{\text{R api lobe}} = (P_{\text{R api}} - P_{\text{R api lobe}}) \times C_{\text{R api lobe}} \qquad \textbf{(3.62)}$$

The mass flow rate into the right cardiac lobe

$$\dot{m}_{\text{R card lobe}} = \left(P_{\text{R card}} - P_{\text{R card lobe}}\right) \times C_{\text{R card lobe}} \quad \textbf{(3.63)}$$

The mass flow rate into the right diaphragmatic lobe from the right major diaphragmatic bronchus

$$\dot{m}_{\text{R maj diaph lobe}} = \left(P_{\text{R maj diaph}} - P_{\text{R diaph lobe}}\right) \times C_{\text{R diaph lobe}} \quad \textbf{(3.64)}$$

The mass flow rate into the right diaphragmatic lobe from the right posterior diaphragmatic bronchus

$$\dot{m}_{\text{R post diaph lobe}} = \left(P_{\text{R post diaph}} - P_{\text{R diaph lobe}}\right) \times C_{\text{R diaph lobe}} \quad \textbf{(3.65)}$$

The mass flow rate into the right diaphragmatic lobe from the right anterior diaphragmatic bronchus

$$\dot{m}_{\text{R ant diaph lobe}} = \left(P_{\text{R ant diaph}} - P_{\text{R diaph lobe}}\right) \times C_{\text{R diaph lobe}} \quad \textbf{(3.66)}$$

The mass flow rate into the left cardiac lobe

$$\dot{m}_{\text{L card lobe}} = \left(P_{\text{L card}} - P_{\text{L card lobe}}\right) \times C_{\text{L card lobe}} \quad \textbf{(3.67)}$$

The mass flow rate into the left diaphragmatic lobe from the left major diaphragmatic bronchus

$$\dot{m}_{\text{L maj diaph lobe}} = \left(P_{\text{L maj diaph}} - P_{\text{L diaph lobe}}\right) \times C_{\text{L diaph lobe}} \quad \textbf{(3.68)}$$

The mass flow rate into the left diaphragmatic lobe from the left posterior diaphragmatic bronchus

$$\dot{m}_{\text{L post diaph lobe}} = \left(P_{\text{L post diaph}} - P_{\text{L diaph lobe}}\right) \times C_{\text{L diaph lobe}} \quad \textbf{(3.69)}$$

$\dot{m}_{\text{R api wall}}$, $\dot{m}_{\text{R card wall}}$, $\dot{m}_{\text{R diaph wall}}$, $\dot{m}_{\text{L card wall}}$ and $\dot{m}_{\text{L diaph wall}}$ are caused by the displacement of the lobe walls and will be defined in the following section.

3.4. Lobe Dynamics

3.4.1. Assumptions and Justifications

The 5-lobe model presented in this section is well suited to describe the uneven distribution of ventilation across the lobes and the inhomogeneities in neonatal lung mechanics. The consideration of the different properties of each lobe increases the number of parameters significantly. So far, the practical value of such a model for simulation studies in premature neonates is limited because a great number of reference values and parameters are unknown. However, in sections 3.5 and 3.6, it will be demonstrated how the various parameters for a premature ovine lung required for the model were collected through experiment and calculations based on reference values from the literature.

A mechanical model which allows direct substitution of most measured parameters is used to describe the mechanics of each lobe. The concept of a moving piston of a mass M_{lobe} forms the basis of the model. It accounts for the motion of the lobe wall and the gas flow effects. A variable spring stiffness (k_{lobe}) describes the elastic properties of the lobe and a constant viscous resistance (f_{lobe}) describes the viscous resistance of the lung tissue. The inertive, elastic and viscous forces caused by these elements act on the piston (lobe) area (A_{lobe}), which is equivalent to the lobe wall. The piston is subject to the pressure in the lobe (P_{lobe}) and the pleural pressure (P_{pleural}). Lobe pressures are assumed to be uniform and the area of the piston remains constant, although in reality there are variations in pressure within the lobe and the surface area of the lobe changes with a change in volume (changing the predicted pressures in the lobe). Such effects can be added to the model in the future by adding more compartments to the individual lobes to account for regional pressure variations and by determining the surface area-lung volume relationship to account for the changing surface area.

3.4.2. Lobe Dynamics Development

A general form of the equation of motion is derived based on the schematic diagram in Figure 3.3. Subsequently, the individual expressions for each lobe are presented.

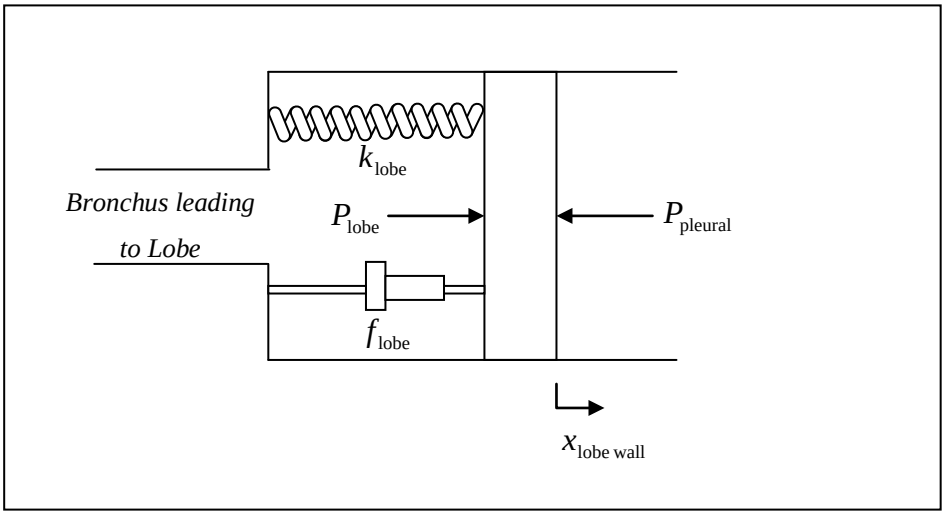

Figure 3.3 General schematic for a lobe spring mass damper system.

Applying Newton's second law, the equation of motion for the lobe wall can be written as:

$$-k_{\text{lobe}}x_{\text{lobe wall}} - f_{\text{lobe}}\frac{dx_{\text{lobe wall}}}{dt} + \left(P_{\text{lobe}} - P_{\text{pleural}}\right)A_{\text{lobe}} = M_{\text{lobe}}\frac{d^2x_{\text{lobe wall}}}{dt^2} \qquad \textbf{(3.70)}$$

where $\frac{d^2x_{\text{lobe wall}}}{dt^2}$, $\frac{dx_{\text{lobe wall}}}{dt}$ and $x_{\text{lobe wall}}$ are the acceleration, velocity and displacement of the lobe wall respectively.

The mass flow rate of air caused by the motion of the lobe wall may be expressed as:

$$\dot{m}_{\text{lobe wall}} = \rho A_{\text{lobe}}\frac{dx_{\text{lobe wall}}}{dt} \qquad \textbf{(3.71)}$$

where ρ is the air density at 312.5K. The lobe volume (V_{lobe}) is regarded as a control volume which is determined from the displacement of the lobe wall ($x_{\text{lobe wall}}$) multiplied by the piston surface area (A_{lobe}), such that

$$V_{\text{lobe}} = A_{\text{lobe}}x_{\text{lobe wall}} \qquad \textbf{(3.72)}$$

Using equations (3.70) to (3.72), the equivalent expressions for each individual lobe are obtained.

For the right apical lobe

$$-k_{\text{R api}}x_{\text{R api wall}} - f_{\text{R api}}\frac{dx_{\text{R api wall}}}{dt} + \left(P_{\text{R api lobe}} - P_{\text{pleural}}\right)A_{\text{R api}} = M_{\text{R api}}\frac{d^2x_{\text{R api wall}}}{dt^2} \quad \textbf{(3.73)}$$

$$\dot{m}_{\text{R api wall}} = \rho A_{\text{R api}}\frac{dx_{\text{R api wall}}}{dt} \quad \textbf{(3.74)}$$

$$V_{\text{R api lobe}} = A_{\text{R api}}x_{\text{R api wall}} \quad \textbf{(3.75)}$$

For the right cardiac lobe

$$-k_{\text{R card}}x_{\text{R card wall}} - f_{\text{R card}}\frac{dx_{\text{R card wall}}}{dt} + \left(P_{\text{R card lobe}} - P_{\text{pleural}}\right)A_{\text{R card}} = M_{\text{R card}}\frac{d^2x_{\text{R card wall}}}{dt^2} \quad \textbf{(3.76)}$$

$$\dot{m}_{\text{R card wall}} = \rho A_{\text{R card}}\frac{dx_{\text{R card wall}}}{dt} \quad \textbf{(3.77)}$$

$$V_{\text{R card lobe}} = A_{\text{R card}}x_{\text{R card wall}} \quad \textbf{(3.78)}$$

For the right diaphragmatic lobe

$$-k_{\text{R diaph}}x_{\text{R diaph wall}} - f_{\text{R diaph}}\frac{dx_{\text{R diaph wall}}}{dt} + \left(P_{\text{R diaph lobe}} - P_{\text{pleural}}\right)A_{\text{R diaph}} = M_{\text{R diaph}}\frac{d^2x_{\text{R diaph wall}}}{dt^2} \quad \textbf{(3.79)}$$

$$\dot{m}_{\text{R diaph wall}} = \rho A_{\text{R diaph}}\frac{dx_{\text{R diaph wall}}}{dt} \quad \textbf{(3.80)}$$

$$V_{\text{R diaph lobe}} = A_{\text{R diaph}} x_{\text{R diaph wall}} \quad \textbf{(3.81)}$$

For the left cardiac lobe

$$-k_{\text{L card}} x_{\text{L card wall}} - f_{\text{L card}} \frac{dx_{\text{L card wall}}}{dt} + \left(P_{\text{L card lobe}} - P_{\text{pleural}}\right) A_{\text{L card}} = M_{\text{L card}} \frac{d^2 x_{\text{L card wall}}}{dt^2} \quad \textbf{(3.82)}$$

$$\dot{m}_{\text{L card wall}} = \rho A_{\text{L card}} \frac{dx_{\text{L card wall}}}{dt} \quad \textbf{(3.83)}$$

$$V_{\text{L card lobe}} = A_{\text{L card}} x_{\text{L card wall}} \quad \textbf{(3.84)}$$

For the left diaphragmatic lobe

$$-k_{\text{L diaph}} x_{\text{L diaph wall}} - f_{\text{L diaph}} \frac{dx_{\text{L diaph wall}}}{dt} + \left(P_{\text{L diaph lobe}} - P_{\text{pleural}}\right) A_{\text{L diaph}} = M_{\text{L diaph}} \frac{d^2 x_{\text{L diaph wall}}}{dt^2} \quad \textbf{(3.85)}$$

$$\dot{m}_{\text{L diaph wall}} = \rho A_{\text{L diaph}} \frac{dx_{\text{L diaph wall}}}{dt} \quad \textbf{(3.86)}$$

$$V_{\text{L diaph lobe}} = A_{\text{L diaph}} x_{\text{L diaph wall}} \quad \textbf{(3.87)}$$

3.4.3. The Pleural Compartment and Chest Wall

The pleural compartment is modelled along similar lines to the lobes as seen in Figure 3.4. However, it has two notable differences, (1) there is no air flow into or out of the compartment and (2) it is a closed compartment that is filled with pleural liquid (instead of air as in the lung).

An equivalent variable stiffness (k_{pleural}) is assumed to represent the elastic properties of the ribcage, diaphragm and pleural fluid and tissue. Also, these properties generate an equivalent viscous resistance (f_{pleural}) which is assumed to act on the pleural wall of an

equivalent surface area $A_{pleural}$. The combined movement of the lobe walls ($x_{\text{lobe wall total}}$) is the sum of $x_{R\,\text{api wall}}$, $x_{R\,\text{card wall}}$, $x_{R\,\text{diaph wall}}$, $x_{L\,\text{card wall}}$ and $x_{L\,\text{diaph wall}}$. The pleural compartment experiences forces generated by the pleural pressure (P_{pleural}), atmospheric pressure (P_{atm}) and the thoracic force (F_{th}). These forces act to change the volume of the compartment. F_{th} is the force generated by the ribcage and diaphragm muscles due to the neurogenic signals sent by the brain to drive lung motion to create the tidal volume. It is the main driving force of the model and idealised as acting on a single point of the pleural surface. It is commonly defined as a signal with a profile that follows the shape (but not the magnitude) of the tidal volume [78].

In reality, it is far more complex with the force adapting itself to respond to the changing levels of oxygen and carbon dioxide in the blood stream. The physiological aspects of gas exchange can be introduced into the model through additional subsystems that account for gas diffusion at the alveolar level, the partial pressures of oxygen in the bloodstream and the resulting neural control of breathing. These elements, however, are out of the scope of this research which concentrates purely on the mechanical aspects of respiration.

In normal adult respiration, regional variations in pleural pressure exist due to the downward-acting weight forces of the lung. However, since neonatal subjects receiving respiratory support are never upright, the regional differences in pleural pressure are much less significant and so can be ignored for the purposes of this model.

Using Newton's second law, the equation of motion of the pleural wall is:

$$F_{\text{th}} - k_{\text{pleural}} x_{\text{pleural}} - f_{\text{pleural}} \frac{dx_{\text{pleural}}}{dt} + \left(P_{\text{pleural}} - P_{\text{atm}}\right) A_{\text{pleural}} = M_{\text{pleural}} \frac{d^2 x_{\text{pleural}}}{dt^2} \qquad \textbf{(3.88)}$$

where M_{pleural} is the mass of the moving part of the chest wall and $\frac{d^2 x_{\text{pleural}}}{dt^2}$, $\frac{dx_{\text{pleural}}}{dt}$ and x_{pleural} are the acceleration, velocity and displacement of the pleural wall respectively.

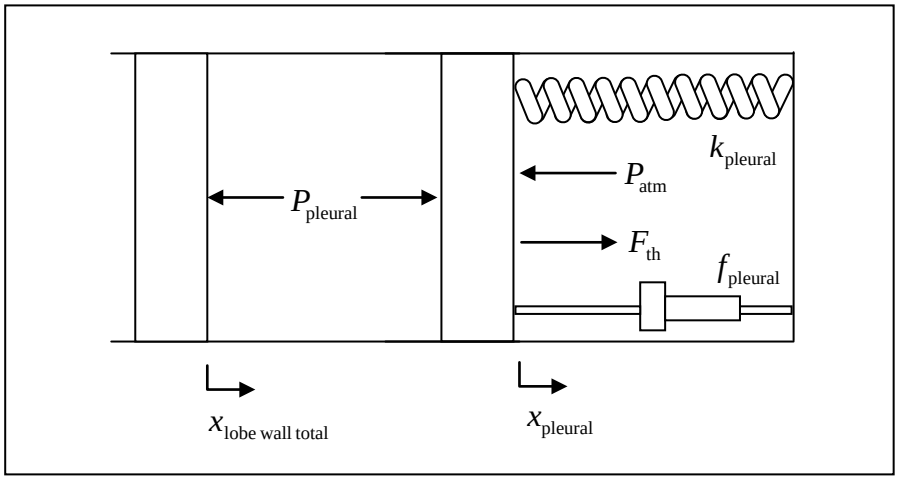

Figure 3.4 Schematic of pleural compartment and chest wall.

Since the fluid inside the pleural compartment is liquid, the rate of change of the pleural pressure depends on the expansion and compression of the pleural fluid and may be derived by using the effective bulk modulus (B_{pleural}). By definition:

$$B_{\text{pleural}} = \frac{\dfrac{dP_{\text{pleural}}}{dt}}{\left(\dfrac{dV_{\text{pleural}}}{dt}\right) \Big/ V_{\text{pleural}}} \qquad \textbf{(3.89)}$$

Rearranging, gives:

$$\frac{dP_{\text{pleural}}}{dt} = \frac{B_{\text{pleural}}}{V_{\text{pleural}}}\left(\frac{dV_{\text{pleural}}}{dt}\right) \qquad \textbf{(3.90)}$$

The change in the pleural compartment volume $\left(\dfrac{dV_{\text{pleural}}}{dt}\right)$ is determined by the displacement of the pleural and lobe walls and so equation (3.90) is expanded to give:

$$\frac{dP_{\text{pleural}}}{dt} = \frac{B_{\text{pleural}}}{V_{\text{pleural}}} \left[\begin{array}{l} A_{\text{pleural}} \frac{dx_{\text{pleural}}}{dt} - A_{\text{R api}} \frac{dx_{\text{R api wall}}}{dt} - A_{\text{R card}} \frac{dx_{\text{R card wall}}}{dt} - \\ A_{\text{R diaph}} \frac{dx_{\text{R diaph wall}}}{dt} - A_{\text{L card}} \frac{dx_{\text{L card wall}}}{dt} - A_{\text{L diaph}} \frac{dx_{\text{L diaph wall}}}{dt} \end{array} \right] \quad \textit{(3.91)}$$

3.5. Empirically Measured Model Parameters

This section describes the procedures used and results obtained to determine lengths and diameters of the airways specified in Table 3.1, the masses of the individual lobes and the chest wall and the pressure-volume (P-V) curves of the whole lung, left lung and right lung. The above parameters were determined for both 128 day and 142 day gestation lambs. Lambs were delivered via caesarean section at 128 day and 142 day gestation and immediately received a lethal dose (100 mg/kg) of pentobarbitone (Virbac, NSW, Australia). They were then weighed and randomly assigned to either be used to make lung casts or conduct P-V curves on. The constant phase model [89] uses in-vivo impedance data to characterise respiratory parameters such as resistance, inertance, tissue damping and tissue elastance. However, values calculated in this fashion are either difficult to convert into their proper SI units to fit the current model or expressions of overall lung properties.

3.5.1. Lung Casts

The following method of producing lung casts was devised for the purposes of this research. Table 3.3 lists a summary of the animals in each gestation that were used to make the lung casts. Following delivery and euthanasia, subjects were placed in the supine position. A 5 cm slit from the base of the larynx was made through the fur, skin and surrounding tissue to expose the trachea. Just below the larynx, an axial cut was made half way through the trachea and a piece of a 4.5 mm internal diameter endotracheal tube was inserted. Two ties were used to fasten the tube to avoid slippage. A syringe was placed at the entrance of the tube and used to suck out any excess fetal lung fluid. 453g of silicone rubber (Dow Corning 3110 RTV mixed with 45 g of S type catalyst) was chosen as the injection material due to its flexibility and fast curing time. Silicone was then injected into the trachea (at 20ml/kg birthweight) using a 60 ml syringe. A moderate to heavy pressure was necessary to allow infusion over 10 minutes. Once the silicone was injected, a haemostat was used to clamp the endotracheal tube at

the entrance. The subject was then placed in the prone position and left for 12 hours for the silicone to cure.

Table 3.3 Description of lambs used in lung casts.

	128 day	***142 day***
Number of subjects	8	4
Male/Female	4/4	3/1
Body weight , kg (±SD)	2.825 (0.34)	5.075 (0.44)

After 12 hours, the lung was removed from the chest cavity and a string was tied around the trachea and suspended from a support into a bucket of 10M solution of potassium hydroxide (KOH). The lung was immersed in the solution for 24 hours. After 24 hours, the lung was removed from the solution and any macerated tissue that was clinging to the cast was rinsed off under cold running water. If required, the cast was then placed in a fresh solution of KOH for another 12-24 hours and rinsed again thereafter to reveal the complete cast.

Figure 3.5 shows the lung cast before and after maceration by KOH. It can be seen that the silicone reaches the level of the terminal bronchioles and alveoli to create a complete cast. The cast was then hung and air dried. Lengths and diameters of the airways identified in Table 3.1 were measured on all casts with vernier calipers. Table 3.4 lists the average length per unit birthweight measured for all 128 day and 142 day gestation lambs. Table 3.5 lists the average diameter per unit birthweight measured for all 128 day and 142 day gestation lambs.

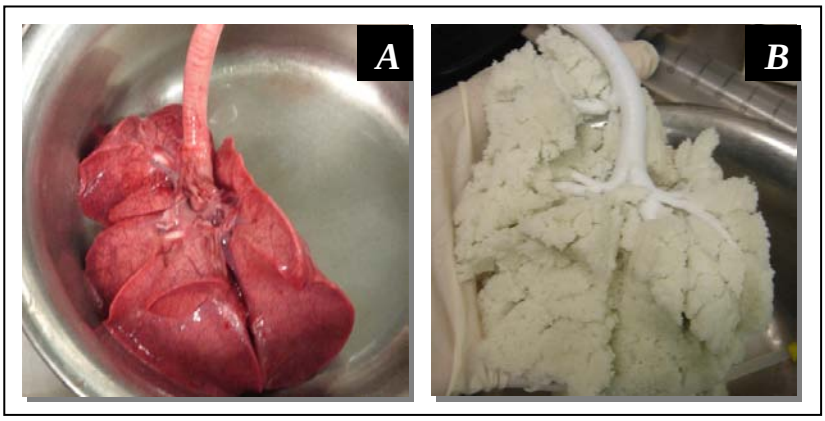

Figure 3.5 Lung casts before (a) and after (b) maceration by KOH.

Table 3.4 Average airway lengths per unit birthweight for 128 day and 142 day gestation lambs.

Airway Number and Description	Length/birthweight, mm/kg (±SD)	
	128 Day	142 Day
1 - Upper trachea	37.11 (2.72)	21.19 (3.11)
2 - Lower trachea	8.85 (1.10)	6.06 (0.49)
3 - Right apical bronchus	2.48 (0.38)	1.71 (0.45)
4 - Right main bronchus	3.59 (0.40)	2.50 (0.12)
5 - Left main bronchus	1.74 (0.30)	1.04 (0.24)
6 - Right cardiac bronchus	2.08 (0.36)	1.39 (0.34)
7 - Left cardiac bronchus	1.99 (0.27)	1.06 (0.11)
8 - Right major diaphragmatic bronchus	2.83 (0.47)	1.56 (0.31)
9 - Left major diaphragmatic bronchus	2.25 (0.31)	1.32 (0.12)
10 - Right posterior diaphragmatic bronchus	1.56 (0.32)	1.21 (0.03)
11 - Left posterior diaphragmatic bronchus	2.88 (0.40)	1.64 (0.16)
12 - Right anterior diaphragmatic bronchus	1.75 (0.23)	1.68 (0.63)

Table 3.5 Average airway diameters per unit birthweight for 128 day and 142 day gestation lambs.

Airway Number and Description	Diameter/birthweight, mm/kg (±SD)	
	128 Day	142 Day
1 - Upper trachea	2.64 (0.20)	1.73 (0.18)
2 - Lower trachea	2.48 (0.24)	1.62 (0.22)
3 - Right apical bronchus	2.35 (0.27)	1.44 (0.21)
4 - Right main bronchus	2.29 (0.27)	1.48 (0.26)
5 - Left main bronchus	2.21 (0.29)	1.38 (0.19)
6 - Right cardiac bronchus	2.16 (0.31)	1.24 (0.28)
7 - Left cardiac bronchus	1.36 (0.16)	0.93 (0.06)
8 - Right major diaphragmatic bronchus	1.03 (0.13)	0.69 (0.18)
9 - Left major diaphragmatic bronchus	1.08 (0.21)	0.73 (0.14)
10 - Right posterior diaphragmatic bronchus	0.84 (0.18)	0.59 (0.07)
11 - Left posterior diaphragmatic bronchus	0.84 (0.11)	0.57(0.09)
12 - Right anterior diaphragmatic bronchus	0.89 (0.11)	0.63(0.09)

3.5.2. Pressure-Volume Curves

Table 3.6 lists a summary of the animals in each gestation that were used in the P-V curves. Repeated P-V curves for each cycle of inflation and deflation due to gas trapping in the lung. Therefore, each measurement was done only once on each lung and

the same lung could not be used for both whole-lung and half-lung P-V curves. For each gestation, the same group of animals was used to determine the P-V curves for both the right and left lung.

Following delivery and euthanasia, subjects were placed in the supine position. The ribcage was opened and separated from the diaphragm to reveal the chest cavity (Figure 3.6), taking care not to puncture the lung. The incision was extended from the top of the chest to the base of the larynx through the fur, skin and surrounding tissue to expose the trachea. Just below the larynx, an axial cut was made half way through the trachea and a 4.5mm internal diameter endotracheal tube was inserted into the upper trachea. Two ties were used to fasten the tube to the trachea to ensure no slippage of the tube or leakage of air.

A syringe attached to a manometer (shown in Figure 3.7) was attached to the endotracheal tube. The lung was first inflated and then deflated at set pressures from 0 – 40 cm H_2O in increments of 5 cm H_2O. The volume was read from the marking of the graduated syringe at each increment. The dead space of the syringe was also measured at the prescribed increments of pressure and subtracted from the inflation and deflation volumes measured. A 250 ml syringe was used for whole-lung measurements, while a 60 ml syringe was used for half-lung measurements.

For the half-lung measurements, haemostats were used to clamp the respective bronchi to allow inflation of the selected areas. The left main bronchus was clamped with a haemostat to inflate/deflate the right lung. After testing the right lung, the haemostat was then removed and used to clamp the right apical bronchus and the right main bronchus to allow the left lung to be inflated/deflated.

Table 3.6 Description of the animals used in pressure-volume curves.

	128 Day		*142 Day*	
	Whole Lung	*Right & Left Lungs*	*Whole Lung*	*Right & Left Lungs*
Number	5	3	4	3
Body weight , kg (±SD)	3.05 (0.48)	3.2 (0.46)	4.99 (0.69)	5.07 (0.16)

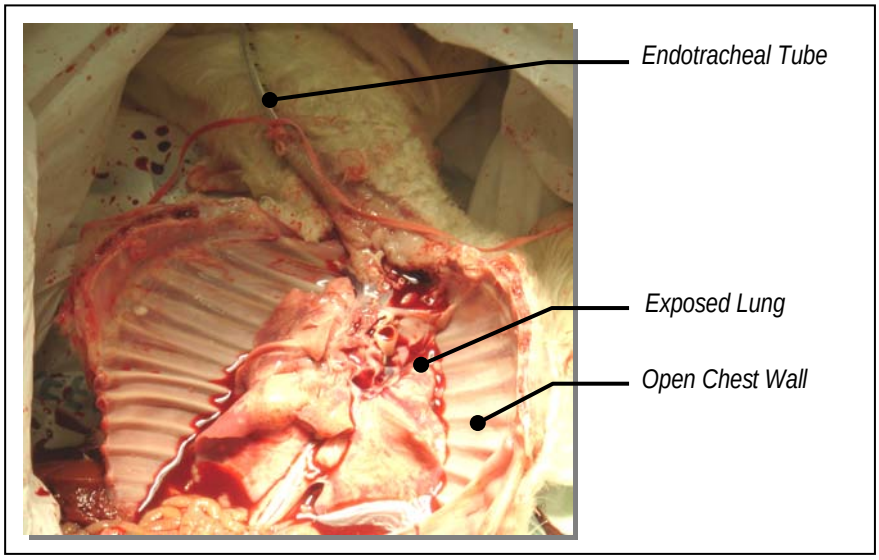

Figure 3.6 Subject in supine position with open chest exposing lung.

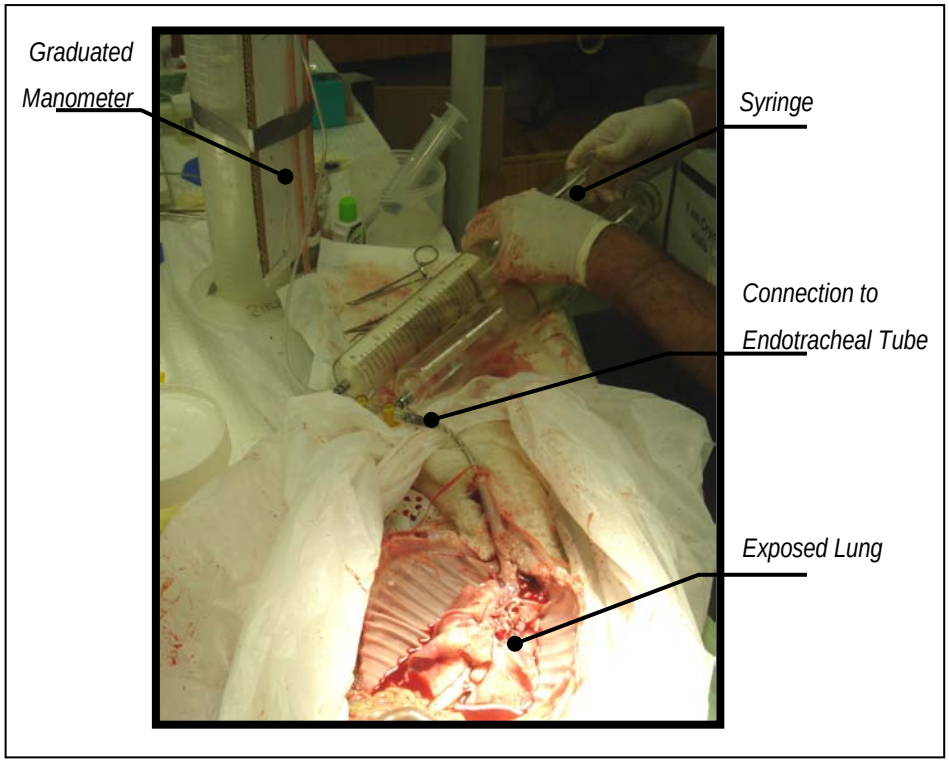

Figure 3.7 Measuring P-V curves with syringe and manometer setup.

Table 3.7 shows the average volume per birthweight measured at each pressure increment of all lungs tested at both 128 day and 142 day gestations. The resulting P-V curves are plotted in Figure 3.8 and Figure 3.9 for 128 day and 142 day gestations respectively.

Table 3.7 Pressure-volume data for 128 day and 142 day gestation lungs.

Pressure (cm Water)	Average Volume/Birthweight , ml/kg (±SD)					
	128 Day			142 Day		
	Whole Lung	Right Lung	Left Lung	Whole Lung	Right Lung	Left Lung
0	0.00	0.00	0.00	0.00	0.00	0.00
5	0.55(0.47)	0.66(0.51)	0.48(0.26)	2.17(1.44)	2.71(2.32)	2.42(1.33)
10	1.35(1.15)	1.53(1.06)	0.73(0.78)	5.24(3.18)	6.46(4.22)	4.59(2.97)
15	2.32(1.47)	2.92(1.06)	1.11(0.88)	11.24(6.32)	11.01(7.12)	7.35(4.18)
20	3.77(2.33)	4.47(1.71)	1.60(1.13)	17.33(5.98)	14.90(9.16)	10.56(5.21)
30	5.84(3.41)	5.98(1.89)	2.90(1.32)	22.66(6.65)	18.66(10.70)	13.34(5.56)
40	8.59(4.39)	7.36(2.29)	5.10(1.79)	28.48(8.55)	23.07(10.32)	16.13(7.27)
30	8.53(4.30)	7.30(2.13)	4.83(1.21)	27.50(8.34)	22.28(10.30)	15.46(6.47)
20	7.08(3.94)	6.39(2.51)	2.86(1.17)	23.82(6.76)	18.85(9.27)	13.88(5.96)
15	6.37(3.39)	5.90(2.58)	2.29(1.03)	22.02(6.47)	16.97(9.22)	12.84(5.51)
10	5.12(2.50)	5.52(2.68)	2.15(0.95)	20.72(5.85)	16.27(8.90)	12.01(5.26)
5	3.38(1.90)	4.47(2.45)	1.77(0.79)	19.18(5.60)	13.86(7.39)	11.18(5.37)
0	0.37(0.74)	2.13(1.87)	0.79(0.51)	9.98(2.03)	8.96(3.79)	8.29(6.00)

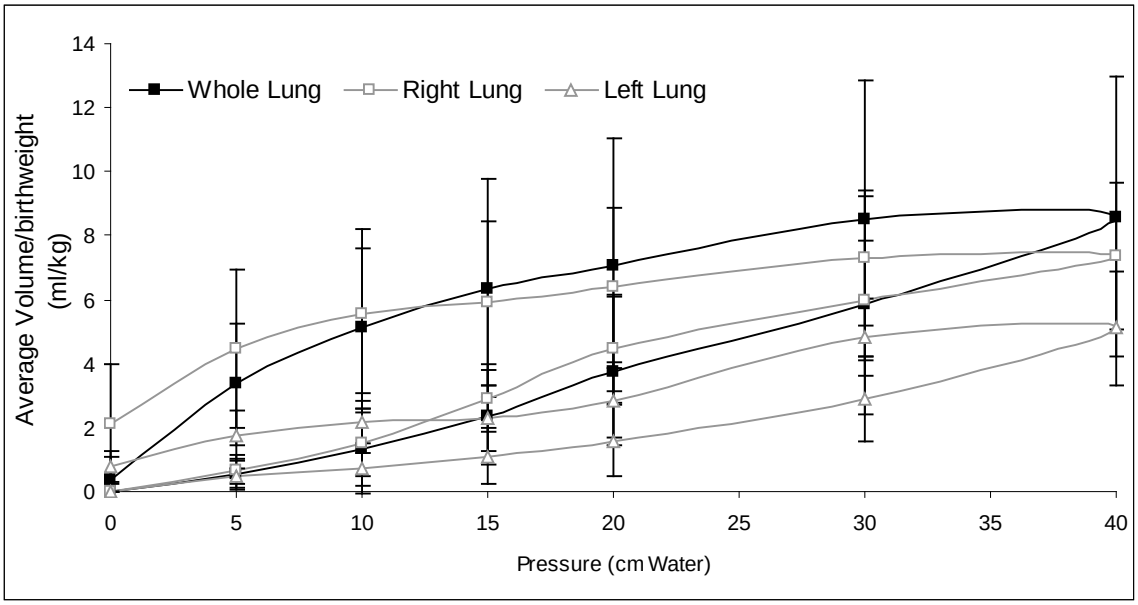

Figure 3.8 Average P-V curves for 128 day gestation whole, right and left lungs.

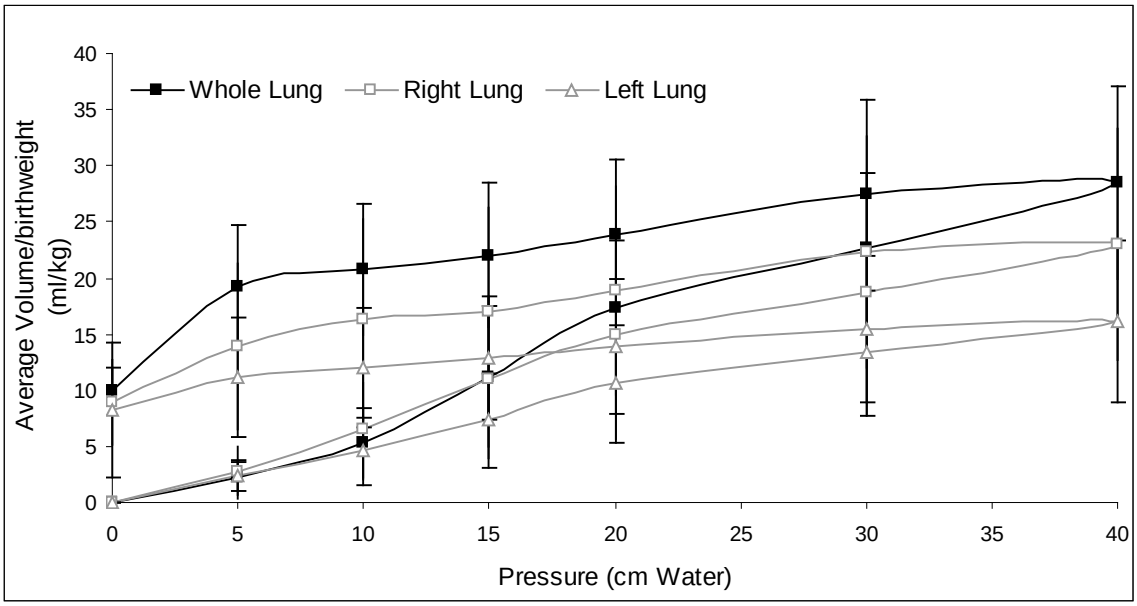

Figure 3.9 Average P-V curves for 142 day gestation whole, right and left lungs.

The P-V curves were measured for the left and right lung since it was not possible to divide the lung further to test P-V curves on individual lobes which would have been the ideal measurements to make in order to get the parameters for the model. Nevertheless, the right and left lung P-V curves were measured to gain some basic insights into how the P-V curve of the whole lung relates to the P-V curve of individual lobes. Possible stress relaxation of the tissue, the large standard deviations in data and leaks through the manometer equipment connections and perforations on the surface of the lung meant that the average volumes in the right and left lung do not exactly add up to the average volumes in the whole lung.

To the best of our knowledge, there is no available literature that determines the relationship between the whole-lung P-V curves and individual lobe P-V curves for newborn lambs. Mortola et al. [90] have published data for kittens where individual lobe and whole lung P-V curves are expressed as a percentage of the maximum volume. They noticed no systematic difference in the static behaviour of the individual lobes in comparison to the whole lung. The same shape was retained and the maximum volume was always approximately 3-3.5 times the volume at FRC for kittens.

To determine whether similar relations are applied to the lamb lung, Figure 3.10 and Figure 3.11 show the P-V curves plotted as a percentage of the maximum volume of each type of lung for 128 day and 142 day gestations respectively. The P-V curves of the 142 day lung (Figure 3.11) show behaviour congruent to that described by Mortola et al. [90] and so it can be assumed that the P-V curves of the individual lobes will follow the same shape and static behaviour of the whole-lung when expressed as a percentage of the maximum volume. Thus, knowing the maximum volume of each lobe, one is able to calculate the P-V curve of the individual lobe based on the shape of the whole-lung P-V curve. These calculations are performed in Section 3.6.

It is noted that the half-lung P-V curves of the 128 day lung (Figure 3.10) does not follow such a close relation to the whole-lung P-V curves as those for the 142 day lung (Figure 3.11) because there is a lot of variability in the data measured. The large standard deviations in the 128 day lungs may indicate the large biological variability in premature lambs, or that there is no relationship to be drawn at all between the P-V curves of half-lungs and whole-lungs.

Due to the exploratory nature of the initial investigations in this study and the fact that the half-lung measurements in the 128 day lung still lie within the standard deviation of the whole lung measurements, the relationship can be assumed to be that of the simplest case where the shape and static behaviour of the half-lung P-V curves in the 128 day lung also follow the same trends as the P-V curves of the whole-lung.

In diseased states in reality, this relationship will not hold due to the heterogeneity of the diseased lung. However, once characterized, these relationships can be added to the present model to extend its capabilities in describing ventilation during diseased states.

This data is used in the following section to estimate the stiffness-volume relationship for each lobe based on assumption derived from the literature.

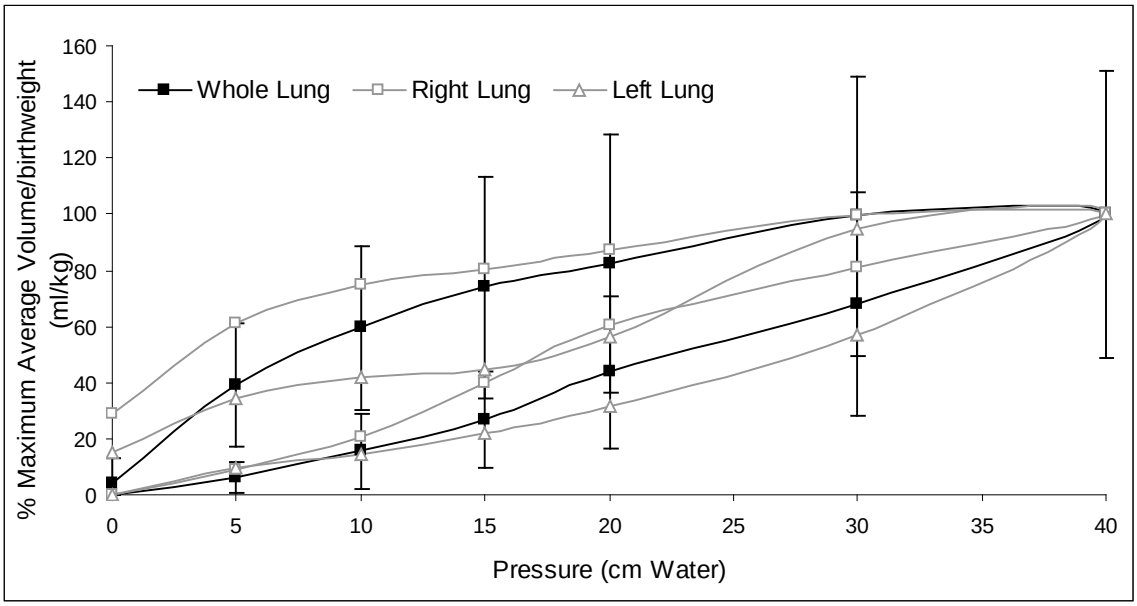

Figure 3.10 Average P-V curves as a percentage of maximum volume for 128 day gestation whole, right and left lungs.

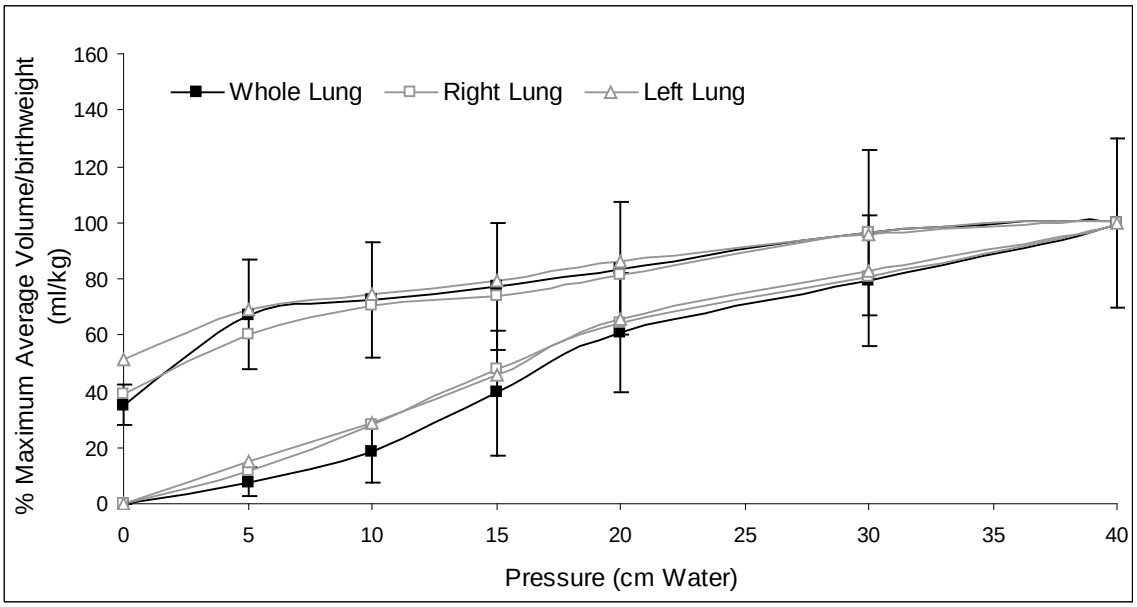

Figure 3.11 Average P-V curves as a percentage of maximum volume for 142 day gestation whole, right and left lungs.

3.5.3. Lung and Lobe Masses

After conducting the P-V curves, lungs were separated into the different lobes and weighed. The chest wall (i.e. the ribcage with the intercostal muscles) was also weighed. Table 3.8 describes the animals used in measuring the masses. Table 3.9 contains the average masses per birthweight for the chest wall, total lung, left lung, right lung and all the individual lobes for both 128 day and 142 day gestation lambs. The mass distribution of the lobes, right and left lung and the chest wall as a percentage of the total lung mass is also calculated. These percentages will be useful in the allocation of surface areas, resistances and lung volumes in the following section.

Table 3.8 Description of animals used to measure lung, lobe and chest wall masses.

	128 Day	*142 Day*
Number of subjects	8	7
Body weight , kg (±SD)	3.11 (0.45)	5.02 (0.50)

Table 3.9 Masses of lungs, lobes and chest wall of 128 day and 142 day gestation lambs.

	128 Day		142 Day	
	Average Mass/Birthweight, g/kg (±SD)	*% of Average Total Mass,* (±SD)	*Average Mass/Birthweight, g/kg* (±SD)	*% of Average Total Mass,* (±SD)
Chest Wall	74.83(6.82)	256.07(23.91)	69.25(7.10)	205.04(23.57)
Total Lung Mass	29.30(2.37)	100.00(0.00)	33.94(3.37)	100.00(0.00)
Left Lung Mass	12.45(1.14)	42.50(1.82)	14.45(1.38)	42.66(2.70)
Right Lung Mass	16.85(1.43)	57.50(1.82)	19.49(2.47)	57.34(2.70)
Right Apical Lobe	4.02(0.84)	13.65(2.44)	4.38(0.97)	12.82(2.00)
Right Cardiac Lobe	2.64(0.42)	9.06(1.67)	2.62(0.69)	7.66(1.54)
Right Diaphragmatic Lobe	10.19(0.84)	34.79(1.63)	12.49(1.12)	36.86(1.72)
Left Cardiac Lobe	3.95(0.48)	13.44(0.94)	4.32(0.56)	12.77(1.50)
Left Diaphragmatic Lobe	8.51(0.72)	29.06(1.53)	10.13(0.98)	29.89(1.83)

3.6. Literature Derived Model Parameters

Some of the model parameters were derived from values found in the literature. This section details the calculations and estimations performed to generate parameters suitable for the present model.

3.6.1. Volumes and Surface Areas

Ashrafi et al. [91] measured both the weight and volume of the left and right lung in newborn lambs. Also, Ting et al. [92] measured the surface area distribution across the right and left lung in newborn lambs by electron microscopy. These data are summarised in Table 3.10.

They suggest that the volume and surface area divide themselves across the left and right lung in similar proportions to the mass of the lung. It can therefore be reasoned that the surface areas and lobe volumes for the lungs measured in Section 3.5.3 can be calculated by assuming that the percentage distribution of surface area and lobe volume across the lobes is the same as the percentage distributions of masses identified in Table 3.9.

The total surface area per unit birthweight for 140 day gestation lambs is given as 3.39 m^2/kg by Lipsett et al. [93] and 4.85 m^2/kg by Ting et al. for new born lambs [92]. An average value of 4.12 m^2/kg is taken as the value for a 142 day gestation lamb (near term). The surface area per unit birthweight is less for the smaller 128 day lung, with less alveoli to contribute to surface area. It is felt that the best way to estimate the surface area for the 128 day gestation lung is by multiplying the value at 142 day gestation by the ratio of the 128 day birthweight to the 142day birthweight (i.e. 0.56), since birthweight is commonly used to scale physiological data. The surface area/unit birthweight for a 128 day gestation lamb is thus calculated as 2.31 m^2/kg. Average birthweight values are calculated from all animals used in empirical measurements (i.e. values from Tables 3.8 and 3.6) The resulting surface areas for each lobe, as determined by the allocated percentage area distribution, is shown in Table 3.11 for both 128 day and 142 day gestation lungs.

The maximum volume achieved in the whole lung in the pressure-volume data in Table 3.7 is 28.5 ml for a 142 day lung and 8.59 ml for a 128 day lung. The maximum volume achieved in each lobe is then calculated and given in Table 3.12 by using the allocated percentage distribution of volume. These values will be used to calculate the individual pressure-volume and elastance-volume relationships as follows.

Table 3.10 Weight, volume and surface area distribution in newborn lambs.

	Right Lung	*Left Lung*	*Literature Reference*
Weight (%total lung weight)	59.5	40.5	Ashrafi et al. [91]
Volume (%total lung volume)	58	42	Ashrafi et al. [91]
Surface Area (%total lung surface area)	65	35	Ting et al. [92]

Table 3.11 Surface areas per unit birthweight for individual lobes for 128 day and 142 gestation lungs.

	128 Day		142 Day	
	Surface Area/Birthweight, m^2/kg	*% of Total Surface Area*	*Surface Area/Birthweight, m^2/kg*	*% of Total Surface Area*
Right Apical Lobe	0.32	13.65	0.53	12.82
Right Cardiac Lobe	0.21	9.06	0.32	7.66
Right Diaphragmatic Lobe	0.80	34.79	1.52	36.86
Left Cardiac Lobe	0.31	13.44	0.53	12.77
Left Diaphragmatic Lobe	0.67	29.06	1.23	29.89

Table 3.12 Maximum lobe volume per unit birthweight for individual 128 day and 142 gestation lobes.

	128 Day		142 Day	
	Volume/Birthweight, ml/kg	*% of Maximum Whole Lung Volume*	*Volume/Birthweight, ml/kg*	*% of Maximum Whole Lung Volume*
Right Apical Lobe	1.17	13.65	3.65	12.82
Right Cardiac Lobe	0.78	9.06	2.18	7.66
Right Diaphragmatic Lobe	2.99	34.79	10.51	36.86
Left Cardiac Lobe	1.15	13.44	3.64	12.77
Left Diaphragmatic Lobe	2.50	29.06	8.52	29.89

3.6.2. Pressure-Volume and Elastance-Volume Curves

To formulate the P-V curves for individual lobes, the value at 100% of maximum volume in whole-lung P-V curves in Figure 3.10 and Figure 3.11 is set to the maximum volume of each lobe calculated in Table 3.12, such that the P-V data for each lobe is as described in Table 3.13.

Table 3.13 Scaled pressure-volume data for each lobe in 128 day and 142 day gestation lungs.

Pressure (cm H_2O)	Scaled Volume/Birthweight , ml/kg									
	128 Day					142 Day				
	Right Apical	Right Cardiac	Right Diaph	Left Cardiac	Left Diaph	Right Apical	Right Cardiac	Right Diaph	Left Cardiac	Left Diaph
0	0.00	0.00	0.00	0.00	0.00	0.00	0.00	0.00	0.00	0.00
5	0.08	0.05	0.19	0.07	0.16	0.28	0.17	0.80	0.28	0.65
10	0.18	0.12	0.47	0.18	0.39	0.67	0.40	1.93	0.67	1.57
15	0.32	0.21	0.81	0.31	0.68	1.44	0.86	4.15	1.44	3.36
20	0.51	0.34	1.31	0.51	1.10	2.22	1.33	6.39	2.21	5.18
30	0.80	0.53	2.03	0.78	1.70	2.91	1.74	8.36	2.89	6.78
40	1.17	0.78	2.99	1.15	2.50	3.65	2.18	10.51	3.64	8.52
30	1.16	0.77	2.97	1.15	2.48	3.53	2.11	10.14	3.51	8.22
20	0.97	0.64	2.46	0.95	2.06	3.05	1.83	8.79	3.04	7.12
15	0.87	0.58	2.21	0.86	1.85	2.82	1.69	8.12	2.81	6.59
10	0.70	0.46	1.78	0.69	1.49	2.66	1.59	7.64	2.65	6.20
5	0.46	0.31	1.17	0.45	0.98	2.46	1.47	7.08	2.45	5.74
0	0.05	0.03	0.13	0.05	0.11	1.28	0.76	3.68	1.27	2.98

Venegas et al. [94] demonstrated a sigmoidal relation that fits with excellent precision the inflation and deflation P-V curves of lungs as shown by equation (3.92).

$$V = a + \left[\frac{b}{1 + e^{-(P-c)/d}} \right] \qquad \textbf{(3.92)}$$

where V is the volume, P is the pressure and a,b,c and d are fitting parameters. In addition to characterizing the P-V curve, equation (3.92) can also accurately estimate respiratory parameters such as the elastance which can be expressed as

$$\text{Elastance} = \frac{\partial P}{\partial V} = \frac{d}{b}\frac{\left[1+e^{-(P-c)/d}\right]^2}{e^{-(P-c)/d}} \qquad \textbf{(3.93)}$$

The P-V data in Table 3.13 was fitted using equation (3.92) in Microsoft Excel by using the least squares method where the sum of the squared residuals was minimized yielding estimates of the fitting parameters *a*,*b*,*c* and *d* and the best-fit coefficient R^2. Table 3.14 shows the fitting parameters and best fit coefficient for the deflation data of each lobe for both 128 day and 142 day gestation lungs. The deflation data is used since it is closer to P-V curves in reality (since the inflation curve starts from a completely collapsed lung which has never been ventilated before).

Using the values in Table 3.14 and equations (3.92) and (3.93), the volume and elastance values at each distending pressure (from 0-40 cm H_2O in increments of 0.1 cm H_2O) are determined and implemented in the model as Look-Up Tables within the Simulink model.

Table 3.14 Fitting parameters and best-fit coefficient for individual lobe deflation curves for 128 day and 142 day gestation lungs.

	128 Day					142 Day				
	Right Apical	Right Cardiac	Right Diaph	Left Cardiac	Left Diaph	Right Apical	Right Cardiac	Right Diaph	Left Cardiac	Left Diaph
a	-288.30	-288.56	-287.90	-288.62	-288.17	-287.27	-287.85	-284.49	-287.36	-285.48
b	289.54	289.38	291.05	289.84	290.81	290.94	290.09	295.04	291.11	294.04
c	-69.69	-74.96	-57.62	-70.03	-59.95	-61.04	-74.73	-47.30	-69.71	-50.02
d	12.67	12.68	12.63	12.69	12.64	12.58	13.97	12.45	14.41	12.48
R^2	0.997	0.997	0.997	0.997	0.997	0.954	0.953	0.954	0.953	0.954

3.6.3. Lobe Resistances

The values of the collective airway resistance in each lobe (defined here as the equivalent resistance of all airways from Weibel generation 3-23 in each lobe) for 128 day and 142 day gestation lambs are not available in the literature and so are estimated in the following manner. Values of total airway resistance (equivalent resistance of all Weibel generations from 0-23) for a 125 (~128) day and 146 (~142) day gestation lamb is given by Pillow et al. [95] as 3.45 and 2.6 (cm H_2O/(L/s))/kg respectively. The

collective airway resistance can be estimated by using the relations developed by Kobayashi et al. [96] which determined the percentage distribution of airway resistance across each Weibel generation in humans (Figure 3.12). Although the symmetric Weibel model is not used in the present study, the Kobayashi relationship is the only study found in the literature to develop such a relationship that can be used for the present purposes.

From Figure 3.12 it can be seen that the collective resistance of the trachea, primary and secondary bronchi is 39.18% of the total airway resistance and the collective resistance of the lobes (i.e. generations 3-23) constitute 60.82% of the total airway resistance. However, the ovine lung has a different structure to the human lung. The secondary bronchus leading to the right upper lobe in the human lung lies in the same generation as the rest of the secondary bronchi. In the sheep lung, instead of running off the right primary bronchus, the secondary bronchi that leads to the right apical lobe runs off the middle of the trachea. Although this structure is different, it may be assumed that the collective resistance of the sheep trachea, primary bronchi, secondary bronchi and bronchus leading to the right apical lobe is still 39.18% of the total airway resistance.

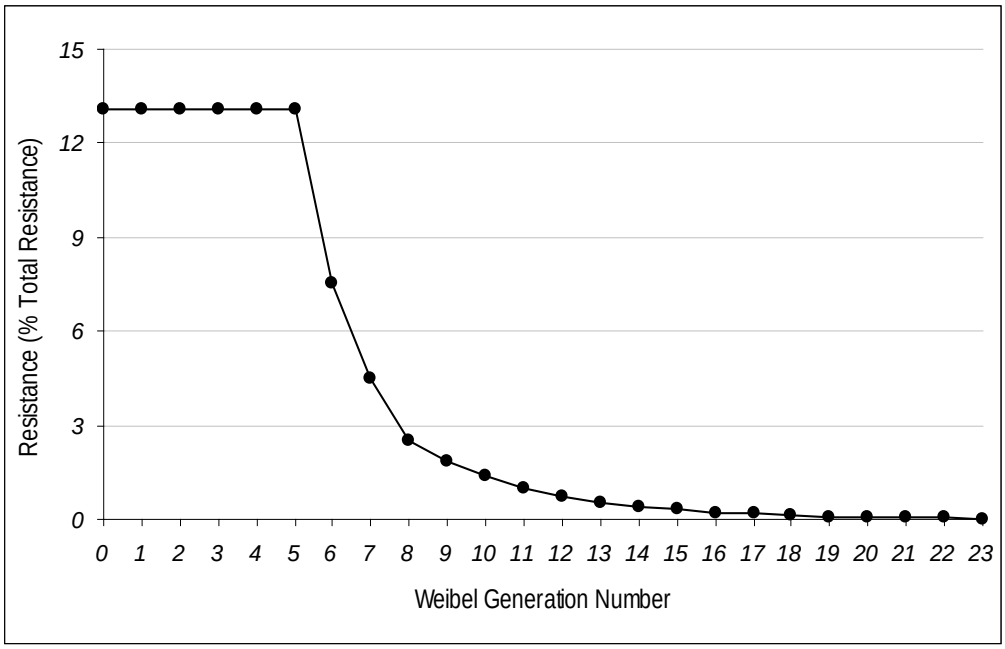

Figure 3.12 Distribution of airway resistance across each Weibel generation in humans.

Assuming the same percentage distribution of resistance to apply for the neonatal lamb branching structure, the collective resistance of the lobes ($R_{\text{lobes total}}$) is calculated to be 2.10 (cm H_2O/(L/s))/kg for the 128 Day lamb and 1.58 H_2O/(L/s))/kg for the 142 Day lamb.

The next step is to separate the collective resistance of all the lobes into resistances for each individual lobe. The lobe resistances can be considered to be connected in parallel since flow divides at each branching point of the airway network. A larger lobe will have less airway resistance and a smaller lobe will have more airway resistance since the flow going through the smaller lobe is less.

There is no measured data in the literature on how the resistance splits between the lobes. Asgharian and Price [97], determined that flow in the human lung divides itself in such a manner that 60% goes to the right lung and 40% goes to the left lung. This is similar to the percentage distributions of weight, lobar volume and surface area.

The resistance is inversely proportional to flow so it can be extrapolated that the percentage distribution of the resistance of each lobe will be inversely proportional to the previously defined percentage distributions of flow, weight, lobar volume and surface area across each lobe. A more convenient expression is that of the conductance of each lobe (C_{lobe}) as calculated by

$$C_{\text{lobe}} = \frac{1}{R_{\text{lobe}}} = \frac{1}{R_{\text{lobes total}}} \times \frac{\text{Lobe Volume}}{\text{Total Lobe Volume}} \qquad \textbf{\textit{(3.94)}}$$

The conductance per unit birthweight of individual lobes in both 128 day and 142 day gestation lungs are determined using equation (3.94) and listed in Table 3.15.

Table 3.15 Conductance of individual lobes in both 128 day and 142 day gestation lungs.

	128 Day		142 Day	
	Conductance ((kg/s)/Pa)/kg	*% of Total Lung Mass*	*Conductance ((kg/s)/Pa)/kg*	*% of Total Lung Mass*
Right Apical Lobe	8.77E-09	13.65	4.00E-09	12.82
Right Cardiac Lobe	5.82E-09	9.06	2.39E-09	7.66
Right Diaphragmatic Lobe	2.24E-08	34.79	1.15E-08	36.86
Left Cardiac Lobe	8.64E-09	13.44	3.98E-09	12.77
Left Diaphragmatic Lobe	1.87E-08	29.06	9.32E-09	29.89

3.6.4. Pleural Volume

Noppen et al. [98] measured the pleural fluid in adult lungs to be 0.26 ±0.1 ml/kg and suggest that this was not age dependant and can be extrapolated to infants. Light and Hamm [99] suggest that pleural fluid formation can be extrapolated from humans to sheep. Hence, the value from Noppen et al. [98] of 0.26 ml/kg for both 128 day and 142 Day lambs is used.

3.6.5. Damping coefficients

The damping coefficient (c_{damp}) is chosen as a single value, calculated at the FRC volume. For each lobe, the elastance at the chosen distending pressure is calculated using equation (3.93) and then multiplied by the square of the lobe surface area to determine the equivalent stiffness (k_{lobe}). Equation (3.95) is used to calculate the damping coefficient (c_{damp}) for each lobe [100].

$$\xi = \frac{c_{damp}}{2\sqrt{k_{lobe} M_{lobe}}} \qquad \textbf{(3.95)}$$

The damping factor ξ has been reported for an over-damped 2nd order system for an adult human lung to be 8.45 [78]. Since human and ovine lungs are considered to be physiological similar in a number of cases in this research, it is used in this work to determine the mechanical damping coefficient (c) for premature lambs.

3.6.6. Tidal Volumes and Respiratory Rates

The following values of tidal volumes and respiratory rates are not used directly in the simulations since these values are set according to the chosen experimental breath pattern under consideration for better model-experiment comparison. They are described here however to demonstrate typical values in practice and during simulation.

Davis et al. [101] measured the tidal volume of 145 day lambs to be 11.2 ml/kg. Willet et al. [102] measured a value of 7.8 ± 0.4 ml/kg for tidal volume for 128 Day lambs. During mechanical ventilation Pillow et al. [95] reported adjusting ventilator settings to maintain a tidal ventilation of less than 10ml/kg for both 125 and 146 Day lambs.

Respiratory rates have been reported to be approximately 40 breaths per minute (bpm) for 125 day and 135 day gestation lambs and 30 bpm for 146 day lambs [95, 102].

3.7. Simulink Model

Separate models were formulated for 128 day and 142 day gestation lambs. The Simulink models contained look-up tables which contain input and output numeric values to describe the relationship between elastance and lobe volume for each lobe. Since these relationships were different at each lobe and at each gestation, two separate models were created.

The model is able to predict the pressure, flow rate and volume at each of the 17 sections identified in Table 3.1. Figure 3.13 shows the 3 main subsystems of the model within the Simulink environment i.e. the tracheo-bronchial subsystem, the viscoelastic subsystem. and the respiratory support device subsystem. Each subsystem is a modular, connectable subroutine (consisting of many smaller subroutines) based on the equations derived in this chapter.

The tracheo-bronchial system contains equations (3.10) to (3.25) and (3.37) to (3.60). The viscoelastic system contains equations (3.26) to (3.32), (3.62) to (3.69) and (3.73) to (3.91).

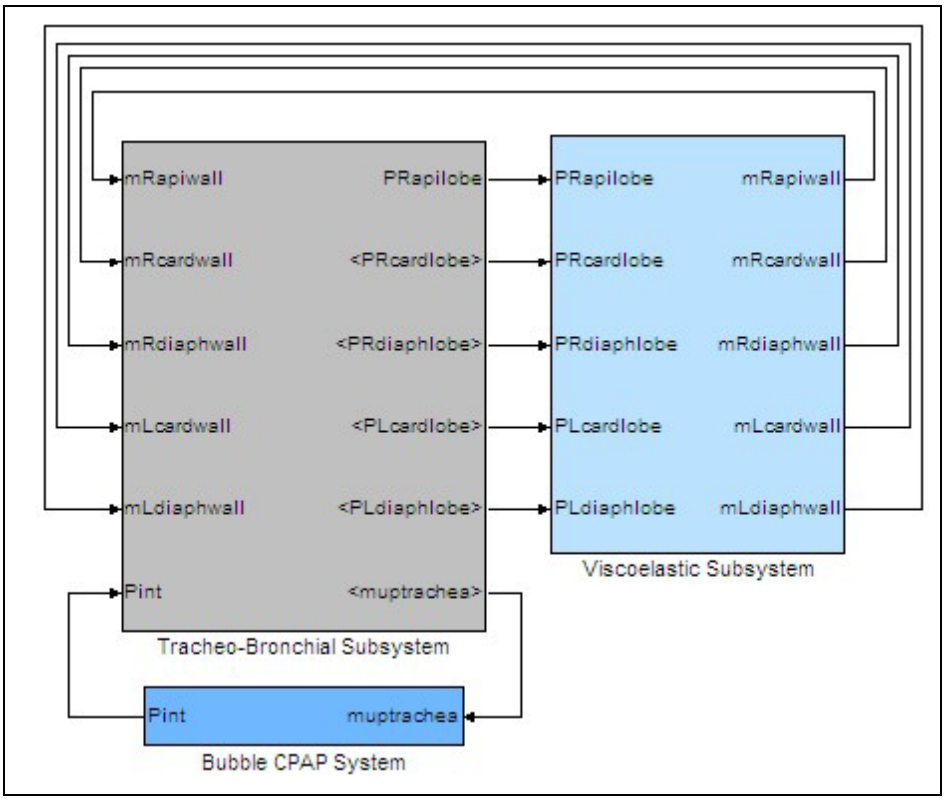

Figure 3.13 Elements of the Simulink Model.

Figure 3.14 shows the general form of the block diagrams used for equations (3.10) to (3.25) and (3.37) to (3.60) in the trachea-bronchial system, using the general forms in equations (3.7) and (3.36). This arrangement constitutes the subsystems in the model that calculate the mass flow rates and pressures in each airway section.

Figure 3.15 shows the general form of the block diagrams used for equations (3.26) to (3.32) and (3.62) to (3.69) in the viscoelastic system, using the general forms in equations (3.9) and (3.61) This arrangement constitutes the subsystems in the model that calculate the pressures in each lobe and the mass flow rates into the lobes from the connecting airway sections.

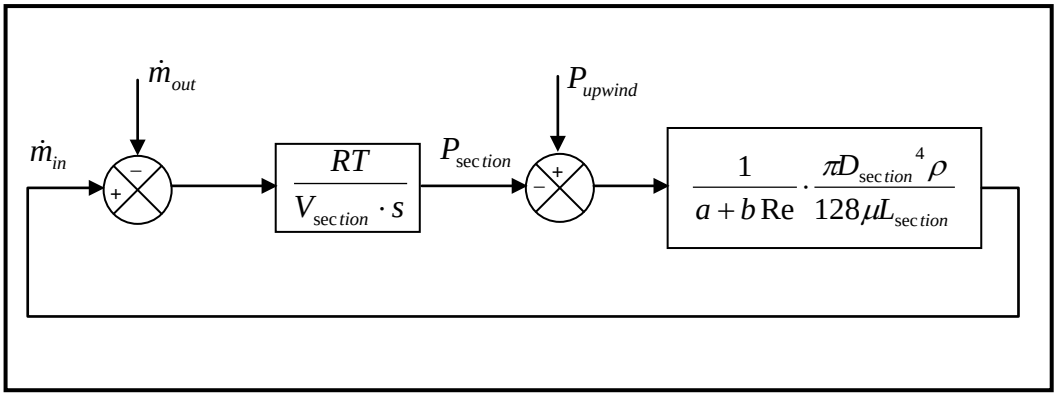

Figure 3.14 General form of the block diagram for equations (3.10) to (3.25) and (3.37) to (3.60).

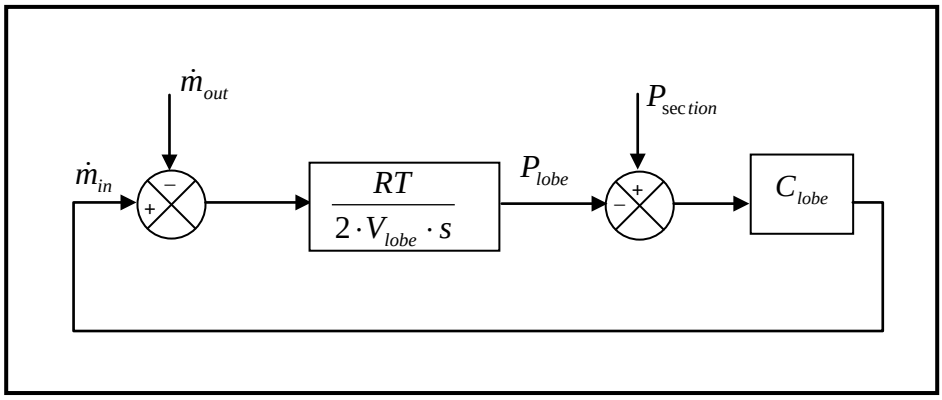

Figure 3.15 General form for the block diagram for equations (3.26) to (3.32) and (3.62) to (3.69).

Figure 3.16 shows the general form of the block diagrams used for equations (3.73) to (3.87) in the viscoelastic system, using the general forms of equations (3.70) to (3.72). This arrangement constitutes the subsystems in the model that calculates the individual lobe wall movement due to the various forces acting on the lobe walls and hence the mass flow rate generated by each lobe due to patient breathing.

Figure 3.17 shows the block diagram for equation (3.88) in the viscoelastic system. This arrangement constitutes the subsystem in the model that calculates the movement of the pleural wall due to the forces that act on it.

Figure 3.18 shows the block diagram for equation (3.91) in the viscoelastic system. This arrangement constitutes the subsystem in the model that calculates the pleural pressure which acts on the wall of the individual lobes.

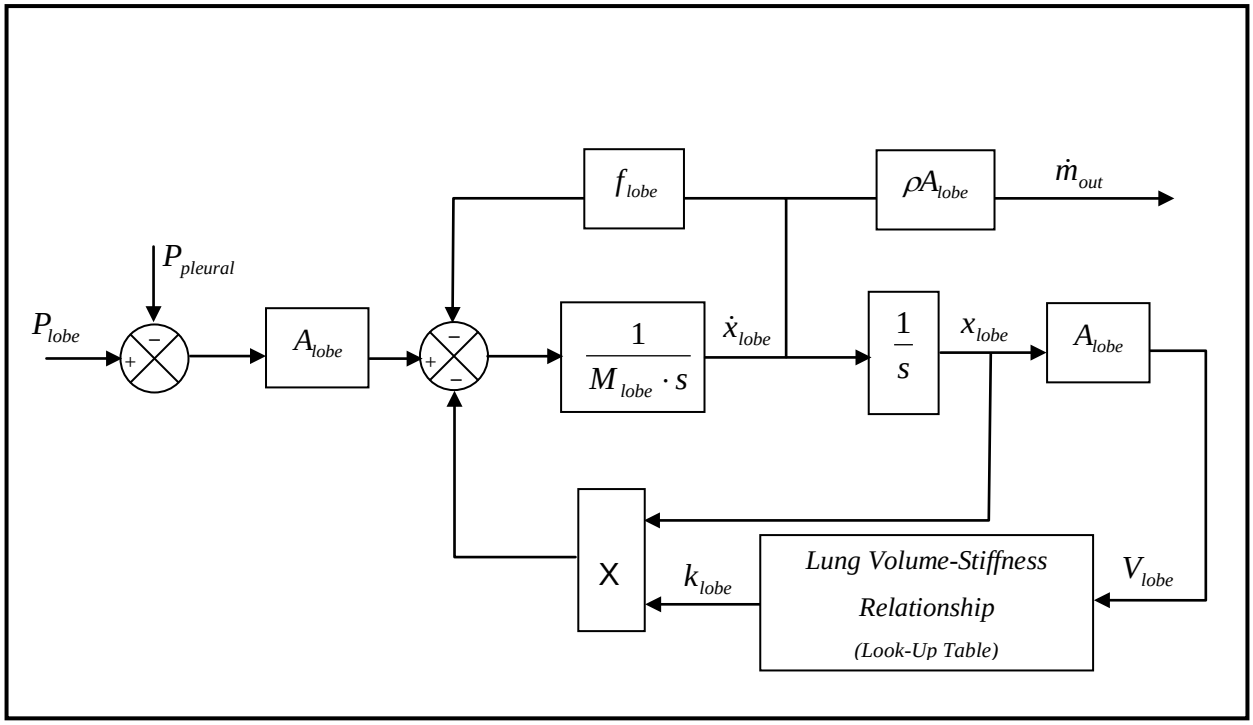

Figure 3.16 General form for the block diagram for equations (3.73) to (3.87).

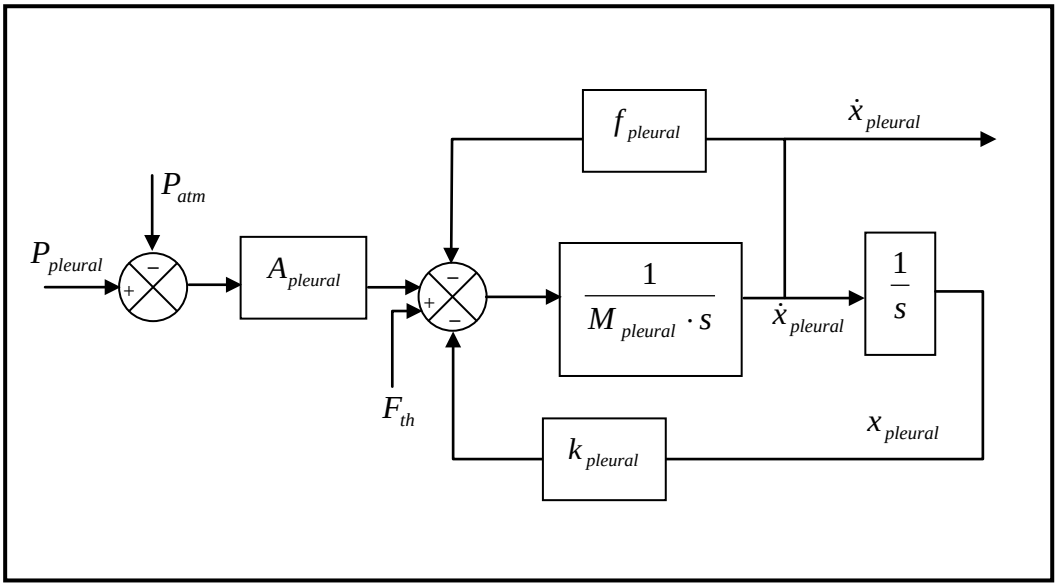

Figure 3.17 Block diagram for equation (3.88).

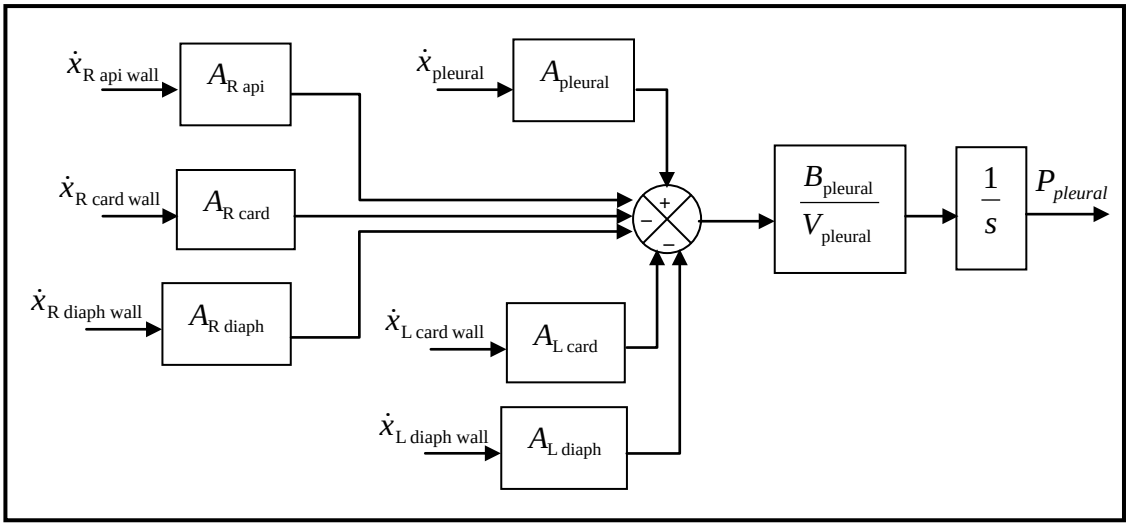

Figure 3.18 Block diagram for equation (3.91).

The respiratory support device subsystem is the Simulink model developed previously by the author [56] which models the Bubble CPAP device. The mass flow rate generated by the patient ($\dot{m}_{\text{up trachea}}$) flows into the patient interface of the Bubble CPAP device and contributes to the pressure generated at the interface ($P_{\text{interface}}$) which in turn acts on the upper trachea as in equation (3.37). The Bubble CPAP System can be substituted for any other model of a respiratory device (i.e. CPAP, HFV, MV etc.)

The parameters for the model are stored in a Matlab m-file which is loaded before performing any simulation. Again, separate m-files are created for 128 day and 142 day gestation lamb models due to the different parameters and physical relationships. Desired outputs (i.e. pressure, flow rate and volume) are obtained by placing scopes in the desired locations (i.e. sections 1 and 13-17) which log the data into arrays in the Matlab workspace.

The sample time for all simulations is 0.004 seconds (250Hz) since frequencies up to 125Hz were used. The “ode23s” variable-step continuous solver in Simulink was used. It computes the model's state at the next time step using a modified Rosenbrock formula of the order 2. It is a one-step solver, needing only the solution to the preceding time point. It showed more efficiency at the crude tolerances that were used in the simulation.

After simulation, the power spectral density and work of breath (WOB) calculations are performed in Matlab at each specified location and then stored in an Excel spreadsheet for further analysis. The details of each simulation with results are discussed in Chapter 4.

3.8. Closure

Models of the 128 day and 142 day gestation ovine respiratory system have been developed in this chapter. First, the equations to predict pressure and mass flow rate were developed. The empirical and literature derived parameters required for the model were then identified and defined. The elements of the Simulink model and its use within the Matlab environment were described. In the following chapter, the simulations and experiments performed to validate the model are presented.

CHAPTER 4

Model Validation and Results

4.1. Introduction

This chapter begins by describing the experimental procedure used to collect data from 133 day gestation lambs (Section 4.2). Section 4.3 then compares the experimental data collected with the predictions from the Simulink model developed in Chapter 3. Section 4.4 presents the model predictions of the effect of using pressure oscillations on the WOB. The method of calculating WOB is first described (Section 4.4.1) and a comparison of the WOB between premature (128 day gestation) and near term (142 day gestation) lungs is then established (Section 4.4.2). The predictions of WOB at specified locations in the 128 day lung are then performed by adding pressure oscillations at the CPAP generator (Section 4.4.3) and at the patient interface (Section 4.4.4). These WOB calculations help determine if WOB increases from prematurity to near-term upon addition of particular pressure oscillation frequencies.

4.2. Collation of Experimental Data

The experimental sets of data used to validate the 128 day gestation model were obtained from an earlier study performed by Pillow et al. [13] on 133 day gestation lambs (the closest gestational data available). The protocols were a collaborative study between The Cincinnati Children's Hospital Medical Centre, Cincinnati, Ohio; The School of Women's and Infants Health, The University of Western Australia, Perth, Australia; and Fisher & Paykel Healthcare Ltd, Auckland, New Zealand. Investigations were approved by the Animal Ethics Committee of the Western Australia Department of Agriculture and Cincinnati Children's Hospital Medical Centre.

The study proved that “in an ovine model of preterm lung disease, treatment with Bubble CPAP immediately after birth enhances gas exchange, lung mechanics, gas mixing efficiency and lung volume compared with constant pressure CPAP”. A brief summary of the methods as published in Pillow et al. [13] is given as follows.

Lambs were delivered by caesarian section at 133 day gestation, dried and intubated with a 4.5 mm internal diameter cuffed, tracheal tube. They were then treated with CPAP using heated humidification with 100% oxygen. The unsedated, spontaneously breathing lambs were randomized into 3 groups:

- Group 1 - Constant Pressure CPAP with a bias flow of 8L/min (n=12)
- Group2 - Bubble CPAP with a bias flow of 8 L/min (n=12)
- Group 3 - Bubble CPAP with a bias flow of 12 L/min (n=10)

The depth of the CPAP probe in the Bubble CPAP System was adjusted to maintain similar mean pressures as those obtained with CPAP. Lambs were delivered to a mobile radiant warmer (CosyCot Infant Warmer, Fisher & Paykel Healthcare) and covered in occlusive wrap to maintain body temperature at approximately 39^{o}C (see Figure 4.1).

At study completion (150 minutes) a variety of physiological measurements were performed which included arterial blood gases, oxygraphy, capnography, multiple breath washout and lung mechanics. Of interest to this study are the flow rate, tidal volume and pressure measurements recorded at a sampling frequency of 200 Hz at the airway opening.

Table 4.1 lists a summary of the animals of interest to this study i.e. animals in group 1 and 2. The average birthweight, tidal volume and respiratory rate are listed in the table for each group. Typical pressure, volume and flow rate signals are presented in Appendix A for each animal.

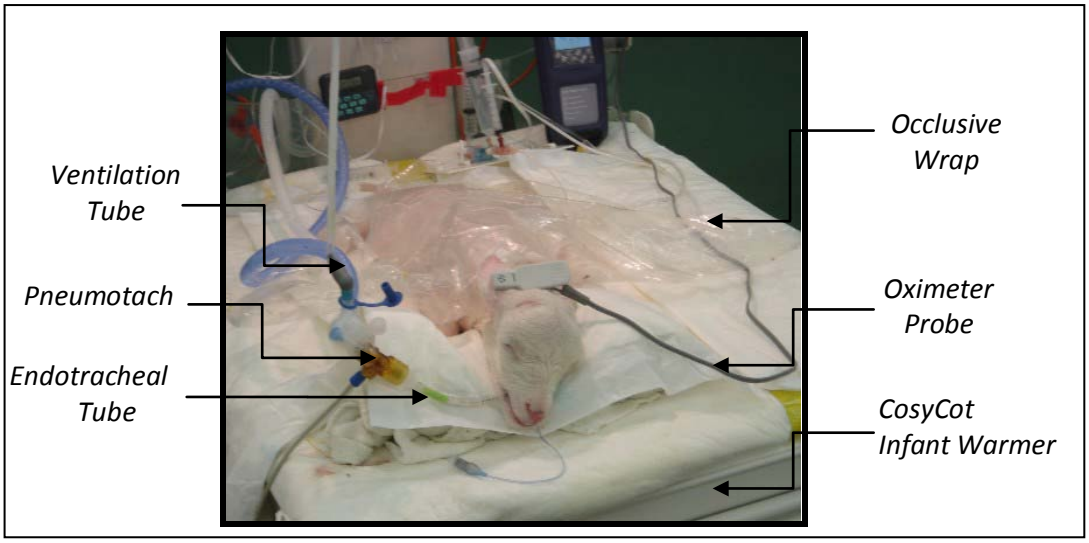

Figure 4.1 Animal prepared for trials on infant warmer with occlusive wrap.

Table 4.1 Details of animals and ventilation strategies used in experiments.

	Bubble CPAP	*CPAP*
Number of animals	*12*	*12*
Average Birthweight ± SD (kg)	*3.25±0.51*	*3.21±0.27*
Average Tidal Volume ± SD (ml/kg)	*5.38±1.31*	*4.72±1.4*
Average Respiratory Rate ± SD (bpm)	*68.83±22.89*	*74.36±25.0*

For the purposes of validation, however, typical pressure, volume and flow rate signals of only 1 animal were used to compare the model results to the experimental values. The animal whose tidal volume was closest to the average value of the sample population was chosen for comparison purposes and is further detailed in Section 4.3.

4.3. Comparison of Model and Experimental Results

The first step of the modelling process before proceeding to subsequent simulations was to validate the model predictions of pressure, flow rate and volume at the airway opening with experimental data collected in Section 4.2.

4.3.1. Comparison of Model Predictions with CPAP measurements

The details for the animal selected for comparison are shown in Table 4.2. The animal-specific parameters in the 128 day gestation model were adjusted to match those of Table 4.2.

Table 4.2 Details of selected animal from group 1.

Treatment Type	*CPAP*
Birthweight (kg)	*3.15*
Tidal Volume (ml/kg)	*4.65*
Respiratory Rate (bpm)	*60*
Mean CPAP (cm H_2O)	*6.75*

As mentioned in Chapter 3, the profile of the thoracic force was defined so as to follow the shape (but not magnitude) of the tidal volume profile. To show a more faithful comparison, the thoracic force is set to match the tidal volume profile of the experimental tidal volume (Figure 4.2). The magnitude of the thoracic force is set by increasing its value until the tidal volume of the model prediction matches that of the experimental tidal volume. This, in effect, calibrates the driving input of the system. This method assumes, however, that the relationships of all other parameters in the model are accurate.

The result of matching the model tidal volume to the experimental tidal volume of a 128 day gestation lamb receiving CPAP is shown in Figure 4.2. The model predictions in comparison to the experimental values of airway opening pressure and flow are shown in Figure 4.3 and Figure 4.4 respectively. Figure 4.3 and Figure 4.4 show a close correlation between experimental and model results. The deviation of the model results from the experimental results are quantified as a percentage difference with respect to the experimental results at the points of maximum, minimum and mean pressure and flow (Table 4.3). Of particular interest in RDS is the unevenness in ventilation across different lobes in the lung due to their widely differing mechanical properties.

Model predictions for the pressures, flow rates and volumes in each lobe are shown in Figure 4.5. Figure 4.5 (a) to (c) show the pressures, flow rates and volumes respectively for lobes in the left lung i.e. the left cardiac lobe and the left diaphragmatic lobe. Figure 4.5 (d) to (f) show the pressures, flow rates and volumes respectively for lobes in the right lung i.e. the right apical lobe, the right cardiac lobe and the right diaphragmatic lobe.

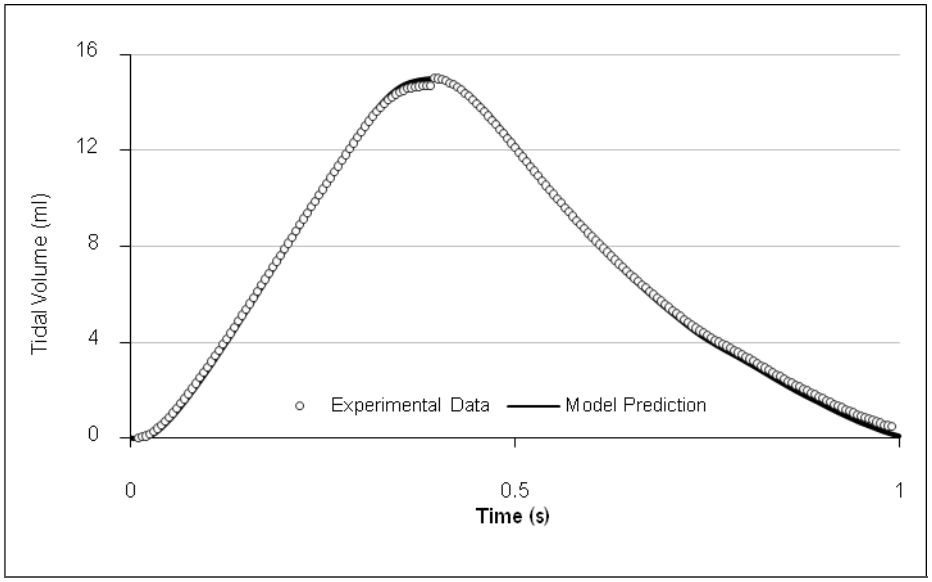

Figure 4.2 Model-experiment tidal volume calibration of a 128 day gestation lamb.

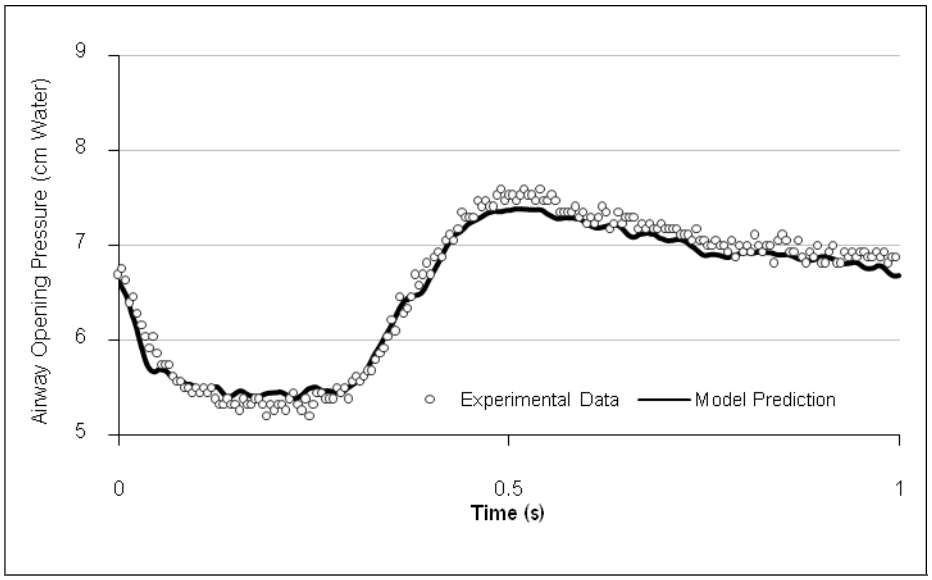

Figure 4.3 Model-experiment comparison of airway opening pressure for a 128 day gestation lamb receiving CPAP.

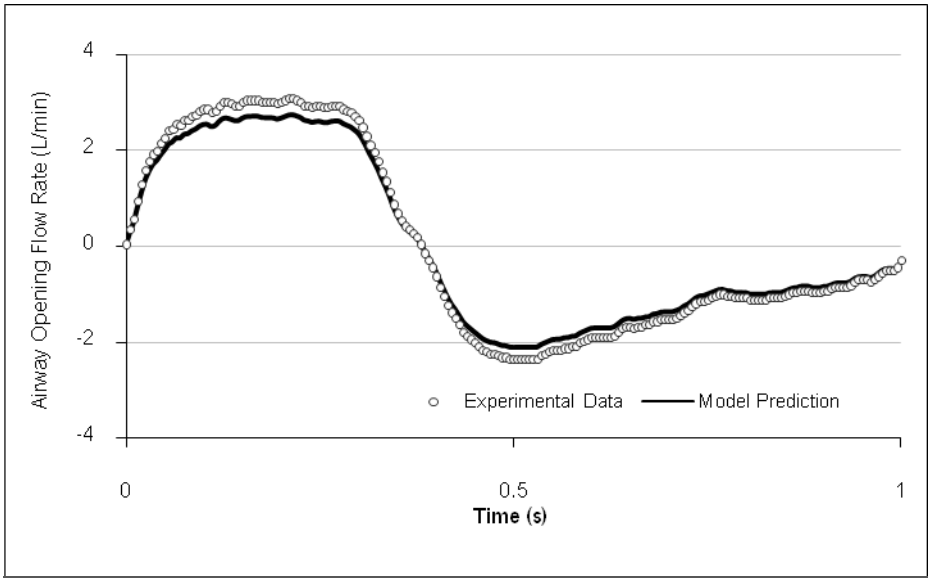

Figure 4.4 Model-experiment comparison of airway opening flow rate for a 128 day gestation lamb receiving CPAP.

Table 4.3 Percentage difference of pressure and flow between model and experiment.

% Difference in Pressure			% Difference Flow		
Max	Mean	Min	Max	Mean	Min
2.64	0.83	3.33	11.0	0.68	10.5

The pressures in the lobes show higher mean values and larger pressure swings than those predicted at the airway opening. The pressure in the right diaphragmatic lobe (the largest lobes) shows the smallest pressure swings. The left diaphragmatic lobe (which is slightly smaller than the right diaphragmatic lobe) shows a slightly greater pressure swing. The left cardiac lobe and right apical lobe (which are similar in size and smaller than the diaphragmatic lobes) show similar magnitudes of pressure swings to each other which are larger than those for the diaphragmatic lobes. The right cardiac lobe (which is the smallest lobe) shows the largest pressure swing during expiration but pressure swings remain between the right apical and right diaphragmatic lobe during inspiration.

The right diaphragmatic lobe has the highest flow rate, followed by the left diaphragmatic lobe. The left cardiac and right apical lobes have similar flow rates while the right cardiac lobe has the lowest flow rate. Hence, the larger the lobe, the larger the

flow rate generated. A similar relationship exists for the lobe volumes (at both FRC and peak inspiration) as seen in Figure 4.5 (c) and (f).

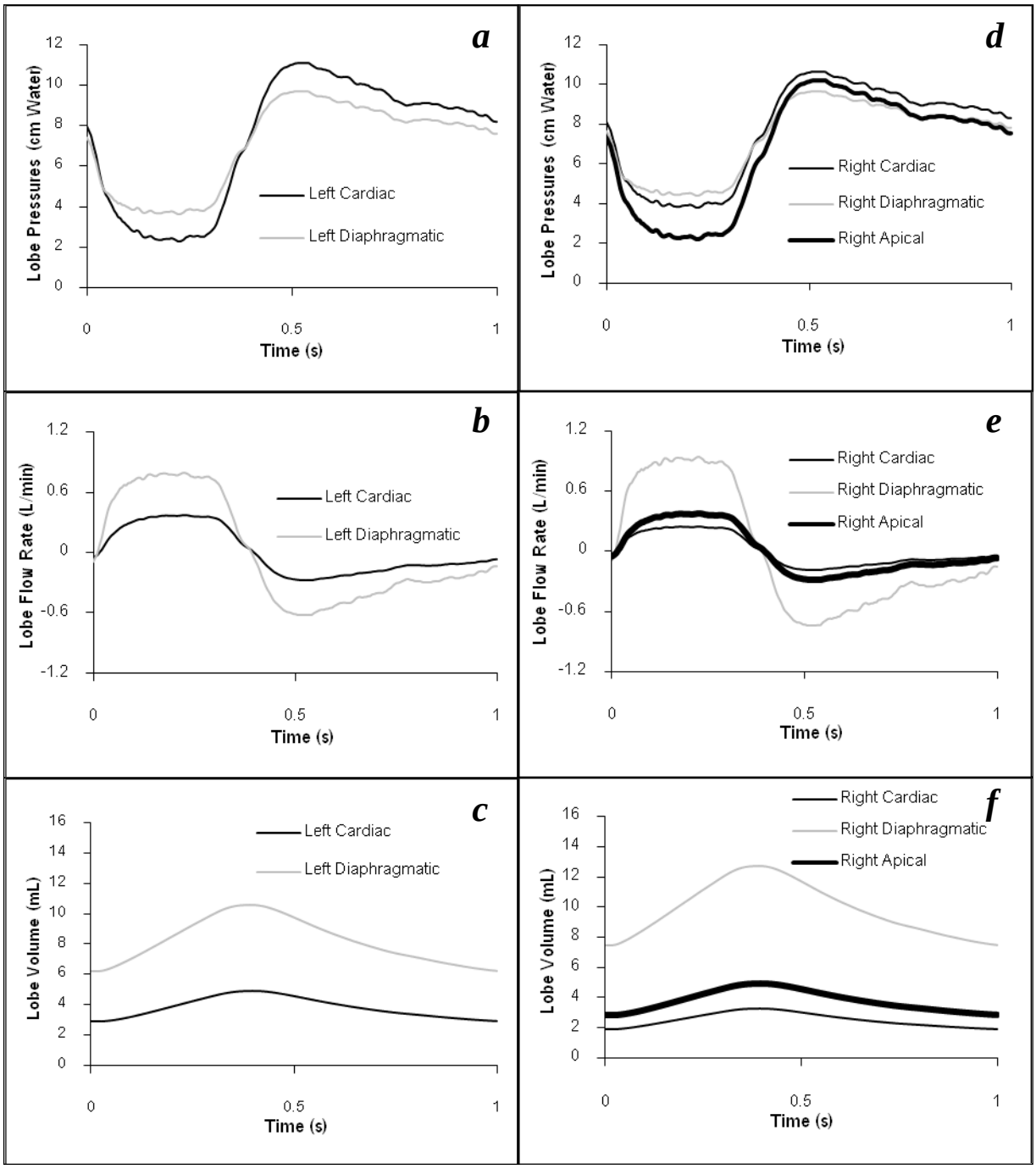

Figure 4.5 Model predictions for lobe pressures, flows and volumes in a 128 day gestation lamb receiving CPAP.

4.3.2. Comparison of Model Predictions with Bubble CPAP measurements

The respiratory parameters of a subject receiving Bubble CPAP is of primary interest to this research. More specifically, the model is used to determine the pressure, flow rate and volume profiles at the level of the individual lobes.

As in Section 4.3.1, the animal in group 2 which had the tidal volume closest to the average tidal volume of the sample population was chosen for the purposes of comparison. The animal-specific parameters in the model were adjusted to those described in Table 4.4. All other parameters and settings were left unchanged.

In addition to the prescribed level of mean CPAP (6.75 cm H_2O) as used in the initial simulation, a typical signal of the superimposed pressure oscillations generated at the level of the CPAP generator of the Bubble CPAP System is introduced into the model. This was obtained from previous measurements by Manilal [56]. The comparisons of pressure, flow and volume predictions of the model to the experimental measurements are shown in Figure 4.6 to Figure 4.8 respectively.

Overall, the model predictions show good comparisons with the experimental data. The superimposed pressure oscillations are clearly visible in Figure 4.6. Because of the random nature of the bubble oscillations, the experimental and model values do not match exactly but lie in the same pressure range. Due to the high amplitude of pressure oscillations relative to that of the breath pattern alone, the breath pattern in the pressure values of Figure 4.6 is not as distinctly visible at the airway opening during Bubble CPAP as compared to CPAP. The breath pattern is clearly visible in Figure 4.7 with superimposed oscillations.

Table 4.4 Details of selected animal from group 2.

Treatment Type	*Bubble CPAP*
Birthweight (kg)	*3.2*
Tidal Volume (ml/kg)	*4.17*
Respiratory Rate (bpm)	*98*
Mean CPAP (cm H_2O)	*6.75*

The tidal volume values during Bubble CPAP (Figure 4.8) show some unevenness in profile due to the pressure oscillations which are not as distinct as those seen in the pressure and flow profiles. The tidal volume is calculated in the model (as well as measured in clinical practice) by the mathematical integration of the flow rate signal and so the oscillations present in the flow rate measurements have effectively been 'integrated out' in process of calculating the tidal volume.

Various questions have arisen regarding the transmission of pressure oscillation amplitude and frequency from the airway opening to the individual lobes. In the hope of answering such questions, the model was also used to predict the respiratory parameters in the individual the lobes during Bubble CPAP as seen in Figure 4.9 to Figure 4.14.

The oscillations in pressure and flow are visible at the level of the individual lobes. The magnitude of the pressure oscillations in Figure 4.9 and Figure 4.10 are not markedly decreased to those compared with Figure 4.6. The magnitude of the flow oscillations in Figure 4.11 and Figure 4.12 shows a decrease in magnitude to those compared with Figure 4.7. Again, the volumes in the lobes (Figure 4.13 and Figure 4.14) show no noticeable change in profile with the addition of oscillations.

In-vivo experimental values of pressure and flow rate in each lobe during Bubble CPAP has neither been measured in previous work by the author nor recorded in the literature due to the difficult and impractical nature of the testing. Thus, the model predictions remain unvalidated and only serve as an indication of the transmission of the pressure oscillations. The accuracy and utility of the predictions are further discussed in Chapter 6.

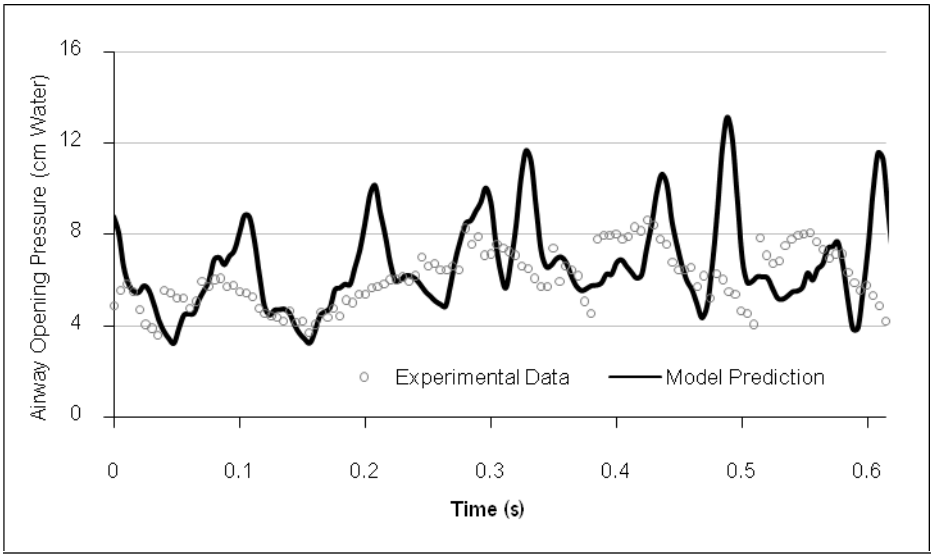

Figure 4.6 Model-experiment comparison for airway opening pressure in a 128 day gestation lamb receiving Bubble CPAP.

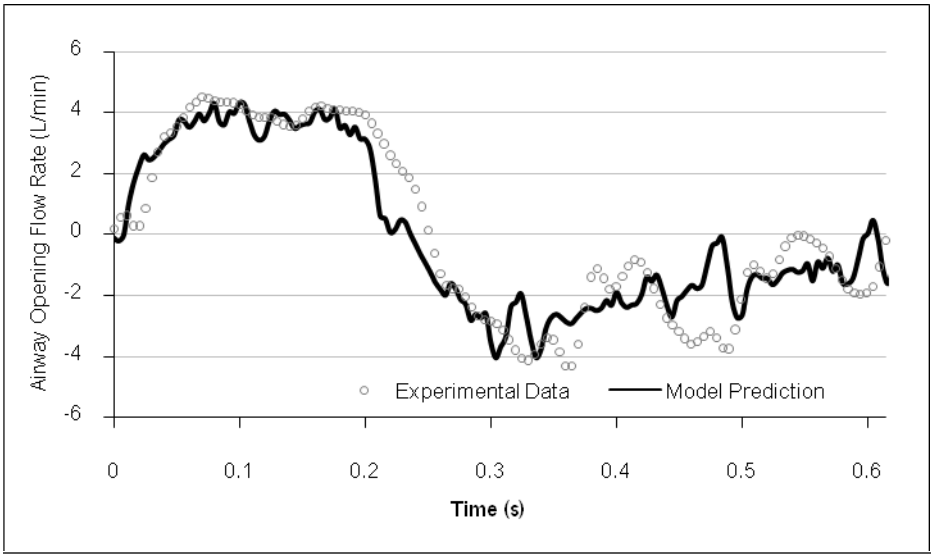

Figure 4.7 Model-experiment comparison for airway opening flow rate in a 128 day gestation lamb receiving Bubble CPAP.

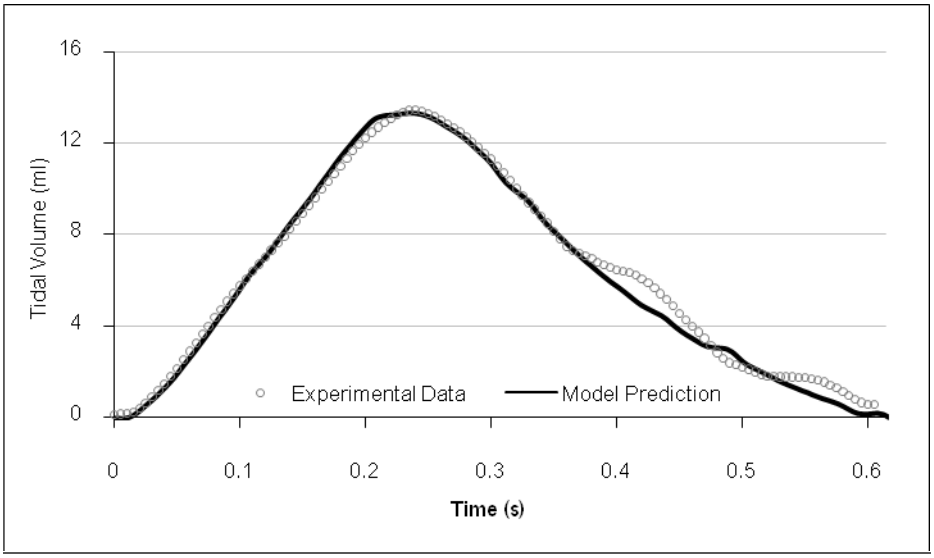

Figure 4.8 Model-experiment comparison for tidal volume in a 128 day gestation lamb receiving Bubble CPAP.

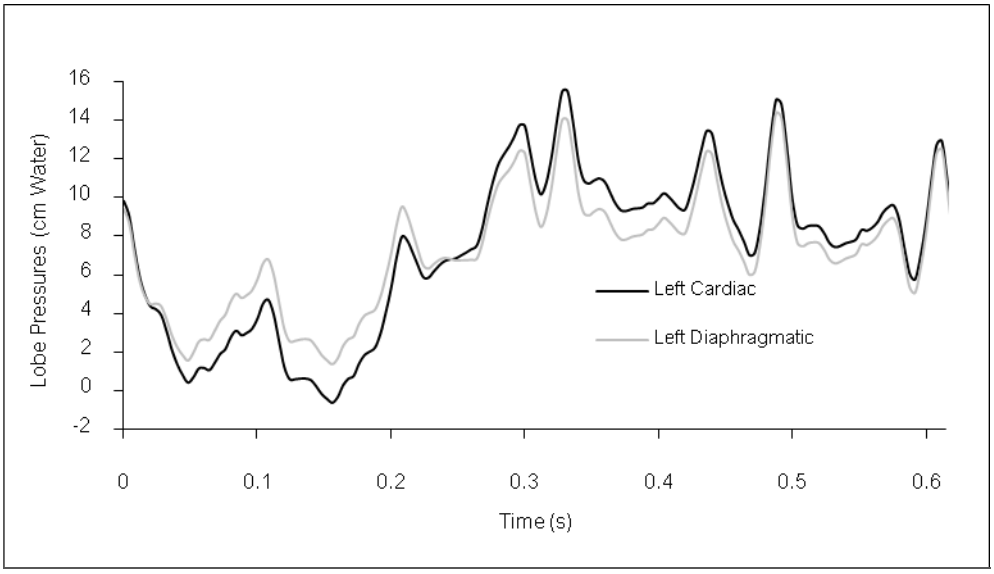

Figure 4.9 Pressures in left lobes of a 128 day gestation lamb receiving Bubble CPAP.

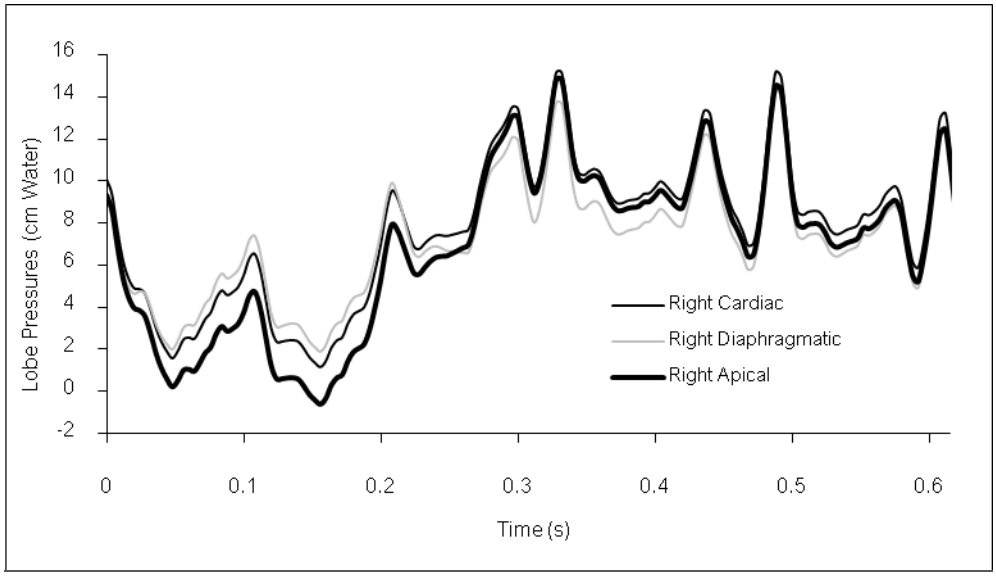

Figure 4.10 Pressures in right lobes of a 128 day gestation lamb receiving Bubble CPAP.

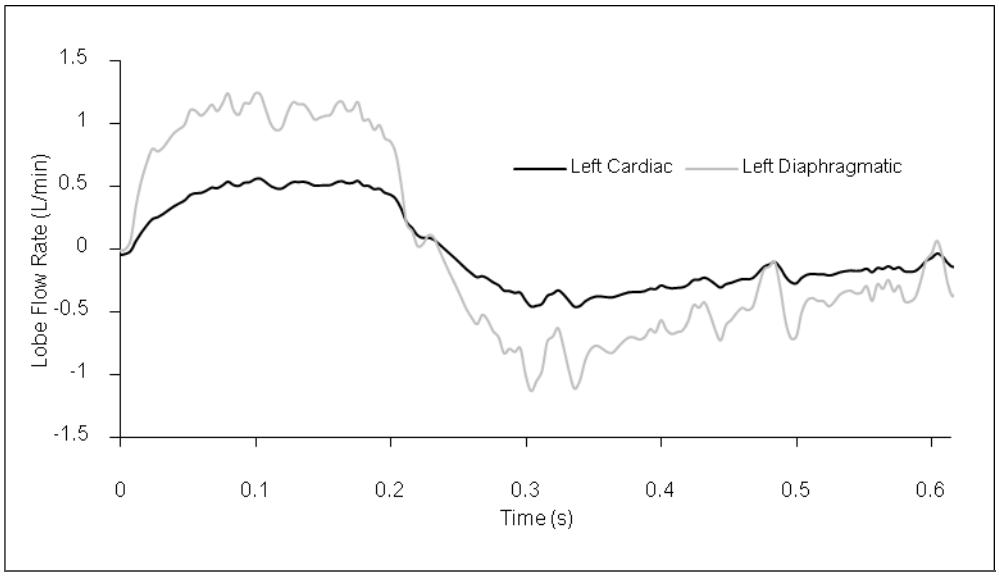

Figure 4.11 Flow in left lobes of a 128 day gestation lamb receiving Bubble CPAP.

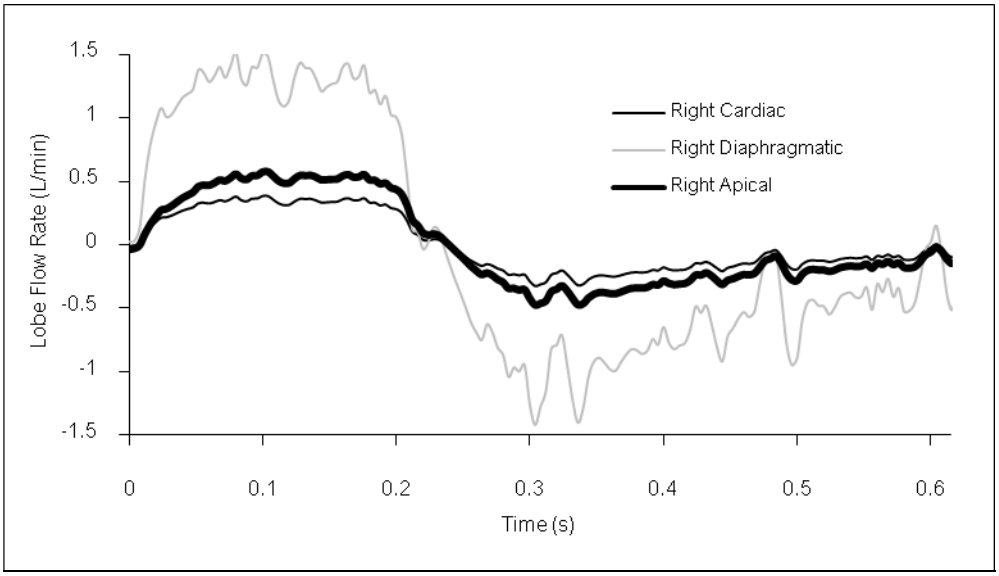

Figure 4.12 Flow in right lobes of a 128 day gestation lamb receiving Bubble CPAP.

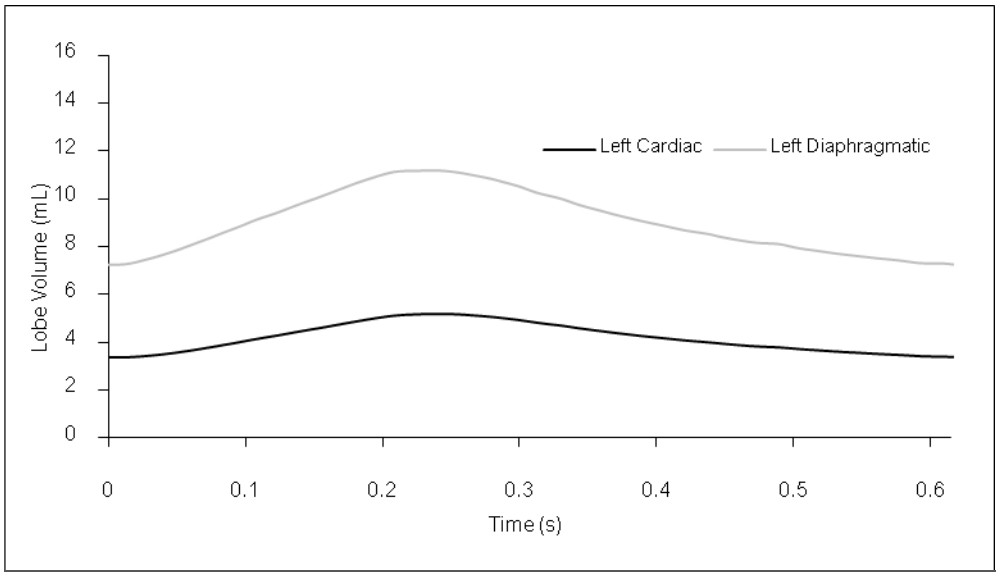

Figure 4.13 Volume in left lobes of a 128 day gestation lamb receiving Bubble CPAP.

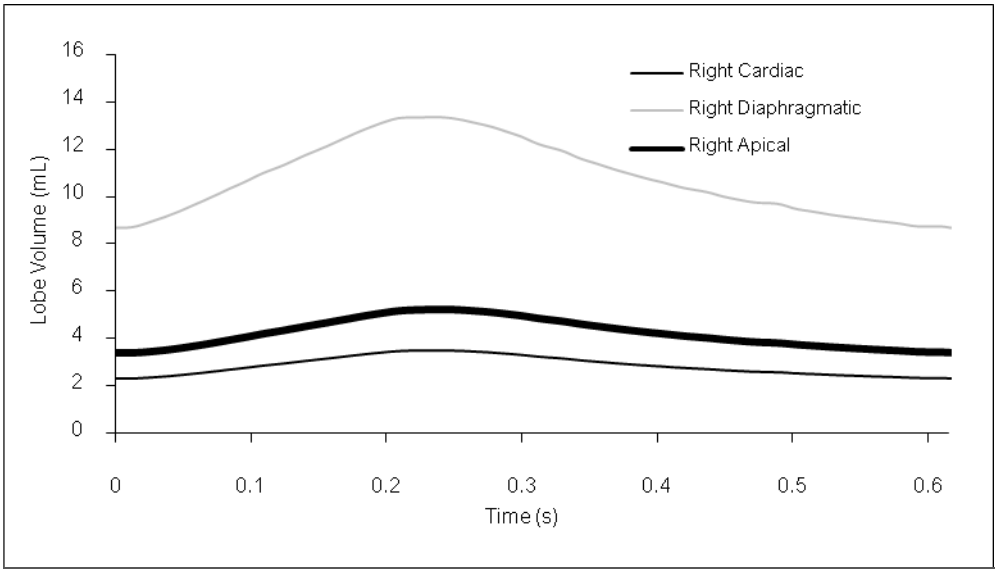

Figure 4.14 Volume in right lobes of a 128 day gestation lamb receiving Bubble CPAP.

4.4. Model Predictions of Pressure Oscillation Effects

Before continuing with simulations on the effect of pressure oscillations, a distinction must be made between the respiratory parameters of a healthy and unhealthy lung. The WOB is used to demonstrate respiratory and device performance in this section and is calculated for lambs of 128 day gestation (representing a premature lung) and 142 day gestation (representing a near-term lung).

4.4.1. Calculating the WOB

The WOB calculates the combined effort of all the respiratory components of the neonatal respiratory system and the device during a breath cycle and is the mechanical work done on the specified control volume. Since the tidal volume, respiratory rate and work done by the neonatal lung are not altered across simulations, any changes in WOB are due to the work done by the device. Although complex integrations of individual pressure-volume loops are required for more sophisticated estimates of WOB, an expression of the mean WOB over inspiration and expiration are calculated in this analysis as it provides sufficient information for the purposes of describing the difference between the premature and near term lung as well as the overall improvement of adding oscillations to neonatal breathing.

To determine the WOB, the work-time product (WTP) is calculated by integrating the instantaneous work (i.e. the product of pressure and tidal volume vs. time) over time (i.e. $\int Wdt$). A more convenient expression of the WTP is the mean WOB ($\overline{WOB}$) generated over a certain time as per equation (4.1)

($\overline{WOB}$) = WTP/sampling period ***(4.1)***

For example, if WTP is calculated for inspiration, then the sampling period is the duration of inspiration and if WTP is calculated for expiration, then the sampling period is the duration of expiration. The mean WOB done in one complete breath $\overline{WOB}_{total}$ is the sum of the mean WOB during inspiration $\overline{WOB}_{insp}$ and the mean WOB during expiration $\overline{WOB}_{\exp}$.

4.4.2. WOB Comparison of premature and near-term lungs

The $\overline{WOB}_{total}$ was calculated for both a 128 day (premature) and 142 day (near term) lamb from the model simulations. The animal specific parameters for the 128 day model are those used in Table 4.2. Since no in-vivo measurements on 142 day lambs were available to produce validated pressure, flow and volume predictions for that gestation, the tidal volume/kg birthweight, respiratory rate and mean pressure were those of Table 4.2 and the birthweight was set at 5.02 kg as per the average measured birthweight for 142 day gestation lambs in Table 3.8. Other gestation specific parameters used in the 142 day model are as defined in Section 3.5.

The $\overline{WOB}_{total}$ at the specified locations for both gestational ages are shown in Appendix B and normalized with respect to the individual values at each location for the 128 day gestation lamb in Figure 4.15.

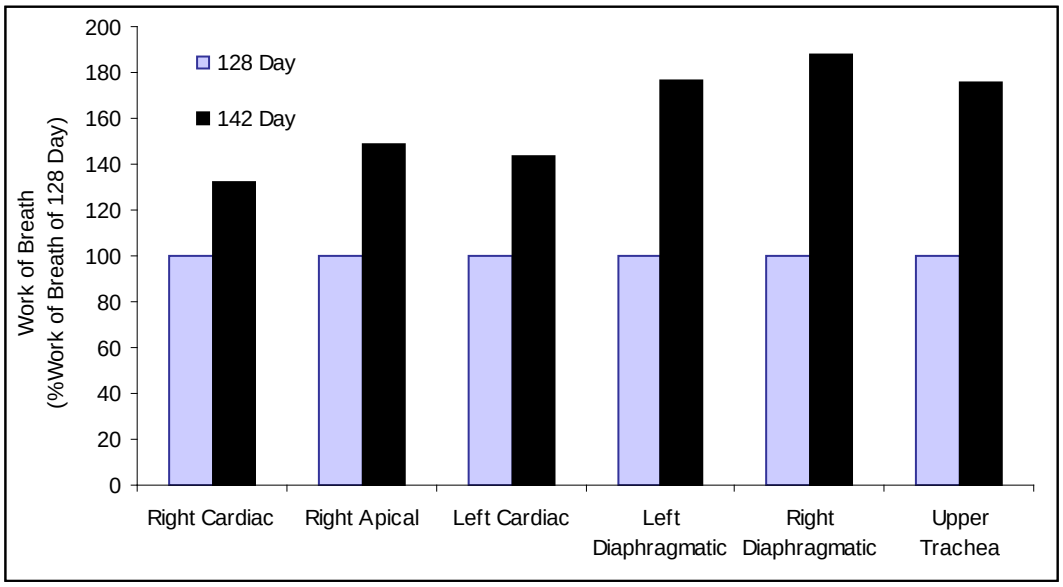

Figure 4.15 Normalized values of WOB of 128 day and 142 day gestation lambs receiving 6.75 cm H_2O CPAP.

Figure 4.15 shows that $\overline{WOB}_{total}$ is higher for the 142 day gestation lamb due to the higher tidal volume resulting from the added birthweight and compliance of the lung and the added muscle energy available to a larger animal. The percentage increase in $\overline{WOB}_{total}$ at each location for the 142 day gestation when compared to values at the 128 day gestation are presented in Table 4.5.

The 142 day gestation, being near term, represents 'healthier' values of WOB. Any increase of $\overline{WOB}_{total}$ from the values at the 128 day gestation due to the addition of the various ventilation profiles used in subsequent simulations is seen as beneficial in that they perform the additional work required to increase $\overline{WOB}_{total}$, which the neonate cannot perform itself.

Table 4.5 Percentage increase in $\overline{WOB}_{total}$ at each location.

Location	Percentage increase in $\overline{WOB}_{total}$ (%) from values at 128 day gestation
Right Cardiac Lobe	32
Left Cardiac Lobe	43
Right Apical Lobe	49
Left Diaphragmatic Lobe	76
Right Diaphragmatic Lobe	88
Upper Trachea	76

4.4.3. Adding pressure oscillations at the CPAP generator

In order to quantify the effect of oscillations on the respiratory parameters, the following procedure was adopted for the subsequent simulations. A white noise pressure signal (a signal that contains all frequencies in equal amounts) was introduced at the CPAP generator in place of the Bubble CPAP pressure oscillation signal. The use of the white noise signal stems from the power spectral density (PSD) analysis in engineering where it has proven to be a useful test signal to determine the frequency response of non-linear systems [100]. In terms of stochastic resonance, the white noise signal effectively allows the lung to 'select the frequencies it prefers' to initiate any resonance-based improvements.

The noise could be added at any point in the system, but since the CPAP generator is the source of the oscillations in practice, it presents the most practical place to introduce white noise into the system in reality. The standard deviation of the white noise pressure signal was set to equal that of the Bubble CPAP pressure signal (i.e. ±2.58 cm H_2O). The white noise signal contains pressure oscillation frequencies up to 125 Hz since previous investigations by other authors [12, 56] have revealed that no significant frequencies are present in Bubble CPAP above this range.

A PSD analysis of the instantaneous work (i.e. the product of pressure and tidal volume vs. time) at the airway opening and at the level of the individual lobes was then performed to determine the frequencies that contain the highest power (i.e. those that contribute the most to the value of the work). The normalized power (the power expressed as a fraction of the highest magnitude of power present in the data set) at the airway opening for a 128 day gestation lamb receiving CPAP and white noise is shown in Figure 4.16. For the purposes of the current investigation, the frequency with the strongest power and all other frequencies which have magnitudes that are greater than 40% of the maximum powers are defined as frequencies of 'significant power'.

The spectrum in Figure 4.16 shows significant power at 19 and 23 Hz. The power spectra of the instantaneous work calculated at the level of the individual lobes identify the same strong frequencies with only very slightly different magnitudes relative to the highest power. The powers of significant frequencies normalized to the maximum power in each data set at each location are summarized in Table 4.6.

The power spectrum identifying significant frequencies will change with the mechanical properties of the lung [56]. The values of frequencies identified in this work are only valid for 128 day gestation ovine lungs.

A series of subsequent simulations were performed to predict the respiratory parameters of a 128 day gestation lamb receiving CPAP superimposed with oscillations at the individual frequencies identified in Figure 4.16. Simulations were also performed for a signal containing equal magnitudes of both strong frequencies as well as for ventilation under Bubble CPAP. Once again, the magnitude of the oscillations was set to ±2.58 cm H_2O (i.e. 1 standard deviation of the noisy Bubble CPAP oscillations).

For all simulations, the mean WOB for inspiration ($\overline{WOB}_{insp}$), expiration ($\overline{WOB}_{\exp}$) and the total breath ($\overline{WOB}_{total}$) were determined at the airway opening and in each individual lobe. These values are archived in Appendix C. The values relative to the $\overline{WOB}_{total}$ value at CPAP-only treatment are shown in Figure 4.17 for each location.

Although the relative magnitudes at each location are vastly different, when the results are normalized relative to the CPAP-only WOB value at each location, as seen in Figure 4.17, the upward trends are the same for all locations.

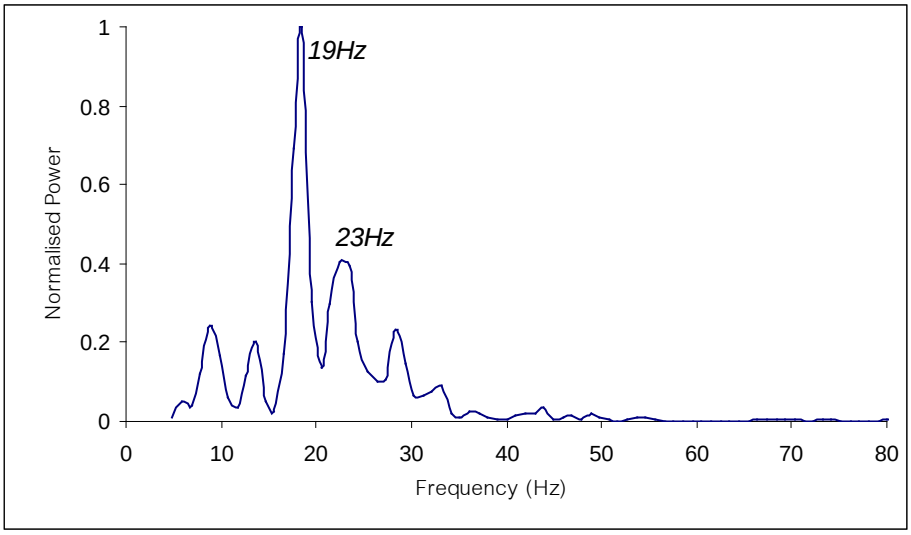

Figure 4.16 Power spectrum of the instantaneous work at the airway opening of a 128 day gestation lamb receiving CPAP and white noise.

Table 4.6 Normalized power of significant frequencies at different locations on addition of white noise at the CPAP generator.

	19Hz	23Hz
Airway Opening	1	0.402
Left Cardiac Lobe	1	0.396
Right Cardiac Lobe	1	0.414
Right Apical Lobe	1	0.403
Left Diaphragmatic Lobe	1	0.422
Right Diaphragmatic Lobe	1	0.429

The WOB for the ventilation profile that uses an oscillation frequency of 19 Hz is higher than that which uses 23 Hz. The largest increase in WOB (4-6% increase across all locations) is observed when both significant frequencies (19 and 23 Hz) are combined in one ventilation profile. Both ventilation profiles show a higher WOB than using Bubble CPAP.

The model predicts that using Bubble CPAP shows a 1-2% increase in WOB across all locations when compared to using CPAP alone. The average WOB at the airway opening calculated from the in-vivo measurements of the 2 groups of animals receiving CPAP and Bubble CPAP (groups 1 and 2) in Section 4.2 are presented in Figure 4.18 after being corrected for birthweight and tidal volume. The in-vivo measurements show that using Bubble CPAP increases the WOB at the interface by 14% when compared to CPAP alone. The differences between the values predicted by the model and the in-vivo measurements are discussed in Chapter 6.

The significant frequencies present in Bubble CPAP are of interest to understand the role that any frequencies therein play in the WOB calculation when compared to the other ventilation profiles.

The PSD of the instantaneous work calculated at the airway opening during the model simulation is shown in Figure 4.19. Significant frequencies are present at 17 Hz and 23 Hz , close to the most powerful frequencies identified in Figure 4.16. Other peaks, although below 40% of the maximum power, are present at 9 Hz and 33 Hz and contribute to the calculated value of the WOB.

Similar frequencies were identified when performing PSD calculations on the in-vivo data acquired from the 12 Bubble CPAP animals (group 2) identified in Section 4.2 and are shown in Table 4.7. The values calculated from the model are highlighted in grey to illustrate that they lie within the range of typical experimental values.

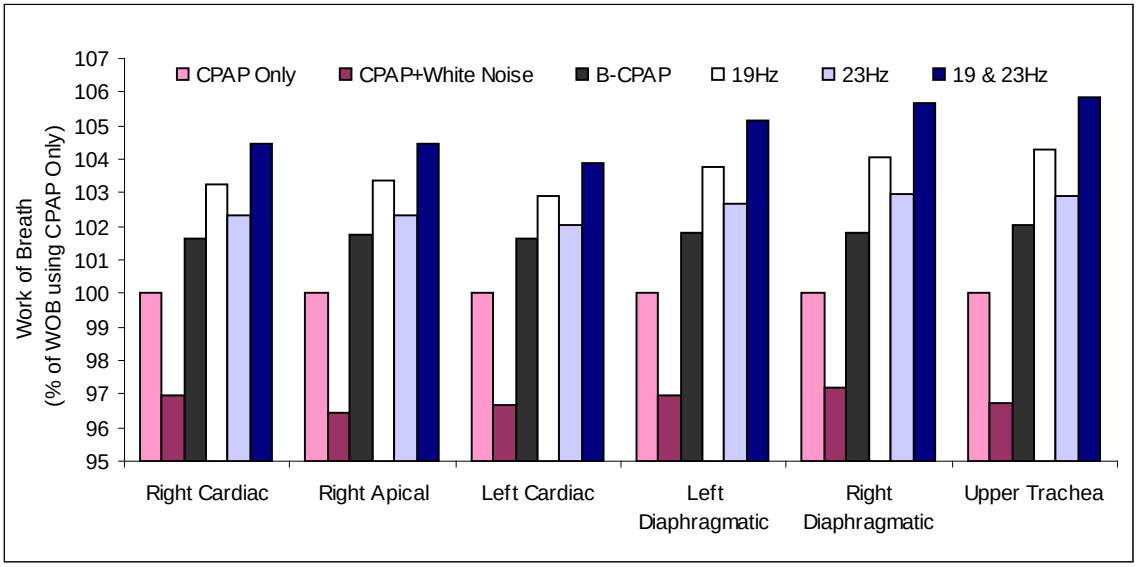

Figure 4.17 WOB (relative to CPAP-only treatment) at specified locations for a variety of oscillatory treatments on a 128 day gestation lamb.

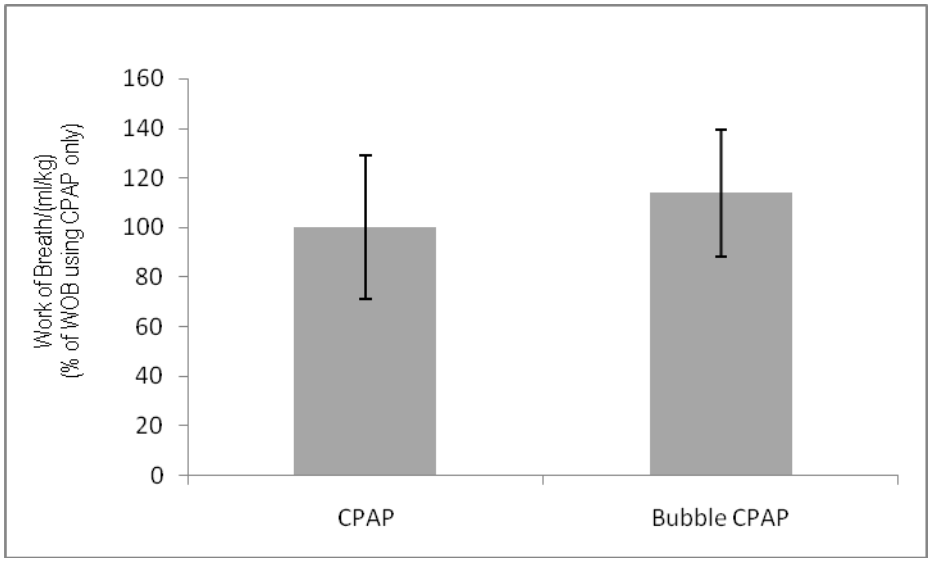

Figure 4.18 Average WOB (relative to CPAP-only treatment) at the patient interface calculated from experimental data

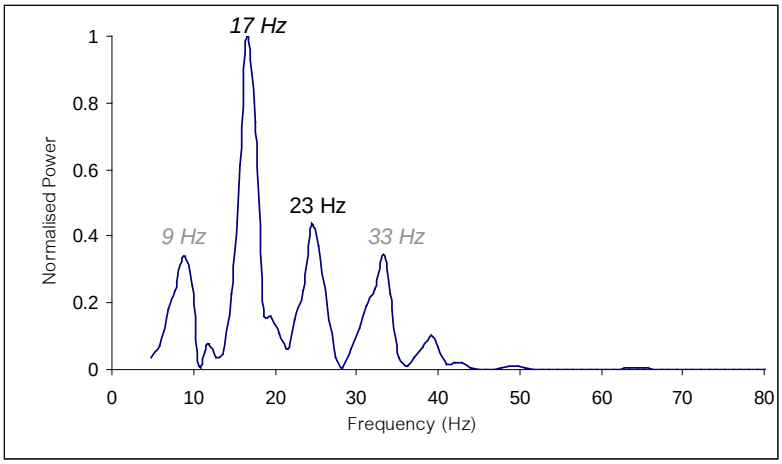

Figure 4.19 Power spectrum of the instantaneous work at the airway opening of a 128 day gestation lamb receiving Bubble CPAP.

Table 4.7 Significant frequencies identified in PSD analysis of experimental data. (Key: Stem units=10 Hz, Leaf units=1 Hz)

STEM	LEAF
0	9
1	1 3 3 3 3 5 5 6 6 7
2	0 2 2 3 3 3 3 5 5 6 7 9 9
3	0 0 0 0 1 1 1 3 3 4 5 9
4	0 8 9
5	4 8
6	
7	0 0 5 8 8
8	1
9	5

4.4.4. Adding pressure oscillations at the patient interface

Even though frequencies up to 125 Hz were recorded in the CPAP generator of the Bubble CPAP device, the attenuation of frequencies above 45 Hz through the expiratory limb makes it impossible to determine the effect of higher frequencies on respiratory parameters [56]. To determine this effect, the white noise pressure signal is added at the patient interface instead of at the level of the CPAP generator. Since the expiratory tube is eliminated from the system, pressure oscillations will not be attenuated at the patient interface, thus allowing investigations of the effect of higher frequencies.

First, a simulation was performed for CPAP with white noise at the interface up to 125 Hz. The PSD is calculated at the airway opening and at the level of the individual lobes

to determine the frequencies with the strongest power. Figure 4.20 shows the PSD of the instantaneous work at the airway opening. The significant frequencies are noted on the figure. The power spectra of the instantaneous work calculated at the level of the individual lobes identify the same strong frequencies of only very slightly different magnitudes relative to the highest power.

A series of subsequent simulations were performed to predict the respiratory parameters of a 128 day gestation lamb receiving CPAP superimposed with oscillations at the interface using the individual frequencies identified in Figure 4.20. A simulation was also performed for a signal containing equal magnitudes of all frequencies. Once again, the magnitude of the oscillations was set to ±2.58 cm H_2O.

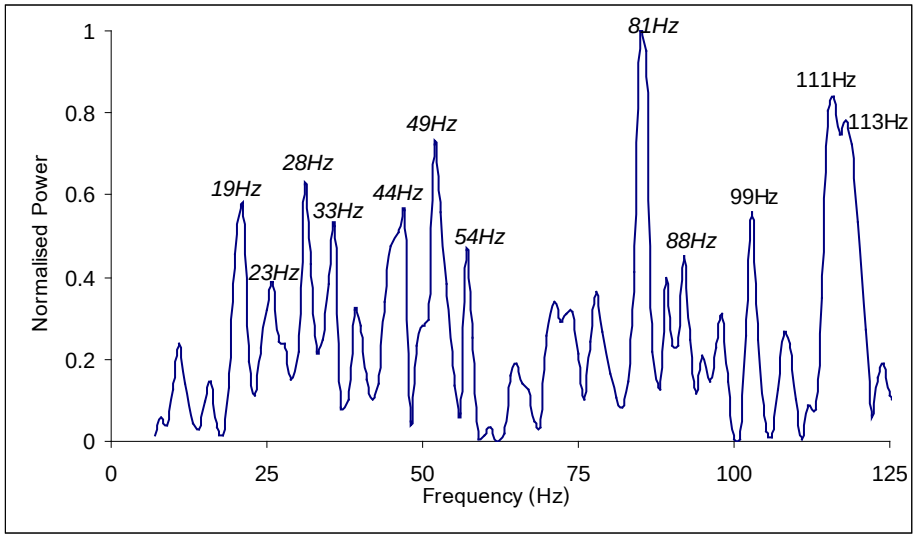

Figure 4.20 Power spectrum of the instantaneous work at the airway opening of a 128 day gestation lamb receiving CPAP and white noise at the interface.

$\overline{WOB}_{total}$, $\overline{WOB}_{insp}$ and $\overline{WOB}_{\exp}$ at each specified location for each simulation are archived in Appendix D. At each location, the values of $\overline{WOB}_{total}$ relative to the value of CPAP-only treatment are calculated and shown in Figure 4.21 to Figure 4.23 for the upper trachea, right lobes and left lobes respectively.

Figure 4.21 to Figure 4.23 show similar trends in WOB and also show that adding single frequencies as well as an 'equal mixture' of all significant frequencies increases

WOB above the values calculated for CPAP-only treatment. The amount of increase in WOB for any particular single frequency used is congruent with the strength of the frequency identified in Figure 4.20, such that the increase in WOB at 81, 88 and 99Hz, (which show the highest power contributions to the work in Figure 4.20) is greater than that at 23 Hz which shows the lowest power contribution of the significant frequencies.

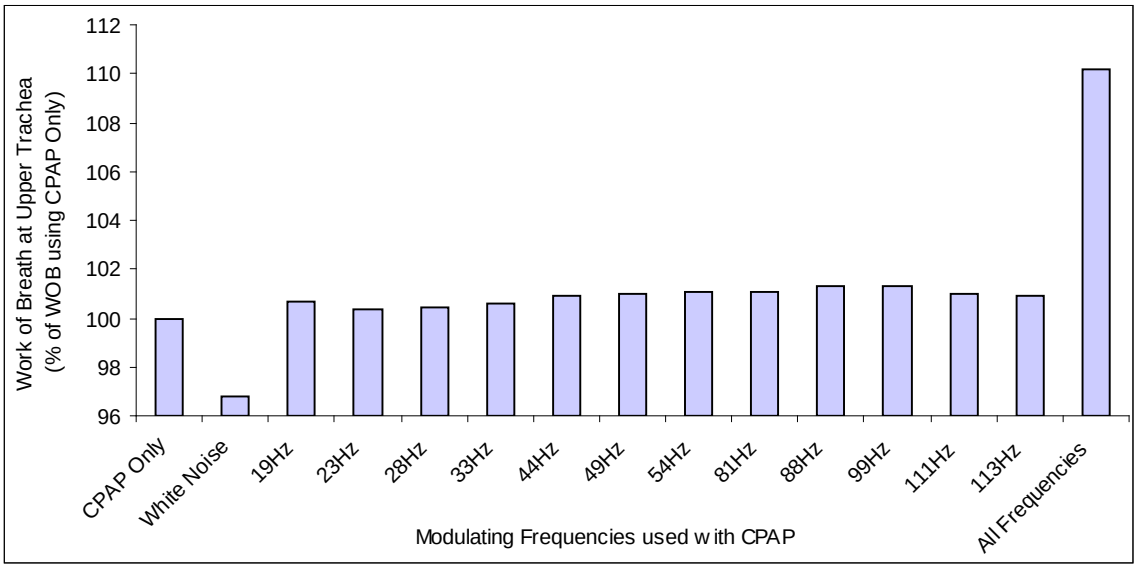

Figure 4.21 WOB (relative to CPAP-only treatment) at the upper trachea for a variety of oscillatory treatments on a 128 day gestation lamb.

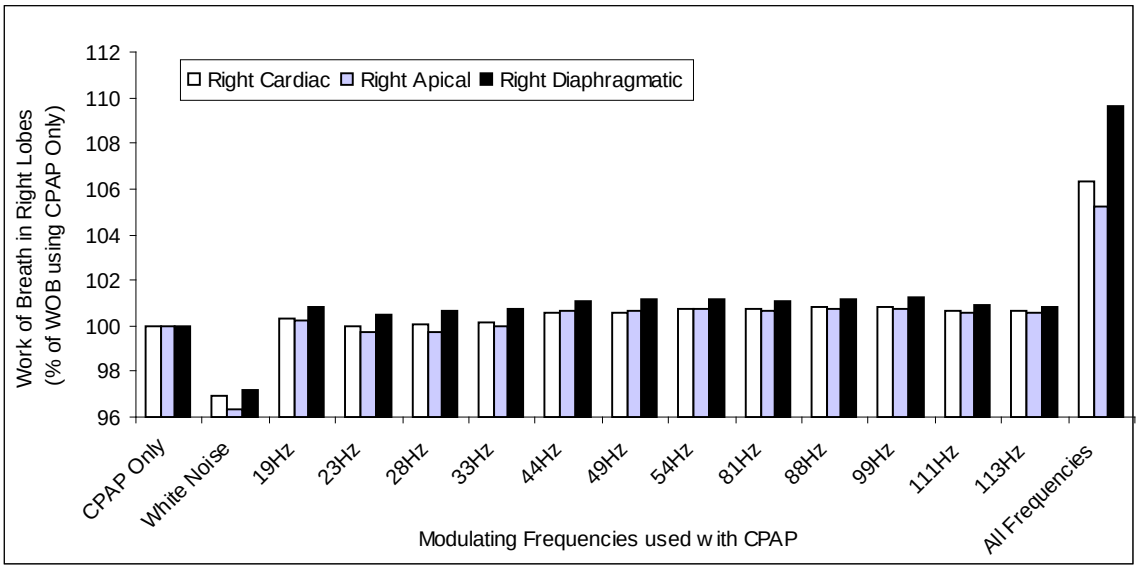

Figure 4.22 WOB (relative to CPAP-only treatment) at the right lobes for a variety of oscillatory treatments on a 128 day gestation lamb.

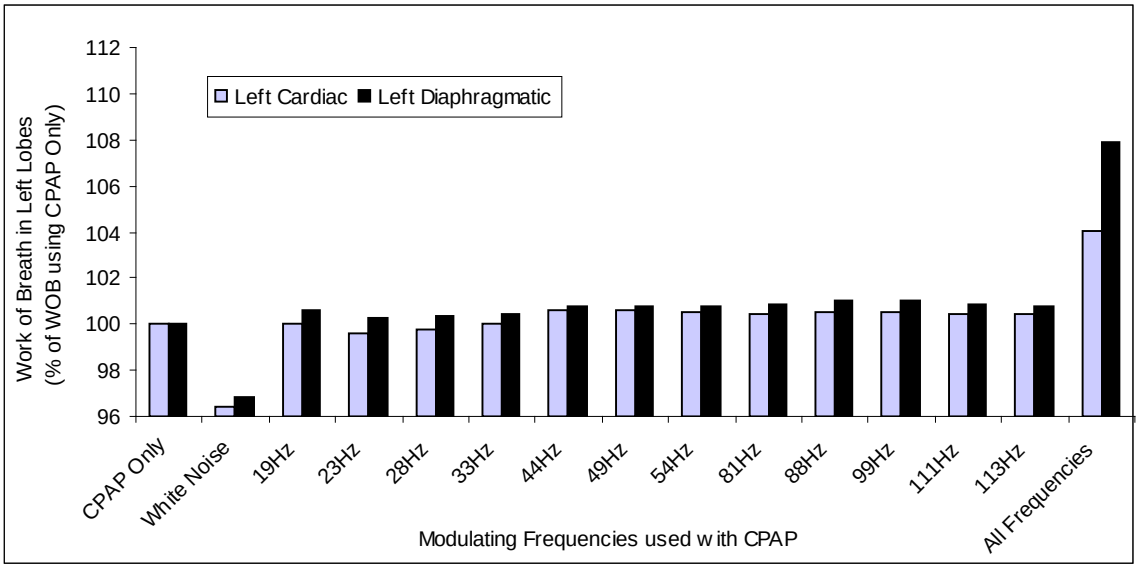

Figure 4.23 WOB (relative to CPAP-only treatment) at the left lobes for a variety of oscillatory treatments on a 128 day gestation lamb.

The greatest increase in WOB is observed when all significant frequencies are combined, showing a 4-10% increase in WOB across all locations. The larger diaphragmatic lobes show a slightly greater percentage increase in WOB when compared to the smaller apical and cardiac lobes.

4.5. Closure

The procedure and results of the animal experiments have been presented in this chapter and compared to the model predictions to validate the model. The calculation of the WOB in the context of this research was described and then the WOB was calculated for both premature (128 day) and near-term (142 day) lungs to establish the baseline and desired WOB. Simulations to determine the effect of adding pressure oscillations on the value of WOB were then performed on the 128 day gestation model to observe the trends towards the WOB value of a 142 day gestation lung. The results generated in this chapter are discussed in Chapter 6.

CHAPTER 5

Surface Tension Model

5.1. Introduction

Surfactant is important at birth because it prevents the lungs from collapsing. Surfactant deficiency is an important cause of RDS in infants. Natural surfactants are currently used in the treatment of RDS but are expensive. Newer, cheaper, effective technologies that can reduce the expense of or optimize surfactant use are sought. This research seeks to determine whether natural surfactant (Curosurf) accompanied with pressure oscillations at the level of the alveoli can reduce the surface tension in the lung, thereby making it easier for the infant to maintain the required level of FRC without collapse.

This chapter contains the complete derivation and numerical methods used to construct the computational model that predicts the effect of using modulated waveforms on the surface tension in the alveoli. The modelling methods follow those of Morris et al. [84, 85]. The discretization, numerical modelling steps and adjustments of adsorption and diffusion parameters needed to be performed by the author and so are shown in this chapter. The model predictions are compared with experiments performed on Curosurf in a PBS which simulates the oscillating air-liquid interface of the alveoli. Section 5.2 presents the derivation of the convection-diffusion equation used to describe the transport of surfactant to the air-liquid interface of the bubble. The boundary conditions and the three regimes of mass transport that govern surfactant movement at the interface are described. The numerical methods are also described with the discretization of all appropriate elements of the model in Section 5.3. Finally, the tri-diagonal matrix, which forms the framework of the model, is presented followed by demonstration of the proper functionality of the model in Section 5.4. Section 5.5 details the equipment setup,

methodology and results of the experimental validation performed using a custom-built PBS. Finally, Section 5.6 compares the minimum and maximum surface tension values during a breath cycle (at different frequencies and amplitudes) measured by experimental results with the model predictions.

5.2. Computational Model Formulation

This section presents the derivation of the computational model illustrating the diffusive convective effects. The surfactant dynamics are also governed by Langmuir kinetics and mass transport phenomena which are explained in detail. The numerical methods applied to solve the convection-diffusion equation are also given. Finally, the functionality of the model is illustrated by comparison with data from the literature.

5.2.1. Convection-Diffusion Equation

An indication of how surfactant will perform physiologically is the variation of surface tension in a small spherical air bubble surrounded by surfactant. As seen in Figure 5.1, the air bubble serves to simulate an alveolus during a breath cycle. The time-varying interface between the bulk liquid and the air bubble is of interest since this simulates the thin film or liquid layer of surfactant coating an alveolus. As the film expands and contracts during the breath cycle, the surfactant molecules move between the bulk liquid and the interface, thereby resulting in a periodic variation of surface tension.

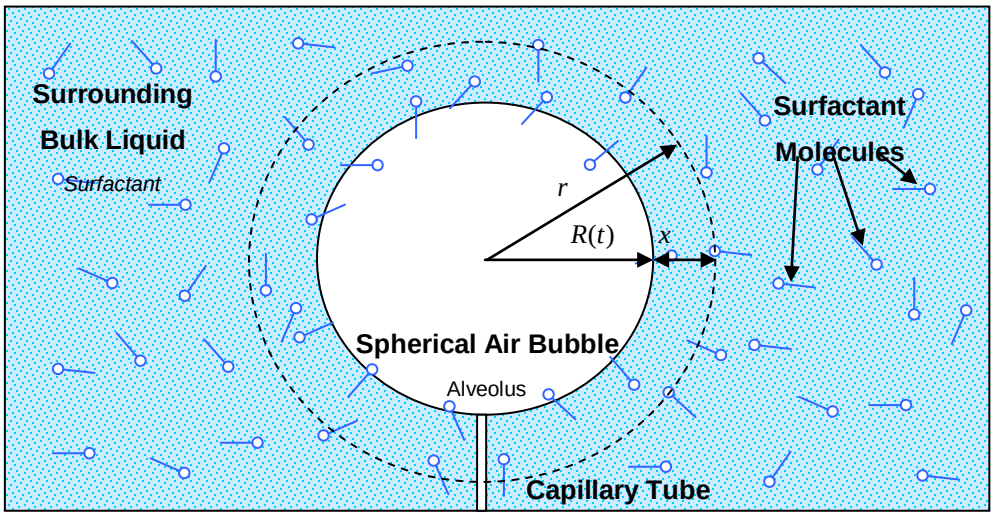

Figure 5.1 Schematic of a bubble in a bulk liquid containing surfactant.

The movement of surfactant molecules to and from the interface is governed by adsorptive and desorptive effects at the interface as well as convective and diffusive effects through the bulk liquid.

Adsorption is the process whereby a molecule forms a bond to a surface. Diffusion is the spontaneous, natural process where a substance diffuses from a region of higher concentration to lower concentration. Convection is the transfer of solute with the current in the fluid. The equations that govern these phenomena are introduced and applied to the situation depicted in Figure 5.1.

The derivation for the convection-diffusion equation based on Fick's second law [103] is well established and presented in Appendix E. Using spherical coordinates, the convection-diffusion equation can be written as

$$\frac{\partial C}{\partial t} + v\frac{\partial C}{\partial r} = D\left[\frac{1}{r^2}\frac{\partial}{\partial r}\left(r^2\frac{\partial C}{\partial r}\right)\right] \qquad \textbf{(5.1)}$$

where C is the concentration (kg.m^{-3}), D is the diffusion coefficient (m^2.s^{-1}), v is the velocity of the fluid (m.s^{-1}) and r is the bubble radius (m). Alternatively, the convection-diffusion expression for spherical co-ordinates can be more descriptively written as [85, 86]

$$\frac{\partial C(r,t)}{\partial t} + v(r,t)\frac{\partial C(r,t)}{\partial r} = D\left[\frac{1}{r^2}\frac{\partial}{\partial r}\left(r^2\frac{\partial C(r,t)}{\partial r}\right)\right] \qquad \textbf{(5.2)}$$

Equation (5.2) is used to model surfactant transport to and from a bulk suspension to the interface of a spherical air bubble.

Working in a coordinate system moving relative to the moving interface, r is the radial distance from the centre of the bubble such that

$$r = x + R(t) \qquad \textbf{(5.3)}$$

where $R(t)$ is the time-varying radius of the bubble and x is the distance into the bulk from the bubble radius $R(t)$.

Substituting equation (5.3) into the equation (5.2) transforms it into the following form [85].

$$\frac{\partial C(x,t)}{\partial t} + v_{rel}(x,t)\frac{\partial C(x,t)}{\partial x} = \frac{D}{\left(x+R(t)\right)^2}\frac{\partial}{\partial x}\left[\left(x+R(t)\right)^2\frac{\partial C(x,t)}{\partial x}\right] \qquad \textbf{(5.4)}$$

To gain an expression for $v_{rel}(x,t)$, a spherical bubble in an infinite amount of liquid is considered.

Working in spherical coordinates and considering conservation of mass for a bubble in an infinite liquid mass requires that [86, 104]

$$v_{rel}(r,t) = \frac{F(t)}{r^2} \qquad \textbf{(5.5)}$$

where $F(t)$ is the force on a rigid particle in the bulk flow.

In the case of an air-liquid interface there is no mass transport across the interface so the relative velocity of the fluid at the bubble radius ($R(t)$) is the same as the velocity of the moving interface, which is expressed as:

$$v_{rel}(R,t) = \frac{F(t)}{R^2(t)} = \frac{dR(t)}{dt} \qquad \textbf{(5.6)}$$

Therefore

$$F(t) = R^2(t)\frac{dR(t)}{dt} \qquad \textbf{(5.7)}$$

Substituting this into equation (5.5) gives

$$v_{rel}(r,t) = \frac{R^2(t)}{r^2}\frac{dR(t)}{dt} \qquad \textbf{(5.8)}$$

An expression for $v_{rel}(x,t)$ can now be obtained as

$$v_{rel}(x,t) = v_{rel}(r,t) - v_{rel}(R,t) = \frac{R^2(t)}{r^2}\frac{dR(t)}{dt} - \frac{dR(t)}{dt} = \left(\frac{R^2(t)}{r^2} - 1\right)\frac{dR(t)}{dt} \qquad \textbf{(5.9)}$$

Substituting $r = x + R(t)$ into equation (5.9), gives

$$v_{rel}(x,t) = \left[\left(\frac{R(t)}{x+R(t)}\right)^2 - 1\right]\frac{dR(t)}{dt} \qquad \textbf{(5.10)}$$

Substituting into equation (5.4) gives the final form of the convection-diffusion equation as

$$\frac{\partial C(x,t)}{\partial t} + \left[\left(\frac{R(t)}{x+R(t)}\right)^2 - 1\right]\frac{dR(t)}{dt}\frac{\partial C(x,t)}{\partial x} = \frac{D}{\left(x+R(t)\right)^2}\frac{\partial}{\partial x}\left[\left(x+R(t)\right)^2\frac{\partial C(x,t)}{\partial x}\right] \qquad \textbf{(5.11)}$$

5.2.2. Initial and Boundary Conditions

An initial condition and two boundary conditions are required to solve equation (5.11).

Initial Condition:

It is assumed that initially (i.e. at $t = 0$), the surfactant concentration is uniform throughout the bulk liquid at a concentration of C_{bulk}:

$$C(x,0) = C_{bulk} \qquad \textbf{(5.12)}$$

Boundary Condition 1:

Since the bulk liquid is modelled as being spatially infinite, the mass transport to and from the interface of the bubble is assumed to have no effect on the concentration far from the bubble interface. The concentration at infinity can be considered to remain at the initial bulk concentration:

$$C(\infty, t) = C_{bulk} \tag{5.13}$$

Boundary Condition 2:

Having established the boundary condition at $x = \infty$, the boundary condition at $x = 0$ i.e at the air-liquid interface is required. The boundary condition is specified as a flux condition and equates the interfacial mass flux to the diffusive mass flux at the surface. Applying Fick's law at the interface

$$J = \frac{\frac{dM}{dt}}{A(t)} = D\frac{\partial C(0,t)}{\partial x} \tag{5.14}$$

J is the diffusive flux and M is the mass of surfactant at the interface given by

$$M = A(t)\Gamma(t) \tag{5.15}$$

where $A(t)$ is the time varying area of the bubble (alveolus) (where $A(t) = 4\pi R^2(t)$) and $\Gamma(t)$ is the interfacial concentration (kg.m^2). Substituting equation (5.15) into (5.14) gives

$$\frac{d\left[A(t)\Gamma(t)\right]}{dt} = A(t)D\frac{\partial C(0,t)}{\partial x} \tag{5.16}$$

$\frac{d[A(t)\Gamma(t)]}{dt}$ represents the mass transport into and out of the interface as is characterized by three different regimes which more accurately describes surfactant transfer in an oscillating bubble.

5.2.3. Regimes of Mass Transport

This section describes the three regimes of mass transport which arise as a result of the established general behaviour of a pulsating surfactant bubble [83, 85]. For clarity, the theory of the general behaviour is first presented in this section, followed by the resulting equations that govern mass transport in these regimes in Section 5.2.4.

The domains of the regimes are defined by the value of $\Gamma(t)$, the interfacial concentration, the equilibrium interfacial concentration (Γ^*) and the maximum interfacial concentration (Γ_{max}). $\Gamma(t)$ is the number of occupied binding sites per unit area by surfactant molecules on the interface of the bubble (as seen in the visual representation of Figure 5.2) and is hence used to calculate the surface tension at the interface (as further illustrated in Section 5.2.5).

Starting at A in Figure 5.2 and following a clockwise direction, the bubble is compressed till point E and then expanded from E to A. For a clearer understanding, the bubbles are also marked as a percentage of the maximum interfacial area such that bubble A is at 100%, bubble B is at 99% of the maximum interfacial area and so forth. These percentages are typical values but change for different types of surfactant, concentrations and cycling times. The regimes which arise from the interfacial concentration $\Gamma(t)$ are noted at each labelled bubble.

The locations of the three regimes on a typical surface tension-area ($\gamma - A$) loop can be seen in Figure 5.3. The $\gamma - A$ loop is a typical surface tension vs. area relationship for an air bubble surrounded in a bulk fluid carrying surfactant which can be derived from experiments on a PBS or previous mathematical models.

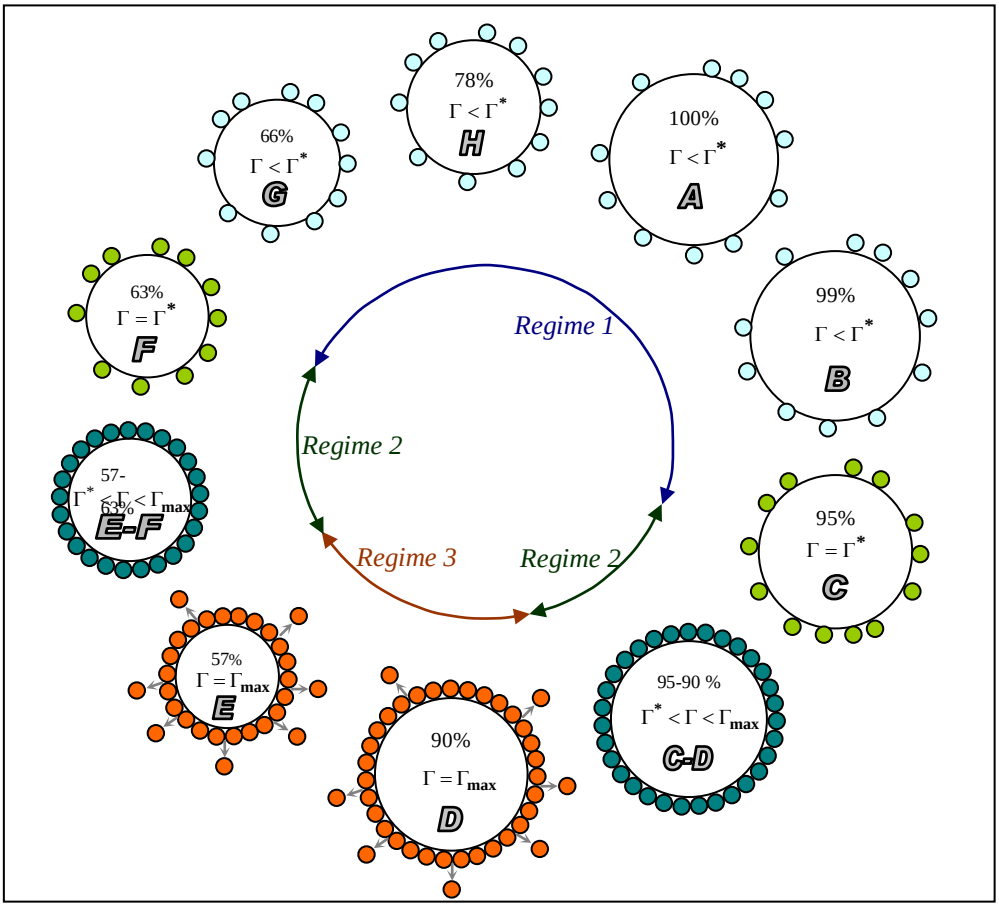

Figure 5.2 Visual representation of the interfacial concentration $\Gamma(t)$.

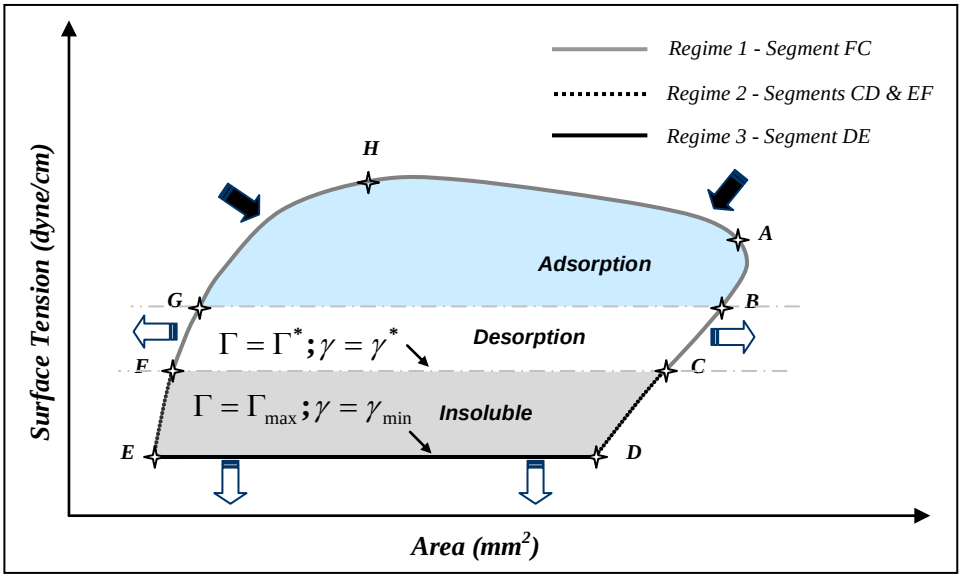

Figure 5.3 The locations of the three regimes on the $\gamma - A$ ***loop [83, 85].***

The arrows normal to the loop indicate whether the mass flux moves into or out of the interface during different regimes or parts thereof. The black arrows indicate an influx of surfactant to the bubble interface and the white arrows indicate an efflux, such that the net flux into or out of the interface is zero, making the $\gamma - A$ loop representative of a steady state process.

Each regime and the relationship between the interfacial concentration and surface tension are described more in depth as follows:

Regime 1

Following a clockwise fashion, regime 1 corresponds to the surface tensions on the curve in Figure 5.3 from F to C. The corresponding pictograms of $\Gamma(t)$ at points F, G, H, A, B and C are shown in Figure 5.2.

At equilibrium (points F and C) there is a maximum number of binding sites that can be occupied at the interface and is known as Γ^* (defined the maximum interfacial concentration that corresponds to a minimum equilibrium surface tension γ^* measurement for a particular value of C_{bulk} determined by equilibrium measurements on a PBS. Hence, the first regime is said to occur when $\Gamma < \Gamma^*$.

Γ is directly related to the surface tension γ. A greater amount of surfactant molecules at the interface (a larger Γ) means that there is a greater disruption of the attracting forces of the liquid molecules at the interface (a smaller γ). Hence, when Γ approaches Γ^*, γ approaches γ^*, which is known as the minimum equilibrium surface tension (line FC in Figure 5.3).

Regime 2

Regime 2 occurs in two parts of the $\gamma - A$ loop (CD and EF). Here, $\Gamma(t)$ exceeds Γ^* due to dynamic compression of the interface during the cycling of the area A. The surfactant molecules are packed so tightly that it can be considered to be an insoluble monolayer (as seen in Figure 5.3 in bubbles C-D and E-F). However $\Gamma(t)$ is still less than Γ_{max}, which is the maximum interfacial concentration possible i.e. the most dense

packing of surfactant molecules possible in a monolayer. Hence, regime 2 occurs when $\Gamma^* < \Gamma < \Gamma_{max}$.

Regime 3

In the third regime (segment DE), when $\Gamma(t)$ reaches the value of Γ_{max} the surface tension reaches a minimum value γ_{min}. In this regime the surfactant molecules are packed as tightly as possible and a further compression of the interface results in a "squeeze out" of extra surfactant molecules into the bulk. This squeeze-out of extra molecules means that the interfacial concentration remains at Γ_{max} while the area decreases from point D to E such that $\Gamma = \Gamma_{max}$ and $\gamma = \gamma_{min}$ for the segment DE.

5.2.4. Mass transport equations for each regime

Regime 1

Since regime 1 occurs when $\Gamma < \Gamma^*$, mass transport is governed by adsorption and desorption of surfactant molecules to and from the interface as well as the subsurface concentration C_s. This can be expressed using the following Langmuir relationship [82, 83, 105]:

$$\frac{d\left[A(t)\Gamma(t)\right]}{dt} = \frac{dM}{dt} = A\left[k_1 C_s\left(\Gamma^* - \Gamma\right) - k_2\Gamma\right] \qquad \textbf{(5.17)}$$

where k_1 is the adsorption coefficient and k_2 is the desorption coefficient.

Regime 2

Since the surfactant behaves as an insoluble monolayer in this regime, there is no mass transport to and from the interface, so that

$$\frac{d\left[A(t)\Gamma(t)\right]}{dt} = \frac{dM}{dt} = 0 \qquad \textbf{(5.18)}$$

Regime 3

Since $\Gamma = \Gamma_{max}$ in regime 3, the rate of change of mass at the interface can be considered to be:

$$\frac{d\left[A(t)\Gamma(t)\right]}{dt} = \frac{dM}{dt} = \frac{d\left[A(t)\Gamma_{max}\right]}{dt} = \Gamma_{max}\left[\frac{dA}{dt}\right] \qquad \textbf{(5.19)}$$

An expression for Γ_{max}/Γ^* is found by inserting $\gamma = \gamma_{min}$ into the isotherm equation (equation (5.23)), which is described in the following section. To summarize, the mass flux at the interface for the three different regimes, gives the following equation

$$\left.\begin{array}{lll} \dfrac{d\left[A(t)\Gamma(t)\right]}{dt} = A\left[k_1 C_s\left(\Gamma^* - \Gamma\right) - k_2\Gamma\right] & \text{when} & \Gamma < \Gamma^* \\ \dfrac{d\left[A(t)\Gamma(t)\right]}{dt} = 0 & \textit{when} & \Gamma^* < \Gamma < \Gamma_{max} \\ \dfrac{d\left[A(t)\Gamma(t)\right]}{dt} = \Gamma_{max}\left[\dfrac{dA}{dt}\right] & \text{when} & \Gamma = \Gamma_{max} \end{array}\right\} \qquad \textbf{(5.20)}$$

Equation (5.20) along with the convection-diffusion equation (equation (5.11)) and the equations describing the initial and boundary conditions (equations (5.12), (5.13) and (5.16)) will be quantitatively determined after using the numerical methods in Section 5.3.

5.2.5. Isotherm

The relationship between the normalized interfacial concentration Γ/Γ^* and the surface tension γ is found from an isotherm which is assumed to be a function of only interfacial concentration. This is described in Otis et al. [83], Morris et al. [85] and Morris [84] and summarized here as follows.

The isotherm is defined by two linear slopes, m_1 and m_2 as seen in Figure 5.4 which reflects the change of surface tension at the interface of the bubble as a function of the surfactant coverage at the interface.

Slope m_1 occurs during regime 1 where the surface tension lies between points corresponding to $\Gamma/\Gamma^* = 0$ and $\Gamma/\Gamma^* = 1$. The surface tension at $\Gamma/\Gamma^* = 0$ is the surface tension of pure water, γ_0 and the surface tension at $\Gamma/\Gamma^* = 1$ is the maximum equilibrium surface tension of the surfactant.

A linear form of the isotherm was assumed as a simple and reasonable approximation of the surface tension. The surface tension in regime 1 is thus expressed as

$$\gamma = \gamma_0 - m_1 \frac{\Gamma}{\Gamma^*} \qquad \textbf{(5.21)}$$

and m_1 can be simply expressed as $m_1 = \gamma_0 - \gamma^*$. Otis et al. [83] derived an expression for m_2 based upon average experimental $\gamma - A$ data. The resulting expression for m_2 is

$$m_2 = \frac{\left(\gamma^* - \gamma_{\min}\right)}{\left(1 - \frac{A^*}{A_{\gamma_{\min}}}\right)} \qquad \textbf{(5.22)}$$

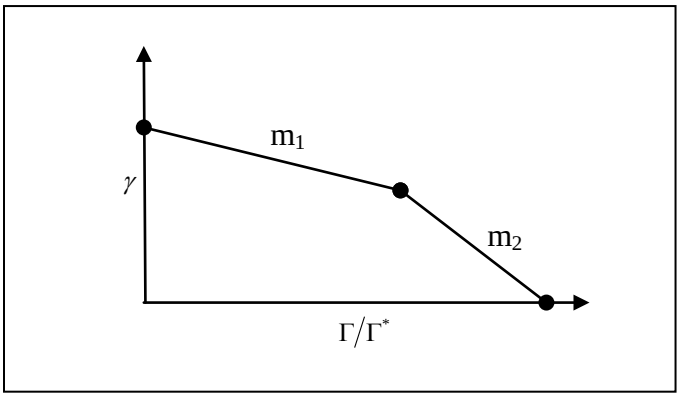

Figure 5.4 Isotherm relating surface tension (γ) to surface concentration (Γ/Γ^*) of surfactant.

where A^* and $A_{\gamma_{\min}}$ are the interfacial areas corresponding to γ^* at the onset of regime 2 compression and $\gamma_{\min}$ at the end of regime 2 compression respectively. These occur at points C and D in Figures 5.2 and 5.3. The surface tension relationship for regime 2 is

$$\gamma = \gamma^* - m_2\left(\frac{\Gamma}{\Gamma^*} - 1\right) \qquad \textbf{(5.23)}$$

5.3. Numerical Solution

In this section the partial differential equations that specify the mass transport of surfactant molecules to and from the bubble interface are solved using numerical methods. Numerical methods have been used in the literature to successfully model oscillatory surfactant dynamics [83, 85, 86].

This work follows the method proposed by Morris [84] where a control volume approach is used where the bulk is spatially discretized into nodes with each node at the centre of a control volume. The implicit Euler scheme [106, 107] is used to simultaneously approximate the future values of all nodes at the next time step (referred to herein as the n+1st time step) by using a system of linear equations.

5.3.1. Discretization of Time

An appreciation of how time is discretized in the model is shown in Figure 5.5 as bubble displacement vs. the number of time steps per cycle (N_{SC}) where the bubble is cycled from a minimum to maximum displacement and back to the minimum value.

T_{cycle} is the time taken for a cycle and hence is equal to $1/\omega$, where ω is the cycling frequency. N_{SC} is chosen as 1000 (the smallest value that was found to produce accurate results) [84] . Δt is the time step and is set to be $1/N_{SC}\,\omega$.

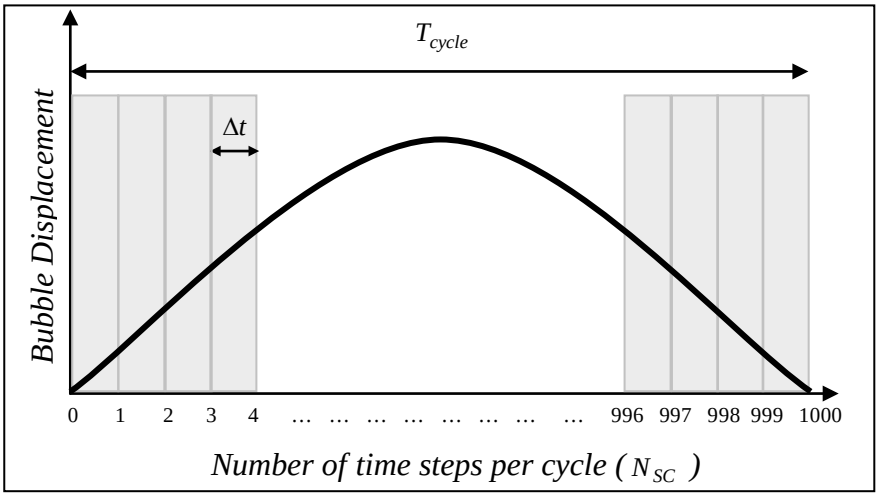

Figure 5.5 Discretization of time.

5.3.2. Discretization of Space

A one dimensional discretization of the space is shown in Figure 5.6. The bulk is discretized into an i amount of nodes that are Δx apart. The 0^{th} and 1^{st} (subsurface) nodes are located at a distance $\Delta x/2$ from the interface such that during the subsequent numerical procedures, the interfacial flux occurs at the midpoint of the 0^{th} and 1^{st} nodes, allowing a more accurate and elegant solution.

The distance x_i is the distance between the interface and the i^{th} node and is given by

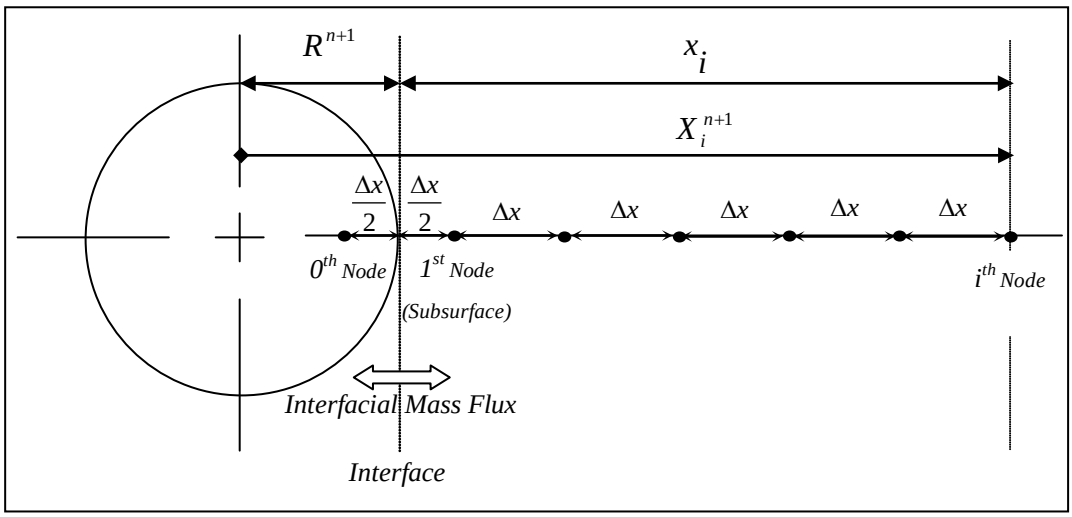

Figure 5.6 Discretization of space.

$$x_i = \left(i - \frac{1}{2} \right) \Delta x \qquad \textbf{(5.24)}$$

At the n+1st time step, the bubble radius is R^{n+1} and the distance from the centre of the bubble to the i^{th} node is

$$X^{n+1} = R^{n+1} + x_i \qquad \textbf{(5.25)}$$

Next, we define the spatial increment Δx as half the characteristic diffusion length l_D, (the distance travelled by the surfactant molecules for a time step of Δt). l_D can thus be expressed as

$$l_D = \sqrt{D \Delta t} \qquad \textbf{(5.26)}$$

where D is the diffusion coefficient with the units of cm^2/s and so

$$\Delta x = \frac{\sqrt{D \Delta t}}{2} \qquad \textbf{(5.27)}$$

By making the mesh size smaller than the diffusion length, we ensure that the mesh size is small enough to resolve the computations necessary to describe the diffusion process.

The number of special nodes N_{SN} is related to the depth of the bulk L_∞ by the relationship $N_{SN} = L_\infty / \Delta x$. The depth of the bulk L_∞ is chosen to be 5 times the adsorptive length (l_A) or diffusive characteristic length (l_D), whichever is larger for the process. This can all be expressed as

$$N_{SN} = \frac{L_\infty}{\Delta x} = \frac{5 \times \left(l_D \text{ or } l_A \right)}{\Delta x} \qquad \textbf{(5.28)}$$

We now find individual expressions for $\frac{l_D}{\Delta x}$ and $\frac{l_A}{\Delta x}$.

If t is the total time of the simulation and N_C is the number of cycles in the simulation, then the total time of the simulation can also be expressed as $t = N_{SC} N_C \Delta t$, such that

$$\frac{l_D}{\Delta x} = \frac{\sqrt{Dt}}{\Delta x} = \frac{\sqrt{DN_{SC} N_C \Delta t}}{\Delta x} = \frac{\sqrt{DN_{SC} N_C \Delta t}}{\sqrt{D\Delta t}/2} = 2\sqrt{N_{SC} N_C} \qquad \textbf{(5.29)}$$

Since $\frac{\sqrt{Dt}}{\Delta x} = 2\sqrt{N_{SC} N_C}$,

$$\frac{1}{\Delta x} = \frac{2\sqrt{N_{SC} N_C}}{\sqrt{Dt}} = \frac{2\sqrt{N_{SC} N_C}}{\sqrt{DN_{SC} N_C \Delta t}} = \frac{2\sqrt{N_{SC}}}{D/\omega} \qquad \textbf{(5.30)}$$

$\frac{l_A}{\Delta x}$ can now be evaluated as

$$\frac{l_A}{\Delta x} = \frac{1}{\Delta x}\frac{\Gamma^*}{C_{bulk}} = \frac{2\sqrt{N_{SC}}}{D/\omega}\frac{\Gamma^*}{C_{bulk}} \qquad \textbf{(5.31)}$$

A new operator $\|A, B\|$ is defined, to denote the greater of A and B, so N_{SN} can be expressed as

$$N_{SN} = 5 \times \left(2\sqrt{N_{SC}}\right) \times \left\| \sqrt{N_C}, \frac{1}{D/\omega}\frac{\Gamma^*}{C_{bulk}} \right\| \qquad \textbf{(5.32)}$$

5.3.3. Discretization of Bubble Dimensions

The bubble volume $V(t)$ is prescribed for the model as in equation (5.33) and is shown in Figure 5.7. The volumes in Figure 5.7 can be related to those of the alveoli during a typical breath cycle as follows:

$$V(t) = V_{\text{mean}} + \frac{V_{\text{cycle}}}{2}\sin\left(2\pi\omega t - \frac{\pi}{2}\right) \qquad \textbf{(5.33)}$$

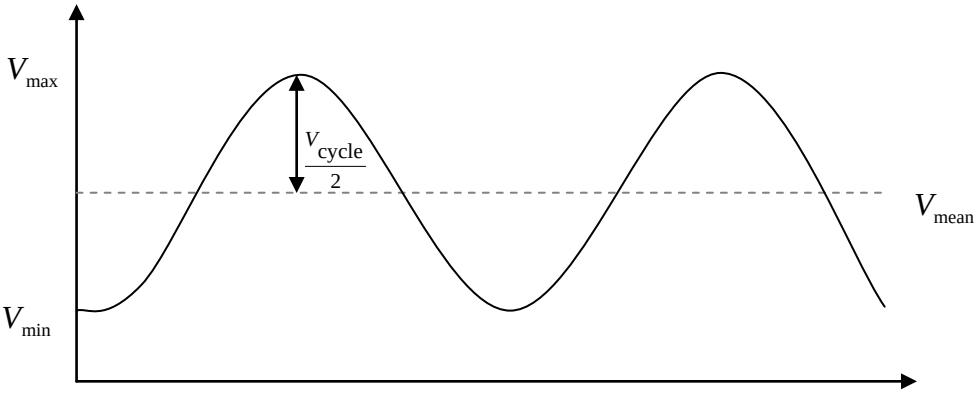

Figure 5.7 Discretization of bubble dimensions.

- V_{min} is the volume of an alveolus when the lung volume is at FRC.
- V_{cycle} is the cyclic volume change that the alveoli goes through during the TV of the lung.
- V_{max} is the volume of an alveoli when the lung is at FRC+TV.
- V_{mean} can be expressed as FRC + 0.5TV.

The discretized form of the bubble volume is

$$V^n = V_{\text{mean}} + \frac{V_{\text{cycle}}}{2}\sin\left(2\pi\omega\Delta t - \frac{\pi}{2}\right) \qquad \textbf{(5.34)}$$

where V^n is the volume at the n^{th} time step, $V^n = \frac{4}{3}\pi\left(R^n\right)^3$. Using the assumption that the bubble follows spherical geometry and behaviour, the radius R^n and interfacial area A^n can be calculated as $R^n = \sqrt[3]{\frac{3V_n}{4\pi}}$ and $A^n = 4\pi(R^n)^2$ respectively.

5.3.4. Discretization of Cross-sectional Area

Mass flux between two adjacent nodes passes through the surface area at the midpoint of the nodes as noted in Figure 5.8. The notations in Figure 5.8 are explained as follows:

- The surface area at the midpoint of nodes *i* and *i+1* at the n+1st time step is denoted by $A_{i,i+1}^{n+1}$.
- The surface area at the midpoint of nodes *i* and *i-1* at the n+1st time step is denoted by $A_{i,i-1}^{n+1}$.
- The surface area at node *i* at the n+1st time step is denoted by $A_{i,i}^{n+1}$ or more succinctly as A_i^{n+1}.
- The interfacial surface area at the n+1st time step is denoted by $A_{1,0}^{n+1}$ or more succinctly as A^{n+1} in subsequent operations.

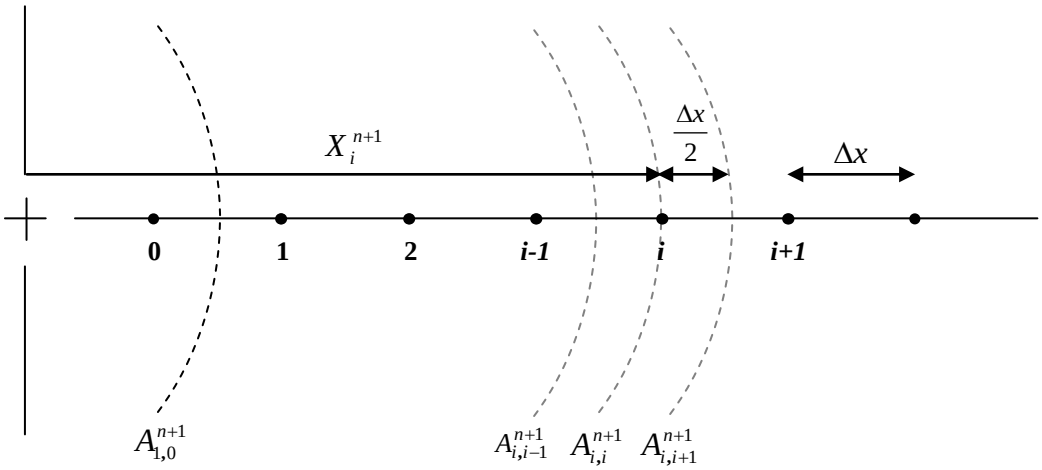

Figure 5.8 Discretization of the cross sectional area.

Following the relationship of spherical geometry, the discretized equations for the area are

$$\left.\begin{aligned} A_{i,i-1}^{n+1} &= 4\pi\left(X_i^{n+1} - \frac{\Delta x}{2}\right)^2 \\ A_{i,i}^{n+1} &= A_{i,i}^{n+1} = 4\pi\left(X_i^{n+1}\right)^2 \\ A_{i,i+1}^{n+1} &= 4\pi\left(X_i^{n+1} + \frac{\Delta x}{2}\right)^2 \end{aligned}\right\} \qquad \textbf{(5.35)}$$

5.3.5. Discretization of the Diffusion Equation

Here, the convection-diffusion equation is discretized using the implicit Euler scheme [106, 107] with a control volume approach. The centred-finite difference formulas are used to discretize the equations. Both the convection and diffusion terms are dealt with. An upwind scheme [107] is necessary to better approximate the convection term.

Preliminary Derivation

A three grid-point cluster for a one dimensional control volume approach is shown in Figure 5.9. It is used to define the concentration at each node where:

- C_i is the concentration at the i^{th} node
- C_{i+1} is the concentration on the east side (the positive direction)
- C_{i-1} is the concentration on the west side (the negative direction)
- C_{bot} is the concentration at the midpoint of C_{i-1} and C_i
- C_{top} is the concentration at the midpoint of C_i and C_{i+1}
- v_{relbot} is the relative velocity between the fluid and the moving interface at midpoint of C_{i-1} and C_i
- v_{reltop} is the relative velocity between the fluid and the moving interface at the midpoint of C_i and C_{i+1}

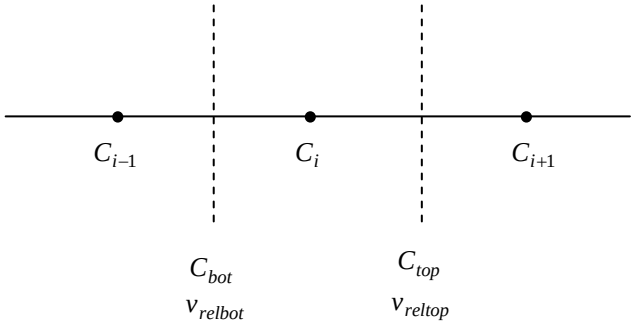

Figure 5.9 A three grid-point cluster for a one dimensional control volume approach.

The governing differential equation is

$$\frac{\partial C}{\partial t} + v_{rel}\frac{\partial C}{\partial x} = D\frac{\partial^2 C}{\partial x^2} \qquad \textbf{(5.36)}$$

It follows now to discretize each term of equation (5.36) by using the notations in the three grid-point cluster. For the first term,

$$\frac{\partial C}{\partial t} \approx \frac{C_i^{n+1} - C_i^{\,n}}{\Delta t} \qquad \textbf{(5.37)}$$

One could assume that the concentration at the midpoint of adjacent nodes (which is in fact the interface of the control volume) is the average value of the concentration of the two adjacent nodes, C_{top} and C_{bot}. However, it has been reported that using this assumption will only be able to produce realistic results for low Reynolds numbers and may cause the solution to diverge and thus to seek a better formulation, the upwind scheme (also known as the upwind difference scheme, the upstream-difference scheme, the donor-cell method, etc) [107] is employed.

A better prescription is presented by the upwind difference scheme by assuming that the value of the concentration *C* at the control volume interface is equal to the value of *C* at the grid point on the upwind side of the face.

C_{top} and C_{bot} can thus be reformulated as

$$C_{top} = C_{i+1} \quad \text{when} \quad v_{reltop} < 0 \tag{5.38}$$

$$C_{top} = C_i \quad \text{when} \quad v_{reltop} > 0 \tag{5.39}$$

$$C_{bot} = C_i \quad \textit{when} \quad v_{relbot} < 0 \tag{5.40}$$

$$C_{bot} = C_{i-1} \quad \textit{when} \quad v_{relbot} > 0 \tag{5.41}$$

Recalling a previously introduced operator $\|A,B\|$, which denotes the greater of A and B, the upwind scheme can be more compactly written as:

$$v_{reltop} C_{top} = C_i \left\| v_{reltop}, 0 \right\| - C_{i+1} \left\| - v_{reltop}, 0 \right\| \tag{5.42}$$

$$v_{relbot} C_{bot} = C_{i-1} \left\| v_{relbot}, 0 \right\| - C_i \left\| - v_{relbot}, 0 \right\| \tag{5.43}$$

For the second term, using the centred-finite difference formula for the first derivative, gives

$$v_{rel} \frac{\partial C}{\partial x} \approx v_{reltop} \frac{C_{top}}{\Delta x} - v_{relbot} \frac{C_{bot}}{\Delta x} \tag{5.44}$$

For the third term, using the centred-finite difference formula for the second derivative, gives

$$D \frac{\partial^2 C}{\partial x^2} = \frac{D_{i+1}\left(C_{i+1}^{n+1} - C_i^{n+1}\right)}{\Delta x^2} - \frac{D_{i-1}\left(C_i^{n+1} - C_{i-1}^{n+1}\right)}{\Delta x^2} \tag{5.45}$$

Collecting all the terms, the discretized governing equation now becomes

$$\frac{C_i^{n+1} - C_i^{\,n}}{\Delta t} + v_{reltop}\frac{C_{top}}{\Delta x} - v_{relbot}\frac{C_{bot}}{\Delta x} = \frac{D_{i+1}\left(C_{i+1}^{n+1} - C_i^{n+1}\right)}{\Delta x^2} - \frac{D_{i-1}\left(C_i^{n+1} - C_{i-1}^{n+1}\right)}{\Delta x^2} \qquad \textbf{(5.46)}$$

To arrange the equation more compactly, both sides of the equation are multiplied by Δt to obtain

$$C_i^{n+1} - C_i^{\,n} + v_{reltop}C_{top}\frac{\Delta t}{\Delta x} - v_{relbot}C_{bot}\frac{\Delta t}{\Delta x} = \frac{D_{i+1}\left(C_{i+1}^{n+1} - C_i^{n+1}\right)\Delta t}{\Delta x^2} - \frac{D_{i-1}\left(C_i^{n+1} - C_{i-1}^{n+1}\right)\Delta t}{\Delta x^2} \qquad \textbf{(5.47)}$$

The equation can be further simplified by setting $\alpha = \frac{D\Delta t}{\Delta x^2}$. This is known as the dimensionless diffusion coefficient. For present purposes, the diffusion coefficient is assumed to be constant since the bulk is assumed to be well mixed such that

$$\alpha = \frac{D_{i+1}\Delta t}{\Delta x^2} = \frac{D_{i-1}\Delta t}{\Delta x^2} \qquad \textbf{(5.48)}$$

to get the following

$$C_i^{n+1} - C_i^{\,n} + v_{reltop}C_{top}\frac{\Delta t}{\Delta x} - v_{relbot}C_{bot}\frac{\Delta t}{\Delta x} = \alpha\left(C_{i+1}^{n+1} - C_i^{n+1}\right) - \alpha\left(C_i^{n+1} - C_{i-1}^{n+1}\right) \qquad \textbf{(5.49)}$$

and consequently by substituting in equations (5.42) and (5.43), we get

$$C_i^{n+1} - C^{n} + C_i^{\,n+1}\left\|v_{reltop},0\right\|\frac{\Delta t}{\Delta x} - C_{i+1}^{n+1}\left\|- v_{reltop},0\right\|\frac{\Delta t}{\Delta x}$$

$$- C_{i-1}^{n+1}\left\|v_{relbot},0\right\|\frac{\Delta t}{\Delta x} + C_i^{n+1}\left\|- v_{relbot},0\right\|\frac{\Delta t}{\Delta x} = \alpha C_{i+1}^{n+1} - \alpha C_i^{n+1} - \alpha C_i^{n+1} + \alpha C_{i-1}^{n+1} \qquad \textbf{(5.50)}$$

At this point, the volume flow rate is defined as Q, such that

$$v_{reltop} = \frac{Q_{i+1}^{n+1}}{A_{i,i+1}^{n+1}} \qquad \textit{and} \qquad v_{relbot} = \frac{Q_{i-1}^{n+1}}{A_{i,i-1}^{n+1}} \tag{5.51}$$

Collecting all like terms in equation (5.50), gives

$$C_i^{n+1} - C_i^n + C_i^{n+1}\left(\left\| v_{reltop}, 0 \right\| \frac{\Delta t}{\Delta x} + - \left\| v_{relbot}, 0 \right\| \frac{\Delta t}{\Delta x} + \alpha + \alpha \right)$$

$$= C_{i+1}^{n+1}\left(\alpha + \left\| - v_{reltop}, 0 \right\| \frac{\Delta t}{\Delta x} \right) + C_{i-1}^{n+1}\left(\alpha + \left\| v_{relbot}, 0 \right\| \frac{\Delta t}{\Delta x} \right) \tag{5.52}$$

Since

$$\left(\alpha + \left\| - v_{reltop}, 0 \right\| \frac{\Delta t}{\Delta x} \right) \approx v_{reltop} = \frac{Q_{i+1}^{n+1}}{A_{i,i+1}^{n+1}} \tag{5.53}$$

and

$$\left(\alpha + \left\| v_{relbot}, 0 \right\| \frac{\Delta t}{\Delta x} \right) \approx v_{reltbot} = \frac{Q_{i-1}^{n+1}}{A_{i,i-1}^{n+1}} \tag{5.54}$$

Equation (5.52) can be simplified to read

$$\Delta C_i + C_i^{n+1}\left(v_{reltop} + v_{relbot} \right) = C_{i+1}^{n+1} v_{reltop} + C_{i-1}^{n+1} v_{relbot} \tag{5.55}$$

Substituting the values of $v_{reltop} = \frac{Q_{i+1}^{n+1}}{A_{i,i+1}^{n+1}}$ and $v_{relbot} = \frac{Q_{i-1}^{n+1}}{A_{i,i-1}^{n+1}}$ into equation (5.55), gives

$$\Delta C_i + C_i^{n+1} \frac{Q_{i+1}^{n+1}}{A_{i,i+1}^{n+1}} + C_i^{n+1} \frac{Q_{i-1}^{n+1}}{A_{i,i-1}^{n+1}} = C_{i+1}^{n+1} \frac{Q_{i+1}^{n+1}}{A_{i,i+1}^{n+1}} + C_{i-1}^{n+1} \frac{Q_{i-1}^{n+1}}{A_{i,i-1}^{n+1}} \tag{5.56}$$

Assuming that the surface area at node *i* is approximately equal to the areas located at the midpoint between the two nodes on either side of it,

$$A_i^{n+1} = A_{i,i-1}^{n+1} = A_{i,i+1}^{n+1} \tag{5.57}$$

This allows equation (5.56) to be simplified to

$$A_i^{n+1}\Delta C_i + C_i^{n+1}Q_{i+1}^{n+1} + C_i^{n+1}Q_{i-1}^{n+1} = C_{i+1}^{n+1}Q_{i+1}^{n+1} + C_{i-1}^{n+1}Q_{i-1}^{n+1} \tag{5.58}$$

By definition

$$C_i^{n+1} = C_i^n + \Delta C_i \qquad C_{i+1}^{n+1} = C_{i+1}^n + \Delta C_i \qquad C_{i-1}^{n+1} = C_{i-1}^n + \Delta C_i \tag{5.59}$$

So equation (5.58) can be rewritten as

$$A_i^{n+1}\Delta C_i + C_i^n Q_{i+1}^{n+1} + \Delta C_i Q_{i+1}^{n+1} + C_i^n Q_{i-1}^{n+1} + \Delta C_i Q_{i-1}^{n+1} = C_{i+1}^n Q_{i+1}^{n+1} + \Delta C_{i+1} Q_{i+1}^{n+1} + C_{i-1}^n Q_{i-1}^{n+1} + \Delta C_{i-1} Q_{i-1}^{n+1} \tag{5.60}$$

Collecting all like terms, the final discretized form of the convection-diffusion equation is

$$-Q_{i-1}^{n+1}\Delta C_{i-1} + \left(Q_{i-1}^{n+1} + A_i^{n+1} + Q_{i+1}^{n+1}\right)\Delta C_i - Q_{i+1}^{n+1}\Delta C_{i+1} = Q_{i-1}^{n+1}C_{i-1}^n - \left(Q_{i-1}^{n+1} + Q_{i+1}^{n+1}\right)C_i^n + Q_{i+1}^{n+1}C_{i+1}^n \tag{5.61}$$

$Q\Delta C$ is the mass flux between adjacent nodes with the units of kg/s.

5.3.6. Defining the Volume Flow Rate

To define the *Q* terms (Q_{i+1}^{n+1} and Q_{i-1}^{n+1}) in equation (5.61), the relationships in equations (5.53) and (5.54) are recalled to arrive at

$$Q_{i+1}^{n+1} = A_{i,i+1}^{n+1}\left(\alpha + \left\|- v_{reltop},0\right\|\frac{\Delta t}{\Delta x}\right) \qquad and \qquad Q_{i-1}^{n+1} = A_{i,i-1}^{n+1}\left(\alpha + \left\|v_{relbot},0\right\|\frac{\Delta t}{\Delta x}\right) \quad \textbf{(5.62)}$$

5.3.7. The Dimensionless Diffusion Coefficient

Because the spatial increment is set as $\Delta x = \frac{\sqrt{D\Delta t}}{2}$, then

$$\frac{D\Delta t}{\Delta x^2} = 4 = \alpha \quad \textbf{(5.63)}$$

Therefore, the dimensionless diffusion coefficient α has a set value of 4.

5.3.8. Discretization of Relative Velocities

The relative velocity is given by equation (5.10) in terms of x and $R(t)$. To define the relative velocity in terms of area, both sides of the equation are multiplied by 4π as follows

$$4\pi v_{rel} = 4\pi\left[\left(\frac{R(t)}{x+R(t)}\right)^2 - 1\right]\frac{dR}{dt} \quad \textbf{(5.64)}$$

so that

$$v_{rel} = \left[\frac{4\pi}{4\pi}\left(\frac{R(t)}{x+R(t)}\right)^2 - \frac{4\pi}{4\pi}\times 1\right]\frac{dR}{dt} = \left[\frac{4\pi R^2(t)}{4\pi\left[x+R(t)\right]^2} - 1\right]\frac{dR}{dt} \quad \textbf{(5.65)}$$

The term $4\pi R^2(t)$ represents the surface area at the interface and $4\pi\left[x+R(t)\right]^2$ represents the surface area at node *i* as seen Figure 5.10(a). To gain a discretized expression of v_{reltop} and v_{relbot} using equation (5.65), we use the notation in Figure 5.10 (b) to gain v_{reltop} and v_{relbot} in terms of $A_{i,i+1}^{n+1}$ and $A_{i,i-1}^{n+1}$ respectively.

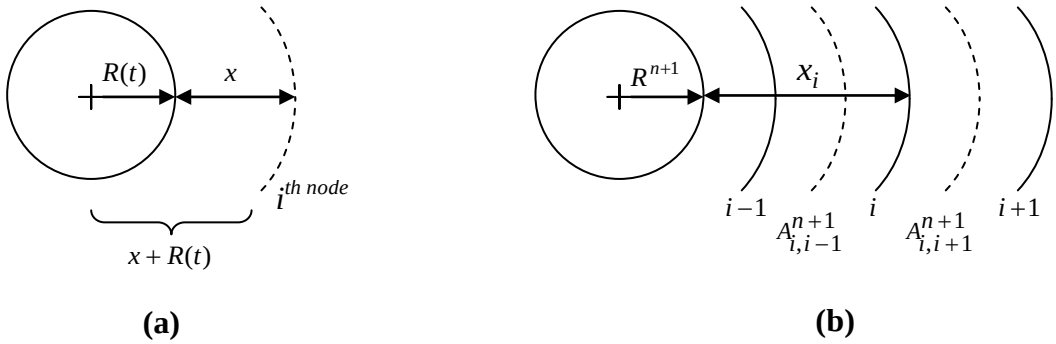

Figure 5.10. Notations used to discretize relative velocities.

Thus at $A_{i,i+1}^{n+1}$

$$v_{reltop} = \left[\frac{4\pi\left(R^{n+1}\right)^2}{A_{i,i+1}^{n+1}} - 1 \right] \frac{dR}{dt} \tag{5.66}$$

and at $A_{i,i-1}^{n+1}$

$$v_{relbot} = \left[\frac{4\pi\left(R^{n+1}\right)^2}{A_{i,i-1}^{n+1}} - 1 \right] \frac{dR}{dt} \tag{5.67}$$

To gain a physical appreciation, it is worthy to note that at the interface $A_{1,0}^{n+1} = 4\pi\left(R^{n+1}\right)^2$ such that the relative velocity of the fluid is zero as shown in equation (5.68).

$$v_{rel} = \left[\frac{4\pi\left(R^{n+1}\right)^2}{A_{1,0}^{n+1}} - 1 \right] \frac{dR}{dt} = \left[\frac{4\pi\left(R^{n+1}\right)^2}{4\pi\left(R^{n+1}\right)^2} - 1 \right] \frac{dR}{dt} = 0 \tag{5.68}$$

Also, for nodes far away from the interface, the area is much larger than that of the interface such that the term $\frac{4\pi R^{n+1}}{A^{n+1}}$ approaches 0 and hence $v_{rel} = -\frac{dR}{dt}$.

5.3.9. Discretization of the Boundary Conditions

Using Figure 5.11, the boundary condition at the interface (equation (5.16)) is discretized.

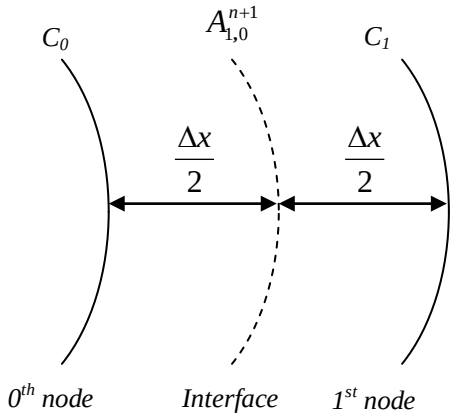

Figure 5.11 Discretization at the interface.

The mass flux across the interfacial area $A_{1,0}^{n+1}$ can be expressed as

$$\frac{\Delta M}{\Delta t} = A_{1,0}^{n+1} D \frac{\partial C(0,t)}{\partial x} = A_{1,0}^{n+1} \frac{\alpha \Delta x^2}{\Delta t} \frac{\partial C(0,t)}{\partial x} \qquad \textbf{(5.69)}$$

where

$D = \frac{\alpha \Delta x^2}{\Delta t}$ from the previously established relationship in equation (5.48).

Using the central difference approximation for the first derivative, the term $\frac{\partial C(0,t)}{\partial x}$ is discretized as

$$\frac{\partial C}{\partial x} = \frac{C_1^{n+1} - C_0^{n+1}}{2\left(\frac{\Delta x}{2}\right)} = \frac{C_1^{n+1} - C_0^{n+1}}{\Delta x} \qquad \textbf{(5.70)}$$

noting that in this case, the spatial increment between the interface and the two adjacent nodes, nodes 0 and 1, is $\frac{\Delta x}{2}$ as seen Figure 5.11.

$$\frac{\Delta M}{\Delta t} = A_{1,0}^{n+1} \frac{\alpha \Delta x^2}{\Delta t} \left(\frac{C_1^{n+1} - C_0^{n+1}}{\Delta x} \right) = A_{1,0}^{n+1} \frac{\alpha \Delta x}{\Delta t} \left(C_1^{n+1} - C_0^{n+1} \right) \quad \textbf{(5.71)}$$

and so

$$\Delta M = A_{1,0}^{n+1} \alpha \Delta x \left(C_1^{n+1} - C_0^{n+1} \right) \quad \textbf{(5.72)}$$

which can be rearranged as follows

$$\frac{\Delta M}{\Delta x} = A_{1,0}^{n+1} \alpha \left(C_1^{n+1} - C_0^{n+1} \right) \quad \textbf{(5.73)}$$

then the right hand side is equal to the flux term between the 0th and 1st nodes. The flux term between the 0th and 1st nodes is also contained in equation (5.61) (the discretized convection-diffusion equation) for the case of i=1.

Looking at equation (5.61), we substitute for i=1 to get

$$-Q_0^{n+1} \Delta C_0 + \left(Q_0^{n+1} + A_1^{n+1} + Q_2^{n+1} \right) \Delta C_1 - Q_2^{n+1} \Delta C_2 = Q_0^{n+1} C_0^n - \left(Q_0^{n+1} + Q_2^{n+1} \right) C_1^n + Q_2^{n+1} C_2^n \quad \textbf{(5.74)}$$

Collecting all terms containing Q_0 to the left hand side, reveals

$$\left(-Q_0^{n+1} \Delta C_0 + Q_0^{n+1} \Delta C_1 - Q_0^{n+1} C_0^n + Q_0^{n+1} C_1^n \right) + \left(A_1^{n+1} + Q_2^{n+1} \right) \Delta C_1 - Q_2^{n+1} \Delta C_2 = Q_2^{n+1} \left(C_2^n - C_1^n \right) \quad \textbf{5.75)}$$

Rearranging, gives

$$-Q_0^{n+1}\left(C_0^n+\Delta C_0\right)+Q_0^{n+1}\left(C_1^n+\Delta C_1\right)+\left(A_1^{n+1}+Q_2^{n+1}\right)\Delta C_1-Q_2^{n+1}\Delta C_2=Q_2^{n+1}\left(C_2^n-C_1^n\right) \quad \textbf{(5.76)}$$

and subsequently

$$Q_0^{n+1}\left(C_1^{n+1}-C_0^{n+1}\right)+\left(A_1^{n+1}+Q_2^{n+1}\right)\Delta C_1-Q_2^{n+1}\Delta C_2=Q_2^{n+1}\left(C_2^n-C_1^n\right) \quad \textbf{(5.77)}$$

where the term $Q_0^{n+1}\left(C_1^{n+1}-C_0^{n+1}\right)$ is actually the flux term between the 0th and 1st nodes. Equating this to equation (5.73), gives

$$Q_0^{n+1}\left(C_1^{n+1}-C_0^{n+1}\right)=A_{1,0}^{n+1}\alpha\left(C_1^{n+1}-C_0^{n+1}\right)=\frac{\Delta M}{\Delta x} \quad \textbf{(5.78)}$$

Substituting $\frac{\Delta M}{\Delta x}$ into equation (5.77) gives the final discretized form as

$$\frac{\Delta M}{\Delta x}+\left(A_1^{n+1}+Q_2^{n+1}\right)\Delta C_1-Q_2^{n+1}\Delta C_2=Q_2^{n+1}\left(C_2^n-C_1^n\right) \quad \textbf{(5.79)}$$

5.3.10. Discretization of the equations describing the three regimes

Regime 1 – Langmuir Regime

The Langmuir equation as seen in equation (5.20) can be simply discretized as

$$\frac{\Delta M}{\Delta t}=A^{n+1}\left[k_1C_1^{n+1}\left(\Gamma^*-\Gamma^{n+1}\right)-k_2\Gamma^{n+1}\right] \quad \textbf{(5.80)}$$

where C_s which is the subsurface concentration is actually substituted for C_1^{n+1} in the discretization since it represents the same quantity at the n+1st time step.

As it stands, equation (5.80) cannot be solved in an implicit scheme because it contains the non-linear product between the subsurface concentration C_1^{n+1} and interfacial mass

($M^{n+1} = \Gamma^{n+1} A^{n+1}$). A linearization needs to be done where the terms C_1^{n+1} and M^{n+1} are expressed in terms of the present time value plus the change in that value going to the next time step, such that $C_1^{n+1} = \left(C_1^n + \Delta C_1\right)$ and $M^{n+1} = \left(M^n + \Delta M\right)$.

Expanding equation (5.80) gives

$$\frac{\Delta M}{\Delta t} = A^{n+1} k_1 C_1^{n+1} \Gamma^* - A^{n+1} k_1 C_1^{n+1} \Gamma^{n+1} - A^{n+1} k_2 \Gamma^{n+1}$$
$$= A^{n+1} k_1 C_1^{n+1} \Gamma^* - M^{n+1} k_1 C_1^{n+1} - M^{n+1} k_2$$
$$= A^{n+1} k_1 \Gamma^* \left(C_1^n + \Delta C_1\right) - \left(M^n + \Delta M\right) k_1 \left(C_1^n + \Delta C_1\right) - \left(M^n + \Delta M\right) k_2 \qquad \textbf{(5.81)}$$

Isolating term $-\left(M^n + \Delta M\right) k_1 \left(C_1^n + \Delta C_1\right)$ and simplifying, gives

$$-\left(M^n + \Delta M\right) k_1 \left(C_1^n + \Delta C_1\right) = \left(-k_1 M^n - k_1 \Delta M\right)\left(C_1^n + \Delta C_1\right)$$
$$= -k_1 M^n C_1^n - k_1 \Delta M C_1^n - k_1 M^n \Delta C_1 - k_1 \Delta M \Delta C_1 \qquad \textbf{(5.82)}$$

Neglecting the second order term $-k_1 \Delta M \Delta C$ and collecting like terms reveals the term to be $-k_1\left(M^n C_1^n + \Delta M C_1^n + M^n \Delta C_1\right)$. Substituting this back into equation (5.81), and expanding gives

$$\frac{\Delta M}{\Delta t} = A^{n+1} k_1 \Gamma^* \left(C_1^n + \Delta C_1\right) - k_1\left(M^n C_1^n + \Delta M C_1^n + M^n \Delta C_1\right) - \left(M^n + \Delta M\right) k_2$$

$$= A^{n+1} k_1 \Gamma^* C_1^n + A^{n+1} k_1 \Gamma^* \Delta C_1 - k_1 M^n C_1^n - k_1 \Delta M C_1^n - k_1 M^n \Delta C_1 - k_2 M^n - k_2 \Delta M \qquad \textbf{(5.83)}$$

Collecting like terms reveals the final form of the equation

$$\left[\frac{1}{\Delta t} + k_1 C_1^n + k_2\right] \Delta M - \left[k_1\left(\Gamma^* A^{n+1} - M^n\right)\right] \Delta C_1 = k_1 C_1^n \left(\Gamma^* A^{n+1} - M^n\right) - k_2 M^n \qquad \textbf{(5.84)}$$

Regime 2 – No Mass Transport

From equation (5.20), the mass transport for regime 2 is described by

$$\frac{dM}{dt} = 0 \qquad \textbf{(5.85)}$$

A discretization of equation (5.85) is simply

$$\Delta M = 0 \qquad \textbf{(5.86)}$$

Regime 3 – "Squeeze Out" Regime

From equation (5.20), the mass transport equation for regime 3 is

$$\frac{dM}{dt} = \Gamma_{\max} \frac{dA}{dt} \qquad \textbf{(5.87)}$$

A discretization of equation (5.87) is

$$\frac{\Delta M}{\Delta t} = \frac{\Delta A}{\Delta t} \Gamma_{\max} \qquad \textit{where} \qquad \Delta A = A^{n+1} - A^{n} \qquad \textbf{(5.88)}$$

so that

$$\Delta M = A^{n+1}\Gamma_{\max} - A^{n}\Gamma_{\max} = A^{n+1}\Gamma_{\max} - A^{n}\Gamma \qquad \textbf{(5.89)}$$

The discretization of the equations governing mass transport in the three regimes can be expressed as

$$\begin{cases} \left[\frac{1}{\Delta t} + k_1 C_1^n + k_2\right]\Delta M - \left[k_1\left(\Gamma^* A^{n+1} - M^n\right)\right]\Delta C_1 = k_1 C_1^n\left(\Gamma^* A^{n+1} - M^n\right) - k_2 M^n & \Gamma < \Gamma^* \\ \Delta M = 0 & \Gamma^* \le \Gamma < \Gamma_{\max} \\ \Delta M = A^{n+1}\Gamma_{\max} - A^n \Gamma & \Gamma = \Gamma_{\max} \end{cases} \quad \textbf{(5.90)}$$

5.3.11. Solution of the Tri-diagonal Matrix

The discretized equations governing diffusion and the boundary conditions are assembled into a tri-diagonal matrix [108]. Equation (5.90) is the first line of the matrix followed by equation (5.79) in the second line. This followed by *m*-1 equations (where *m* is the number of spatial nodes) of the form in equation (5.61). The last row of the matrix incorporates the boundary condition at infinity which is always at C_{bulk} and so there is no change in the concentration hence $\Delta C_m = 0$.

The equation is shown in equation (5.91) for the first regime. For the second and third regimes, the first row of equation (5.91) is changed to equations (5.92) and (5.93) respectively. The vector of unknowns to be solved is $[\Delta M,\ \Delta C_1,\ \Delta C_2,\ \cdots,\ \Delta C_m]$ and is added to the vector of current time values to produce the future time vector of concentrations at which point all matrices are recalculated and the loop begins again. The computational model is solved in Matlab, the numerical code of which is attached in Appendix F.

$$\begin{bmatrix} \frac{1}{\Delta t}+k_1C_1^n+k_2 & k_1\left(\Gamma^* A^{n+1}-M^n\right) & 0 & 0 & 0 & \cdots \\ \frac{1}{x} & A_1^{n+1}+Q_2^{n+1} & -Q_2^{n+1} & 0 & 0 & \cdots \\ 0 & -Q_1^{n+1} & Q_1^{n+1}+A_2^{n+1}+Q_3^{n+1} & -Q_3^{n+1} & 0 & \cdots \\ & & \ddots & & & \\ \cdots & 0 & 0 & -Q_{m-2}^{n+1} & Q_{m-2}^{n+1}+A_{m-1}^{n+1}+Q_m^{n+1} & -Q_m^{n+1} \\ \cdots & 0 & 0 & 0 & 0 & 1 \end{bmatrix} \begin{bmatrix} \Delta M \\ \Delta C_1 \\ \Delta C_2 \\ \vdots \\ \Delta C_{m-1} \\ \Delta C_m \end{bmatrix}$$

$$= \begin{bmatrix} k_1C_1^n\left(\Gamma^* A^{n+1}-M^n\right)-k_2M^n \\ Q_2^{n+1}\left(C_2^n-C_1^n\right) \\ Q_1^{n+1}C_1^n-\left[Q_1^{n+1}+Q_3^{n+1}\right]C_2^n+Q_3^{n+1}C_3^n \\ \vdots \\ Q_{m-2}^{n+1}C_{m-2}^n-\left[Q_{m-2}^{n+1}+Q_m^{n+1}\right]C_{m-1}^n+Q_m^{n+1}C_m^n \\ 0 \end{bmatrix} \qquad \textit{(5.91)}$$

$$\begin{bmatrix} 1 & 0 & 0 & \cdots \end{bmatrix}\begin{bmatrix} \Delta M \end{bmatrix} = \begin{bmatrix} 0 \end{bmatrix} \qquad \textit{(5.92)}$$

$$\begin{bmatrix} 1 & 0 & 0 & \cdots \end{bmatrix}\begin{bmatrix} \Delta M \end{bmatrix} = \left[A^{n+1}\Gamma_{\max}-A^n\Gamma\right] \qquad \textit{(5.93)}$$

5.4. Model Validation

To validate the model, the numerical code in Appendix F was applied to match the experimental data of Schurch et al. [87] where a bubble was oscillated in a 1 mg/ml solution of Curosurf. The model parameters used in the simulation (Table 5.1.) were adopted from Morris [84] who successfully used the model to match the same set of data from Schurch et al. [87].

The results of the simulation and the comparison to the experimental data by Schurch et al. [87] i.e. the $\gamma - A$ loops at steady state are shown in Figure 5.12. The present code shows a similar match of the experimental data to that of Morris [84], thus demonstrating proper function of the Matlab code.

Table 5.1 Model parameters used by Morris [84] to match experimental data of Schurch et al [87].

Parameter	*Value*	*Units*
ω	20	cycles/min
C_{bulk}	1	mg/ml
γ^*	25	dyn/cm
$\gamma_{\min}$	1	dyn/cm
m_2	100	dyn/cm
D	1×10^{-9}	cm^2/sec
k_1	0.07×10^5	ml/(g.min)
k_1/k_2	1.2×10^5	ml/g
Γ^*	3×10^{-7}	g/cm^2
$m_1 = \gamma_{water} - \gamma^*$	70 – 25= 45	dyn/cm
$\Gamma_{\max} = \Gamma^*[1+(\gamma^* - \gamma_{\min})/m_2]$	$3x10^{-7}[1+(25-1)/100] = 3.72x10^{-7}$	g/cm^2

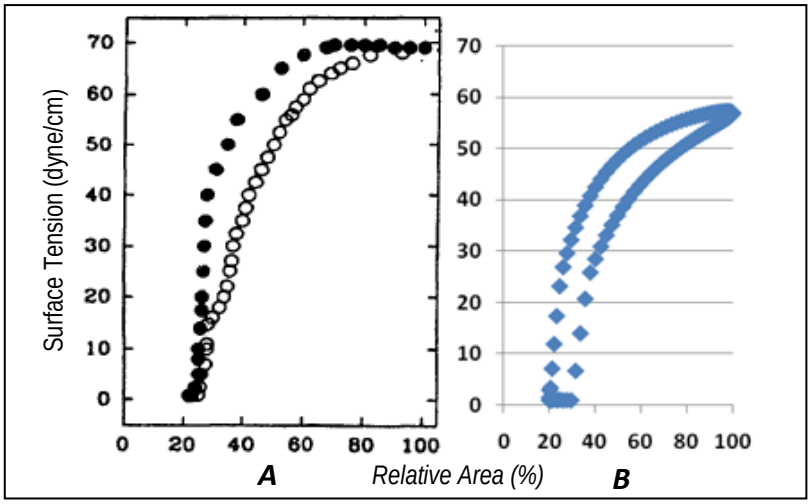

Figure 5.12 Comparison of $\gamma - A$ loops at steady state for (A) experimental data from Schurch et al .[87] , (B) match of Schurch data using computational model.

5.5. Experiments on Curosurf using Modulated Frequencies

Previous experiments on Curosurf [87] have only been done on cycling frequencies in the order of breathing frequencies. Commercial PBS devices to date have therefore been designed to have pumps that deliver the oscillating tidal volume and software and camera resolutions to suit [83, 86, 87, 109]. Since the present study uses oscillating frequencies that are beyond the range of commercial pump, camera and software

operation, a custom built surfactometer had to be made. The aim of the experimentation was to determine the surface tension of an oscillating bubble immersed in a surfactant solution thus simulating surface tension dynamics in the alveoli under the following conditions:

- ***Oscillation at a breathing frequency of 0.5 Hz and V_{min}/V_{max} of 70%***

  V_{min}/V_{max} is the ratio of the minimum volume over the maximum volume. These values were chosen to represent the breath cycle of a 142 day gestation lamb where the tidal volume (TV) = 8 ml/kg during mechanical ventilation as in Pillow et al. [95] and FRC is the value at 5 cm H_2O in the pressure-volume curves of the samples collected in Chapter 3. A V_{min}/V_{max} ratio smaller than 70% saw the bubble disappearing into the tube and so restricted the possibility of testing different V_{min}/V_{max} ratios with the current setup.

- ***Oscillation at a breathing frequency of 0.5 Hz and V_{min}/V_{max} of 70% + Modulated Frequencies***

  Frequencies from 10-70 Hz were chosen for the study to represent the range of frequencies present in the Bubble CPAP System under normal operating conditions. Frequencies were tested from 10 to 70 Hz at 10 Hz intervals at 3 amplitudes i.e. 15% of TV, 22.5% of TV and 30% of TV. Modulated amplitudes above 30% of TV caused the bubble to become unstable and detach.

Table 5.2 details the conditions of each experiment (each of which was repeated thrice). The breath cycle frequency and the breath cycle V_{min}/V_{max} ratio were kept constant for all experiments at 0.5 Hz and 70% respectively. The experiments were performed at 39^oC to represent the core temperature of newborn lambs.

Table 5.2 Experimental details.

Experiment Name	Modulating Frequency (Hz)	Modulating Amplitude (%TV)
Breath Cycle	0	0
F10-A15	10	15
F10-A22.5	10	22.5
F10-A30	10	30
F20-A15	20	15
F20-A22.5	20	22.5
F20-A30	20	30
F30-A15	30	15
F30-A22.5	30	22.5
F30-A30	30	30
F40-A15	40	15
F40-A22.5	40	22.5
F40-A30	40	30
F50-A15	50	15
F50-A22.5	50	22.5
F50-A30	50	30
F60-A15	60	15
F60-A22.5	60	22.5
F60-A30	60	30
F70-A15	70	15
F70-A22.5	70	22.5
F70-A30	70	30

5.5.1. Experimental Equipment and Setup

The schematic diagram of the complete experimental setup is shown in Figure 5.13 and a photograph of the actual setup is shown in Figure 5.14.

The bubble chamber is the focus of the experiment and is shown in closer detail in Figure 5.15(a) and (b). The bubble chamber consists of a 2 ml transparent cuvette containing a surfactant solution with a small air gap. The cuvette has a flat surface to avoid optical distortion of the bubble as is common with cylindrical bubble chambers. LED backlighting is used to light up the bubble from behind for the best contrast during bubble monitoring. A rubber plug is used to create an airtight seal through which two needles are inserted; (1) the ‘Bubble Needle’ an 18 gauge non-bevelled needle on which

the bubble is attached and oscillates and (2) the 'Adjuster Needle' an 18 gauge bevelled needle used to create the initial bubble size by sucking out air in the cuvette with a syringe.

A thermocouple wire is also inserted through the plug to a depth which allows the tip to be well immersed in the surfactant solution. Resistive heating elements and conductive paste are placed on the sides of the cuvette and clamped to an aluminium stand. The thermocouple wire and resistive heating elements are connected to a custom made temperature controller accurate to 0.5 ^{o}C in the range of 1-100 ^{o}C.

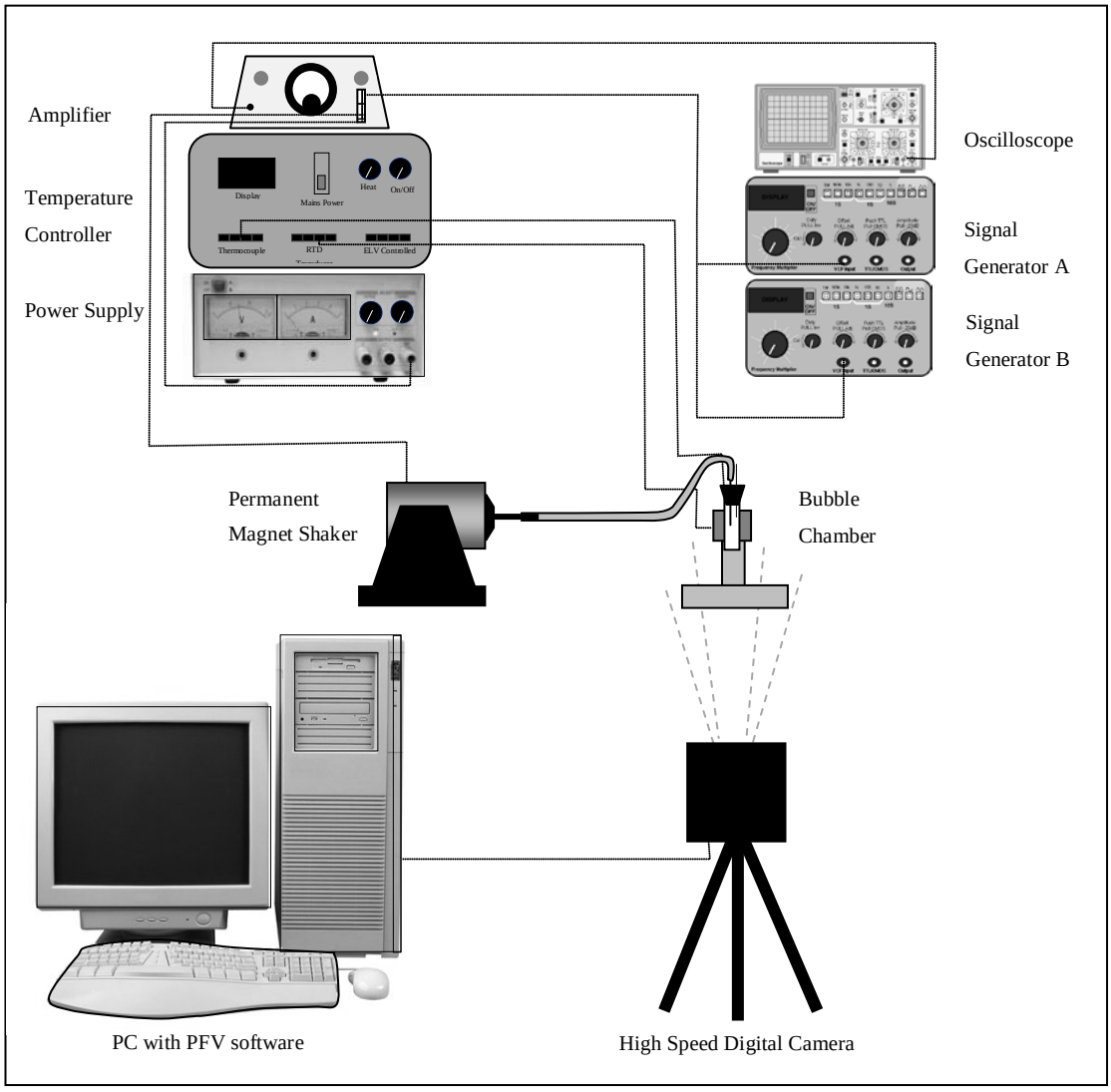

Figure 5.13 Schematic diagram of experimental setup.

A 1.6 mm diameter piston is attached to a permanent magnet shaker (V201/3, LDS, Middleton, WI, USA) and inserted into a flexible tube that attaches to the bubble needle as seen in Figure 5.16. Thick petroleum jelly is used to successfully create an airtight seal with minimal friction.

The permanent magnet shaker is used to deliver the waveforms to simulate neonatal breathing frequencies and the modulated frequencies from 10-70 Hz used in the experiments.

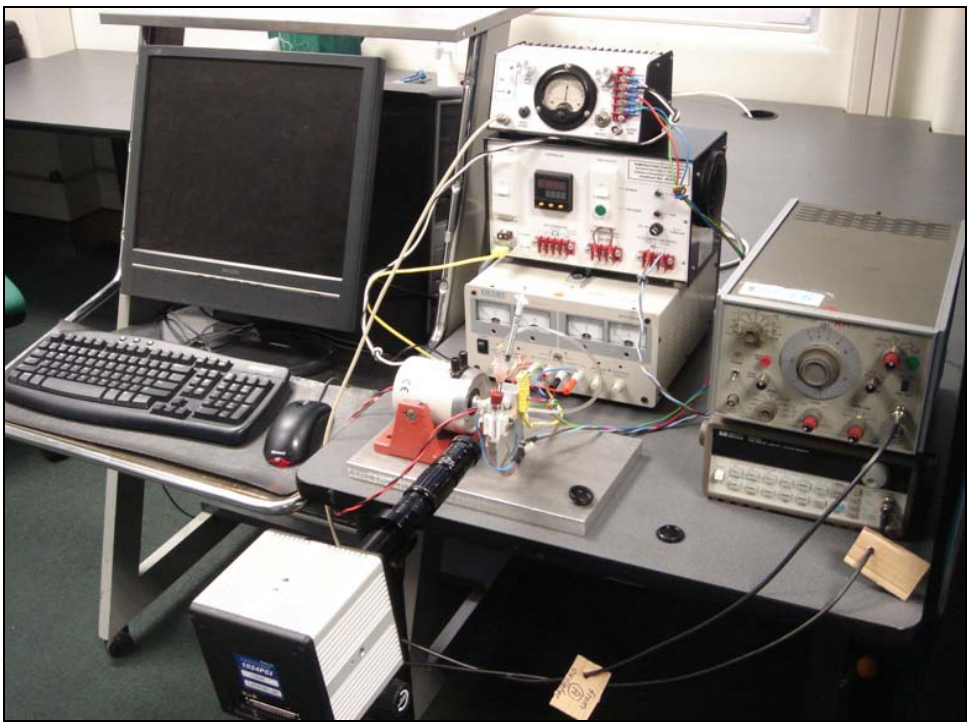

Figure 5.14 Photograph of experimental setup.

A custom-built power amplifier (Figure 5.13) is used to extend the usable frequency range of the permanent magnet shaker from 5-13000 Hz to 0-13000 Hz to accommodate for the low cycling frequency used simulate breathing frequency i.e. 0.5 Hz.

The shaker is driven by the two function generators i.e. Model 5300A (Krohn-Hite, Brockton, MA, USA) and Model 33120A (Hewlett Packard, Englewood, Colorado, USA). An oscilloscope (TDS1012, Tektronix, Oregon, USA) was used to view the driving waveforms from the function generators. A regulated DC power supply (EPS-

3030D, Escort, Taiwan) is used to power the shaker via the power amplifier as well as the LED and resistive heating element (Figure 5.15).

A high speed digital video camera (FASTCAM 1024 PCI, Photron, San Diego, CA, USA) with a long distance microscope (KC/S InFocus™, Infinity, Boulder, USA) shown in Figure 5.17 where used to digitally monitor the bubble oscillations. The Photron Fastcam Viewer (PFV) software was used to capture the digital images which were capable of being used in Matlab to measure the bubble dimensions during data processing.

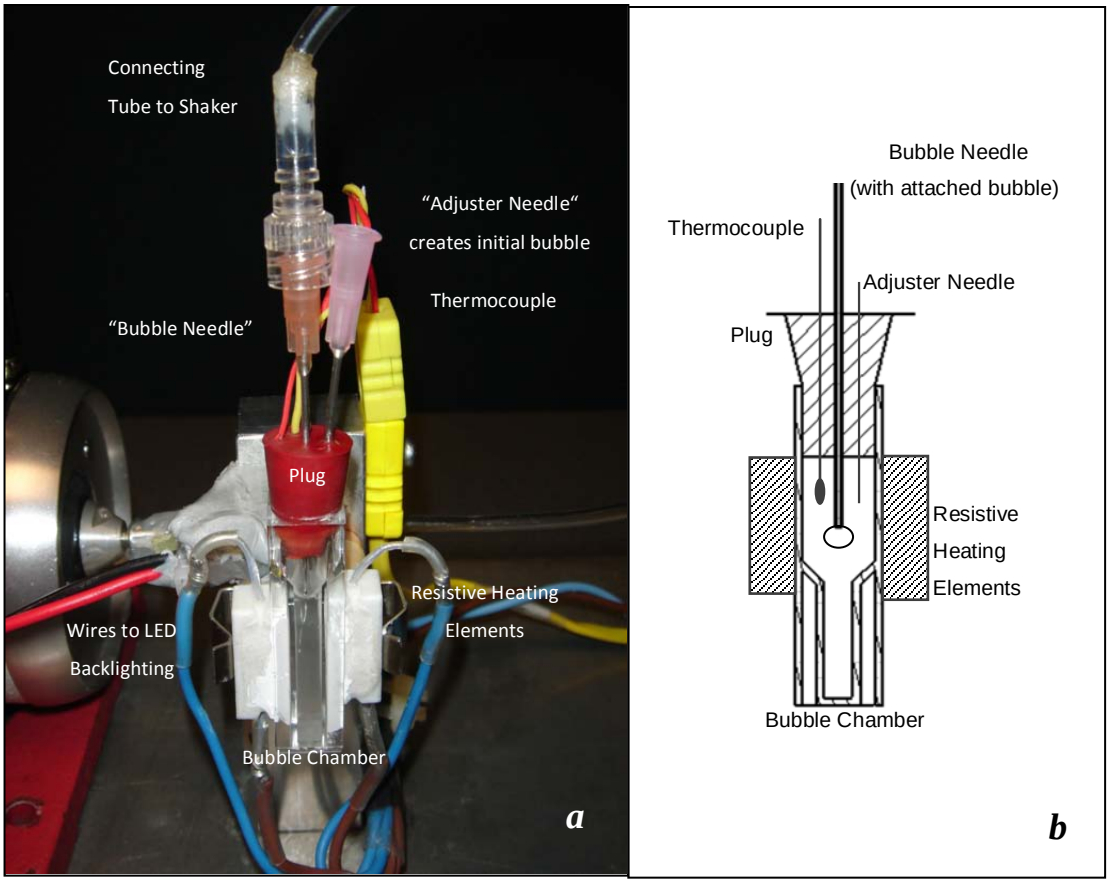

Figure 5.15 Bubble chamber.

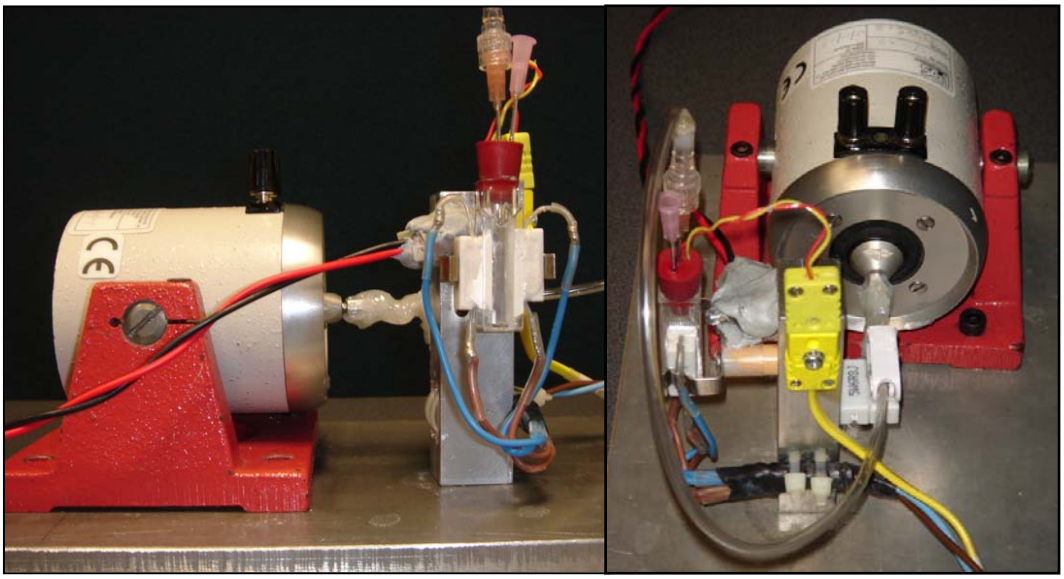

Figure 5.16 Permanent magnet shaker.

Figure 5.17 Photron high speed digital camera and long distance microscope.

5.5.2. Experimental Methodology

The following methodology was performed for each experiment outlined in Table 5.2. After setting up the equipment, the sampling rate of the high speed camera was set to 1000 frames per second (fps) and the shutter speed was set to 1/frame second and the screen resolution to 640 x 528 pixels. This produced the optimal optical contrast and sampling period achievable for the given sampling rate of 1000 fps with the available equipment.

Curosurf was supplied as a 80 mg/ml suspension in a 3 ml vial. Surfactant was withdrawn from the vial with a sterile needle and mixed to the required concentration of 0.5 mg/ml with normal saline (0.9% NaCl) solution. Concentrations greater than 0.5 mg/ml rendered the solution too murky to produce distinct bubble edges in the captured images.

The density of the surfactant solution was measured at 39^{o}C. The solution was then transferred to the bubble chamber and the plug (containing the needles and thermocouple) put in place. The temperature controller was then switched on and the solution was then heated up to 39^{o}C.

Care was taken to ensure that the needle was vertical, the thermocouple wire was not interfering with the bubble motion and that the backlight was set such that the background was as white as possible and the bubble as black as possible to get the best bubble contrast.

The dial on the amplifier was calibrated by performing a few preliminary measurements so that the cycling amplitude was set to generate a V_{min}/V_{max} ratio of 70%.

Keeping the switch on the amplifier which sends the signal to the shaker off, the frequency and amplitude of oscillation was set at the function generator according to the values specified in Table 5.2 for the particular experiment.

The image was calibrated to the bubble needle by measuring the diameter in pixels on the screen since the needle diameter is known. An initial bubble was created by withdrawing air out of the bubble chamber with the adjuster needle. The bubble size was set to 1.5 times the tube diameter. A few preliminary trials showed that an initial bubble size larger than this value caused the bubble to detach during oscillation when the maximum area was reached. Bubble sizes smaller than this value caused the bubble to become too small during oscillation and the bubble would disappear into the bubble needle.

After creating an initial bubble size, the bubble was left to adsorb for 3 minutes to allow the bubble to reach equilibrium. The cycling was then started by turning on the switch on the amplifier to the shaker.

The bubble was cycled for 20 cycles to reach steady state as determined by Schurch et al. [87]. The images were then recorded on the PFV software for as long as the memory on the computer allowed with the chosen camera settings, which was approximately 7 seconds.

The digital images of the bubble were then analysed in a custom generated code (See Appendix G) in Matlab which measured the diameter of the bubble in both the x and y axes. The surface tension was calculated by another code in Matlab (See Appendix H) which was based on the numerical solutions provided by Graves et al. [110] that allow one to relate the shape of a deformed bubble to the surface tension [33, 110].

5.5.3. Experimental Results

Minimum and maximum surface tension for the purposes of this study are defined as the surface tension at minimum and maximum area, respectively. The 21st breath cycle of each experiment was chosen to identify minimum and maximum values achievable at steady state. This was performed to determine whether adding modulated frequencies would positively affect the minimum and maximum surface tensions in the alveoli during a breath cycle. The surface tension values for each experiment including the standard deviations are presented in Table 5.3.

The minimum and maximum surface tension measurements at each modulating frequency are plotted in Figure 5.18 and Figure 5.19 respectively, for the 3 different modulating amplitudes. The surface tension values of the breath cycle without modulation are also shown at each frequency for comparison.

Table 5.3 Surface tension measurements.

Experiment	*Average Minimum Surface Tension, dyne/cm (±SD)*	*Average Maximum Surface Tension, dyne/cm (±SD)*
Breath Cycle	16.56 (2.81)	27.15 (3.36)
F10-A15	13.52 (2.84)	26.76 (3.06)
F10-A22.5	14.48 (0.91)	20.04 (0.63)
F10-A30	11.45 (1.43)	17.84 (1.31)
F20-A15	12.12 (3.84)	24.20 (3.32)
F20-A22.5	13.95 (1.86)	21.74 (3.75)
F20-A30	11.12 (3.51)	16.21 (2.70)
F30-A15	12.59 (2.99)	24.39 (5.91)
F30-A22.5	12.17 (1.63)	20.03 (6.61)
F30-A30	9.28 (2.41)	17.10 (1.97)
F40-A15	12.95 (0.96)	27.55 (2.30)
F40-A22.5	12.29 (0.78)	16.12 (0.85)
F40-A30	9.17 (1.91)	16.52 (1.07)
F50-A15	10.54 (2.1)	20.42 (5.29)
F50-A22.5	11.79 (1.16)	15.71 (1.63)
F50-A30	8.72 (1.15)	15.13 (1.18)
F60-A15	10.20 (3.14)	23.03 (4.79)
F60-A22.5	9.93 (1.04)	14.41 (1.04)
F60-A30	7.97 (1.01)	15.07 (1.74)
F70-A15	11.83 (3.18)	24.89 (4.96)
F70-A22.5	6.73 (1.60)	10.87 (0.70)
F70-A30	6.66 (0.75)	14.88 (0.75)

Figure 5.18 and Figure 5.19 are presented primarily to observe the statistical differences between experiments before further analysis. The observations on statistical differences in the minimum surface tensions in Figure 5.18 are as follows.

The minimum surface tension using a modulated amplitude of 15%TV is not statistically different to the minimum surface tension during an unmodulated breath cycle for all frequencies except at 50 and 60 Hz where the minimum surface tensions are statistically lower at this amplitude.

The minimum surface tension using a modulated amplitude of 22.5%TV is not statistically different to the minimum surface tension during an unmodulated breath

cycle for frequencies from 10-30 Hz. The minimum surface tensions at 40-70 Hz however are statistically lower at this amplitude. The minimum surface tensions at 22.5%TV are also not statistically different to those at 15%TV for all frequencies apart from 70 Hz where it is lower.

The minimum surface tension using a modulated amplitude of 30%TV is statistically lower to the minimum surface tension during an unmodulated breath cycle for all frequencies tested. It is however, not statistically different to both 15%TV and 22.5%TV for all frequencies, except at 40Hz, where it is lower.

The observations on statistical differences of the maximum surface tensions in Figure 5.19 are as follows.

The maximum surface tension using a modulated amplitude of 15%TV is not statistically different to the maximum surface tension during an unmodulated breath cycle for all frequencies, except at 50 Hz where it is lower.

The maximum surface tension using a modulated amplitude of 22.5%TV is statistically lower than the maximum surface tension during an unmodulated breath cycle for all frequencies. It is also statistically lower than the maximum surface tension at 15%TV for all frequencies except 20 Hz and 30 Hz.

The maximum surface tension using a modulated amplitude of 30%TV is statistically lower than the maximum surface tension during an unmodulated breath cycle as well as amplitude modulation at 15%TV for all frequencies. It is not statistically different to the maximum surface tension values at 22.5%TV for all frequencies, except at 70Hz, where it is higher.

Although distinct statistical differences in surface tension between modulating amplitudes and frequencies are not observed in general in Figure 5.18 and Figure *5.19*, trends of decreasing surface tension were noted with an increase in frequency for all modulating amplitudes.

The linear trends of minimum and maximum surface tension with frequency are shown in Figure 5.20 and Figure 5.21 respectively.

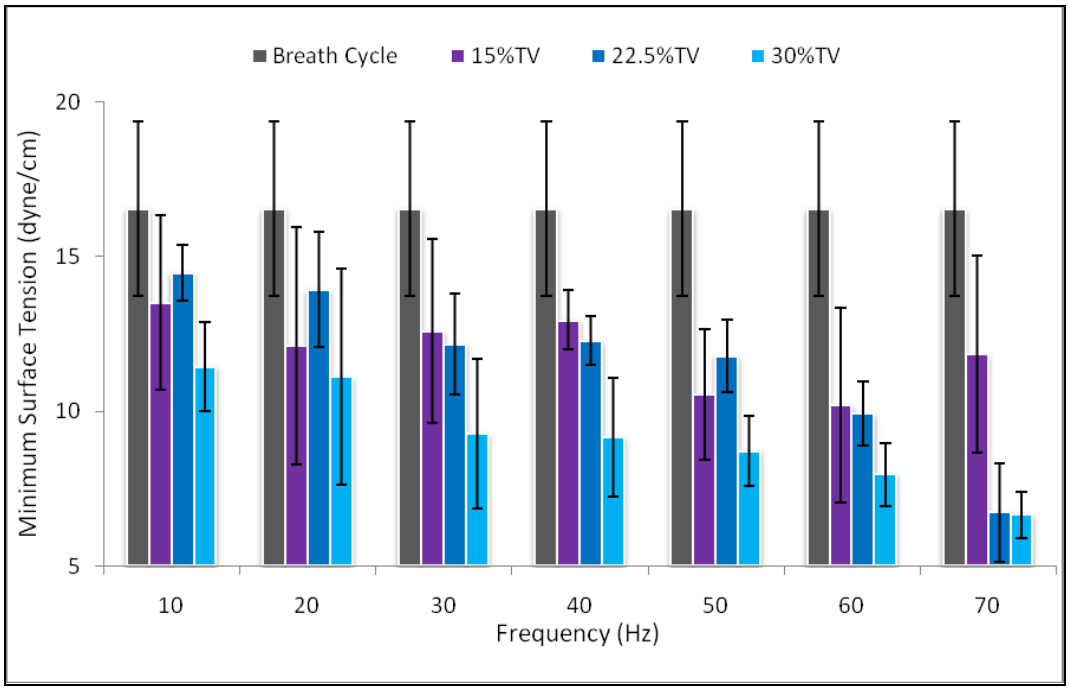

Figure 5.18 Minimum surface tension measurements.

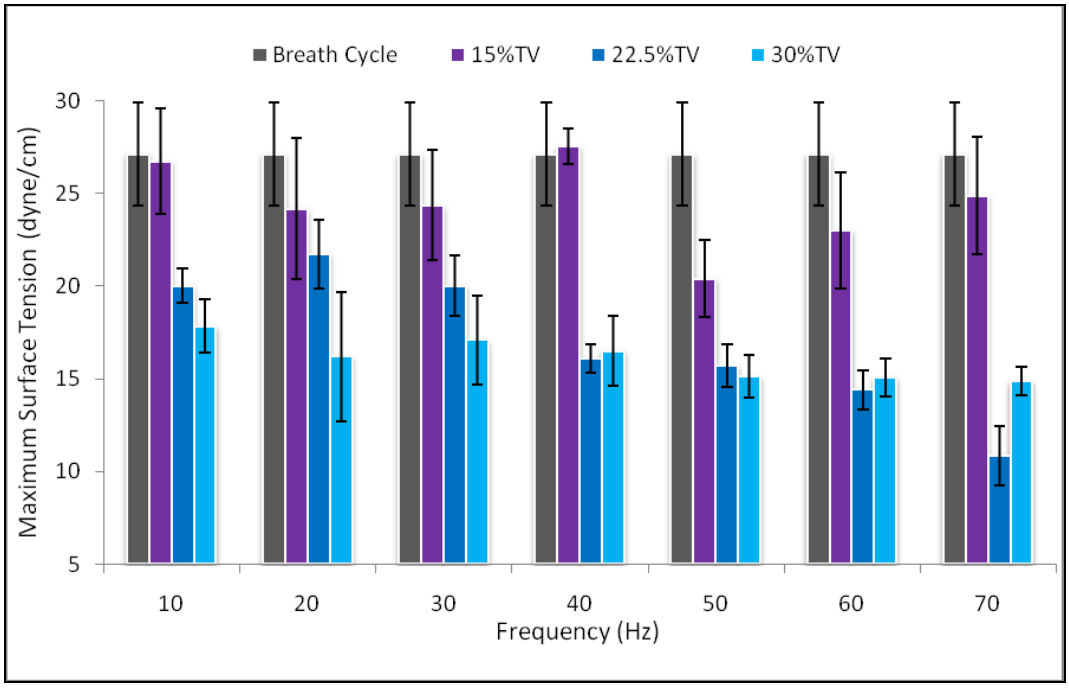

Figure 5.19 Maximum surface tension measurements.

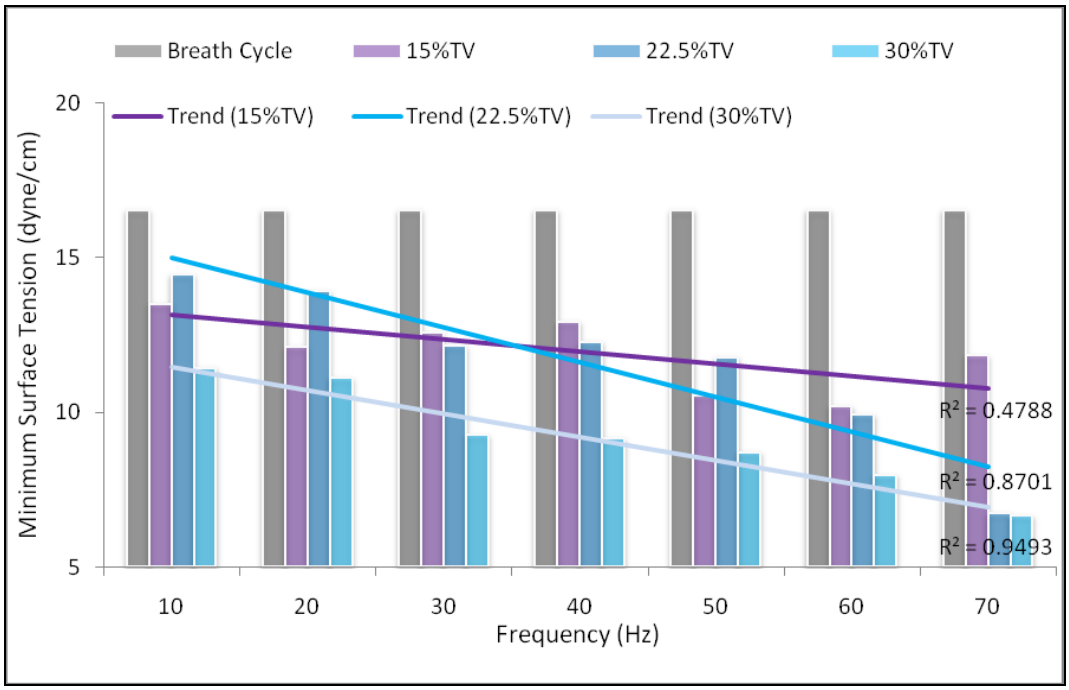

Figure 5.20 Trends in minimum surface tension.

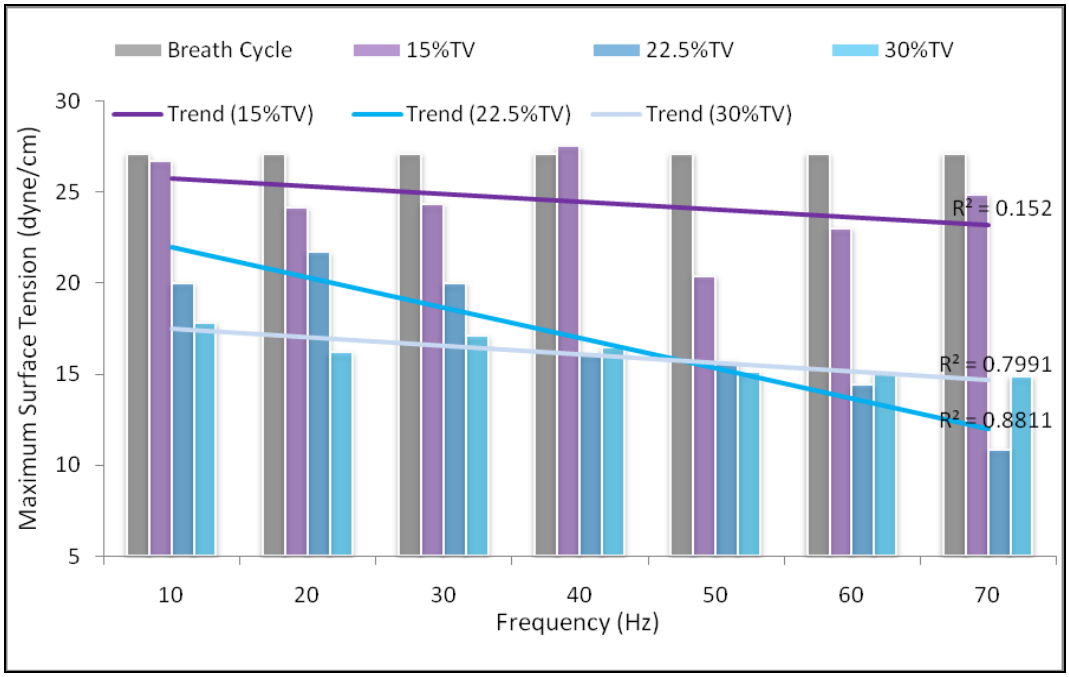

Figure 5.21 Trends in maximum surface tension.

Observations on the trends in minimum and maximum surface tension from Figure 5.20 and Figure 5.21 respectively are presented as follows.

For all modulated amplitudes tested, the minimum and maximum surface tensions are lower than the minimum and maximum surface tension values of an unmodulated breath cycle, respectively.

Overall, the minimum and maximum surface tension decreases across all frequencies tested as the modulated amplitude is increased from 15%TV to 30%TV.

For all modulated amplitudes tested, the minimum and maximum surface tensions decrease with an increase in frequency from 10-70 Hz.

The linear trend fit of the minimum and maximum surface tension data for the modulated amplitude of 15%TV is not as accurate as the fit of the other two modulated amplitudes.

5.6. Model and Experimental Results Comparison

The match of model to the experimentally measured maximum and minimum surface tension in a breath cycle without modulation is shown in Figure 5.22. The model is able to produce accurate predictions for both minimum and maximum surface tension which lie within the limits of the experimental error.

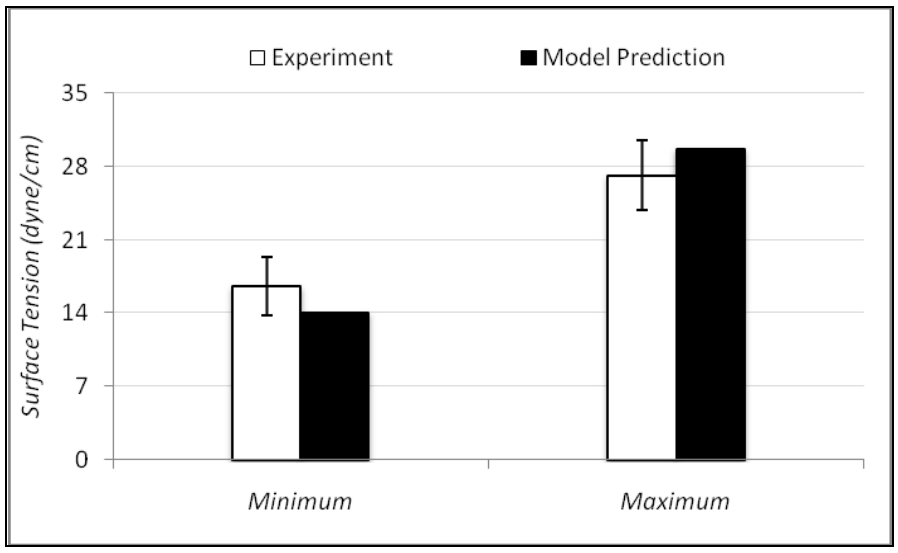

Figure 5.22 Match of maximum and minimum surface tension in a breath cycle.

The model parameters that were used are shown in Table 5.4. Equilibrium surface tension of surfactant and water are evaluated at 39°C to be 22.85 dyne/cm and 69.9 dyne/cm respectively [111]. $\gamma_{\min}$, D, k_1, k_1/k_2 and Γ^* are the same as those used to match the Schurch data [87] in Section 5.4. To increase accuracy, $A_{\gamma_{\min}}$ was refined to occur at 75% of maximum area.

Values of D and k_1 are frequency dependent and have to be evaluated for the identified frequency ranges of cycling. Predictions using the D and k_1 values used to match the breath cycles without frequency modulation were not able to match the experimental values of the experiments with frequency modulation, since the modulating frequencies were many orders of magnitude larger than the breathing frequency. Hence, values of D and k_1 were determined for each modulating frequency using the procedure of Morris [84] as follows. As in the work of Morris [84], determining the the exact values of D and k_1 that match the experimental data is a manual and tedious process, so ranges for the values were determined (as follows) and the best matches at either the minimum or maximum end of the ranges were chosen.

Table 5.4 Model parameters to predict surface tension for a breath cycle without frequency modulation.

Parameter	*Value*	*Units*
ω	30	cycles/min
C_{bulk}	0.5	mg/ml
γ^* at 39°C	22.85	dyn/cm
$\gamma_{\min}$	1	dyn/cm
$m_2 = (\gamma^* - \gamma_{\min})/1-(A^*/A_{\gamma})$	(22.85-1)/1-(100/75) = 66	dyn/cm
D	1 x 10^{-9}	cm^2/sec
k_1	0.07 x 10^5	ml/(g.min)
k_1/k_2	1.2 x 10^5	ml/g
Γ^*	3 x 10^{-7}	g/cm^2
$m_1 = \gamma_{water} - \gamma^*$ at 39°C	69.9– 22.85	dyn/cm
$\Gamma_{\max} = \Gamma^*[1+(\gamma^* - \gamma_{\min})/m_2]$	3x10^{-7}[1+(22.85-1)/66] = 3.99x10^{-7}	g/cm^2

This was established using a scaling analysis which yielded the following helpful relationships [84].

$$0.02\omega \le k_1 C_{bulk} \le 0.2\omega \qquad \textbf{(5.94)}$$

Given small uncertainties in the assumptions, the ranges are commonly extended by an order of magnitude. Once a range for k_1 is determined, it can be substituted into the following relationship to obtain the corresponding ranges for D.

$$k_1 \approx \left(\frac{\omega^{1/2}}{\Gamma^*}\right) D^{1/2} \qquad \textbf{(5.95)}$$

The resulting ranges, calculated for each modulating frequency are summarised in Table 5.5. Preliminary simulations were done in order to acertain which parameters would best predict the experimental data. The best fit to the data at each frequency was obtained using the D and k_1 values at the maximum end of the range identified for that frequency. The chosen D and k_1 values are summarized in Table 5.6.

Table 5.5 Identified ranges for D and k_1 values.

Frequency	k_1 *max*	k_1 *min*	*D max*	*D min*
10	10000	10	1E-08	1E-14
20	10000	10	1E-09	1E-15
30	10000	10	1E-09	1E-15
40	10000	10	1E-09	1E-15
50	100000	100	1E-07	1E-13
60	100000	100	1E-07	1E-13
70	100000	100	1E-07	1E-13

Table 5.6 D and k_1 values that best fit experimental data.

Modulating Frequency	k_1	D
10	10000	1E-08
20	10000	1E-09
30	10000	1E-09
40	10000	1E-09
50	100000	1E-07
60	100000	1E-07
70	100000	1E-07

The match of the minimum surface tension at each frequency for modulation amplitudes of 15%TV, 22.5%TV and 30%TV are shown in Figure 5.23 to Figure 5.25 respectively. Similarly, the match of the maximum surface tension at each frequency for modulation amplitudes of 15%TV, 22.5%TV and 30%TV are shown in Figure 5.26 to Figure 5.28 respectively.

It is not expected that one would get exact matches between experimental and predicted values in this analysis since it was the D and k_1 values at the upper end of the identified ranges that were used in the simulation, such that similar values were used for 10-40 Hz and again for 50-70 Hz (as seen in Table 5.6). To fit the data at each frequency exactly, the D and k_1 values would have to be further refined by a crude trial and error procedure which is neither accurate nor time-efficient. Since the experimental values are not statistically different either (as previously described), it is sufficient for the present study to match results in the same order of magnitude and to study the trends in the behaviour.

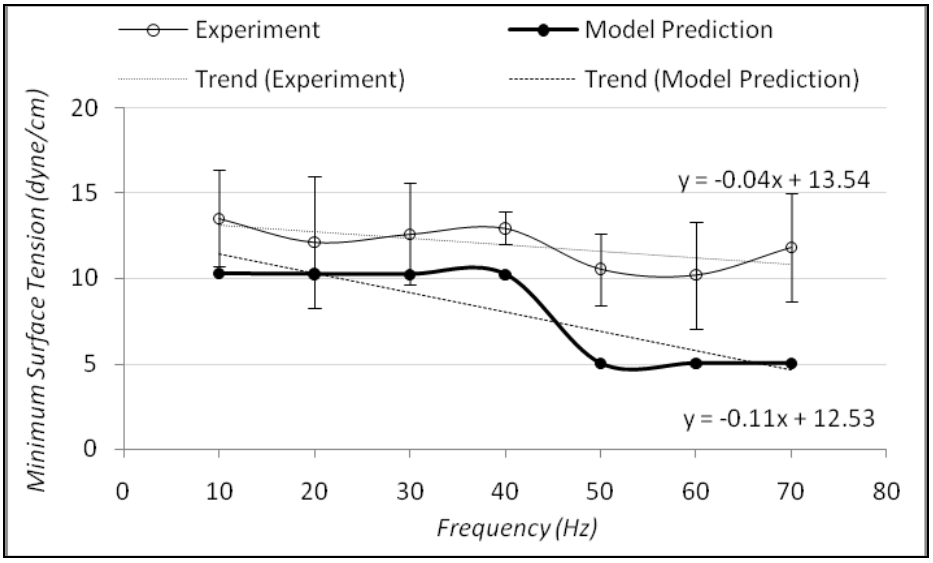

Figure 5.23 Match of minimum surface tension for 15%TV oscillation.

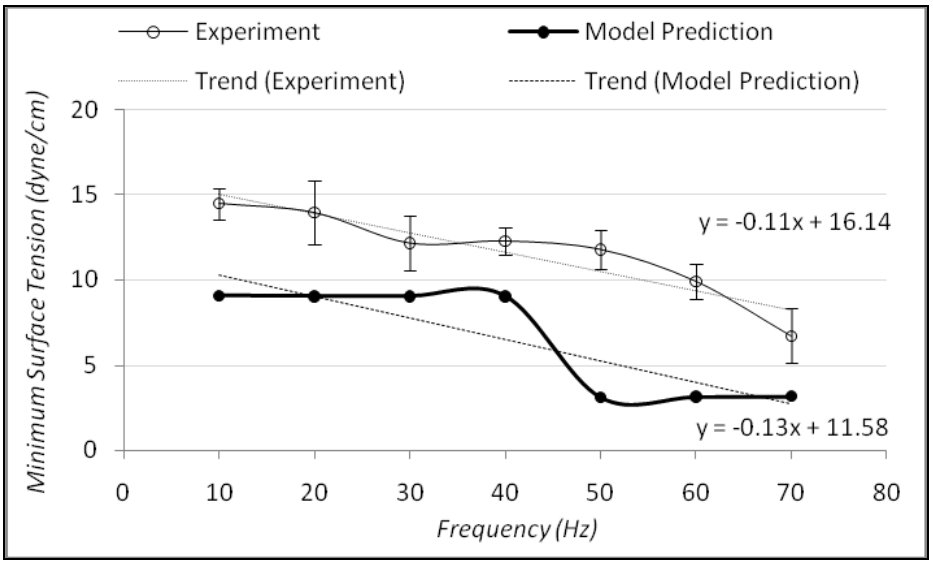

Figure 5.24 Match of minimum surface tension for 22.5%TV oscillation.

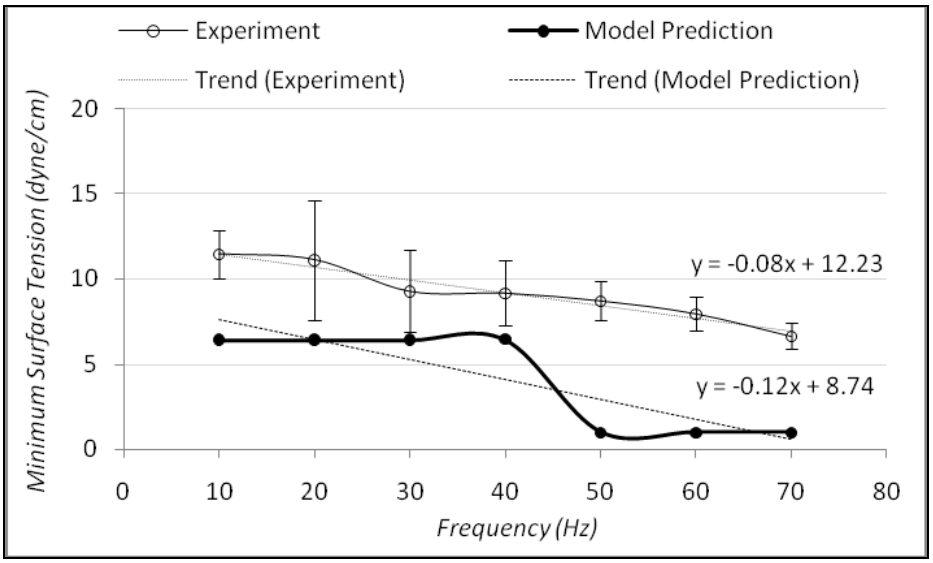

Figure 5.25 Match of minimum surface tension for 30%TV oscillation.

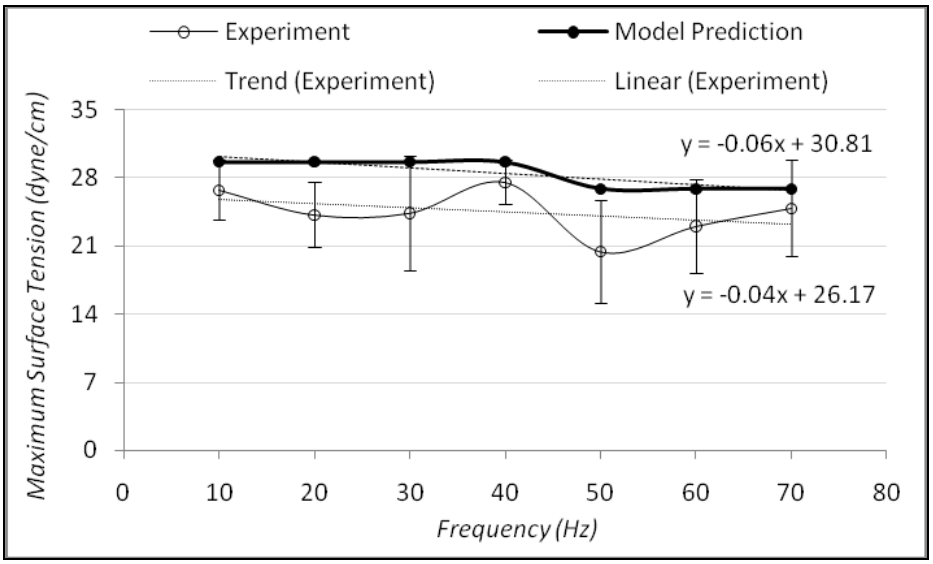

Figure 5.26 Match of maximum surface tension for 15%TV oscillation.

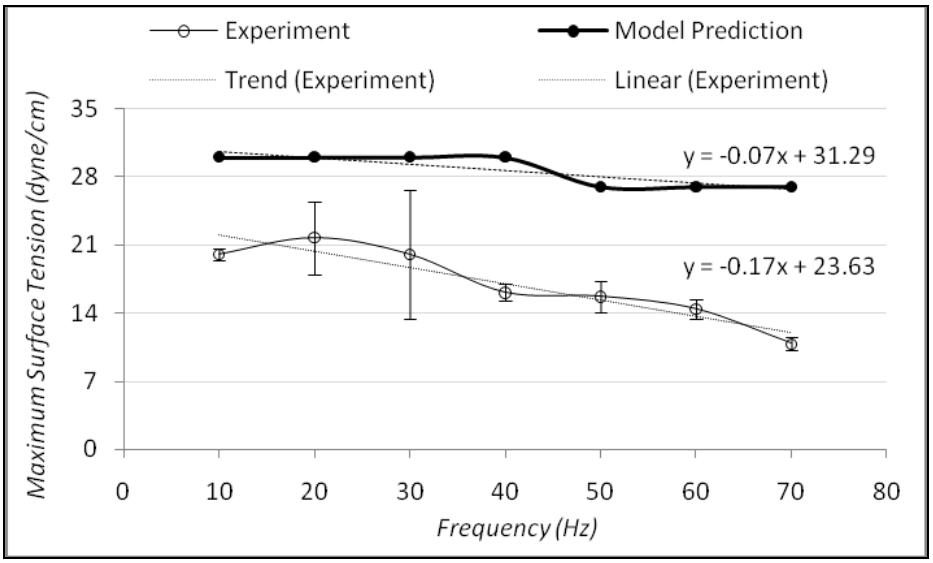

Figure 5.27 Match of maximum surface tension for 22.5%TV oscillation.

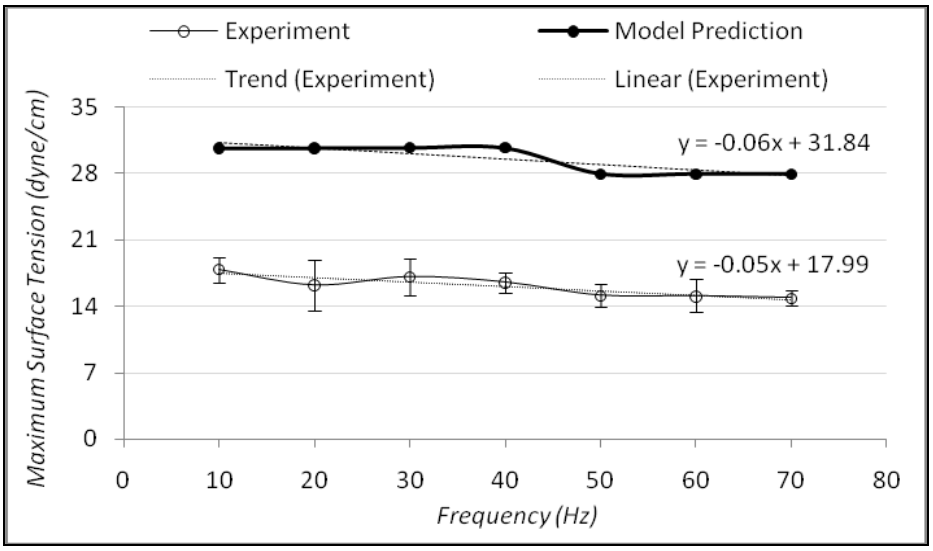

Figure 5.28 Match of maximum surface tension for 30%TV oscillation.

The predicted values of minimum surface tension for all modulated amplitudes lie within the same order of magnitude as the experimental results, although they are consistently lower than the experimental values for all modulated amplitudes tested.

In most instances, the model predictions do not lie within the limits of the experimental error but do follow the similar downward trend as the experimental results where the minimum surface tension decreases with an increase in frequency from 10-70 Hz. The gradient of the linear fits of the experimental and predicted data show the closest match at 22.5%TV (Figure 5.24) where the experimental error is the smallest.

The predicted minimum surface tension follows the same trend as experiments where the minimum surface tension decreases with increasing amplitude modulation for all frequencies tested.

The predicted values of maximum surface tension for all modulated amplitudes lie within the same order of magnitude as the experimental results, although they are consistently higher than the experimental values for all modulated amplitudes tested.

As with the predictions of minimum surface tension, the model predictions of maximum surface tension do not lie within the limits of the experimental error, but do follow the similar downward trend as the experimental results where the maximum surface tension

decreases with an increase in frequency from 10-70 Hz. The gradient of the linear fits of the experimental and predicted data show the closest match at 30%TV (Figure 5.28) where the experimental error is the smallest.

5.7. Closure

This chapter has presented the computational model (based on convection-diffusion and mass transport laws) used to predict the effect that modulated waveforms have on surface tension behaviour in the alveoli. Experiments on Curosurf were also performed to understand surfactant dynamics. The minimum and maximum surface tension at frequencies from 10-70 Hz were tested at 3 different amplitudes during experiments and compared to the model predictions. The results generated in this chapter are discussed in Chapter 6.

CHAPTER 6

Overall Discussion

6.1. Introduction

This chapter presents the discussion of the results presented in Chapters 4 and 5. First, Section 6.2 discusses the results of the simulations performed with the five-compartment lung model in Chapter 4. The model predictions for pressure, flow and volume during CPAP and Bubble CPAP treatment in comparison to the experimental results are discussed. The effect of adding pressure oscillations of different frequencies and at different locations are also discussed with the aim of identifying an optimal means of ventilation. Section 6.3 discusses the results of the surfactant experiments presented in Chapter 5. The experimental results are compared with those from the numerical model predictions. The behaviour of surfactant under different superimposed modulating frequencies is discussed. To avoid repetition, the figures in the previous chapters will not be repeated here.

6.2. Ovine Mechanical Model and Experiments

This section discusses the results presented in Sections 4.3 and 4.4. The ability of the model to predict parameters during normal CPAP and Bubble CPAP operating conditions is first discussed in Sections 6.2.1 and 6.2.2. The WOB is then used as an assessment parameter to determine the effect of adding pressure oscillations at the generator and the patient interface of the Bubble CPAP System.

6.2.1. Model Prediction of Experimental Results during CPAP

In the experiments, the average tidal volume of the Bubble CPAP animals was 5.38 ml/kg and for the CPAP animals it was 4.72 ml/kg.

The results showed that Figures 4.3 and 4.4 show excellent predictions of the pressure and flow rate at the airway opening during CPAP. The closeness of the match is due to the technique of using the exact tidal volume profile of the experiment to describe the thoracic force profile. This profile changes from breath to breath slightly due to the spontaneous nature of natural breathing, and so no two profiles are exactly the same in terms of the maximum tidal volume value, duration of inspiration and expiration and the shape of the profile. However, the profiles from breath to breath are not vastly different and so Figures 4.2 to 4.4. are satisfactory in their use as typical examples.

Other authors have produced model predictions in pressure, volume and flow rate at the airway opening that also show good comparison to values measured from real subjects [75-78]. However these investigations involve the healthy adult human lung. Schmidt et al. [73] predicted values of total respiratory system resistance in the newborn infant but these values were not validated with measurements from neonates.

As noted in Section 4.3.1, the magnitude of the pressure swings in each lobe are related to the size of the lobe, such that the larger the lobe, the smaller the pressure swing. This is directly related to the compliance of the lobes as defined by the pressure-volume relationships of each lobe where a more compliant lung can accommodate higher volumes with lower pressures. The mean pressures in each lobe are larger than those at the airway opening, increasing from the value of 6.75 cm H_2O at the airway opening to approximately 8 cm H_2O in the smallest lobe. This is due to the resistances of the airways leading to the lobes and the compliance of the lobe. As a result, the mean pressures in each lobe are also slightly different to each other. The diaphragmatic lobes (which have larger compliances and less airway resistance leading to them) have lower mean pressures than the smaller, stiffer apical and cardiac lobes that have larger resistances leading to them.

This behaviour of the lobe pressures also noted by Polak and Lutchen [81] who (despite neglecting lobe viscoelasticity and heterogeneity in mechanical properties in an asymmetric model of the normal human lung) produced predictions that showed different mean pressures and volumes at the beginning of expiration across the different

lobe compartments due to the variation in the number of alveoli in each lobe. They also noted that because of the non-uniform emptying of compartments, different compartment volumes and pressures can exist at the same time.

The pressures in the lobes range from 2 cm H_2O to 11 cm H_2O. This is much larger when compared to the pressures at the airways that range from 5.5 cm H_2O to 7.5 cm H_2O. The main generating mechanism for the pressure swings is driven by the movement of the chest wall which produces pressure variations at the alveolar region. Due to pressure losses along the tracheo-bronchial tree, the pressure swings are decreased at the airway opening.

Crooke et al. [79] developed relationships for tidal volume and mean alveolar pressure in a generic two-compartment lung model. However, they were neither validated nor solved to determine dynamic volumes and pressures in the adult lung or neonatal lung.

The simulations have shown that when ventilating the neonatal lung, the actual pressure at the level of the lobes could be approximately 2 cm H_2O higher than the level at the airway opening. Also, the range of the pressure swings at the level of the lobes is almost double that of the swings at the mouth. These findings have implications when choosing the ventilation strategy. In addition, new devices that introduce additional resistances to the patient interface need to consider that additional resistances may increase the mean pressure and pressure swings experienced at the level of the lobes. This will over-distend certain lobes, such as the smaller apical and cardiac lobes.

The relationship between the flow rate and the volume between the airway opening and the lobes is a simple cumulative relationship where the maximum values of flow rate and volume at each of the lobes add up to the value measured at the airway opening. The larger the lobe, the higher the FRC, TV and flow rate of the lobe.

The model predictions on the flow rate, pressure and volumes at the lobes are not validated by experimentation. This would require pressure and flow transducers to be introduced at the level of each lobe. To date, no such measurements have been performed in-vivo due to the obvious technical and ethical issues involved of trying to

introduce sensors into the lung of a living subject. In-vitro studies of excised lungs or 3-dimensional lung simulator studies may be able to determine the actual distribution of pressures, flows and volumes across the lobes.

6.2.2. Model Prediction of Experimental Results during Bubble-CPAP

Section 4.3.2 presented the comparison of the experimental values and model predictions of a lamb on Bubble CPAP. Figures 4.6 and 4.7 showed that the model predictions of pressure and flow rate lie in the same typical pressure ranges as those observed in experiment. The oscillations present in the experimental values appeared to be slightly more 'damped out' than the model predictions. These can be attributed to the fact that the fittings at the patient interface in the experiment may have been adapted slightly to incorporate the endotracheal tube and attachments. Also, the model does not account for leaks and shock factors due to fittings in the system, resulting in more of the pressure oscillation frequencies and amplitudes being 'preserved' than would actually be in real life.

The tidal volume profile of both experiment and model predictions in Figure 4.8 contain very little evidence of pressure oscillations. The tidal volume is calculated (both in experiment and model) by the integration of flow rate and as such, the pressure oscillations present on the flow rate profile are not substantial enough to have a significant effect on the tidal volume.

Figures 4.9 and 4.10 show the pressures in the left and right lobes respectively. The pressure oscillation amplitudes do not decrease significantly from the level of the airway opening to the level of the lobes. This may be due to the airways being modelled as rigid tubes. In reality, the first few generations of airways, although they do contain cartilage, are not completely rigid and do have some compliance which will dampen the amplitude and frequencies of oscillations travelling through them. By defining the airway pressure-cross sectional area or volume relationship in the airways, it is possible to achieve a more accurate model of the airway pressure drop. However, to accurately determine these relationships requires detailed empirical measurements on the fragile ovine airways which were beyond the scope of this research and remain a subject of further study. Lambert et al. [112] developed airway pressure-cross sectional area

relationships for airways and these were used by Polak and Lutchen [81] to describe the mechanical characteristics of the airways. However these relationships were developed from a symmetrical Weibel model [68] for adult human lungs for expiratory flow only and any relationships deduced for neonates would be scaled down by lung volume and thus less accurate.

The oscillations in flow rate (Figures 4.11 and 4.12) are still visible at the level of the lobes and although they may decrease in absolute amplitude due to the division of flow across the lobes, they do not decrease relative to the maximum flow rate value in each lobe. This may be attributed to the fact that the mechanical properties of each lobe are more or less homogeneous when corrected for the maximum volume per birthweight (as in the pressure-volume curve of Figure 3.11 which was used to determine the stiffness-volume relationship in each lobe based on the pressure-volume curve of the whole lung).

A more heterogeneous description of the pressure-volume relationship of each lobe (as demonstrated by Figure 3.10) will represent a more diseased state and hence show oscillations in pressure and flow rate of different frequencies and amplitudes. Also, with the correction in the description of the airway pressure calculations, the amplitudes of the oscillations in flow rate will also decrease.

Figures 4.13 and 4.14 clearly indicate that the tidal volume calculations show no significant pressure oscillations due to the integration process.

The predictions of pressure, flow rate and volume at the lobes during Bubble CPAP are also not validated by experimentation for the same practical reasons as highlighted in Section 6.2.1 and remain a subject of further investigation.

6.2.3. Calculating the WOB of premature and near-term lungs

The WOB calculated in this thesis should not be confused with the typical physiological measure of work of breath which calculates the work done by the respiratory muscles. In the traditional sense, a premature infant has to expend more energy to get the required level of ventilation, making its work of breath higher than a healthier infant. In

the present context of this research, a more mechanical approach is taken where the WOB is the mechanical work done on a specified control volume. In this case, a premature infant has less powerful lungs and can only perform a small amount of work on the air in the lungs when compared to a healthier lung, making its WOB smaller. The latter approach makes measurement easier and since the mathematical model does not contain a description of the neurogenic control of the respiratory system that allows it to respond to a specified respiratory load, the mechanical work done is the preferred measure of respiratory performance [36, 78].

As noted in Figure 4.15 and Table 4.5, the total work of breath ($\overline{WOB}_{total}$) calculated at the airway opening of the 142 day gestation (near-term) lung during CPAP is 76% more than that of the 128 day gestation (preterm) lung during CPAP. The percentage improvements from preterm to near-term values at each lobe are dependent on the size and compliance of each lobe, such that the smallest, stiffest lobe (the right cardiac lobe) shows the least increase in WOB (32%) and the largest lobe (the right diaphragmatic lobe) shows the most improvement (88%). In subsequent calculations in Chapter 4, any increase in WOB from 100% at any location is considered desirable. In simple terms, the aim was to determine whether the '76% deficit in WOB' in the preterm lung could be compensated for by adding Bubble CPAP or other ventilation waveforms incorporating pressure oscillations.

6.2.4. Effect of Adding Pressure Oscillations at the Generator

Figure 4.17 shows the percentage improvement in WOB relative to CPAP-only treatment at each location in a preterm lung. Bubble CPAP shows a 1-2% increase in WOB. This is due to the many rapid transient changes in pressure caused by the pressure oscillations. However, due to the stochastic resonance phenomena discussed in Chapter 2 [12, 13, 55], because pressure oscillations at 19 Hz and 23 Hz were identified as frequencies which contributed the most to the instantaneous work of breath (Figure 4.16), using pressure oscillations with these frequencies increases the WOB. As noted in Figure 4.17, the largest increase in WOB is evident when both significant frequencies are combined with equal magnitude in a ventilation profile, providing a 4-6% increase in WOB across all locations. Since 19 Hz shows the most significant power, using this

alone in a ventilation profile predictably showed more improvement in WOB than using 23 Hz alone.

Results presented in Figure 4.17 support suggestions by other researchers that tuning the frequencies of pressure oscillations in ventilation to the optimal frequencies would provide more benefit [13, 55]. Thus, the procedure presented in Section 4.4.3 promises to be a method of identifying such beneficial frequencies in clinical practice and then adjusting oscillation frequencies produced by the respiratory support device to provide optimal ventilation.

The oscillation amplitude of the single frequencies were always ±2.58 cm H_2O (i.e. the standard deviation of Bubble CPAP pressure oscillation amplitudes) in the simulations. This means that the amplitude of oscillating pressures in the lobes will be smaller than those experienced by Bubble CPAP, reducing the risk of over-inflation of the lobes. The mechanism of recruiting lung volume here seems to be a rate dependent-phenomenon. If the optimal frequency is used to recruit the optimal volume in a breath cycle, a higher amplitude of oscillating pressure is not required.

The results also suggest that the oscillations produced by Bubble CPAP would contain some frequencies that improve the WOB values due to stochastic resonance. This was further explored in Figure 4.19 where the most significant frequencies that contributed to the WOB were 17 Hz and 23 Hz during typical Bubble CPAP operation on a 128 day gestation lamb. This is very close to the 'optimal' frequencies identified by the white noise signal in Figure 4.16 showing that the Bubble CPAP System contains frequencies that are beneficial to the ventilation of the lung.

The simulations also demonstrate that the Bubble CPAP System can be used in conjunction with an 'oscillation source' at the level of the CPAP generator to produce single or mixed frequencies in place of the random bubble generation at the CPAP generator to be of further benefit to the neonate. In order to introduce controlled pressure oscillations to the device, a method of controlling the generation of bubbles or introducing another vibratory source can be considered.

The only results in Figure 4.17 that can be validated are those comparing the WOB of the CPAP vs. Bubble CPAP treatment from the data collected in the experiments in Section 4.2. Figure 4.18 shows the WOB values calculated from experiment after correction for tidal volume and birthweight. The WOB of Bubble CPAP at the airway opening is 13.8% (±25%) larger than the value at CPAP-only treatment. Although the upward trend agrees with that of the simulation in that Bubble CPAP shows a higher average value of WOB in comparison to CPAP, this is a considerable difference to the calculated value of just 2% improvement in the simulations.

However, the large standard deviations in the experimental measurements do not allow one to conclusively say that the Bubble CPAP treatment statistically improves the WOB by as much as 13.8% when compared to CPAP-only treatment. Hence, although there is an upward trend in WOB when using Bubble CPAP, no statistical conclusion can be drawn as to the actual percentage of improvement.

The values of experimental pressure, flow rate and tidal volume were recorded after 3 hours of receiving the respective treatment. Hence, they reflect the effects of gas mixing, surfactant maturity, ventilation-perfusion effects and the avalanche effect over a long period which contributes to the recruited volume. These effects are not included in the current model and so any additional improvement in the value of WOB determined from the experiments could be attributed to the effects of these factors on the WOB.

The WOB values calculated by the simulation are thus more of an indication of any instant improvement in WOB that results from the mechanical effects of using pressure oscillations.

6.2.5. Effect of Adding Pressure Oscillations at the Patient Interface

As mentioned in Section 4.4.4, the pressure oscillations about the mean level of CPAP were introduced at the level of the patient interface in the simulations, to avoid attenuating frequencies above 45 Hz through the expiratory tube of the Bubble CPAP System. This allows one to determine whether adding any additional frequencies above 45 Hz increases the WOB value in comparison to CPAP-only treatment. A number of frequencies were identified in Figure 4.20 as having significant power and so the effect

of those individual frequencies on the WOB value as well as an 'equal mixture' of those frequencies at different locations are shown in Figures 4.21 to 4.23.

The improvement in WOB for all significant frequencies is in the order of 1-2% (Figures 4.21 to 4.23) for all locations. However, when all the significant frequencies are combined in equal magnitude, the increase in WOB is approximately 4-10% across all locations in comparison to CPAP-only treatment. This improvement in WOB is larger than the improvement noted previously of combined frequencies that were introduced at the level of the CPAP generator.

These results suggest that increasing the range of the frequencies generated by the Bubble CPAP System to include higher frequencies (up to 125 Hz as used in this study) at the patient interface may provide added benefit to the neonate. However, a practical design that allows the generation and transmission of these frequencies to the neonatal lung remains a challenge. Nevertheless, the results of the simulation suggest that if this were possible, the improvement in the WOB could be doubled in comparison to trying to introduce pressure oscillations at the level of the CPAP generator.

6.2.6. Effect of Pressure Oscillations on the Lung - Summary

Section 6.2 has discussed the model predictions of pressure, flow and volume at different locations in the lung. The predicted respiratory parameters at the airway opening have been validated with experimental data for operation under CPAP and Bubble CPAP treatment. The respiratory parameters in the different lobes have also been predicted. These have not been validated with clinical measurements but do agree with the relative trends and behaviour observed by other authors. The WOB was used as an assessment parameter to predict the effect that different oscillation frequencies had on respiratory performance. Using the PSD of WOB was an effective way of identifying the optimal frequencies that provided optimal lung volume recruitment. It was also predicted that using a combination of all frequencies with significant power, provided more lung volume recruitment than single frequencies alone. It was also found that The Bubble CPAP System produced some frequencies that were in the range of the identified optimal frequencies which may contribute to the added benefit noticed in practice. The possibility of using the Bubble CPAP System to produce 'custom-

generated' frequencies to enhance lung recruitment in any individual lung is also proposed.

6.3. Pulsating Bubble Surfactometer Experiment and Numerical Model

This section discusses the results presented in Sections 5.5 and 5.6 obtained from surface tension measurements performed on a PBS. Section 6.3.1 discusses the experimental results and the trends in surface tension with increasing modulating frequency and amplitude. Section 6.3.2 compares the experimental values to the numerically predicted values of minimum and maximum surface tension. The role of the experimental technique and the model parameters in model-experiment discrepancy is discussed.

6.3.1. Minimum and Maximum Surface Tension Results

Figure 5.18 shows the statistical differences between the minimum surface tension across all experiments. As noted in Section 5.5.3, using a modulated amplitude of 15%TV shows no significant decrease in minimum surface tension that is consistent across all frequencies. However, it does show a trend of decreasing minimum surface tension with frequency and all average values of minimum surface tension across all frequencies are lower than those of the breath cycle without modulation (Figure 5.20).

Using a modulated amplitude of 22.5%TV shows a significant drop in minimum surface tension from 40-70 Hz (i.e. a 26% decrease from the minimum surface tension during an unmodulated breath at 40 Hz and a 59% decrease in minimum surface tension at 70 Hz). Again, looking at Figure 5.20, the minimum surface tension values from 10-30 Hz are not statistically different to the values of the unmodulated breath cycle. However, a trend of decreasing minimum surface tension with frequency is visible and all average values are lower than those of the breath cycle without modulation. Although there is no statistical difference between the corresponding minimum surface tension values at 15%TV and 22.5%TV for all frequencies, Figure 5.20 shows that the 22.5%TV trend line generally lies below the 15%TV trend line.

The minimum surface tension using a modulated amplitude of 30%TV shows a statistically significant drop in minimum surface tension when compared to using no modulated frequencies. (i.e. a 31% decrease from the minimum surface tension during an unmodulated breath at 10 Hz and a 60% decrease in minimum surface tension at 70 Hz). However, it does not show consistent statistical difference to other modulated amplitudes at all frequencies. Nevertheless, Figure 5.20 shows that the average values of the minimum surface tension at 30%TV are lower than other smaller modulating amplitudes. The 30%TV trend line lies below the other trend lines indicating its ability to provide the lowest minimum surface tension of all amplitudes tested.

It can thus be deduced that adding amplitude oscillations of at least 30%TV at the level of the alveoli (for the range of frequencies typically produced by Bubble CPAP at the interface) will statistically reduce the minimum surface tension in the alveoli by 31-60%. Smaller modulating amplitudes indicate a tendency to reduce minimum surface tension but are only statistically significant at frequencies of 40-70 Hz in the case of 22.5%TV amplitude modulation.

This study has enabled important surface tension relationships in the alveoli to be characterized. The minimum surface tension decreases with increasing frequency from 10-70 Hz for all modulated amplitudes. Minimum surface tension decreases with increasing modulating amplitude from 15%TV to 30%TV. This has been qualitatively observed across all frequencies.

Figure 5.19 shows the statistical differences between the maximum surface tension across all experiments. In general, the maximum surface tension of a 15%TV modulated amplitude is not statistically different to that of the unmodulated breath cycle across all frequencies. The average values of maximum surface tension are generally lower than those of the unmodulated breath cycle and show a slight decrease with increasing frequency.

Using a modulated amplitude of 22.5%TV shows statistically lower maximum surface tension values than those of the unmodulated breath cycle i.e. a 26% decrease at 10 Hz and a 60% decrease at 70 Hz. The maximum surface tension values at 22.5%TV are

also statistically lower than those at 15%TV (except at 20 and 30 Hz), demonstrating that the larger modulating amplitude is more effective at decreasing maximum surface tension. The 22.5%TV trend line of maximum surface tension in Figure 5.21 shows a definite decrease in magnitude with an increase in frequency.

The maximum surface tensions using a modulated amplitude of 30%TV is statistically lower than the values of the unmodulated breath cycle across all frequencies i.e. a 34% decrease at 10 Hz and a 45% decrease at 70 Hz. Although they are also statistically lower than those of the 15%TV modulated amplitude at all frequencies, the same does not apply to the values at 22.5%TV. However, as seen in Figure 5.21, the 30%TV trend line generally lies below the 22.5%TV trend line showing its inclination toward lower maximum surface tensions. The maximum surface tension also shows a decrease in magnitude with increasing frequency.

The maximum surface tension experimental data reveal the following. Using modulated amplitudes of 22.5%TV and 30%TV statistically reduces the maximum surface tension by 26-60% and 34-45% respectively when compared to the unmodulated breath cycle across all frequencies tested. Maximum surface tension decreases with increasing modulating amplitude from 15%TV to 30%TV. This has been qualitatively observed across all frequencies.

No studies in the literature have used superimposed modulating frequencies on the breath cycle excursion in surface tension measuring devices. Thus there are no published results in the literature to compare with the experimental results obtained from this study. The only frequency dependant behaviour of lung surfactant that has been investigated in the literature is the effect of increasing breathing frequency from 1 cycle/min to 100cycles/min [83-85]. It was concluded that as the breath cycle frequency increases, so does the maximum surface tension obtained. Since the same breathing frequency is used for all experiments in the current investigation, this effect can be ignored.

The implications of the experimental findings are that the introduction of pressure oscillations superimposed on CPAP treatment to the surfactant in the alveoli at

frequencies from 10-70 Hz can lower the maximum and minimum dynamic surface tension experienced at the air-liquid interface at minimum and maximum surface area during spontaneous breathing when compared to CPAP-only treatment.

Since the frequencies lie in the typical range of frequencies generated by the Bubble CPAP System, it introduces the possibility that some of the improvements in respiratory measurements noted when using Bubble CPAP may be due to the increased compliance in the lung. This results from the decreased surface tension in the alveoli due to the 'vibration' of the air-liquid interface.

Whether the modulating amplitudes that showed statistical differences in experimental surface tension values (i.e. 22.5%TV and 30%TV) are practically achievable at the level of the alveoli remains to be answered.
Of more immediate importance are the mechanisms responsible for the decrease in surface tension with amplitude and frequency. The comparison of the experimental results with those of the numerical model reveal possible mechanisms in the following section.

6.3.2. Comparison of Experimental and Model Results

Figure 5.22 shows excellent comparison between the experimental results and model predictions of the maximum and minimum surface tension in a breath cycle without modulated frequencies. The model parameters in Table 5.4 were able to predict results that were within the limits of the experimental standard deviations. However, because the values of diffusion coefficient D and the adsorption coefficient k_1 are frequency dependent [83-85], they are only accurate for the frequency range that they have been calculated for. No values of D and k_1 are available in the literature since no studies prior to the current one have involved frequencies in the range of 10-70 Hz.

The 'best fit' values of D and k_1 as determined for each model simulation at each modulated frequency were presented in Table 5.6 and the resulting matches to the experimental data using these values were shown in Figures 5.23 to 5.28. Although the model predictions do not lie within the standard deviations of the experimental results,

the values are still in the same order of magnitude and follow the same trends as the experimental results.

Both the experimental and predicted values of minimum and maximum surface tension at all modulated amplitudes show a decrease in magnitude with frequency. The slopes of the predicted and measured trend lines are also generally in the same order of magnitude and show a similar degree of effect when increasing frequency at a particular modulated amplitude.

The gradients of the predicted trend lines are similar across all modulated amplitudes for both maximum and minimum surface tension values. However, the trend lines of the measured values of surface tension show no conclusive relationships in gradient across the different amplitudes. The large standard deviations in some measurements affect the average values at each point and hence the accuracy of the trend lines. It is evident that those experiments which contain small standard deviations (i.e. Figure 5.28 and 5.24) show the closest matches in the gradient to the predicted values.

The effect of increasing the modulated amplitude is also the same for both experiment and prediction. Both the minimum and maximum surface tension values across all frequencies decrease as the modulating amplitude is increased from 15%TV to 30%TV.

It is proposed here that the mechanisms of decreasing surface tension with frequency could be due to the 'improvement' noticed in the model parameters of D and k_1 in Table 5.6. The values of both diffusion coefficient D and adsorption coefficient k_1 need to be increased to show a match with the experimental results. It is likely that as the modulating frequency increases, the relative velocity of the interface increases. This means that over the same time, more surfactant molecules effectively diffuse through the bulk and more are adsorbed to the air-liquid interface. This increases the interfacial surfactant concentration and consequently decreases surface tension. Increasing the amplitude of the modulated oscillation also increases the number of surfactant molecules 'collected' by the moving interface.

The decrease in surface tension with modulating amplitude could also be attributed to similar mechanisms where bigger modulated amplitudes increase the interfacial surface tension.

The difference in experimental and model results may be due to a number of factors. The model parameters and the assumptions made in selecting them may be responsible. The ratio of the adsorption and desorption coefficients, the equilibrium interfacial concentration, minimum surface tension and the area that it occurs at are estimated from literature for unspecified temperatures and are thus bound to introduce some inaccuracies into the model which simulates surfactant behaviour at 39^{o}C rather than 37^{o}C or room temperature as previously done.

Also, the viscoelasticity of the interface plays a part in surface tension dynamics. Horn and Davis [82] performed theoretical analyses which suggested that surface viscoelasticity has a significant effect on pressure-volume curve hysteresis. The Morris model [84, 85] used in this study does not incorporate the effects of the surface viscoelasticity. The effects of viscoelasticity in the model may be neglected at lower frequencies closer to breathing frequencies as modelled previously by other authors [83-86, 105, 113]. However, it is conceivable that the exclusion of viscoelasticity at the higher oscillating frequencies used in this study, may introduce larger errors in the resulting surface tension values. The exclusion of surface viscoelasticity may be a major source of error in the predicted values in this investigation.

To date, no model includes the effects of Langmuir kinetics, convection-diffusion, separated regimes of mass transport and the viscoelasticity of the interface. It is anticipated that the introduction of viscoelasticity into the Morris model [84, 85] in the future will increase its accuracy at higher oscillating frequencies.

Another possible source of discrepancy in the model and experimental results is the fact that the model considers the surfactant bubble to be spherical when it is in fact sessile shaped. However, the effect of this assumption is likely to be relatively small. It was previously found in experiments that the absolute difference between the actual surface tension and the value calculated assuming sphericity is never greater than 0.5 mN/m

[33]. The effect of assuming sphericity in the model is thus likely to introduce less error than the exclusion of the surface viscoelasticity.

Measurement errors are likely to have been introduced during experimentation. Hardware and cost limitations prohibited real-time imaging in the current experimental setup. Therefore, the time to establish equilibrium surface tension before experimentation and steady state oscillation was adopted from previous investigations on Curosurf [87]. This would have introduced more variation in the experimental results than could be avoided by a real-time display system. Although the standard deviations of the experiments were satisfactory for initial investigations such as the present one, the higher accuracy achievable from real-time imaging (as in Seurynck et al. [109]) would have made it possible to reduce the error so that the degree of improvement with frequency could be quantified (from the gradients of the trend lines) for different modulating amplitudes.

Optical backlighting and magnification of the bubble is also a factor in capturing bubble images that have well defined edges. Optical backlighting containing diffusers and a more powerful magnifying lens (although considerably more expensive) would have defined the edges clearer and produced more accurate readings of surface tension in the experiments.

Also, the code generated to measure the dimensions of the bubble was basic in nature. It locates 3 outermost points on the circle (2 horizontal measurements on either side of the bubble and 1 at the bottom) and estimates the centre of the bubble. A more sophisticated code that determined the complete shape of the bubble would definitely increase the accuracy of surface tension measurements. Such commercial software is available but was beyond the budget of the current study.

The size of the bubble chamber and the proximity of the thermocouple wire to the bubble could also have had an effect on the results. It is conceivable that the use of high oscillation frequencies such as that used in this study may produce waves in the bubble chamber that affect the shape of the bubble. However, the high frequency oscillations in the experiments are much smaller than the bubble tidal excursion and no irregular

profiles were noted in bubble measurements to suggest interferences by waves travelling in the bulk fluid.

6.3.3. Effect of Modulated Frequencies on Surface Tension - Summary

Section 6.3 has discussed the results of the surface tension measurements on a PBS. The experimental results revealed that the surface tension at the air-liquid interface of a surfactant bubble decreases with an increase in modulating frequency (10-70 Hz) and amplitude (15%TV-30%TV). The numerical model also predicted surface tension values in the same order of magnitude as the experiments and showed the same behaviour of decreasing surface tension with frequency at all modulating amplitudes. Possible mechanisms of the improvement noted in surface tension were suggested to occur from the increase in diffusion and adsorption of surfactant molecules to the air-liquid interface. The possible sources of the error between experimental and predicted values were discussed with the major contributors suggested to be the exclusion of surface viscoelasticity in the model and the lack of real-time imaging during experimentation to more accurately determine the onset of equilibrium and steady state conditions. The frequencies produced by the Bubble CPAP System (which lie within the range of frequencies tested in this investigation) may contribute to the lowering of surface tension in the alveoli which manifests as increased compliance in clinical practice.

CHAPTER 7

Conclusions and Future Work

7.1. Introduction

The overall research plan and objectives presented in section 2.5 identified the need for a validated multi-compartmental model of the neonatal lung that could be used to study the effect of pressure oscillations in the neonatal respiratory system. The need for a validated model of surfactant dynamics in the lung was also illustrated. In order to fulfill these objectives, Chapter 3 presented the original multi-compartmental model of the neonatal lung. Chapter 4 then discussed the validation of the model and the model predictions on the effect of pressure oscillations on the WOB parameter. Chapter 5 described the numerical model that simulated surfactant dynamics during superimposed oscillations and presented the experimental results that validated the model. All results were then discussed in Chapter 6 to determine the trends in behaviour of WOB and surface tension in the lung upon addition of pressure oscillations. The conclusions derived from the discussions are presented in section 7.2 and recommendations for the direction of future investigations are made in section 7.3.

7.2. Conclusions

- An original model of the neonatal respiratory system was developed. The originality of the model lies in its compartment-specific mechanical properties and tracheo-bronchial structure, developed from measurements on neonatal preterm lungs.

- The model is able to accurately predict the respiratory parameters at the airway opening during CPAP and Bubble CPAP operation, as determined from model comparisons with experimental measurements on preterm lambs.

- The model has predicted alveolar pressures, flows and volumes during CPAP and Bubble CPAP treatment that vary from lobe to lobe depending on the airway resistances leading to the lobes and the lobe mechanical properties. The model can thus predict the uneven ventilation profiles in the neonatal lung.

- Both model predictions and experimental measurements show the trend that the mechanical WOB is qualitatively greater (improved) during ventilation under Bubble CPAP when compared to CPAP.

- The PSD technique is able to identify frequencies of oscillation which show improved WOB measures compared to CPAP-only treatment. Frequencies which showed improvement in WOB measures of the 128 day gestation lung were identified as 19, 23, 28, 33, 44, 49, 54, 81, 88, 99, 111 and 113 Hz. The optimal frequencies would vary for any particular lung depending on size, gestation and diseased state.

- Combining all the significant frequencies of oscillation in equal amplitude provided more improvement in WOB than delivering single frequencies. Model predictions showed the improvement in WOB relative to CPAP-only treatment (due to mechanical effects) was 1-2% when introducing single frequencies at the generator, but increased to 4-6% when introducing “mixed frequencies” at the generator and 4-10% with “mixed frequencies” at the patient interface.

- It was shown that the Bubble CPAP System delivers frequencies similar to the identified optimal frequencies of the 128 day gestation lung (17 and 23 Hz) which contribute to the improvement in WOB. This supports the stochastic resonance phenomenon suggested in the literature.

- Measurements were conducted on a custom-built pulsating bubble surfactometer which introduced modulated frequencies (10-70 Hz) superimposed on the breath cycle at 3 different amplitudes (15%TV, 22.5%TV and 30%TV). The minimum values of surface tension at a modulating amplitude of 30%TV were statistically lower than the minimum surface tension during an un-modulated breath cycle at all frequencies. The maximum values of surface tension at modulating amplitudes of 22.5% and 30%TV were statistically lower than the maximum surface tension during an unmodulated breath cycle at all frequencies. Although statistical significance was only observed at the aforementioned experiments, the average trends of all the experiments revealed that the minimum and maximum surface tension in an alveolus decreases with increasing frequency and increasing amplitude.

- The numerical model was used to predict the minimum and maximum surface tension in an alveoli exposed to modulated frequencies (10-70 Hz) superimposed on the breath cycle at 3 different amplitudes (15%TV, 22.5%TV and 30%TV). The results showed the same trends observed in the experiments i.e. that the minimum and maximum surface tension in an alveolus decreases with increasing frequency and increasing amplitude. the values did not match exactly but were within the same order of magnitude.

- The mechanism of improvement of surface tension in the alveolus with frequency and amplitude is due to the increased diffusion and adsorption of surfactant molecules to the air-liquid interface. This probably results from the increased relative velocity and travel of the interface, thereby collecting more surfactant molecules, increasing the interfacial surface concentration and decreasing the surface tension.

7.3. Future Work

- The main limitation of the ovine mechanical model is that the compliance of the airways is not defined and as such the transmission of the pressure oscillation

frequencies and amplitudes from the airway opening to the alveolar level may not be accurately described in the model. Future work would involve defining the airway pressure vs. cross-sectional area relationship and defining the masses of the airway tissues.

- Even if a more complex model of the airways is achieved, the predicted values of pressure, flow and volume in a preterm lung will still need to be validated by experimental measurements. In-vivo clinical measurements at the level of the lobes may prove to be practically and ethically difficult. In the immediate future, it may be easier to construct a negative pressure lung chamber which will enable in-vitro experiments on excised lungs.

- The surface tension model may be improved by further studies that include surface viscoelasticity, bulk fluid inertia and surfactant layers rather than reservoirs. Also, the accuracy of the model can be improved by better refining values of D and k_1. An optimization code that adjusts the values of D and k_1 to minimize the error between the experimental and predicted values may be added to the numerical code.

- The custom-built PBS needs to be improved by adding real-time imaging, better optical lighting, greater magnification and a more accurate commercial software to measure the bubble dimensions with greater accuracy.

CHAPTER 8

References

1. Goldsmith, J.P. and E.H. Karotkin, *Assisted Ventilation of the Neonate*. 2003, Philadelphia: Saunders.
2. Parker, J.C., L.A. Hernandez, and K.J. Peevy, *Mechanisms of Ventilator-Induced Lung Injury.* Crit Care Med, 1993. **21**: p. 131-143.
3. Dreyfuss, D. and G. Saumon, *Ventilator-induced lung injury: lessons from experimental studies.* Am J Respir Crit Care Med, 1998. **157**: p. 294-323.
4. Pierson, D.J., *Alveolar rupture during mechanical ventilatiob: role of PEEP, peak airway pressure, and distending volume.* Respir Care, 1988. **33**: p. 472-486.
5. Robertson, B., J.J. Batenburg, and L.M. Van Golde, *Pulmonary surfactant*. 1994, Amsterdam: Elsevier.
6. Muscedere, J.G., et al., *Tidal ventilation at low airway pressures can augment lung injury.* Am J Respir Crit Care Med, 1994. **149**(5): p. 1327-1334.
7. Arold, S.P., et al., *Variable ventilation induces endogenuous surfactant release in normal guinea pigs.* Am J Physiol Lung Cell Mol Physiol, 2006. **285**: p. L370-L380.
8. Avery, M.E., et al., *Is Chronic Lung Disease in Low Birth Weight Infants Preventable? A Survey of Eight Centres.* Pediatrics, 1987. **79**(1): p. 26-29.
9. De Klerk, A.M. and R.K. De Klerk, *Nasal continuous positive airway pressure and outcomes of preterm infants* J.Pediatr.Child Health, 2001. **37**: p. 161-167.

10. Gitterman, M.K., et al., *Early nasal continuous positive airway pressure treatment reduces the need for intubation in very low birth weight infants.* Eur J Pedriatr, 1997. **156**: p. 384-388.

11. Jobe, A.H., et al., *Decreased Indicators of Lung Injury with Continuous Positive Expiratory Pressure in Preterm Lambs.* Pediatric Research, 2002. **52**(3).

12. Lee, K.S., et al., *A Comparison of Underwater Bubble Continuous Positive Airway Pressure with Ventilator-Derived Continuous Positive Airway Pressure in Premature Neonates Ready for Extubation.* Biology of the Neonate, 1998. **73**(69): p. 69-75.

13. Pillow, J., et al., *Bubble Continuous Positive Airway Pressure Enhances Lung Volume and Gas Exchange in Preterm Lambs.* Am. J. Respir. Crit. Care Med, 2007. **176**: p. 63-69.

14. Van Marter, L.J., et al., *Do Clinical Markers of Barotrauma and Oxygen Toxicity Explain Interhospital Variation in Rates of Chronic Lung Disease?* Pediatrics, 2000. **105**(6): p. 1194-1201.

15. Gray, H., *Gray's Anatomy of the Human Body*. 2000, Philedelphia: Lea and Febiger, 1918.

16. Polin, R.A. and W.W. Fox, *Fetal and Neonatal Physiology*. 2nd ed. 1997, Philadelphia: WB Saunders Co.

17. Avery, M.E. and J. Mead, *Surface Properties in Relation to Atelectasis and Hyaline Membrane Disease.* A.M.A J Dis Child, 1959. **97**: p. 517-523.

18. Been, J.V. and L.J.I. Zimmerman, *What's new in surfactant?* Eur J Pedriatr, 2007. **166**: p. 889-899.

19. Morley, C. and P. Davis, *Surfactant treatment for premature lung disorders: A review of best practices in 2002.* Paediatric Respiratory Reviews, 2004. **5**(Suppl A): p. S299-S304.

20. Donn, S.M. and S.K. Sinha, *Invasive and Noninvasive Neonatal Ventilation.* Respir Care, 2003. **48**: p. 426-441.

21. Greenough, A. and A. Sharma, *What is new in ventilation strategies for the neonate?* Eur J Pedriatr, 2007. **166**: p. 991-996.

22. Schreiner, R.L. and J.A. Kisling, *Practical Neonatal Respiratory Care*. 1982, New York: Raven Press.

23. Bezzant, T.B. and J.D. Mortensen, *Risks and Hazards of Mechanical Ventilation: A collective review of published literature.* Disease-a-Month, 1994. **40**: p. 581-640.

24. Jobe, A.H. and E. Bancalari, *Bronchopulmonary Dysplasia.* Am J Respir Crit Care Med, 2001. **163**: p. 1723-1729.

25. Slutsky, A.S. and L.N. Tremblay, *Multiple System Organ Failure. Is Mechanical Ventilation a Contributing Factor?* Am J Respir Crit Care Med, 1998. **157**: p. 1721-1725.

26. Coalson, J.J., V. Winter, and R.A. deLemos, *Decreased alveolarisation in baboon survivors with bronchopulmonary dysplasia.* Am J Respir Crit Care Med, 1995. **152**: p. 640-646.

27. Naik, A., et al., *Effects of different styles of ventilation on cytokine expression in preterm lamb lung.* Paediatric Respiratory Reviews, 2000. **47**: p. 370A.

28. Aly, H.Z., *Nasal Prongs Continuous Positive Airway Pressure: A Simple Yet Powerful Tool.* Pediatrics, 2001. **108**(3): p. 759-761.

29. Ganong, W.F., *Review of Medical Physiology*. 2001, New York: McGraw-Hill.

30. Marieb, E.N., *Human Anatomy and Physiology*. 4 ed. 1998, California: Benjamin/Cummings.

31. McKinley, M. and V. O'Loughlin, *Human Anatomy*. 2005, New York: McGraw-Hill.

32. West, J.B., *Respiratory Physiology. The Essentials*. 6th ed. 2000, Baltimore: Lippincott Williams and Wilkins.

33. Hall, S.B., et al., *Approximations in the measurement of surface tension on the oscillating bubble surfactometer.* Journal of Applied Physiology, 1993. **75**(1): p. 468-477.

34. De Jongh, F., *Ventilation Modelling of the Human Lung*, in *Faculty of Aerospace Engineering*. 1995, Delft University of Technology: Delft. p. 197.

35. Hall, S.B., et al., *Approximations in the measurement of surface tension on the oscillating bubble surfactometer.* American Physiological Society, 1993. **75**(1): p. 468-477.

36. *ATS/ERS Statement on Respiratory Muscle Testing.* Am J Respir Crit Care Med, 2002. **166**: p. 518-624.

37. Crimer, G.J., et al., *Critical Care Study Guide*. 2002, Philadelphia: Springer.

38. Kesler, M. and D.J. Durand, *Neonatal high-frequency ventilation. Past, present and future.* Clinical Perinatol, 2001. **28**(3): p. 579-607.

39. Owen, M.R. and M.A. Lewis, *The mechanics of lung tissue under high-frequency ventilation.* SIAM Journal on Applied Mathematics, 2001. **61**(5): p. 1731-1761.

40. Ritacca, F.V. and T.E. Stewart, *Clinical Review: High frequency osillatory ventilation in adults - a review of the literature and practical applications.* Crit Care, 2003. **7**: p. 385-390.

41. Wheeler, H.J., L.D.M. Nokes, and T. Powell, *A review of high frequency oscillation ventilation in the neonate.* Journal of Medical Engineering and Technology, 2007. **31**(5): p. 367-374.

42. Chang, H.K., *Mechanisms of gas transport during ventilation by high frequency oscillation.* J Appl Physiol, 1984. **56**(3): p. 553-563.

43. High, K.C., J.S. Ultham, and S.R. Karl, *Mechanically Induced Pendelluft Flow in a Model Airway Bifurcation During High Frequency Oscillation.* Transactions of the ASME, 1991. **113**: p. 342-347.

44. Courtney, S.E., et al., *High frequency oscillatory ventilation versus conventional mechanical ventilation for very low birth weight infants.* Pediatrics, 2002. **347**: p. 643-652.

45. Rimensberger, P.C., et al., *First Intention High Frequency Oscillation with Early Lung Volume Optimisation Improves Pulmonary Outcome in Low Birth Weight Infants With Respiratory Distress Syndrome.* Pediatrics, 2000. **105**: p. 1202-1208.

46. Locke, R., J.S. Greenspan, and T.H. Shaffer, *Effect of Nasal CPAP on thoracoabdominal motion in neonates with respiratory insufficiency.* Pediatric Pulmonology, 1991. **11**(3): p. 259-264.

47. de Klerk, A.M. and R.K. de Klerk, *Use of Continuous Positive Airways Pressure in Pretern Infants:Comments and Experience from New Zealand.* Pediatrics, 2001. **108**(3): p. 761-763.

48. DeKlerk, A.M. and R.K. DeKlerk, *Nasal continuous positive airway pressure and outcomes of preterm infants.* J Pediatr Child Health, 1987. **79**(1): p. 26-29.

49. Mazzella, M., et al., *A randomised control study comparing the Infant flow driver with nasal continuous positive airway pressure in preterm infants.* Arch Dis Child Fetal Neonatal, 2001. **35**: p. F86-F90.

50. Verder, H., et al., *Nasal Continuous Positive Airway Pressure and Early surfactant Therapy for Respiratory Distress Syndrome in Newborns of Less than 30 Weeks' Gestation.* Pediatrics, 1999. **103**(2): p. E24.

51. De Klerk, A.M. and R.K. De Klerk, *Nasal positive airway pressure and outcomes of preterm infants.* J Pediatr Child Health, 2001. **37**: p. 161-167.

52. Narendran, V., et al., *Early Bubble CPAP and outcomes in ELBW preterm infants.* J Perinatology, 2003. **23**(3): p. 195-9.

53. Avery, M.E., W. Tooley, and J.B. Keller, *Is Chronic Lung Disease in Low Birth Weight Infants Preventable? A Survey of Eight Centres.* Pediatrics, 1987. **79**(1): p. 26-29.

54. Arold, S.P., et al., *Variable Tidal Volume Ventilation Improves Lung Mechanics and Gas Exchange in a Rodent Model of Acute Lung Injury.* Am J Respir Crit Care Med, 2002. **165**: p. 366-371.

55. Suki, B., et al., *Life support system benefits from noise.* Nature, 1998. **393**: p. 127-128.

56. Manilal, P., *The Effect of Pressure Oscillations on Neonatal Breathing, Master of Engineering Thesis*, in *Diagnostics and Control Research Centre*. 2004, Auckland University of Technology: Auckland. p. 134.

57. Manilal, P., A. Al-Jumaily, and N. Prime. *The Effect of Pressure Oscillations on Neonatal Breathing*. in *2004 ASME International Mechanical Engineering Congress & Exposition*. November 13-19, 2004. Anaheim, California.

58. Mutch, W.A.C., et al., *Biologically Variable or Naturally Noisy Mechanical Ventilation Recruits Atelactic Lung.* Am J Respir Crit Care Med, 2000. **162**: p. 319-323.

59. Mutch, W.A.C., et al., *BVV increases arterial oxygenation over that seen with positive end-expiratory prssure alone in a porcine model of acute respiratory distress syndrome.* Crit Care Med, 2000. **28**(7): p. 2457-2463.

60. Otis, A.B., et al., *Mechanical Factors in Distribution of Pulmonasry Ventilation.* J Appl Physiol, 1956. **8**: p. 427-443.

61. Fredberg, J.J. and A. Hoenig, *Mechanical Response of the Lungs at High Frequencies.* J Biomech Eng, 1978. **100**: p. 57-65.

62. Fredberg, J.J., et al., *Canine Pulmonary Input Impedance Measured by Transient Forced Oscillations.* J Biomech Eng, 1978. **100**: p. 57-65.

63. Grimal, Q., A. Watzky, and S. Naili, *A one-dimensional model for the propagation of transient pressure waves through the lung.* Journal of Biomechanics, 2002. **35**(8): p. 1081-1089.

64. Dhanaraj, N. and R.M. Pidaparti. *Smooth Muscle Tissue Reponse to Applied Vibration Following Extreme Isotonic Shortening. Proceedings*. in *ASME International Mech Eng Congress and Exposition*. 2002,17-22 November. New Orleans.

65. Binks, A.P., et al., *Oscillation of the lung by chest-wall vibration.* Respiration Physiology, 2001. **126**: p. 245-249.

66. Homma, I., *Inspiratory inhibitory reflex caused by the chest-wall vibration in man.* Respiration Physiology, 1980. **39**: p. 345-353.

67. Manning, H.L., et al., *Effect of chest-wall vibration on breathlessness in normal subjects.* J Appl Physiol, 1991. **71**: p. 175-181.

68. Weibel, E.R., *Morphometry of the human lung*. 1963, New York: Academic Press: Springer-Verlag.

69. Hansen, J.E. and E.P. Ampaya, *Human air space shapes, sizes, areas, volumes.* J Appl Physiol, 1975. **38**(6): p. 990-995.

70. Horsfield, K., et al., *Models of the human bronchial tree.* J Appl Physiol, 1971. **31**(2): p. 207-217.

71. Tawhai, M.H., K.S. Burrowes, and E.A. Hoffman, *Computational models of structure-function relationships in the pulmonary circulation and their validation.* Exp Physiol, 2006. **91**(2): p. 285-293.

72. Woo, T., et al. *A comparison of various respiratory system models based on parameter estimates from impulse oscillometry data*. in *Proc 26th Annual Conf IEEE EMBS*. 2004. San Francisco.

73. Schmidt, M., et al., *Computer simulation of the measured rspiratory impedance in newborn infants and the effect of the measurement equipment.* Medical Engineering and Physics, 1998. **20**: p. 220-228.

74. Mead, J., *Mechanical properties of the lung.* Physiol Rev, 1961. **41**: p. 281-320.

75. Athanasiades, A., et al., *Energy analysis of a nonlinear model of the normal lung.* Journal of Biological Systems, 2000. **8**(2): p. 115-139.

76. Liu, C.H., et al., *Airway mechanics, gas exchange and blood flow in a nonlinear model of the normal human lung.* J Appl Physiol, 1998. **84**: p. 1447-1469.

77. Tomlinson, S.P., J.K.W. Lo, and D.G. Tilley, *Computer simulation of human interaction with underwater breathing equipment.* Proc Instu Mech Engrs, 1994. **208**: p. 249-261.

78. Tomlinson, S.P., D.G. Tilley, and C.R. Burrows, *Computer simulation of human interaction with underwater breathing equipment.* Journal of Engineering in Medicine, 1994. **208**: p. 249-261.

79. Crooke, P.S. and J.D. Head, *A general two-compartment model for mechanical ventilation.* Mathl Comput Modeling, 1996. **24**(7): p. 1-18.

80. Bates, J.H.T. and J. Milic-Emili, *Influence of the viscoelastic properties of the respiratory system on the energetically optimum breathing frequency.* Annals of Biomedical Engineering, 1993. **21**: p. 489-499.

81. Polak, A.G. and K.R. Lutchen, *Computational model for forced expiration from asymmetric normal lungs.* Annals of Biomedical Engineering, 2003. **31**(8): p. 891-907.

82. Horn, L.W. and S.H. Davis, *Apparent surface tension hysteresis of a dynamical system.* Journal of Colloid and Interface Science, 1975. **51**(3): p. 459-476.

83. Otis, D.R., et al., *Dynamic surface tension of surfactant TA:experiments and theory.* Journal of Applied Physiology, 1994. **77**(6): p. 2681-2688.

84. Morris, J., *Characterization of the Dynamic Behavior of Lung surfactant and its Components*, in *Mechanical Engineering*. 1995, Massachusetts Institute of Technology: Massachusetts. p. 138.

85. Morris, J., et al., *Dynamic Behavior of Lung Surfactant.* Journal of Biomechanical Engineering, 2001. **123**(1): p. 106-113.

86. Chang, C.H. and E.I. Franses, *Dynamic tension behavior of aqueous octanol solutions under constant-area and pulsating-area conditions.* Chemical Engineering Science, 1994. **49**(3): p. 313-325.

87. Schurch, S., et al., *Surface activity of lipid extract surfactant in relation to film area compression and collapse.* Journal of Applied Physiology, 1994. **77**(2): p. 974-986.

88. Reynolds, D.B. and J.-S. Lee, *Steady pressure-flow relationship of a model of the canine bronchial tree.* Journal of Applied Physiology, 1981. **51**(5): p. 1072-1079.

89. Lutchen, K.R., et al., *Airway and tissue mechanics during physiological breathing and bronchoconstriction in dogs.* J Appl Physiol, 1994. **77**: p. 373-385.

90. Mortola, J.P., A. Rossi, and L. Zocchi, *Pressure-volume curve of lung and lobes in kittens.* Journal of Applied Physiology: Respirat. Environ. Exercise Physiol, 1984. **56**(4): p. 948-953.

91. Ashrafi, M., et al., *Analysis of lamb lung development with tracheal ligation in left posterolateral diaphragmatic hernia in cases and controls.* Journal of Research in Medical Sciences, 2006. **11**(5): p. 319-324.

92. Ting, A., et al., *Alveolar Vascularization of the Lung in a Lamb Model of Congenital Diaphragmatic Hernia.* Am. J. Respir. Crit. Care Med., 1998. **157**(1): p. 31-34.

93. Lipsett, J., et al., *Restricted fetal growth and lung development: A morphometric analysis of pulmonary structure.* Pediatric Pulmonology, 2006. **41**(12): p. 1138-1145.

94. Venegas, J.G., R.S. Harris, and B.A. Simon, *A comprehensive equation for the pulmonary pressure-volume curve.* Journal of Applied Physiology, 1998. **84**(1): p. 389-395.

95. Pillow, J., et al., *Effects of Gestation and Antenatal Steroid on Airway and Tissue Mechanics in Newborn Lambs.* Am. J. Respir. Crit. Care Med., 2001. **163**(5): p. 1158-1163.

96. Kobayashi, H., et al., *Estimation of the Distribution Profile of Airway Resistance in the Lungs.* Computers and Biomedical Research, 1987. **20**: p. 507-525.

97. Ashgarian, B. and O.T. Price, *Airflow Distribution in the Human Lung and its Influence on Particle Deposition.* Inhalation Toxicology, 2006. **18**: p. 795-801.

98. Noppen, M., et al., *Volume and Cellular Content of Normal Pleural Fluid in Humans Examined by Pleural Lavage.* Am. J. Respir. Crit. Care Med, 2000. **162**(3): p. 1023-1026.

99. Light, R.W. and H. Hamm, *Malignant pleural effusion: would the real cause please stand up?* Eur Respir J, 1997. **10**: p. 1701-1702.

100. Doeblin, E., *Measurement Systems. Application and Design*. 4th ed. 1990, Singapore: McGraw Hill Inc.

101. Davis, G.M., et al., *Direct measurement of static chest wall compliance in animal and human neonates.* Journal of Applied Physiology, 1988. **65**(3): p. 1093-1098.

102. Willet, K.E., et al., *Pulmonary Interstitial Emphysema 24 Hours after Antenatal Betamethasone Treatment in Preterm Sheep.* Am. J. Respir. Crit. Care Med., 2000. **162**(3): p. 1087-1094.

103. Hiemenz, P.C., *Principles of colloid and surface chemistry*. 1986, New York: M.Dekker.

104. Brennan, C.E., *Fundamentals of Multiphase Flow.* 2005, Cambridge: Cambridge University Press.

105. Borwankar, R.P. and D.T. Wasan, *The kinetics of adsorption of surface active agents at gas-liquid surfaces.* Chemical Engineering Science, 1983. **38**(10): p. 1637-1649.

106. Chapra, S.C. and R. Canale, *Numerical Methods for Engineers w/ Engineering Subscription Card*. 2005: McGraw-Hill Science/Engineering/Math.

107. Patankar, S.V., *Numerical Heat Transfer and Fluid*. 1980, New York: McGraw-Hill Book Company.

108. Do, D.D. and R.G. Rice, *Applied Mathematics and Modeling for Chemical Engineers*. 1995, New York: John Wiley and Sons.

109. Seurynck, S.L., et al., *Optical monitoring of bubble size and shape in a pulsating bubble surfactometer.* Journal of Applied Physiology, 2005. **99**: p. 624-633.

110. Graves, D.J., et al., *Cinematographic Method for Measurement of Rapidly Changing Surface Tension-Area Functions.* Journal of Colloid and Interface Science, 1971. **37**(2): p. 303-311.

111. Lewis, M.J., *Physical Properties of Foods and Processing Systems*. 1990, Cambridge, England: Woodhead Publishing.

112. Lambert, R.K., et al., *A computational model for expiratory flow.* J Appl Physiol, 1982. **52**(1): p. 44-56.

113. Krueger, M.A. and D.P. Gaver, *A Theoretical Model of Pulmonary Surfactant Multilayer Collapse under Oscillating Area Conditions* Journal of Colloid and Interface Science, 2000. **229**: p. 353-364.

APPENDICES

Appendix A

Appendix A contains graphs of the first 5 seconds of recorded pressure, volume and flow rate signals from animals on CPAP and Bubble CPAP treatment, as specified by Table 4.1. Figures A 1 to A 12 contain the respiratory parameters for animals in group 1 i.e. CPAP treatment and Figures A 13 to A 24 contain the respiratory parameters for group 2 i.e. Bubble CPAP treatment.

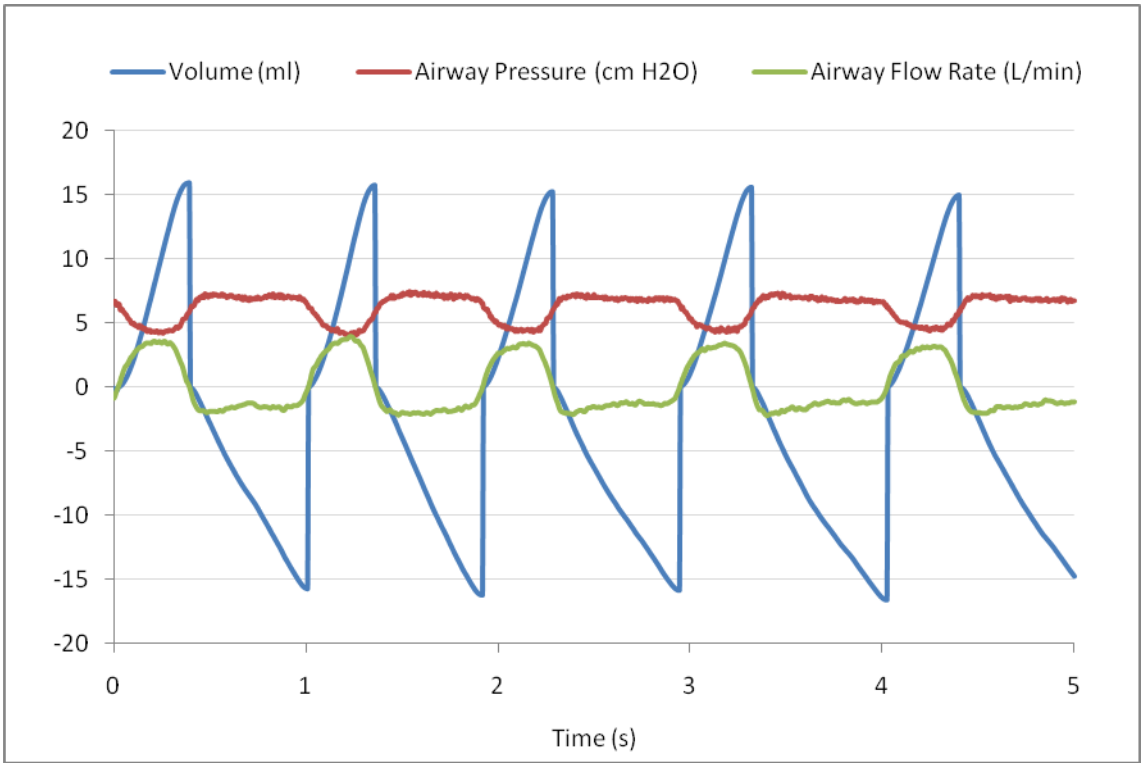

Figure A 1 Respiratory Parameters of Animal 5

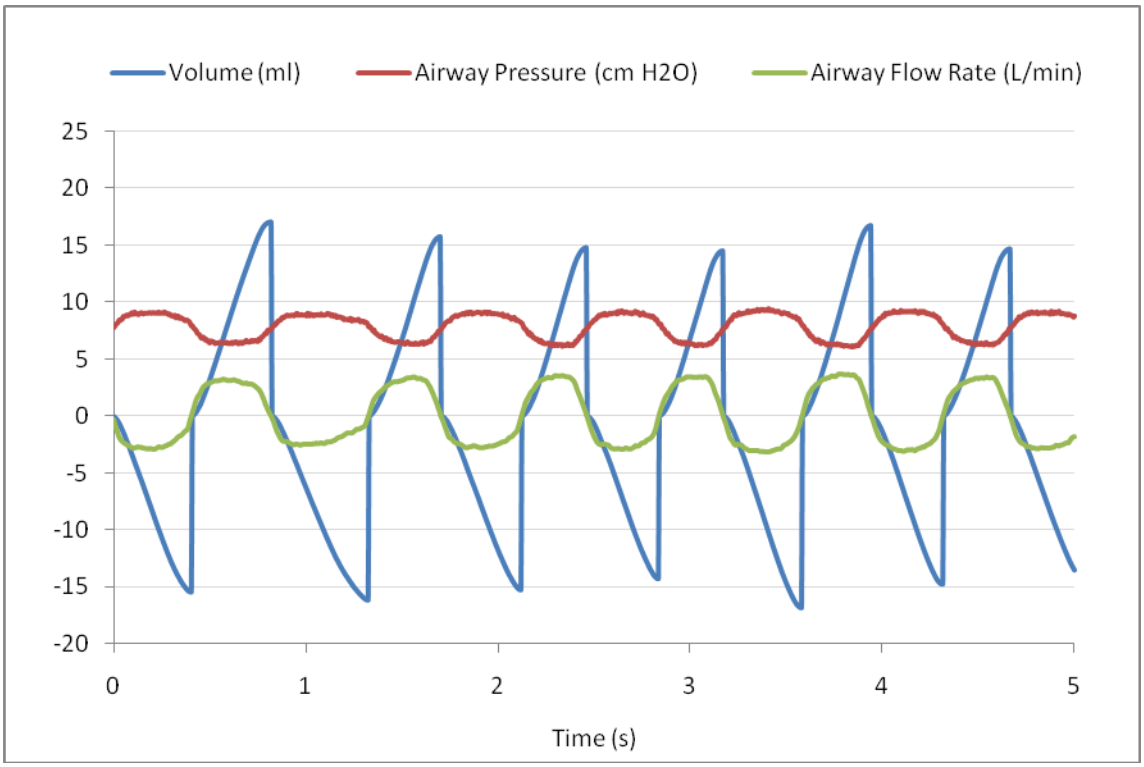

Figure A 2 Respiratory Parameters of Animal 7

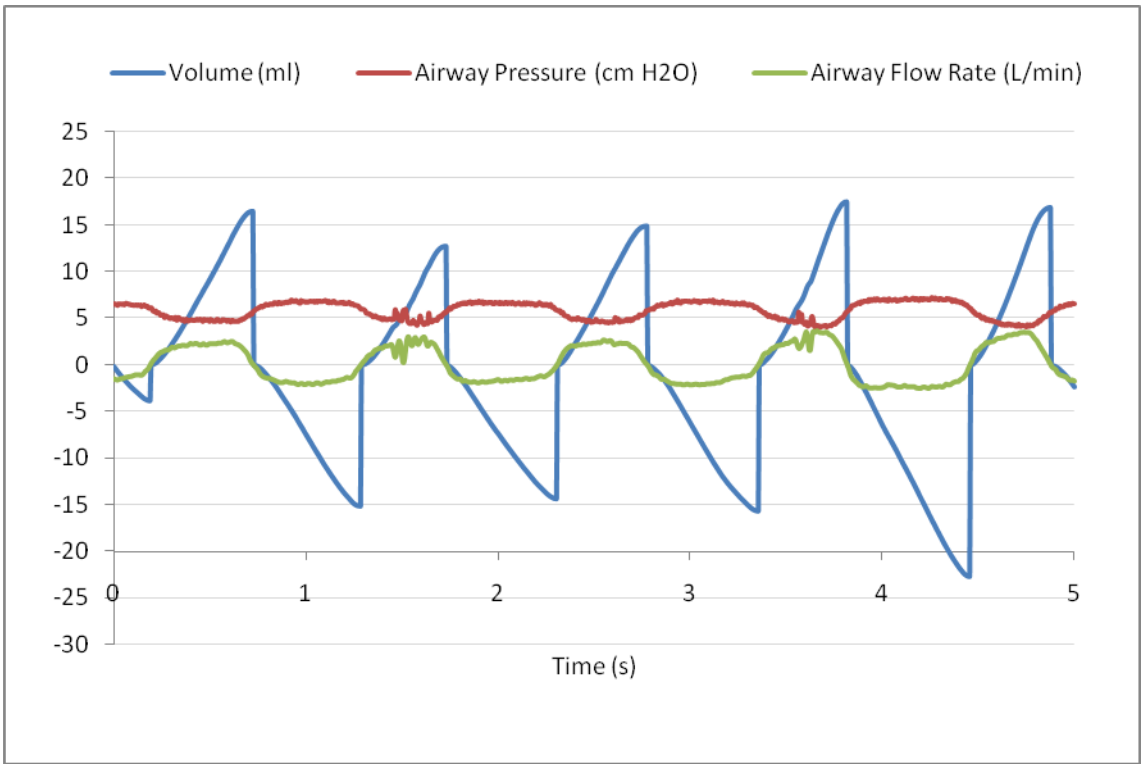

Figure A 3 Respiratory Parameters of Animal 13

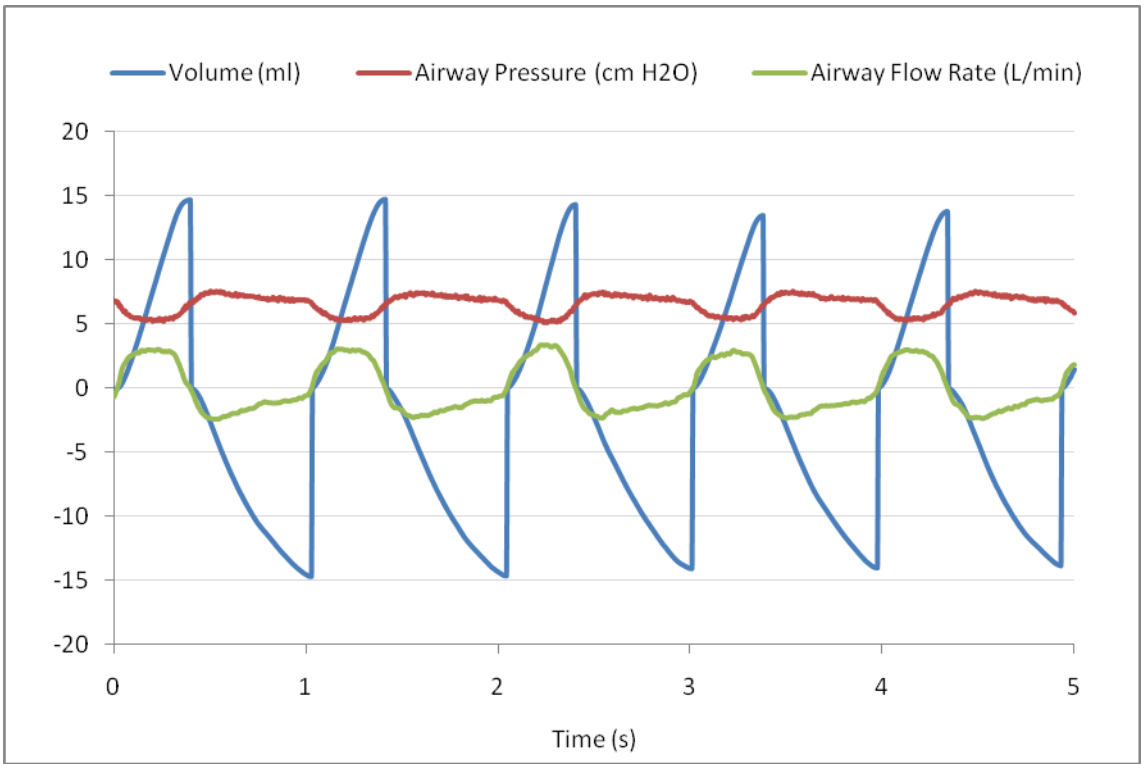

Figure A 4 Respiratory Parameters of Animal 19

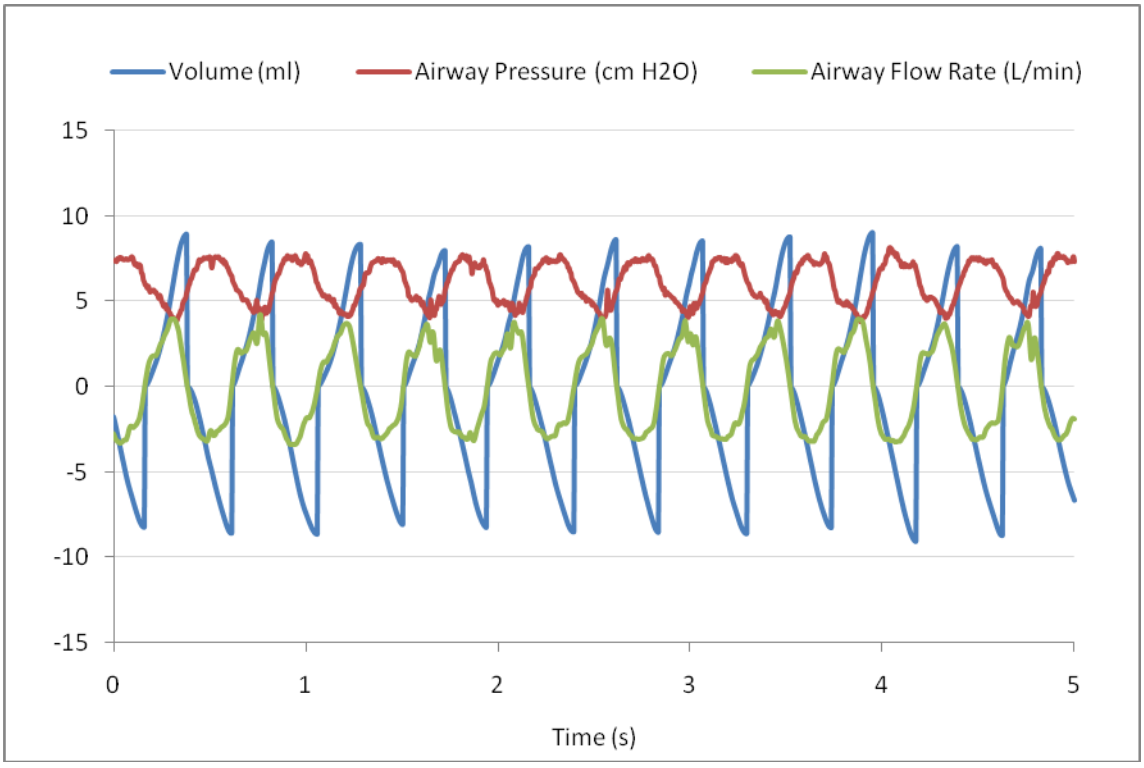

Figure A 5 Respiratory Parameters of Animal 24

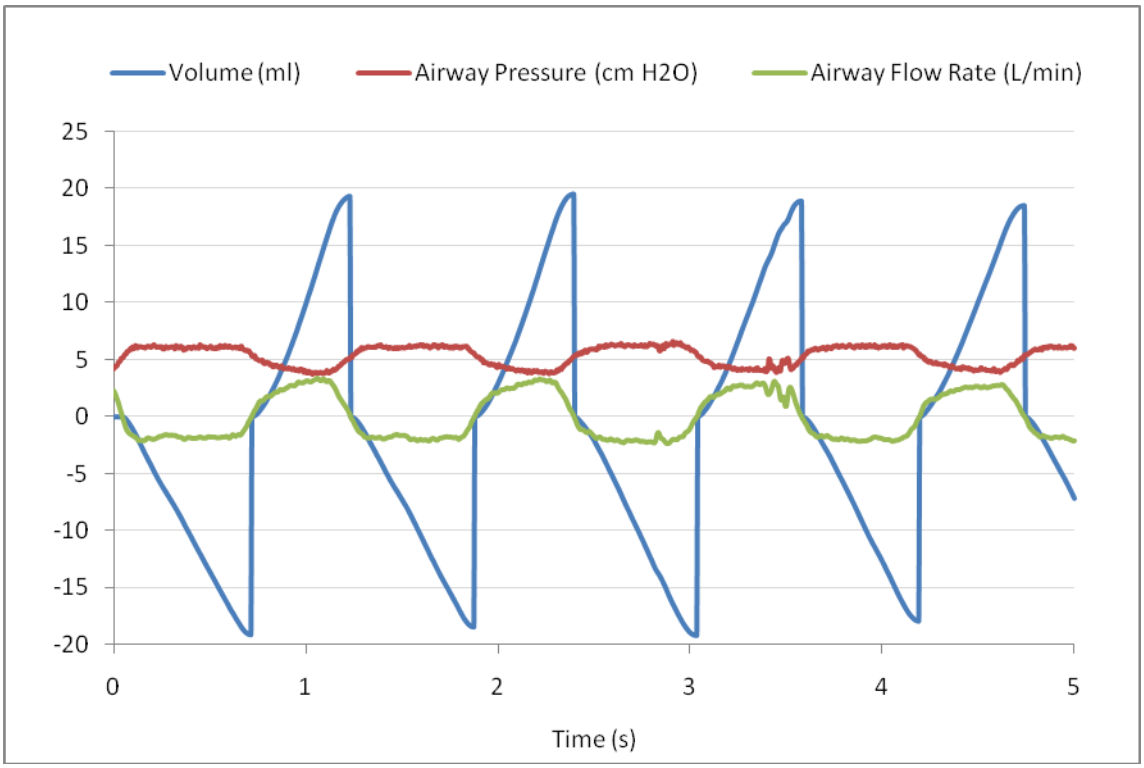

Figure A 6 Respiratory Parameters of Animal 27

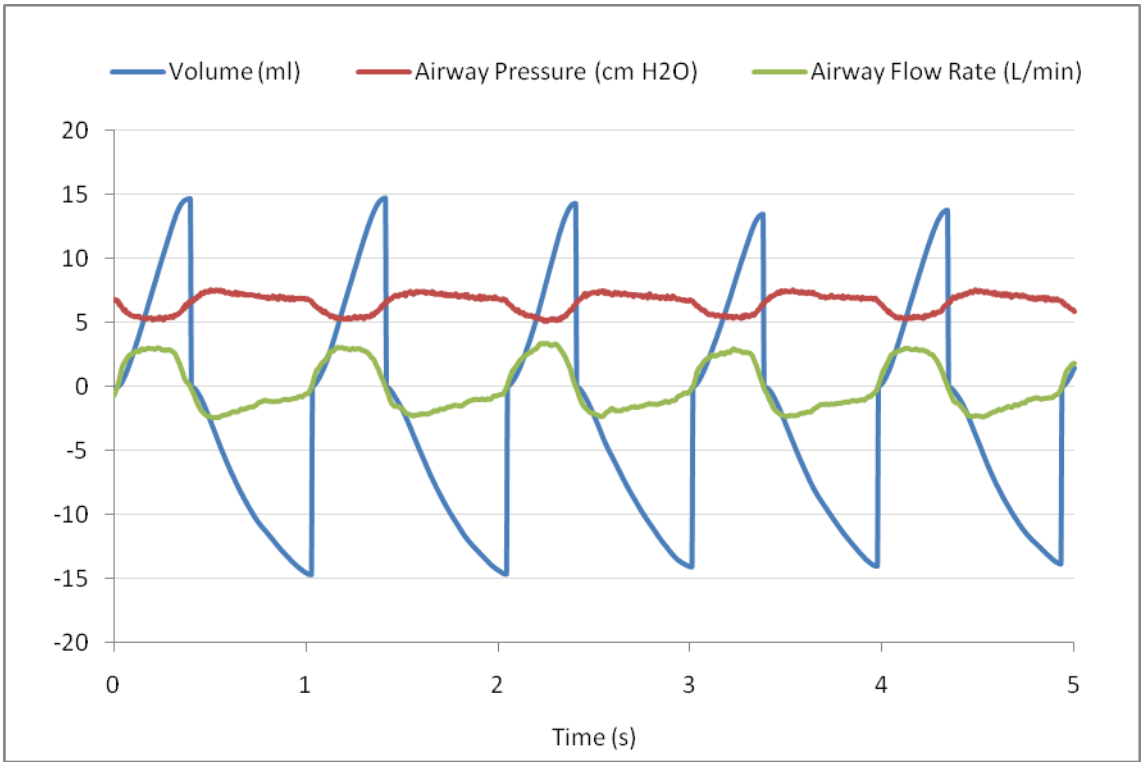

Figure A 7 Respiratory Parameters of Animal 30

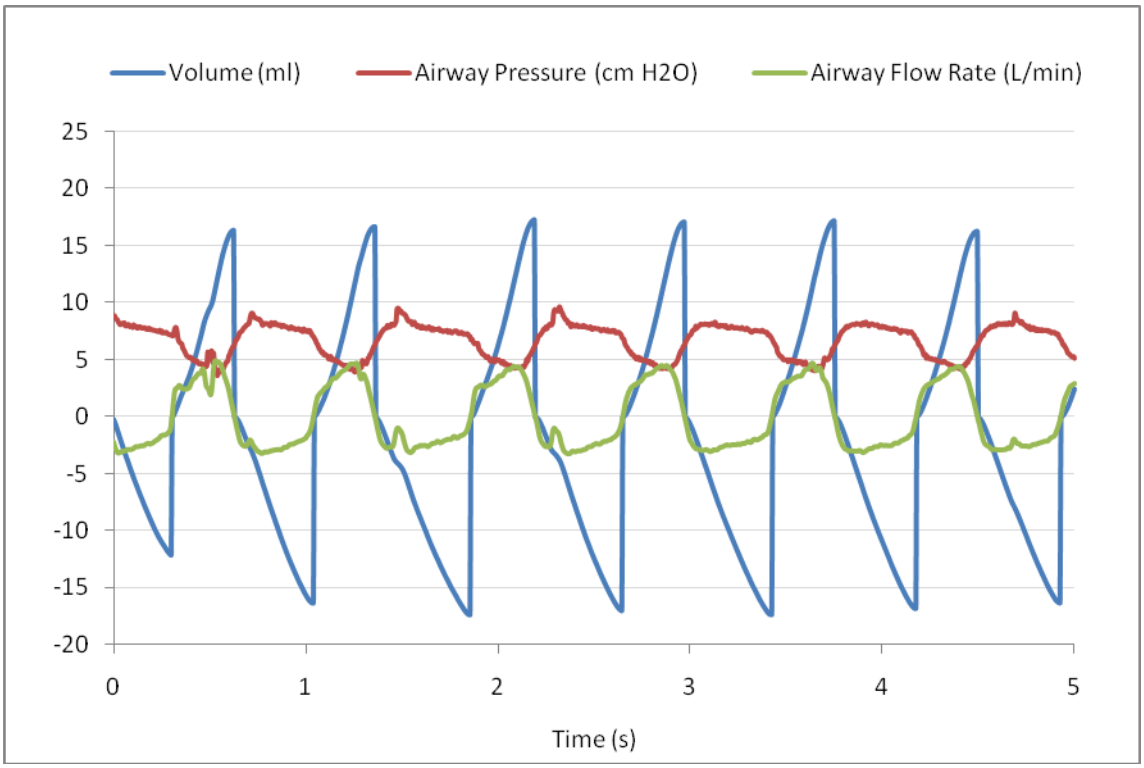

Figure A 8 Respiratory Parameters of Animal 31

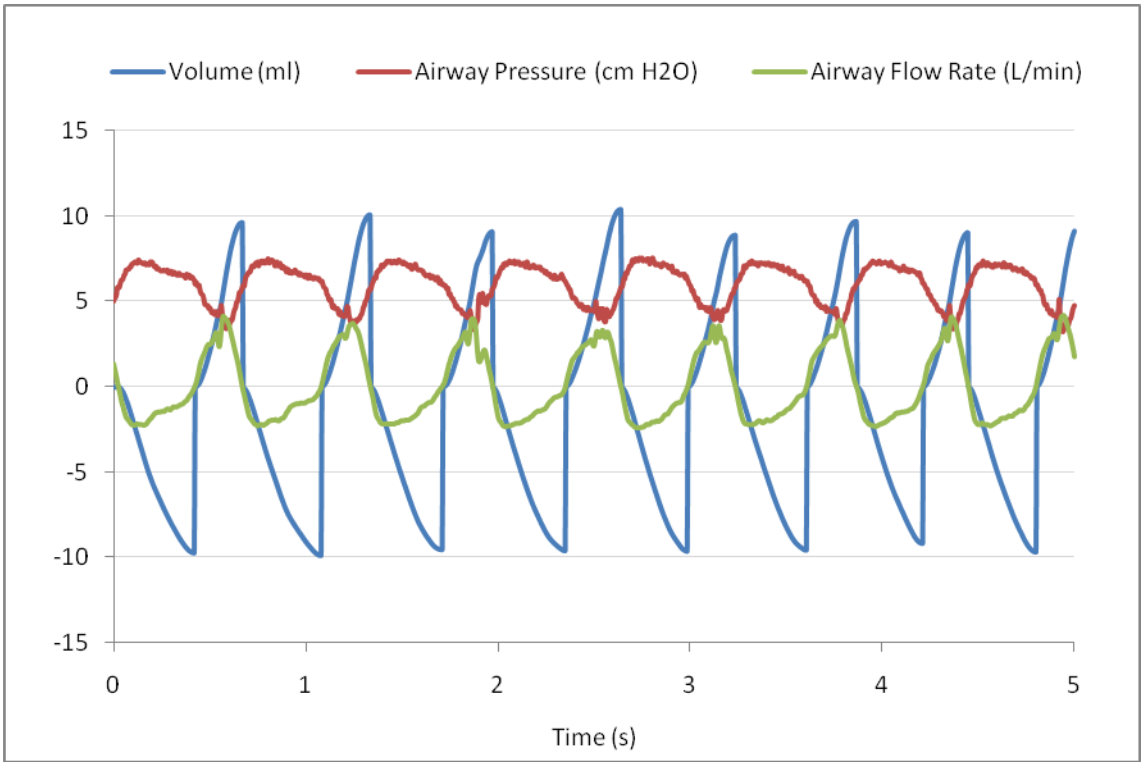

Figure A 9 Respiratory Parameters of Animal 44

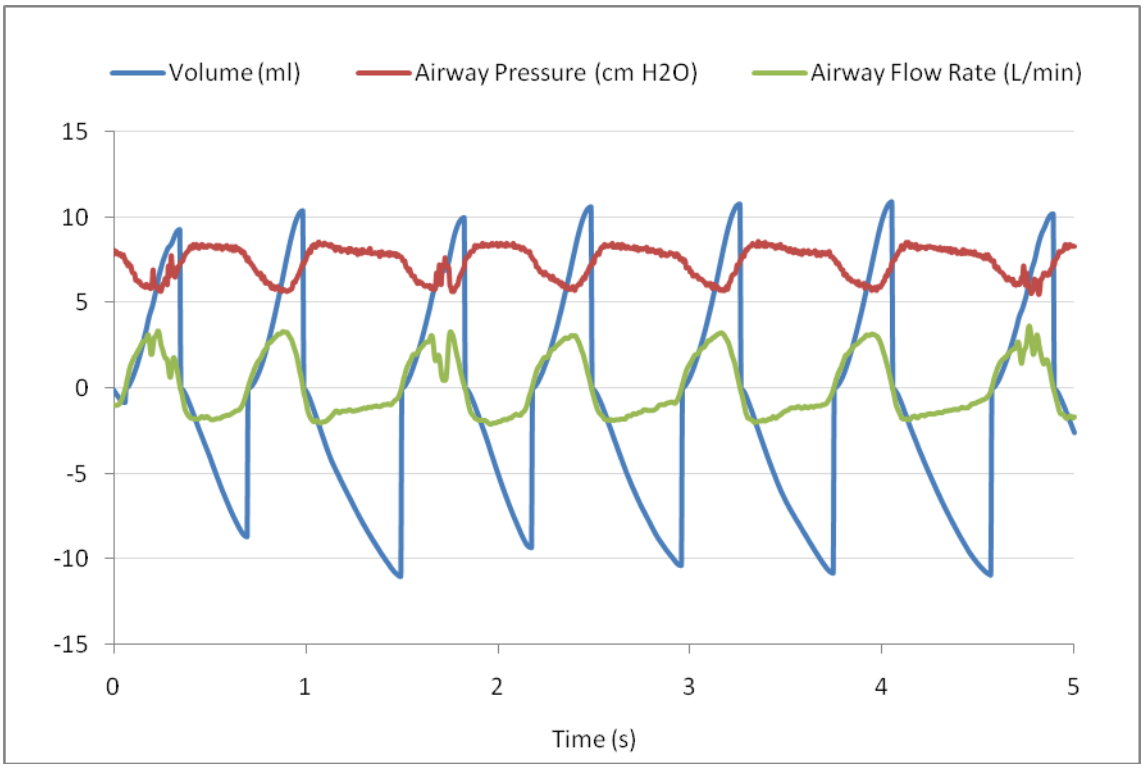

Figure A 10 Respiratory Parameters of Animal 45

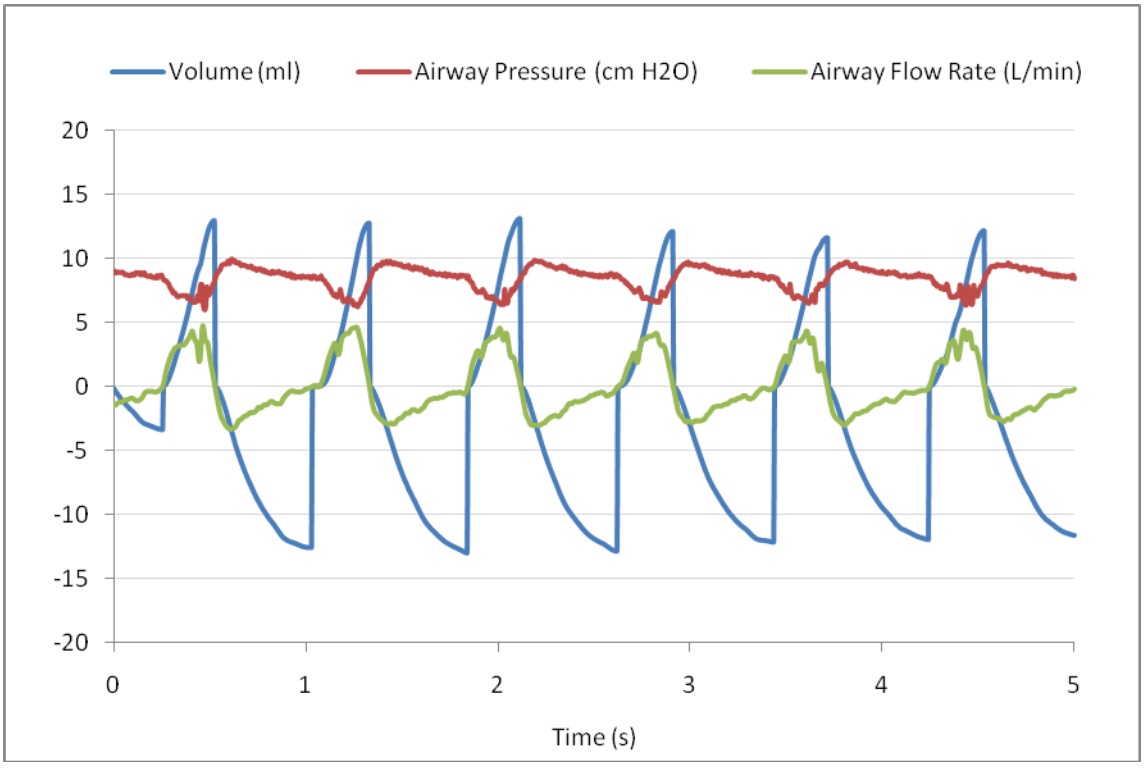

Figure A 11 Respiratory Parameters of Animal 67

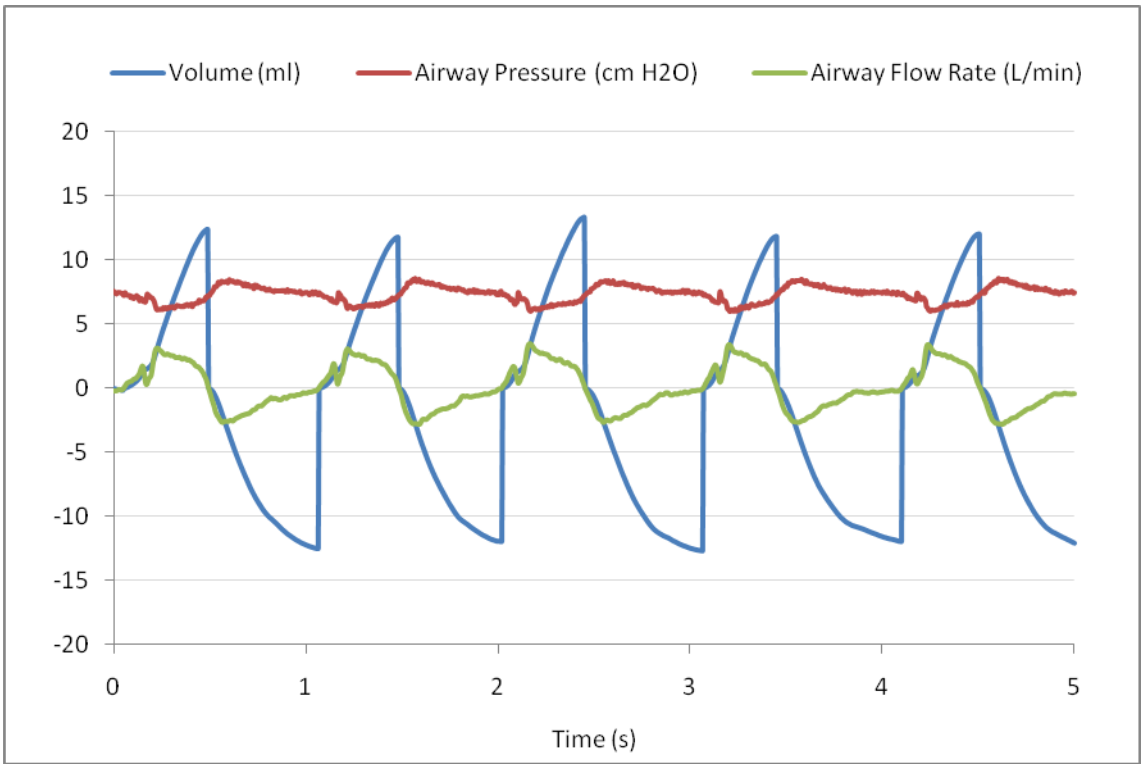

Figure A 12 Respiratory Parameters of Animal 73

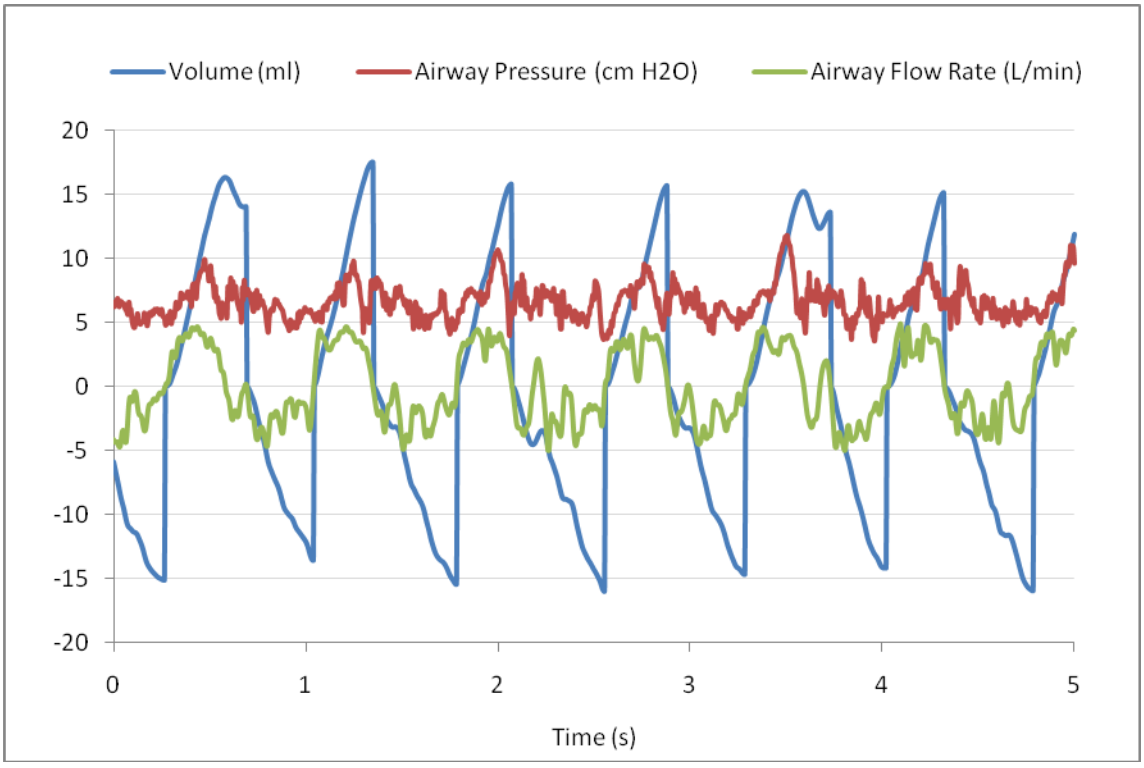

Figure A 13 Respiratory Parameters of Animal 1

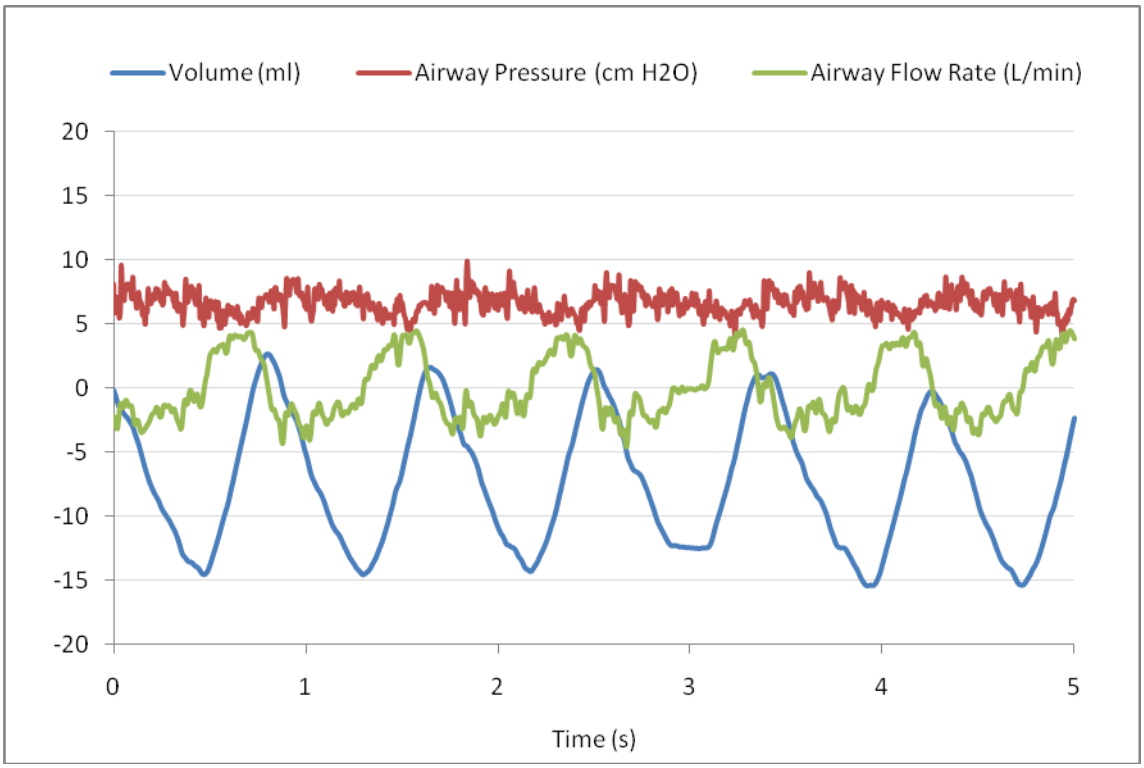

Figure A 14 Respiratory Parameters of Animal 3

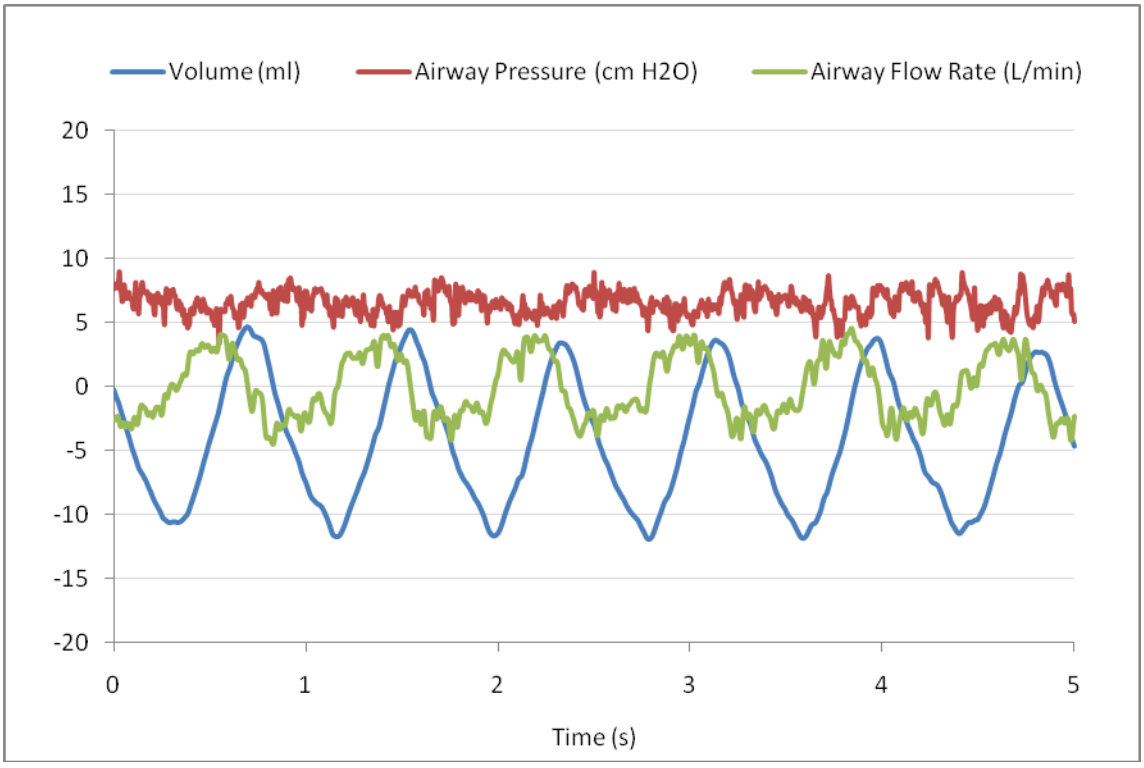

Figure A 15 Respiratory Parameters of Animal 9

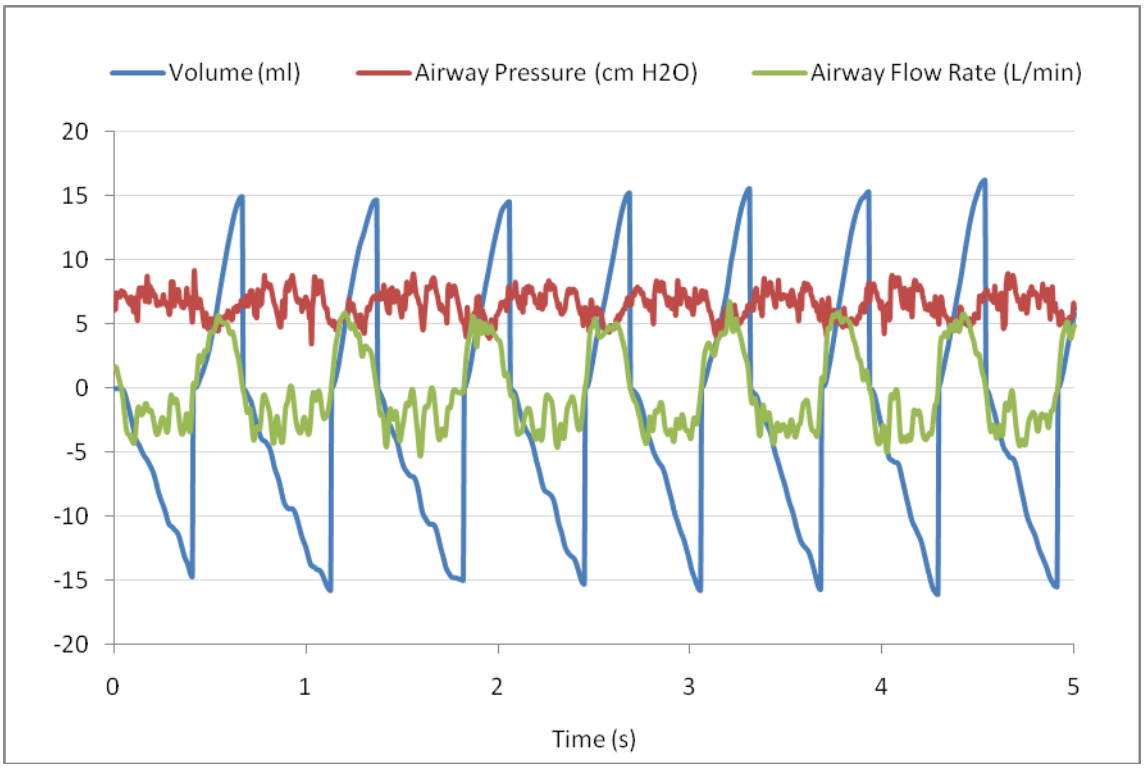

Figure A 16 Respiratory Parameters of Animal 11

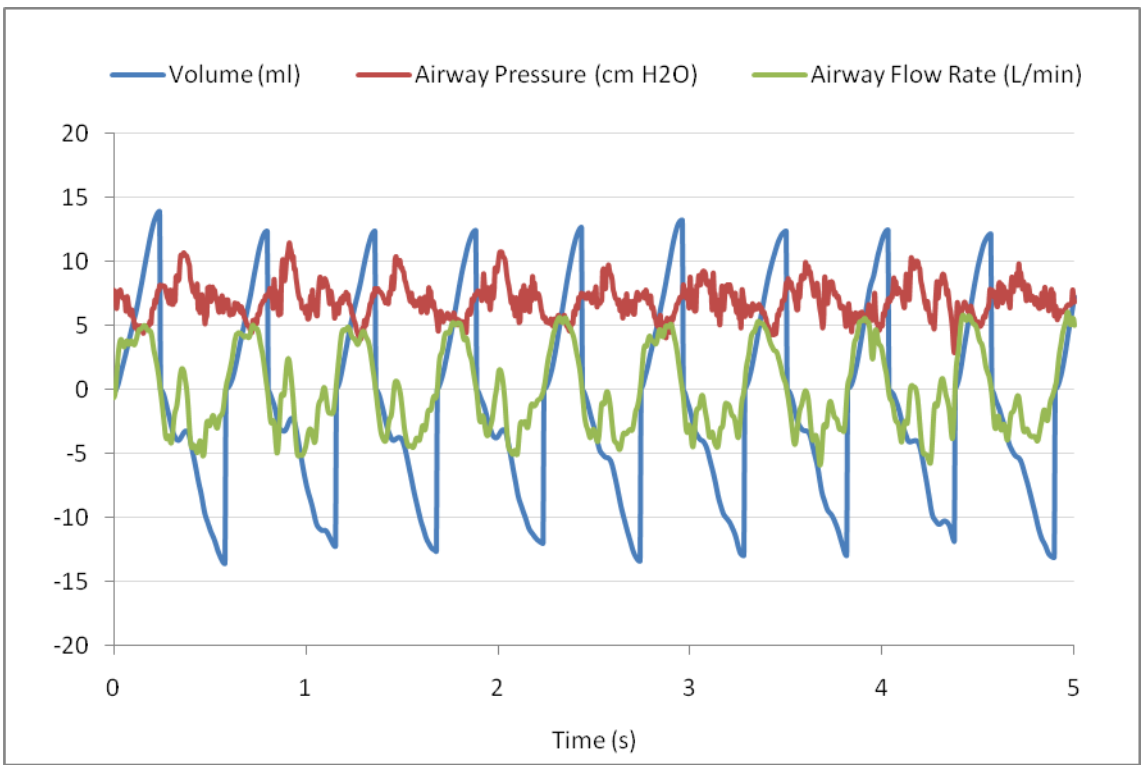

Figure A 17 Respiratory Parameters of Animal 17

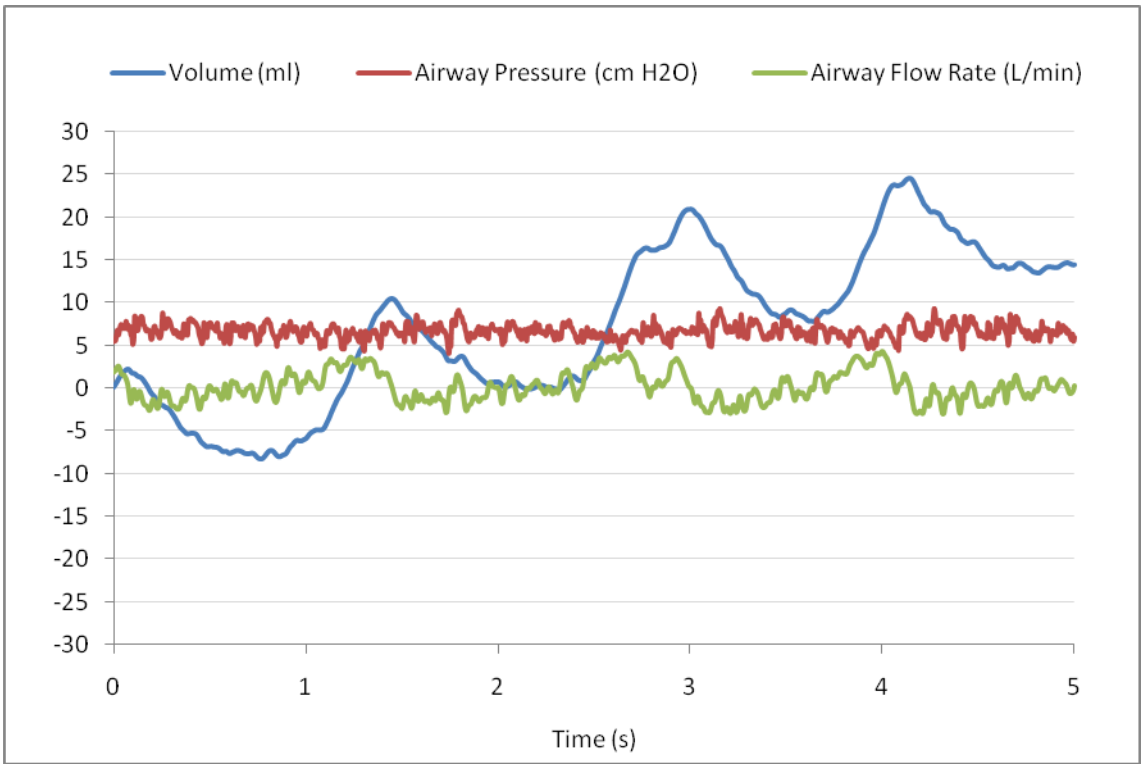

Figure A 18 Respiratory Parameters of Animal 20

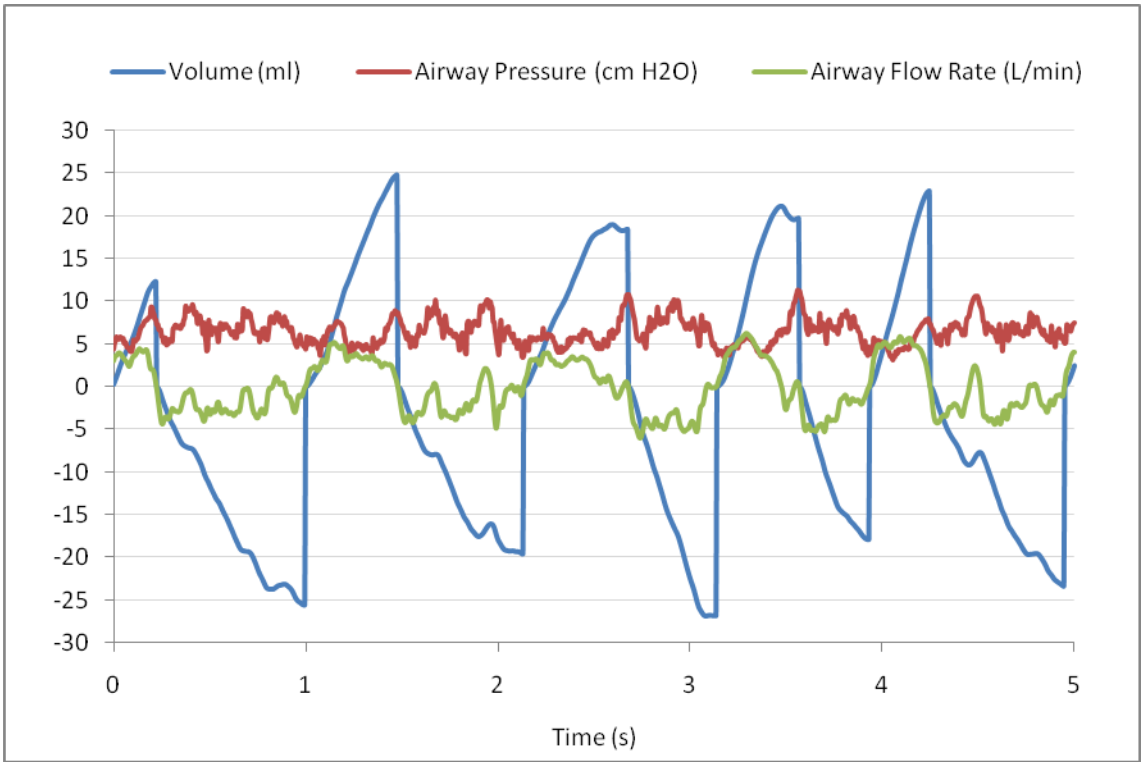

Figure A 19 Respiratory Parameters of Animal 21

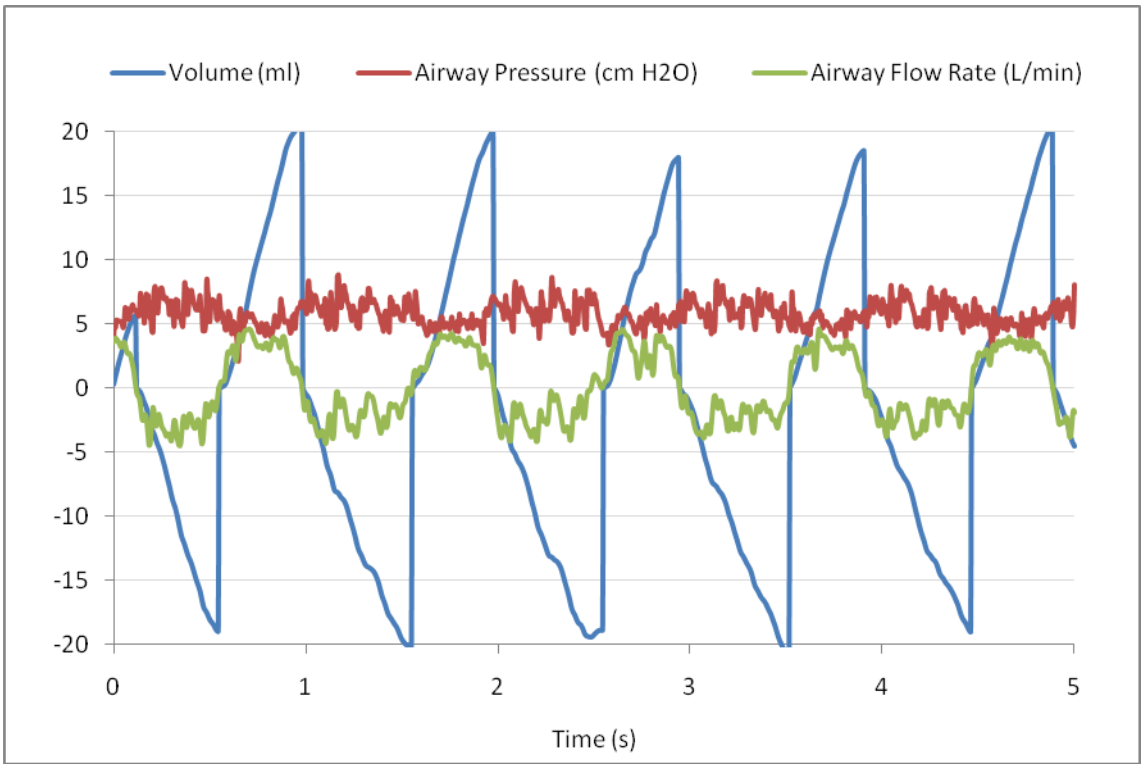

Figure A 20 Respiratory Parameters of Animal 23

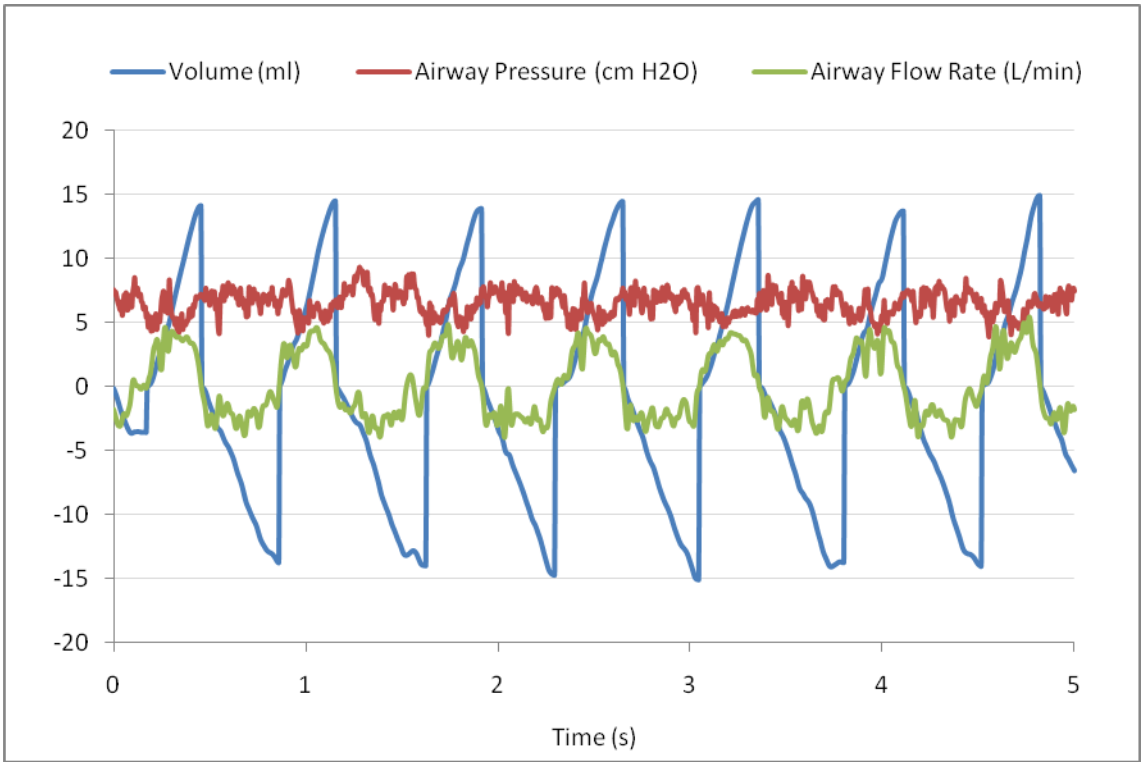

Figure A 21 Respiratory Parameters of Animal 29

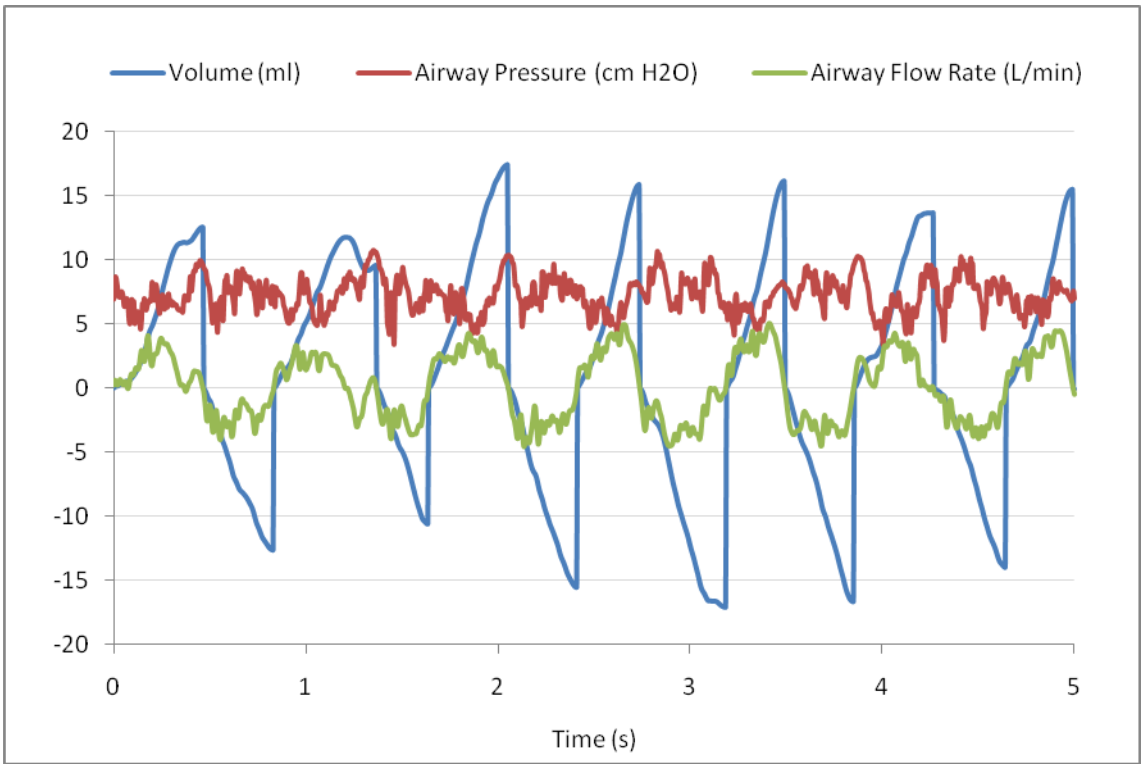

Figure A 22 Respiratory Parameters of Animal 32

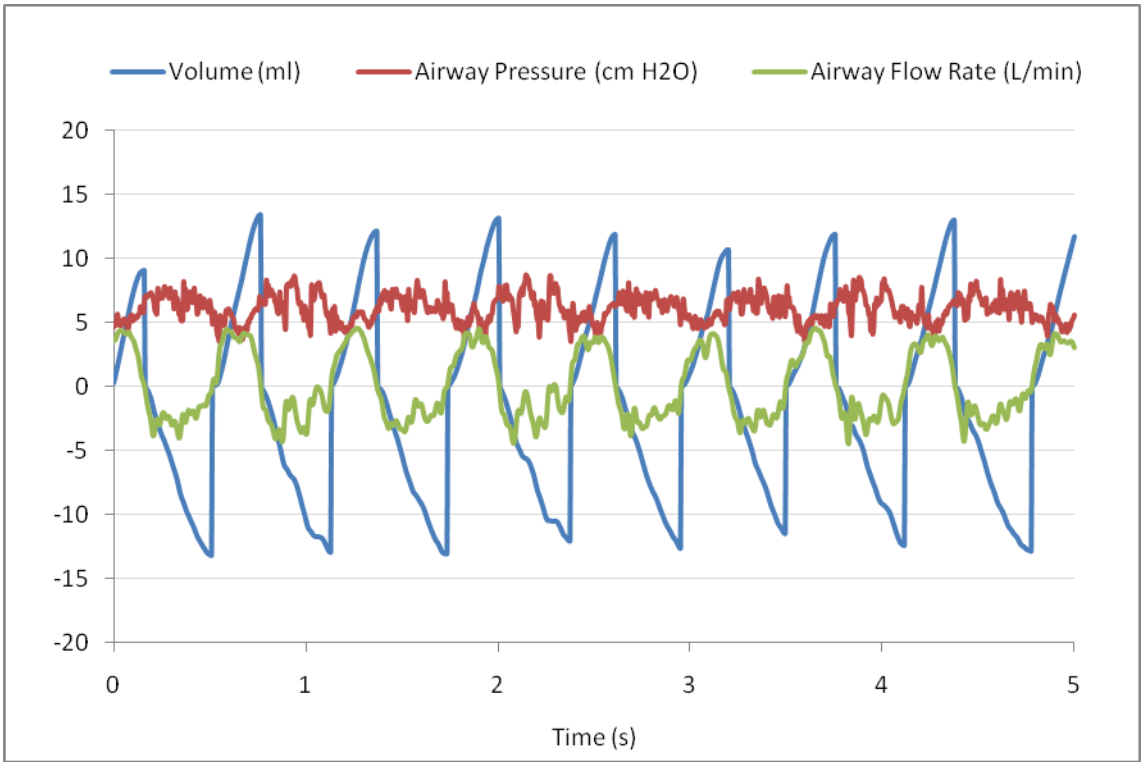

Figure A 23 Respiratory Parameters of Animal 43

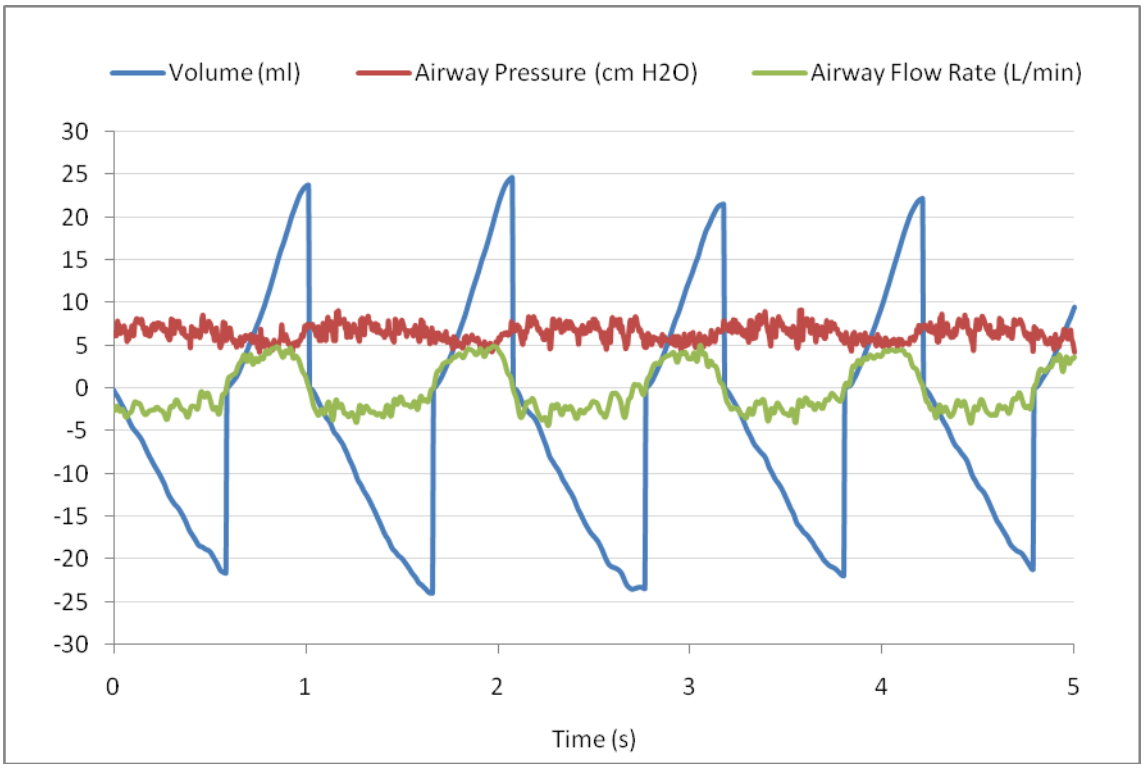

Figure A 24 Respiratory Parameters of Animal 46

Appendix B

Appendix B contains the graph of $\overline{WOB}_{total}$ calculated at the different locations in the lung for 128 day and 142 day gestations receiving 6.75 cm H_2O of CPAP.

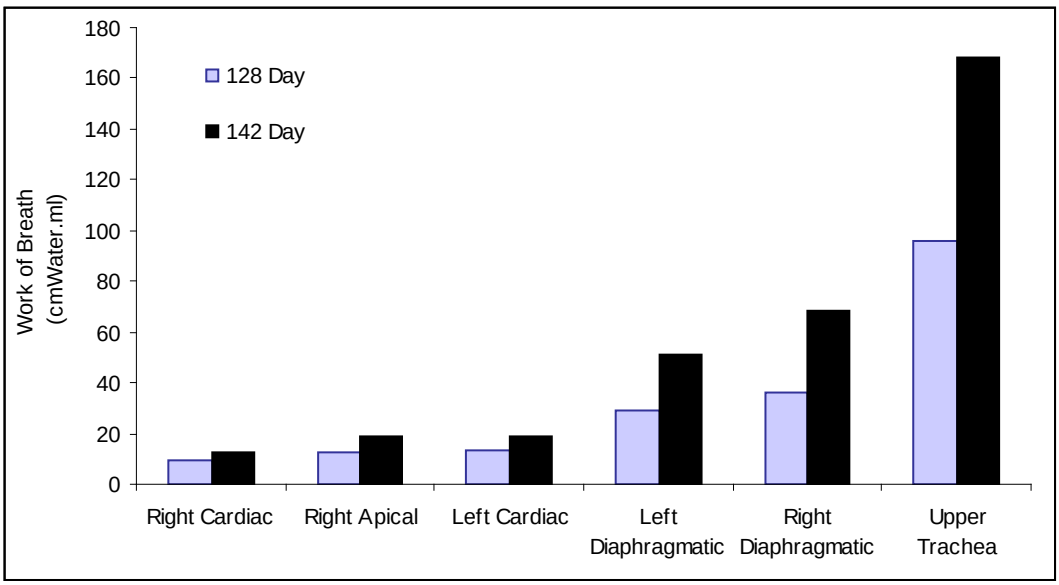

Figure B 1WOB of 128 day and 142 day gestation lambs receiving 6.75cm H_2O CPAP

Appendix C

Appendix C contains the values of the mean WOB for inspiration ($\overline{WOB}_{insp}$), expiration ($\overline{WOB}_{\exp}$) and the total breath ($\overline{WOB}_{total}$) at the airway opening and in each individual lobe that were determined from the simulations in section 4.4.3.

Table C 1 WOB parameters for simulation of CPAP-only simulation.

	$\overline{WOB}_{total}$	$\overline{WOB}_{insp}$	$\overline{WOB}_{\exp}$
Patient Interface	93.17915	49.86901	43.31015
Right Cardiac Lobe	9.569383	3.704735	5.864647
Right Apical Lobe	12.69443	4.120663	8.573765
Left Cardiac Lobe	13.26039	4.171545	9.088847
Left Diaphragmatic Lobe	29.04672	11.65338	17.39334
Right Diaphragmatic Lobe	36.35623	15.72541	20.63083
Airway Opening	95.71955	47.62888	48.09067

Table C 2 WOB parameters for CPAP + white noise simulation.

	$\overline{WOB}_{total}$	$\overline{WOB}_{insp}$	$\overline{WOB}_{\exp}$
Patient Interface	89.95121	48.72422	41.22699
Right Cardiac Lobe	9.279425	3.612391	5.667034
Right Apical Lobe	12.24462	3.976868	8.26775
Left Cardiac Lobe	12.81887	4.030017	8.788855
Left Diaphragmatic Lobe	28.15832	11.37301	16.78531
Right Diaphragmatic Lobe	35.34006	15.40903	19.93103
Airway Opening	92.5776	46.5465	46.0311

Table C 3 WOB parameters for Bubble CPAP simulation.

	$\overline{WOB}_{total}$	$\overline{WOB}_{insp}$	$\overline{WOB}_{\exp}$
Patient Interface	95.01227	49.2529	45.75937
Right Cardiac Lobe	9.726378	3.628242	6.098136
Right Apical Lobe	12.91967	3.997727	8.921947
Left Cardiac Lobe	13.47753	4.050853	9.426682

Left Diaphragmatic Lobe	29.57583	11.41421	18.16163
Right Diaphragmatic Lobe	37.01888	15.45672	21.56216
Airway Opening	97.64883	46.98253	50.6663

Table C 4 WOB parameters for CPAP +19Hz oscillation simulation.

	$\overline{WOB}_{total}$	$\overline{WOB}_{insp}$	$\overline{WOB}_{\exp}$
Patient Interface	97.25117	52.88691	44.36427
Right Cardiac Lobe	9.881578	3.914616	5.966962
Right Apical Lobe	13.11924	4.41252	8.706718
Left Cardiac Lobe	13.64728	4.441267	9.206017
Left Diaphragmatic Lobe	30.14686	12.38395	17.76291
Right Diaphragmatic Lobe	37.82216	16.68571	21.13645
Airway Opening	99.81452	50.54477	49.26975

Table C 5 WOB parameters for CPAP +23Hz oscillation simulation.

	$\overline{WOB}_{total}$	$\overline{WOB}_{insp}$	$\overline{WOB}_{\exp}$
Patient Interface	95.85824	50.77583	45.08241
Right Cardiac Lobe	9.790802	3.782958	6.007844
Right Apical Lobe	12.99331	4.222046	8.771263
Left Cardiac Lobe	13.52944	4.262406	9.267037
Left Diaphragmatic Lobe	29.82529	11.93093	17.89436
Right Diaphragmatic Lobe	37.42317	16.11511	21.30806
Airway Opening	98.52288	48.59974	49.92314

Table C 6 WOB parameters for CPAP +19&23Hz oscillation simulation.

	$\overline{WOB}_{total}$	$\overline{WOB}_{insp}$	$\overline{WOB}_{\exp}$
Patient Interface	98.70039	53.09014	45.61026
Right Cardiac Lobe	9.996129	3.935503	6.060625
Right Apical Lobe	13.25795	4.429182	8.828771
Left Cardiac Lobe	13.7761	4.455921	9.320177
Left Diaphragmatic Lobe	30.54953	12.46129	18.08823
Right Diaphragmatic Lobe	38.41648	16.8225	21.59398
Airway Opening	101.3256	50.79773	50.52789

Appendix D

Appendix D contains the values of the mean WOB for inspiration ($\overline{WOB}_{insp}$), expiration ($\overline{WOB}_{\exp}$) and the total breath ($\overline{WOB}_{total}$) at the airway opening and in each individual lobe that were determined from the simulations in section 4.4.4.

Table D 1 WOB parameters for simulation of CPAP-only simulation.

	$\overline{WOB}_{total}$	$\overline{WOB}_{insp}$	$\overline{WOB}_{\exp}$
Patient Interface	93.17915	49.86901	43.31015
Right Cardiac Lobe	9.569383	3.704735	5.864647
Right Apical Lobe	12.69443	4.120663	8.573765
Left Cardiac Lobe	13.26039	4.171545	9.088847
Left Diaphragmatic Lobe	29.04672	11.65338	17.39334
Right Diaphragmatic Lobe	36.35623	15.72541	20.63083
Airway Opening	95.71955	47.62888	48.09067

Table D 2 WOB parameters for CPAP + white noise simulation.

	$\overline{WOB}_{total}$	$\overline{WOB}_{insp}$	$\overline{WOB}_{\exp}$
Patient Interface	90.07805	50.01135	40.0667
Right Cardiac Lobe	9.275551	3.699186	5.576365
Right Apical Lobe	12.23053	4.101491	8.129038
Left Cardiac Lobe	12.79086	4.144972	8.645892
Left Diaphragmatic Lobe	28.11853	11.64929	16.46923
Right Diaphragmatic Lobe	35.32755	15.75983	19.56772
Airway Opening	92.612	47.6397	44.9723

Table D 3 WOB parameters for CPAP +19Hz oscillation simulation.

	$\overline{WOB}_{total}$	$\overline{WOB}_{insp}$	$\overline{WOB}_{\exp}$
Patient Interface	94.67988	52.35126	42.32862
Right Cardiac Lobe	9.603093	3.886799	5.716294
Right Apical Lobe	12.72228	4.385956	8.336324
Left Cardiac Lobe	13.26848	4.420441	8.848041
Left Diaphragmatic Lobe	29.23182	12.2799	16.95191
Right Diaphragmatic Lobe	36.65268	16.51374	20.13894
Airway Opening	96.39125	49.79217	46.59908

Table D 4 WOB parameters for CPAP +23Hz oscillation simulation.

	$\overline{WOB}_{total}$	$\overline{WOB}_{insp}$	$\overline{WOB}_{\exp}$
Patient Interface	94.57241	51.54629	43.02612
Right Cardiac Lobe	9.568605	3.770938	5.797667
Right Apical Lobe	12.66329	4.210282	8.453008
Left Cardiac Lobe	13.20558	4.24987	8.95571
Left Diaphragmatic Lobe	29.12521	11.90082	17.22438
Right Diaphragmatic Lobe	36.53869	16.06137	20.47732
Airway Opening	96.04413	48.51263	47.5315

Table D 5 WOB parameters for CPAP +28Hz oscillation simulation.

	$\overline{WOB}_{total}$	$\overline{WOB}_{insp}$	$\overline{WOB}_{\exp}$
Patient Interface	94.78439	51.68361	43.10078
Right Cardiac Lobe	9.575143	3.778968	5.796175
Right Apical Lobe	12.66484	4.2195	8.445345
Left Cardiac Lobe	13.23037	4.266001	8.964371
Left Diaphragmatic Lobe	29.15273	11.92897	17.22376
Right Diaphragmatic Lobe	36.58744	16.10102	20.48643
Airway Opening	96.15659	48.61746	47.53913

Table D 6 WOB parameters for CPAP +33Hz oscillation simulation.

	$\overline{WOB}_{total}$	$\overline{WOB}_{insp}$	$\overline{WOB}_{\exp}$
Patient Interface	94.95663	51.78965	43.16698
Right Cardiac Lobe	9.580832	3.785585	5.795247
Right Apical Lobe	12.69442	4.235689	8.458729
Left Cardiac Lobe	13.26665	4.28393	8.98272
Left Diaphragmatic Lobe	29.17632	11.95225	17.22407
Right Diaphragmatic Lobe	36.6291	16.13413	20.49497
Airway Opening	96.25471	48.70516	47.54955

Table D 7 WOB parameters for CPAP +44Hz oscillation simulation.

	$\overline{WOB}_{total}$	$\overline{WOB}_{insp}$	$\overline{WOB}_{\exp}$
Patient Interface	95.48197	52.39683	43.08515
Right Cardiac Lobe	9.622259	3.849884	5.772375
Right Apical Lobe	12.77802	4.336811	8.441208
Left Cardiac Lobe	13.33789	4.377651	8.96024
Left Diaphragmatic Lobe	29.26828	12.15021	17.11807
Right Diaphragmatic Lobe	36.76294	16.38694	20.376
Airway Opening	96.25471	48.70516	47.54955

Table D 8 WOB parameters for CPAP +49Hz oscillation simulation.

	$\overline{WOB}_{total}$	$\overline{WOB}_{insp}$	$\overline{WOB}_{\exp}$
Patient Interface	95.4752	52.36299	43.11221
Right Cardiac Lobe	9.623751	3.846143	5.777608
Right Apical Lobe	12.77934	4.330691	8.44865
Left Cardiac Lobe	13.33981	4.372019	8.967791
Left Diaphragmatic Lobe	29.27013	12.13662	17.13351
Right Diaphragmatic Lobe	36.7712	16.37271	20.39848
Airway Opening	96.63225	49.40558	47.22667

Table D 9 WOB parameters for CPAP +54Hz oscillation simulation.

	$\overline{WOB}_{total}$	$\overline{WOB}_{insp}$	$\overline{WOB}_{\exp}$
Patient Interface	95.37028	52.28493	43.08535
Right Cardiac Lobe	9.636305	3.847101	5.789204
Right Apical Lobe	12.78369	4.326669	8.457019
Left Cardiac Lobe	13.33507	4.36542	8.969647
Left Diaphragmatic Lobe	29.27987	12.12833	17.15154
Right Diaphragmatic Lobe	36.77449	16.35939	20.41511
Airway Opening	96.73566	49.41339	47.32228

Table D 10 WOB parameters for CPAP +81Hz oscillation simulation.

	$\overline{WOB}_{total}$	$\overline{WOB}_{insp}$	$\overline{WOB}_{\exp}$
Patient Interface	95.03028	52.02126	43.00903
Right Cardiac Lobe	9.638297	3.829627	5.80867
Right Apical Lobe	12.77325	4.295767	8.477479
Left Cardiac Lobe	13.31675	4.333468	8.983279
Left Diaphragmatic Lobe	29.30815	12.07782	17.23033
Right Diaphragmatic Lobe	36.73466	16.26841	20.46625
Airway Opening	96.78008	49.19941	47.58067

Table D 11 WOB parameters for CPAP +88Hz oscillation simulation.

	$\overline{WOB}_{total}$	$\overline{WOB}_{insp}$	$\overline{WOB}_{\exp}$
Patient Interface	95.30101	52.0515	43.24951
Right Cardiac Lobe	9.649684	3.837776	5.811908
Right Apical Lobe	12.78674	4.306123	8.480616
Left Cardiac Lobe	13.32898	4.343139	8.985845
Left Diaphragmatic Lobe	29.34833	12.10598	17.24234
Right Diaphragmatic Lobe	36.79395	16.30784	20.48611
Airway Opening	96.94571	49.31921	47.6265

Table D 12 WOB parameters for CPAP +99Hz oscillation simulation.

	$\overline{WOB}_{total}$	$\overline{WOB}_{insp}$	$\overline{WOB}_{\exp}$
Patient Interface	95.27124	52.10623	43.165
Right Cardiac Lobe	9.651363	3.83993	5.811433
Right Apical Lobe	12.78889	4.309146	8.479743
Left Cardiac Lobe	13.33124	4.346067	8.985171
Left Diaphragmatic Lobe	29.35312	12.11297	17.24015
Right Diaphragmatic Lobe	36.79885	16.31637	20.48248
Airway Opening	96.96819	49.3579	47.61029

Table D 13 WOB parameters for CPAP +111Hz oscillation simulation.

	$\overline{WOB}_{total}$	$\overline{WOB}_{insp}$	$\overline{WOB}_{\exp}$
Patient Interface	94.77323	51.83914	42.93409
Right Cardiac Lobe	9.632648	3.832605	5.800043
Right Apical Lobe	12.76761	4.301604	8.46601
Left Cardiac Lobe	13.32405	4.343026	8.981027
Left Diaphragmatic Lobe	29.28403	12.08552	17.19851
Right Diaphragmatic Lobe	36.69018	16.27123	20.41895
Airway Opening	96.67328	49.21016	47.46311

Table D 14 WOB parameters for CPAP +113Hz oscillation simulation.

	$\overline{WOB}_{total}$	$\overline{WOB}_{insp}$	$\overline{WOB}_{\exp}$
Patient Interface	94.63306	51.73567	42.89739
Right Cardiac Lobe	9.628756	3.833308	5.795447
Right Apical Lobe	12.76351	4.303527	8.459979
Left Cardiac Lobe	13.32235	4.345533	8.976822
Left Diaphragmatic Lobe	29.26945	12.08717	17.18228
Right Diaphragmatic Lobe	36.66651	16.27066	20.39585
Airway Opening	96.61098	49.20922	47.40177

Appendix E

Appendix E contains the derivation of the convection-diffusion equation used in section 5.2.1.

Convection-Diffusion Equation Derivation

Much can be learnt from the simplest possible case of convection-diffusion phenomena in a one dimensional situation in which convection and diffusion are present in the x direction only. Two solutions of different concentrations are separated by a hypothetical porous plug of thickness dx in Figure E 1. This plug can be considered as a control volume cell of thickness Δx with flux J_{in} entering at x and flux J_{out} leaving at $x+dx$.

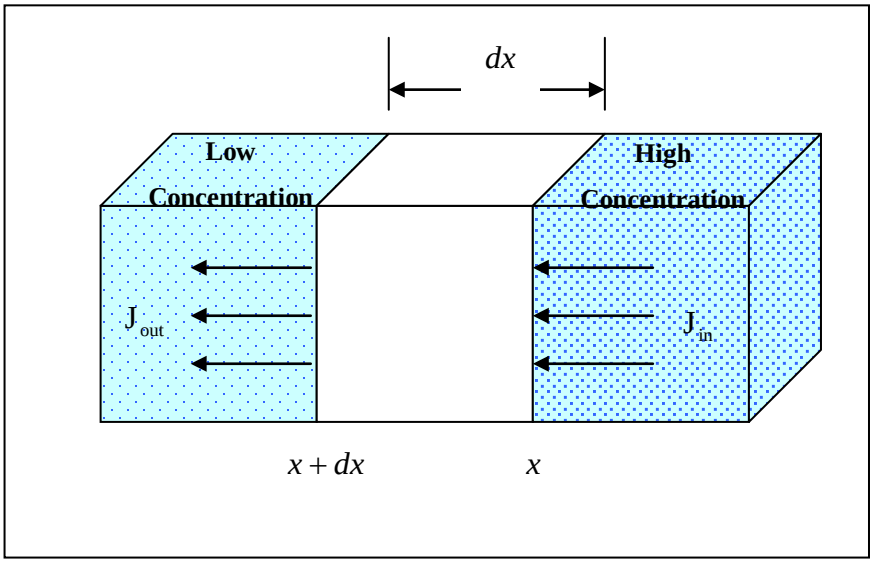

Figure E 1 One dimensional convection-diffusion phenomenon.

J_{in} and J_{out} are defined as the mass flow rate of the solute per unit area over which it occurs and have the units of $kg.m^{-2}.s^{-1}$. The flux has two components; there is a

convective (also known as advective) component J_c and a diffusive (also known as dispersive) component J_d. The convective component J_c can be expressed as

$$J_c = vC \qquad \textbf{(E1)}$$

where v is the velocity of the fluid ($m.s^{-1}$) and C is the concentration ($kg.m^{-3}$). The diffusive component J_d is driven by concentration gradients and can be expressed using Fick's Law for diffusive flux as

$$J_d = -D\frac{\partial C}{\partial x} \qquad \textbf{(E2)}$$

where D is the diffusion coefficient ($m^2.s^{-1}$). To derive the differential equation describing the concentration as a function of time and position, we first we consider the concentration changes in the zone Δx using the mass conservation law i.e. any change in the amount of solute in the zone (ΔM) will equal the difference between the amount of material which enters the zone (M_{in}) and the amount which leaves it (M_{out}):

$$\Delta M = M_{in} - M_{out} \qquad \textbf{(E3)}$$

The amount of material that crosses A in a time interval Δt is given as $M = JA\Delta t$. So,

$$\Delta M = M_{in} - M_{out} = (J_{in} - J_{out})A\Delta t \qquad \textbf{(E4)}$$

The quantity ΔM also equals the product of the volume of the zone ($A\Delta x$) and the concentration change (ΔC) that occurs in it such that

$$\Delta M = A\Delta x\Delta C \qquad \textbf{(E5)}$$

Equating equations (E4) and (E5) and rearranging gives

$$\frac{(J_{in} - J_{out})}{\Delta x} = \frac{\Delta C}{\Delta t} \qquad \textbf{(E6)}$$

Considering the contributions of convective J_c and diffusive J_d flux gives

$$\frac{\left(J_c + J_d\right)\Big|_x - \left(J_c + J_d\right)\Big|_{x+\Delta x}}{\Delta x} = \frac{\Delta C}{\Delta t} \qquad \textbf{(E7)}$$

Substituting the expressions of J_c and J_d from equations (E1) and (E2) respectively gives

$$\frac{\left(vC - D\frac{\partial C}{\partial x}\right)\Big|_x - \left(vC - D\frac{\partial C}{\partial x}\right)\Big|_{x+\Delta x}}{\Delta x} = \frac{\left[vC\big|_x - D\frac{\partial C}{\partial x}\Big|_x - vC\big|_{x+\Delta x} + D\frac{\partial C}{\partial x}\Big|_{x+\Delta x}\right]}{\Delta x} = \frac{\Delta C}{\Delta t} \qquad \textbf{(E8)}$$

Collecting terms containing v and D, gives

$$\frac{v\left(C\big|_x - C\big|_{x+\Delta x}\right)}{\Delta x} + \frac{D\left(-\frac{\partial C}{\partial x}\Big|_x + \frac{\partial C}{\partial x}\Big|_{x+\Delta x}\right)}{\Delta x} = \frac{\Delta C}{\Delta t} \qquad \textbf{(E9)}$$

The first term is simply $\frac{-v\left(-C\big|_x + C\big|_{x+\Delta x}\right)}{\Delta x}$ such that

$$\frac{-v\left(-C\big|_x + C\big|_{x+\Delta x}\right)}{\Delta x} + \frac{D\left(-\frac{\partial C}{\partial x}\Big|_x + \frac{\partial C}{\partial x}\Big|_{x+\Delta x}\right)}{\Delta x} = \frac{-v\Delta C}{\Delta x} + \frac{D\frac{\Delta \partial C}{\partial x}}{\Delta x} = \frac{\Delta C}{\Delta t} \qquad \textbf{(E10)}$$

Shrinking Δx to differential size by taking the limit as Δx and Δt approach zero produces

$$-v\frac{\partial C}{\partial x} + D\frac{\partial^2 C}{\partial x^2} = \frac{\partial C}{\partial t} \qquad \textbf{(E11)}$$

or equivalently

$$\frac{\partial C}{\partial t} + v\frac{\partial C}{\partial x} = D\frac{\partial^2 C}{\partial x^2} \qquad \textbf{(E12)}$$

Appendix F

Appendix F contains the Matlab™ numerical code for the surface tension model presented in section 5.3.

Numerical Code of Surface Tension Model

```
clear;
clc;
close all;
format long;


Cbulk = 0.5;            %mg/ml (Bulk Concentration)
w = 30;                 %cyc/min (Breathing Frequency of 0.5Hz)
BubbleDiameter=0.19;    %cm  (Minimum Bubble Diameter)
Nc = 20;                % Number of cycles


ModAmp=0.1;             %Modulated Amplitude (Fraction of "Vcyc")
ModFreqHz=70;           %Modulated Frequency in "Hz"

Nsc = ModFreqHz*100*2;  %Number of time steps in one cycle

GAMMA_STAR=22.85;       %Equillibrium Surface Tension
GAMMA_MIN=1;            %Minimum Surface Tension
m1=69.9-GAMMA_STAR;
m2=66;

gamma_star = 3e-7;      %mg/cm^2(Equilibrium Interfacial Concentration)
gamma_max = gamma_star*(1+(GAMMA_STAR-GAMMA_MIN)/m2)
gamma = 3.72e-7;

D = ((1e-7)/0.0166);    %Diffusion coefficient converted to cm^2/min
K1 = 100000/1000;       %ml/ (g/min) converted to ml/(mg/min)
K2 = K1/1e2;

Rmin=BubbleDiameter/2;
Amin=4*pi()*(Rmin)^2;


Rmax=Rmin/0.89
Amax=4*pi()*(Rmax)^2;

Vmin=(4/3)*pi()*(BubbleDiameter/2)^3;
Vmax=(4/3)*pi()*(Rmax)^3;
```

```
Vmean=Vmin+(Vmax-Vmin)/2;
Vcyc=(Vmax-Vmin);


delt = 1/(Nsc*w);       % delta t
delx = (sqrt(D*delt))/2;% delta x
t = Nsc*Nc*delt;        % total simulation time
alpha = (D*delt)/delx^2;
Nsn=round(5*2*sqrt(Nsc)*max(sqrt(Nc),(1/(sqrt(D/w)))*(gamma_star/Cbulk
)));  % Number of spatial nodes

C = ones(Nsn+1,1)*Cbulk;  %concentration vector
delC = zeros(Nsn+1,1);    %change in concentration
Cmat = zeros(Nsn+1,Nsn+1);%coefficient matrix
Cvect = zeros(Nsn+1,1);   % RHS of equation
count = 1;

%% MAIN TIME LOOP %%

for k=0:delt:(t)

%% Calculate k values - needed before assembly of coefficient matrix

     if gamma <= gamma_star && gamma > (0.96*gamma_star) && (Rn1-Rn)<0
         k1 = 25*(1-(gamma/gamma_star)) * K1;
        k2 = 25*(1-(gamma/gamma_star)) * K2;
     else
        k1 = K1;
        k2 = K2;
    end

%% Bubble parameters - needed for relative velocity %%

    Vn       =       Vmean       +       (Vcyc/2)*sin(2*pi*w*k       -
(pi/2))+(ModAmp*Vcyc)*sin(2*pi*(ModFreqHz*60)*k);   % current timestep
    Rn = nthroot(0.75*Vn/pi,3);

    Vn1      =      Vmean      +      (Vcyc/2)*sin(2*pi*w*(k+delt)      -
(pi/2))+(ModAmp*Vcyc)*sin(2*pi*(ModFreqHz*60)*(k+delt));%next timestep
    Rn1 = nthroot(0.75*Vn1/pi,3);

    delR = (Rn1-Rn);               % change in radius

 %% Build 1st line of coefficient matrix %%

    X = Rn;
    Xn = Rn1;
    A = 4*pi*X^2;
    An = 4*pi*Xn^2;

    if k == 0
        M = gamma_star*A;           % initial total mass
    end;

    if gamma < gamma_star                                % regime 1
        Cmat(1,1) = (1/delt) + k1*C(2,count)+ k2;
        Cmat(1,2) = -k1*(gamma_star*An - M);
        Cvect(1) = k1*C(2,count)*(gamma_star*An - M) - k2*M;
```

```
    elseif gamma >= gamma_star & gamma < gamma_max % regime 2
        Cmat(1,1) = 1;
        Cvect(1) = 0;

    elseif gamma >= gamma_max                     % regime 3
        Cmat(1,1) = 1;
        Cvect(1) = An*gamma_max - A*gamma;

     end

    %% Build 2nd line of coefficient matrix %%

    X = Rn1 + (0.5*delx);           % second coordinate
    A = 4*pi*X^2;
    Ap = 4*pi*(X+(delx/2))^2;
    Vreltop = ((4*pi*Rn1^2/Ap)-1)*(delR/delt);
    Qp = Ap*(alpha + max(-Vreltop,0)*(delt/delx));

    Cmat(2,1) = 1/delx;
    Cmat(2,2) = A + Qp;
    Cmat(2,3) = -Qp;
    Cvect(2) = Qp*(C(3,count)-C(2,count));

    %% Build remainder of coefficient matrix %%

    for j=3:Nsn

        X = Rn1 + ((j-1.5)*delx);
        A = 4*pi*X^2;
        Ap = 4*pi*(X+(delx/2))^2;
        An = 4*pi*(X-(delx/2))^2;
        Vreltop = ((4*pi*Rn1^2/Ap)-1)*(delR/delt);
        Vrelbot = ((4*pi*Rn1^2/An)-1)*(delR/delt);
        Qp = Ap*(alpha + max(-Vreltop,0)*(delt/delx));
        Qn = An*(alpha + max(Vrelbot,0)*(delt/delx));
        Cmat(j,j-1) = -Qn;
        Cmat(j,j) = Qn + A + Qp;
        Cmat(j,j+1) = -Qp;
        Cvect(j)   =   Qp*C(j-1,count)   -   (Qn   +   Qp)*C(j,count)   +
Qp*C(j+1,count);
    end;

 %% Build last line of coefficient matrix %%

    Cmat(Nsn+1,Nsn+1) = 1;
    Cvect(Nsn+1) = 0;

    %% Solve matrix for delta C %%
    delC = Cmat \ Cvect;
    C(:,count+1) = C(:,count)+delC;
    M = M + delC(1);
    gamma = M/An;

    %% Trouble shooting %%

    clc;
```

```
    count;

   temp(count) = gamma/gamma_star;%delC(1);
   time(count)=k;

     %%%%Surface Tension Isotherm
   if gamma < gamma_star                              % regime 1

GAMMA=-m1*temp(count)+72;

elseif gamma >= gamma_star & gamma < gamma_max      % regime 2

GAMMA=GAMMA_STAR-m2*(temp(count)-1);

elseif gamma >= gamma_max                          % regime 3
GAMMA=GAMMA_MIN;

   end

   time_seconds(count)=k*60;

   Area(count)=An; %cm^2
   RelArea(count)=(An/Amax)*100;

   SurfaceTension(count) = GAMMA;

   Amount(count)=M;


    figure (1): subplot (2,2,1); plot (Area,SurfaceTension);
    xlabel({'Area';' (cm^2)'});
    xlim([0.09 0.13]);
    ylabel({'GAMMA';' (dyne/cm)'});
    ylim([0 70]);
    grid on;

      subplot(2,2,2); plot(time_seconds,SurfaceTension);
      xlabel('time (seconds)');
      ylabel({'Surface Tension';' (dyne/cm)'});
      grid on;

    subplot (2,2,3); plot (time_seconds,Amount);
    xlabel('time (seconds)');
    ylabel({'Surfactant Amount';'(g)'});
    grid on;


     subplot (2,2,4); plot (time_seconds,Area);
     xlabel('time (seconds)');
     ylabel({'Area';'(cm^2)'});
     grid on;

count = count + 1;

 end;    %END OF MAIN TIME LOOP
```

Appendix G

Appendix G contains the Matlab™ code that measures the dimensions of the surfactant bubble from captured images as mentioned in section 5.5.2.

Matlab™ Code to Measure Bubble Dimensions

```
clear

for k=1:846 % The value of k changes depending on the number of stored
images

filename=['D:\Ddrive\AA PHD Stuff\SURFACTOMETER\Image Analysis\Final
Trials\breathcycle\breathcycleRun1_C001S0001\breathcycleRun1_c001s000'
, int2str(k+1000000), '.jpg'];

A=imread(filename);
            yup=168;
            ybot=418;
            xleft=47;
            xright=462;
            grayvalue=225;

B=A(yup:ybot,xleft:xright); %selects area in image for analysis
search = true;
search2=true;
clear C
for i = 1: ybot-yup
    for j=1:xright-xleft
        % Thi searches for the first spot on the picture to fall below
          225 which is almost full white.
        if B(i,j) < grayvalue & search == true
          C(i,1)=j;
            search=false;

        end
        % this searches from the other side
        if B(i,(xright-xleft+1)-j) < grayvalue & search2 == true
            C(i,2)=(xright-xleft+1)-j;
            search2=false;
        end
    end
    search=true;
    search2=true;
```

```
end
        % diameter is simply at the widest point

x=0;
l=0;
m=0;
while x > -0.0000001
   l=l+1;
   x=C(l+1,2)-C(l,2)+x;
end
x=0;
while x < 0.0000001
   m=m+1;
   x=C(m+1,1)-C(m,1)+x;
end
centre=[0.25*(l+m)
0.5*(C(round(0.25*(l+m)),2)+C(round(0.25*(l+m)),1))];

for n=1:length(C)-centre(1)
    dist1=centre(1)-(n-1+centre(1));
    dist2=0.5*(abs(centre(2)-(C(n+round(centre(1)),2)))+abs(centre(2)-
C(n+round(centre(1)),1)));
    radius(n)=sqrt(dist1^2 +dist2^2);
end
X=[ones(length(radius),1) (1:1:length(radius))'];
a=[X\radius' X\radius'];
radii(k,:)=[a(1) a(1)+length(radius)*a(2) k]
clear radius
clear X
end
```

Appendix H

Appendix H contains the Matlab™ code that calculates the surface tension from the measured bubble dimensions as mentioned in section 5.5.2.

Matlab™ Code to Calculate Surface Tension

```
k=4960 % value of k depends on the number of captured images

t=[0:0.001:(k-1)*0.001];

Xe_pixel=radii(1:k,1);
Ye_pixel=radii(1:k,2);

a = 1;
b = [1/4 1/4 1/4 1/4];
Ye_pixel = filter(b,a,Ye_pixel);
Ye_pixel = filter(b,a,Ye_pixel);

Ratio=Xe_pixel./Ye_pixel;

Tube_pixel=(377-190)% measured from image

rho_air=1.1232e-3%g/cm^3
rho_liquid=0.972%g/cm^3
gravity=980.6%cm/s^2
Tube_actual=1.18e-1%cm
delta_rho=(rho_liquid-rho_air)

Z=(Ratio-1.5922)/0.5922;
alphaZ=2.5924+Z.*(2.1838+Z.*(-0.1302+Z.*(-0.1347+Z.*(0.1141))));
Bond_NmZ=exp(alphaZ)-1.7;
Xe_bZ = 0.5864+Z.*(-.3512+Z.*(0.0859+Z.*(0.00898+Z.*(-0.01415))));
Ye_bZ = 0.3684+Z.*(-0.3555+Z.*(0.1857+Z.*(-0.07188+Z.*(0.01830))));


Y = ((2.*(Ratio-1.9770849))/(2.3830324)) - 1.;
alphaY      =      7.5552+Y.*(3.3776+Y.*(-0.160502+Y.*(0.0869371+Y.*(-
0.0399012))));
Bond_NmY = exp(alphaY);
Xe_bY             =             0.1092+Y.*(-0.14115+Y.*(0.090578+Y.*(-
0.04132675+Y.*(0.0123094))));
```

```
Ye_bY           =           0.0345+Y.*(-0.0551257+Y.*(0.04901677+Y.*(-
0.04104224+Y.*(0.01978285))));



GAMMAX = 980.6/(delta_rho)./(Bond_NmZ.*(Xe_bZ.^2));
GAMMAY=980.6/(delta_rho)./(Bond_NmY.*(Ye_bY.^2));

Xe=(Tube_actual/Tube_pixel).*Xe_pixel;
Ye=(Tube_actual/Tube_pixel).*Ye_pixel;
Ye_exp=(Tube_actual/Tube_pixel).*Ye_pixel;



SurfaceTensionY=((gravity*delta_rho)/980.6).*(Ye.^2).*GAMMAX

SurfaceTensionZ=((gravity*delta_rho)/980.6).*(Xe.^2).*GAMMAX
SurfaceTensionZ = filter(b,a,SurfaceTensionZ);



Area=4*pi()*Xe.^2; % in cm^2
Area = filter(b,a,Area);

Volume=4/3*pi().*Xe.^3;
Volume=Volume*1000 %convert to micro litres
Volume = filter(b,a,Volume);

 figure (1):subplot (2,2,1); plot (Area*100,SurfaceTensionZ);
     title('Surface Tension vs Area');
     xlabel('Area (mm^2)');
     ylabel({'Surface Tension';'(dyne/cm)'});
     grid on;

    subplot(2,2,2); plot(t,SurfaceTensionZ);
    title('Surface Tension  vs Time (s)');
    xlabel('Time (s)');
    ylabel({'Surface Tension';'(dyne/cm)'});
    grid on;


   subplot(2,2,3);plot(t,Xe*10,t,Ye*10);
    title('Radius vs Time');
    xlabel('Time (s)');format short;
    ylabel('Radius (mm)');
    grid on;

   subplot(2,2,4);plot(t,Area*100);
   title('Bubble Area vs Time (s)');
    xlabel('Time (s)');
   ylabel('Area (mm^2)');

  grid on;
```